Numerical modeling for comprehensive human exposure and infection control assessment based on fluid engineering and statistical physics

久我, 一喜

Numerical modeling for comprehensive human exposure and infection control assessment based on fluid engineering and statistical physics

Kazuki Kuga

A thesis for the degree of
Doctor of Engineering

Department of Energy and Environmental Engineering
Interdisciplinary Graduate School of Engineering Sciences
Kyushu University
Japan

August 2020

ABSRACT

In this research, we developed a numerical human model for comprehensive human exposure risk assessment based on fluid engineering and a mathematical epidemic model for infectious disease control assessment based on statistical physics. The contents of each chapter are summarized below.

As an introduction, Chapter 1 clarifies the research background and the purpose of this research on the exposure phenomenon hidden in the living environment. In particular, in this study, we will tackle the three individual issues: (1) prediction of epidemic spreading for infectious diseases and elucidation of vaccination dilemma by mathematical epidemic model and multi-agent simulation (MAS), (2) development of a numerical human model for indoor environment analysis that enables risk assessment of inhalation and dermal exposure, (3) development of a model for predicting the amount of carbon dioxide emitted form humans by subjective experiments. in addition, we also clarify the importance, necessity, and academic novelty of this research.

In Chapter 2, we developed a mathematical epidemic model by a closed ordinary differential equation whose solution can be uniquely determined if the initial value is given. Firstly, we reviewed three mathematical models that capture the infection transmission phenomenon on networks from the previous studies, and determined the infection parameters from the final epidemic size. In addition to incorporating the effects of vaccination into these mathematical models, we developed a mathematical model that takes into account the probability of immunity associated with vaccination and the reduction of infection probability due to protective behavior such as mask use. Furthermore, by integrating the transmission dynamics and the vaccination decision-making dynamics, it is adapted to the framework of vaccination games. The prediction accuracy of these developed mathematical models has been verified by comparison with the corresponding MAS results.

In Chapter 3, applying the mathematical model developed in Chapter 2, we investigated the optimal design of subsidizing policy for vaccination. To minimize the total social cost, which includes all illness costs, vaccination costs, and the tax burden imposed on all social members, four subsidy policy were prepared and explored. Furthermore, this mathematical model quantitatively evaluates the impact of the effectiveness of vaccination on subsidy policy for vaccination. In addition, MAS investigated the effect of difference of network topologies.

In vivo studies targeting mammalian surrogate models for toxicity studies have various limitations due to animal protection and ethical problems. On the other hand, the so-called in silico model based on the numerical analysis model has a great potential to contribute to the understanding of heat and mass transport phenomena in the respiratory tract, and can be an alternative method for in vivo and in vitro tests. In Chapter 4, a numerical airway model for the upper airways of rat, dog, monkey, and humans were created based on CT data. We analyzed the heat and mass transport in each upper airway model by applying it to CFD technique. The convective heat transfer coefficient corresponding to the breathing

flow rate was calculated and organized by various dimensionless numbers. We confirmed that the heat transfer efficiency in the upper airways of dog is approximately the same as that of the human, while the rat and monkey monkeys are significantly different from the human. Identification of the basic state of convective heat transfer in the upper airway of rats, dogs, monkeys, and humans is an important finding in discussing the quantitative difference in heat and mass transfer efficiency between different species.

In Chapter 5, focusing on the high-concentration short-term exposure problem caused by environmental tobacco smoke, a risk assessment for first- and second hand exposure due to the use of electronic cigarettes was conducted by using the numerical analysis method. Due to lack of combustion process, e-cigarette has been perceived hermless than conventional cigarettes, and the number of users has been increasing in recent years. However, e-cigarettes have the potential to release hermful substances by the components of vapor, and the significant number of epidemiological studies have been conducted and the health effects of using e-cigarettes have been shown. On the other hand, there was no debate about the effects of contaminants emitted by e-cigarette users on indoor air quality and second hand exposure to nonsmokers. In this chapter, we develop a new numerical human model integrated with the numerical human respiratory tract model. The physiological pharmacokinetic (PBPK) model was newly developed, which reproduces inhalation exposure through the respiration and dermal exposure from the skin surface in order to study the absorption mechanism of pollutants into local tissues. By integrating these models into the developed numerical human model and reproducing transient puffing of e-cigarettes, the numerical simulations reproduced the exposure process from (i) the first-hand exposure by inhalation of e-cigarettes, (ii) the dispersion of contaminants exhaled by e-cigarette user in the indoor environment, up to (iii) the second hand exposure by inhalation or dermal absorption of passive smoker.

In Chapter 6, focusing on the gas exchange in the respiratory system from the viewpoint of improving the accuracy of the physiological model of the numerical human model, the effects of indoor carbon dioxide concentration and room temperature on the carbon dioxide production from the human body were investigated by subjective experiments using a small chamber in the Technical University of Denmark. For the subjective experiments, six male subjects were recruited and each had a small chamber of 1.7 m^3 for light office work. Five different environmental conditions with two temperature levels and three carbon dioxide concentration levels are prepared to study the effects of indoor environmental conditions. The CO_2 concentration is adjusted by dosing CO_2 gas or changing the ventilation rate. Moreover, the carbon dioxide concentration is monitored and the carbon dioxide emission rate is calculated by the mass balance equation. In addition to carbon dioxide concentration, physiological response parameters such as respiratory rate and end-tidal carbon dioxide partial pressure ETCO2 were also measured.

Chapter 7 summarized the results obtained throughout this paper, mentioned academic and engineering contributions, and organized future works.

ACKNOWLEDGEMENTS

This thesis is based on my research work carried out since April 2015 at Ito Laboratory, Interdisciplinary Graduate School of Engineering Sciences, Kyushu University, and since September 2017 at Tanimoto Laboratory, Interdisciplinary Graduate School of Engineering Sciences, Kyushu University, and since Febuarry 2019 at the International Centre for Indoor Environment and Energy, Technical University of Denmark (ICIEE, DTU).

For the completion of this dissertation, I would like to express my sincere gratitude to my supervisor, Professor Kazuhide Ito, Interdisciplinary Graduate School of Engineering Sciences, Kyushu University. His precise advices and warm and generous supports that enabled me to continue and finish up the research. He has been the great professor providing me uncountable opportunities to experience many things at each stage of my study since I became a member of his laboratory to prepare my bachelor thesis in April 2015.

I wish to acknowledge my examiners, Professor Kazuhide Ito, Professor Jun Tanimoto, and Associate Professor Naoki Ikegaya, Interdisciplinary Graduate School of Engineering Sciences, Kyushu University; and Dr. Pawel Wargocki, Associate Professor at the ICIEE, DTU. The quality of the thesis was obviously improved by their extensive reviews and precious advices and suggestions.

Many thanks to Professor Jun Tanimoto for his supervising and great advises. I leared the modeling of epidemic dynamics based on the stastical physics

Special thanks to Associate professor Pawel Wargocki for his supervising and a significant support during and after my stay at the ICIEE, DTU. I learned how to conduct the laboratory research from the beginning.

I would like to express my gratitude to Assistant Professor Sung-Jun Yoo for his help and advice during this investigation. He was my roll model to advance my research.

I would also like to express my appreciation for my colleague Mr. Mitsuharu Sakamoto for his accurate contributions to the research related to Chapter 6 and also my appreciation for all former and current members of Ito Laboratory in the department of Energy and Environmental Engineering, IGSES, Kyushu University, especially Dr. Nguyen Lu Phuong, Dr. Alicia Murga with whom I share many memories of these past years.

Finally, I would like to express my sincere appreciation to my beloved family for their generosity, patience and unlimited support.

Contents

Nomenclature

Chapter 2 and 3

$S(t)$	The fraction of susceptible individuals at time t ([0,1] for non-vaccination case, [0, 1 – x] for vaccination case)
$I(t)$	The fraction of infected individuals at time t [0,1]
$R(t)$	The fraction of recovered individuals at time t [0, 1]
$V(t)$	The fraction of vaccinated individuals at time t [0,1]
β	Disease transmission rate (person^{-1} day^{-1})
γ	Recovery ratge (day^{-1})
R_0	Basic reproduction number (= β/γ)
x	Vacciantion coverage, which means the fraction of initial vaccinatied individuals or individuals prepared intermediate protective measure [0,1]
e	Effectiveness of vaccination
η	Efficiency of intermediate protective measure
k	The number of degree (connectivity with neighbers)
P(k)	Degree distribution, which means the probability that an arbitral individual has degerr k
$\langle k \rangle$	Average degree
λ	Disease transmission rate used in network model
Q	The number of degree (connectivity with neighbers) used in pair approximation model
$[X](t)$	The fraction of individuals in state X at time t [0,1]
$[XY](t)$	The number of X – Y edges (pairs) linking a node in state X with a node in state Y on networks at time t
$Q(I\|SS)$	The average number of infected neighbors of a susceptible, given that the susceptible already has at least one susceptible neighbor
$Q(I\|SI)$	The average number of infected neighbors of a susceptible, given that the susceptible already has at least one infected neighbor
$Q(I\|SR)$	The average number of infected neighbors of a susceptible, given that the susceptible already has at least one recovered neighbor
α	The vaccinator-nonvaccinator connection coefficient, which can be said dissortativity observed at initial moment of every season (time-evolved in repeating seasons), and is less than x and 1 – x
C_v	Vaccination cost

C_i	Infection cost
C_r	Relative cost of vaccination ($C_r = C_v / C_i$, $C_i = 1$) [0,1]
$<\pi>$	The average social payoff
$<\pi_C>$	The average corporative (vaccinated) payoff
$<\pi_D>$	The average defective (non-vaccinated) payoff
$P(s_i \leftarrow s_j)$	The probability that individual i adopts the selected neighbor j's strategy
s_i	The strategy of i
κ	the strength of selection (the sensitivity of individuals to differences in their payoffs); smaller κ means that an individual is more sensitive to a payoff difference ($\kappa > 0$)
SFR	Successful free-rider who pays nothing
FFR	Failed free-rider who pays −1
IV	Infected vaccinator who pays $-C_r-1$
HV	Healthy vaccinator who pays $-C_r$
$P(A \rightarrow V \mid AB)$	The transition probability that the focal A of pair AB change to the opposite strategy (vaccinator)
Subscripts	
V	Vaccinated individauls
N	Non-vaccianted individuals
σ	The population fraction to be subsidized
TAX	Tax burden per capita, ($TAX = C_r \sigma$)
TSP	Total social payoff per capita due to an epidemic
SB	Total subsidy budget
σ'	Subsidy distribution ratio
f_C	The fraction of voluntary vaccinators (corparator)
f_D	The fraction of non-vaccinators (defector), $f_D=1-f_C$

Chapter 4

v	Kinematic viscosity
ρ	Air density
τ_w	Wall shear stress
$u*$	Friction velocity ($=\sqrt{\tau_w/\rho}$)
h_c	Respiratory convective heat transfer coefficient
Q_c	Heat flux
T_w	Respiratory wall temperature (K)

T_{air}	inhaled air temperature (K)
Nu	Nusselt number
λ	Thermal conductivity of the air (W/m-K)
D_T	Representative diameter (m), the diameters in the trachea
Re	Reynolds number
Pr	Prandtl numbers
u	Representative axial velocity
α	Thermal diffusivity

Chapter 5

$\overline{C_a}$	Ensemble mean contaminant concentration in a grid point
D_a	Diffusion coefficient of contaminant in air
v_t	Turbulent viscosity
σ	Turbulent Schmidt number.
H_m	Thickness of mucus (μm)
H_t	Thickness of epithelium (μm)
H_b	Thickness of sub-epithelium (μm)
C_m	Contaminant concentrations in the mucus ($\mu g/m^3$),
C_t	Contaminant concentrations in the epithelium ($\mu g/m^3$),
C_b	Contaminant concentrations in the sub-epithelium ($\mu g/m^3$),
D_m	Diffusion coefficients in the mucus (m^2/s)
D_t	Diffusion coefficients in the epithelium (m^2/s)
D_b	Diffusion coefficients in the sub-epithelium (m^2/s)
Q_b	Blood flow rate in the sub-epithelium (ml/s)
V_b	Volume of sub-epithelium (ml)
y	Distance in the respiratory tissue from the interface between air and mucus (m)
P_{ma}	Mucus-air partition coefficient
P_{tm}	Tissue-mucus partition coefficient
P_{bt}	Blood-tissue partition coefficient
k_f	Non-specific first-order metabolic clearance
V_{maxC}	Coefficient that represents saturable metabolism per unit volume of tissue
K_m	Michaelis constant
K	Boltzmann constant
η	Viscosity of water
r_s	Solute radius (Å)
MW	Molecular weight of chemicals

P_{ba}	Blood-air partition coefficient
a	The fraction of neutral lipids in blood
b	The fraction of phospholipids in blood
c	The fraction of water in blood
P_{ow}	Octanol-water partition coefficient.
I	Turbulent intensity
T_{sk}	Skin surface temperature (K)
Q_t	The amount of sensible heat flux from the skin surface (W/m^2)
R_{cl}	Thermal resistance of the clothes ((m^2 K)/W) (reciprocal of the heat conductance value)
C_{SSL}	Contaminant concentrations in the skin surface lipid ($\mu g/m^3$)
C_{SC}	Contaminant concentrations in the stratum corneum ($\mu g/m^3$)
D_{SSL}	Diffusion coefficients in the skin surface lipid (m^2/s)
D_{SC}	Diffusion coefficients in the stratum corneum (m^2/s)
H_{SSL}	Thickness of the skin surface lipid (m)
H_{SC}	Thickness of the stratum corneum (m)
y	Distance in the respiratory tissue from the interface between air and skin surface lipid (m)
$P_{SSL:a}$	Lipid-air partition coefficient
$P_{SC:SSL}$	Stratum corneum-lipid partition coefficient

Chapter 6

C_{in}	Indoor CO_2 concentration at steady state (ppm)
Q	Volumetric airflow rate (m^3/h)
C_{out}	Outdoor CO_2 concentration (ppm)
G	CO_2 emission rate (mL/h)
$C_{pure+met}$	CO_2 concentration comprising the pure CO_2 delivered from the cylinder and the metabolically generated CO_2 that was emitted by the subject
C_{pure}	CO_2 concentration contributed only by pure CO_2, which was measured from the indoor CO_2 level that was reached within a few minutes after the subject had left the chamber.

Chapter 1: General introduction

1.1 Background and Motivation

In our life, there are multiple exposure risks on various scales from social scale to indoor scale. Taking the problem of epidemic spreading of infectious diseases caused by contact between people as an example of exposure in social scale, this dynamics is on complicated and wide scale such as human relations and society. Kermack and McKendrick [1] developed a mathematical general theory of epidemics of infectious diseases and compared them with actual data. Their work provided a modern basis for subsequent mathematical models of epidemics [2-5]. Based on them, the theoretical epidemic model (macro model) using the differential equations has been used. Moreover, various infectious disease epidemic models have been proposed, including an agent-based simulation model (micro model). Recently, based on the complicated network science that represents individual contact relationships with nodes and edges, multi agent simulations (MAS) have been conducted with relatively easy analysis and a certain reality [6]. In addition, although there are many infectious diseases in which preemptive vaccination such as influenza is effective for public health, the vaccination is generally self-paid and not compulsory. Therefore, the vaccination coverage and morbidity in the entire society strongly depends on individual decision making. To reproduce this decision-making dilemma associated with vaccination, a framework for "vaccination game" has been proposed that incorporates the effects of vaccination into a mathematical epidemic model and integrates evolutionary game theory [7,8]. To date, the stochastic MAS has been adopted for modeling and analysis of vaccination games, which can flexibly predict dynamics only by accumulating a priori local rules based on the bottom-up principle. However, because it is a stochastic method, it requires a sufficient number of trials, and the analysis takes much time. Thus, the theoretical (deterministic) epidemic model corresponding to the stochastic MAS approach must be developed to quickly analyze the epidemic spreading. In addition, the theoretical epidemic model can help us deeply understand the epidemic dynamics compared to the stochastic MAS approach.

Focusing on relatively small scale, indoor environment, most of modern people spend more than 90% of their time indoors. Thus, the indoor air quality (IAQ) greatly affects the quality of life. Because people now stay indoors much time compared to the past, IAQ issues are becoming increasingly important in terms of the health risks of building occupants [9,10]. Although human health problems caused by various types of indoor air pollutions, they can be classified in terms of the level of contaminant concentration, exposure time, types of contaminants. We listed three as representative cases: (i) highly concentrated short-term exposure to environmental tobacco smoke (ETS), including mainstream smoke (first-hand smoke) and side-stream smoke (second-hand smoke), and exhaust gas

from combustion equipment; (ii) low-concentration long-term revelation by a very small amount of volatile organic compounds (VOCs) represented by the sick-house syndrome; and (iii) air pollution caused by various fine/ultrafine particles, biological aerosols, and infectious contaminants (e.g., PM2.5, PM10, fungal spores, pollen, and influenza virus via coughing and sneezing).

First, focusing on the impact of ETS in indoor environments as an example of highly concentrated short-term exposure, smoking is one of the leading risk factors for premature death and disability. The mortality and morbidity associated with cigarette smoking is caused by the inhalation of various highly concentrated contaminants, which are generated through the tobacco combustion process. In addition to the effects of direct inhalation of first-hand smoke, the impacts of second-hand smoke on IAQ after being used indoors have been recognized.

Second, paying attention to low-concentration long-term exposure, in recent years, the number of houses that are airtight, have effective thermal insulation, and are insufficiently ventilated has been increasing [11]. As a result of this, residents are exposed to VOCs emitted from new building materials used in new construction methods. Although the concentration of VOCs is relatively low, people inhale them by constant respiration and absorb them through the skin for a long time and suffer from sick-house syndrome.

Finally, recent epidemiological studies indicate that exposure to particulate air pollution (e.g., PM2.5 and PM10) is associated with increased risk of lung cancer, asthma, and chronic diseases, as well as increased risk of induced mortality and morbidity in humans [12-15]. When individuals are indoors, they can be exposed to particulate matter that originates from the outdoor environment and penetrates the indoor environment through ventilation. Moreover, in public accommodations, which an unspecified number of people use, the spread of infectious diseases caused by droplets or air infections, such as influenza, tuberculosis, or measles, is a concern.

In order to solve these problems and realize a good indoor air environment design, it is essential accurately predict concentration distributions for various gaseous and aerosol pollutants existing in the indoor environment is essential. It is important research issue to establish the technology for reducing contaminant concentration based on the prediction results. For realizing the good indoor air environment, the design goal should be the minimization of the human exposure of the occupants. Considering that non-uniform flow patterns and contaminant concentration distribution are formed in the indoor environment, it is essential to incorporate the human model into the predictive design method. Many numerical human models for prediction of thermal comfort and indoor air quality have been proposed [16-19]. However, the numerical human model has not been developed for risk assessment of inhalation exposure due to breathing indoor air and dermal exposure due to contact between air and skin or the building surface materials and furniture and the skin.

In addition to risk assessment of inhalation and dermal exposures, to further expand the numerical human model to indoor environmental design, it is important to precisely reproduce the relationship

between the indoor environment and the human physiological mechanism. Focusing on carbon dioxide emission from humans as a future work, we will develop a mathematical model that describes the generation, release, and transport mechanism of carbon dioxide and integrate it into the numerical human model. In this way, the research approaches that have been conducted is so-called numerical analysis. It is essential to validate the prediction accuracy of the model by experiments because the numerical analysis reproduces the phenomenon based on the model after modeling the phenomenon in advance. On the other hand, targeting exposure risks and health effects, there are physical parameters that are difficult to observe and measure due to ethical problems and limitations of measuring instruments. With regard to such parameters, we have to rely on the development and numerical analysis of mathematical models. In order to solve the problems by these two research approaches, the numerical analysis approach and the experimental approach should be incorporated so as to complement each other from the planning stage of the research.

1.2 Structure of thesis

This thesis is organized into seven chapters as follows:

- In Chapter 2, we developed a mathematical epidemic model by a closed ordinary differential equation whose solution can be uniquely determined if the initial value is determined. Firstly, we reviewed three mathematical models that capture the infection transmission phenomenon on networks from the previous studies, and determined the infection parameters from the final epidemic size. In addition to incorporating the effects of vaccination into these mathematical models, we developed a mathematical model that takes into account the probability of immunity associated with vaccination and the reduction of infection probability due to protective behavior such as mask use. Furthermore, by integrating the transmission dynamics and the vaccination decision-making dynamics, it is adapted to the framework of vaccination games. The prediction accuracy of these developed mathematical models has been verified by comparison with the corresponding MAS results.
- In Chapter 3, applying the mathematical model developed in Chapter 2, we investigated the optimal design of subsidizing policy for vaccination. To minimize the total social cost, which includes all illness costs, vaccination costs, and the tax burden imposed on all social members, four subsidy policy were prepared and explored. Furthermore, this mathematical model quantitatively evaluates the impact of the effectiveness of vaccination on subsidy policy for vaccination. In addition, MAS investigated the effect of difference of network topologies.
- In vivo studies targeting mammal surrogate models for toxicity studies have various limitations due to animal protection and ethical problems. On the other hand, the so-called in silico model based on the numerical analysis model has a great potential to contribute to the deep understanding of heat and mass transport phenomena in the respiratory tract, and can be an alternative method for in

vivo and in vitro tests. In Chapter 4, a numerical airway model for the upper airways of rats, dogs, monkeys, and humans was developed based on CT data, and by applying it to computational fluid dynamics (CFD), heat and mass transport in each upper airway model were analyzed. The convective heat transfer coefficient corresponding to the respiratory flow rate is calculated and arranged by various dimensionless numbers.

- In Chapter 5, focusing on the high-concentration short-term exposure problem caused by environmental tobacco smoke, a risk assessment for first- and second hand exposure due to the use of electronic cigarettes was conducted by using the numerical analysis method. Due to lack of combustion process, e-cigarette has been perceived hermless than conventional cigarettes, and the number of users has been increasing in recent years. However, e-cigarettes have the potential to release hermful substances by the components of vapor, and the significant number of epidemiological studies have been conducted and the health effects of using e-cigarettes have been shown. On the other hand, there was no debate about the effects of contaminants emitted by e-cigarette users on indoor air quality and second hand exposure to nonsmokers. In this chapter, we develop a new numerical human model integrated with the numerical human respiratory tract model. The physiological pharmacokinetic (PBPK) model was newly developed, which reproduces inhalation exposure through the respiration and dermal exposure from the skin surface in order to study the absorption mechanism of pollutants into local tissues. By integrating these models into the developed numerical human model and reproducing transient puffing of e-cigarettes, the numerical simulations reproduced the exposure process from (i) the first-hand exposure by inhalation of e-cigarettes, (ii) the dispersion of contaminants exhaled by e-cigarette user in the indoor environment, up to (iii) the second hand exposure by inhalation or dermal absorption of passive smoker.
- In Chapter 6, focusing on the gas exchange in the respiratory system from the viewpoint of improving the accuracy of the physiological model of the numerical human model, the effects of indoor carbon dioxide concentration and room temperature on the carbon dioxide production from the human body were investigated by subjective experiments using a small chamber in the Technical University of Denmark. For the subjective experiments, six male subjects were recruited and each had a small chamber of 1.7 m^3 for light office work. Five different environmental conditions with two temperature levels and three carbon dioxide concentration levels are prepared to study the effects of indoor environmental conditions. The CO_2 concentration is adjusted by dosing CO_2 gas or changing the ventilation rate. Moreover, the carbon dioxide concentration is monitored and the carbon dioxide emission rate is calculated by the mass balance equation. In addition to carbon dioxide concentration, physiological response parameters such as respiratory rate and end-tidal carbon dioxide partial pressure $ETCO_2$ were also measured.
- Chapter 7 summarized the results obtained throughout this paper, mentioned academic and

engineering contributions, and organized future works.

Figure 1.1 shows the structure of this thesis.

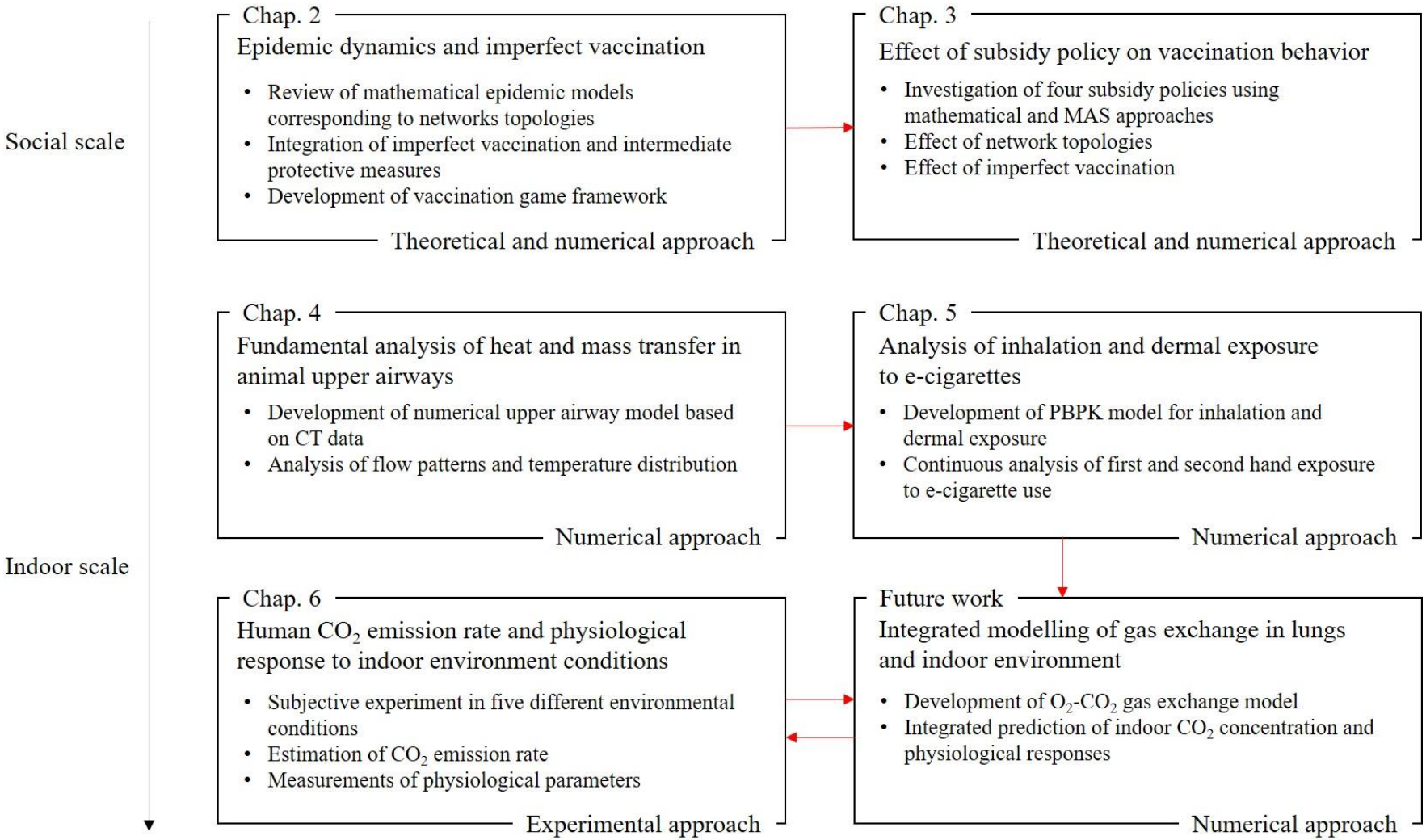

Figure 1.1. Structure of thesis

References

1. Kermack WO, McKendrick AG. 1927. A contribution to the mathematical theory of epidemics. Proceedings of the royal society of london. Series A, Containing papers of a mathematical and physical character, 115(772), 700-721.
2. Dietz K. 1988. The first epidemic model: a historical note on PD En'ko. Australian Journal of Statistics, 30(1), 56-65.
3. Dietz K. 1997. Introduction to McKendrick (1926) Applications of mathematics to medical problems. In Breakthroughs in Statistics (pp. 17-57). Springer, New York, NY.
4. Heesterbeek JAP. 2002. A brief history of R 0 and a recipe for its calculation. Acta biotheoretica, 50(3), 189-204.
5. Nishiura H, Dietz K, Eichner M. 2006. The earliest notes on the reproduction number in relation to herd immunity: Theophil Lotz and smallpox vaccination. Journal of Theoretical Biology, 241(4), 964.
6. Keeling MJ, Eames KT. 2005. Networks and epidemic models. Journal of the Royal Society Interface, 2(4), 295-307.
7. Bauch CT. 2005. Imitation dynamics predict vaccinating behaviour. Proceedings of the Royal Society B: Biological Sciences, 272(1573), 1669-1675.
8. Fu F, Rosenbloom DI, Wang L, Nowak MA. 2011. Imitation dynamics of vaccination behaviour on social networks. Proceedings of the Royal Society B: Biological Sciences, 278(1702), 42-49.
9. European Concerted Action. Guideline for the characterization of Volatile Organic Compounds Emitted from Indoor Materials and Products Using Small Test Chambers. Indoor Air Quality and Its Impact on Man, Report No. 8, 1991.
10. Hays SM. 1995. Indoor Air Quality, Solutions and Strategies. McGraw-Hill, Inc., New York.
11. Weschler CJ. 2006. Ozone's impact on public health: contributions from indoor exposures to ozone and products of ozone-initiated chemistry. Environmental health perspectives, 114(10), 1489-1496.
12. Dockery DW, Pope CA, Xu X, Spengler JD, Ware JH, Fay ME, Ferris BG, Speizer FE. 1993. An association between air pollution and mortality in six U.S. cities. N. Engl J. Med. 329, 1753–1759
13. Krewski D, Burnett RT, Goldberg MS, Hoover K, Siemiatycki J, Jerrett M, Abrahamowicz M, White WH. 2000. Reanalysis of the Harvard Six Cities Study and the American Cancer Society Study of particulate air pollution and mortality. Health Effects Institut, Cambridge, MA.
14. Krewski D, Burnett RT, Goldberg M, Hoover K, Siemiatycki J, Abrahamowicz M, White W. 2005. Reanalysis of the Harvard Six Cities Study, part I: validation and replication. Inhalation toxicology, 17(7-8), 335-342.
15. Krewski D, Burnett RT, Goldberg M, Hoover K, Siemiatycki J, Abrahamowicz M, Villeneuve PJ, White W. 2005. Reanalysis of the Harvard Six Cities Study, part II: sensitivity analysis. Inhalation toxicology, 17(7-8), 343-353.

16. Murakami S. 1997. Flow and temperature fields around human body with various room air distributions, CFD study on computational thermal manikin-Part 1. AHSRAE Transactions, 103, 3-15.
17. Murakami S, Kato S, Zeng J. 1998. Numerical simulation of contaminant distribution around a modeled human body: CFD study on computational thermal manikin--Part II. ASHRAE Transactions, 104, 226.
18. Sorensen DN, Voigt LK. 2003. Modeling flow and heat transfer around a seated human body by Computational Fluid Dynamics, Building and Environment, 38 (6) 753-762
19. Topp C, Nielsen PV, Sørensen DN. 2002. Application of computer simulated persons in indoor environmental modeling, ASHRAE Transactions 108 (2) 1084-9

Chapter 2: Epidemic dynamics with consideration of imperfect vaccination

2.1 Introduction

Human society has long suffered from the spread of infectious diseases such as measles, influenza, Ebola and SARS. To help reduce the impact of these infections disease, several mathematical models and methods have been developed to understand epidemic dynamics and the effect of preventive strategies. Pre-emptive vaccination is one of the most effective preventative measures in modern society to control the epidemic and reduce morbidity and mortality [1,2]. However, voluntary vaccination policies pose a social dilemma, which is difficult to resolve in normal social situations [3,4]. With increased vaccination coverage and achieved herd immunity, there are no new infections. Therefore, these vaccinated individuals can help non-vaccinated individuals escape the infection and save vaccination costs. As a result, a significant number of people stopped vaccinating and benefiting from the efforts of the remaining vaccinators. Under such a voluntary vaccination policy, people decide whether to vaccinate or not depending on various factors such as the cost of vaccination, self-interest, potential risk entailed with vaccination, and how others in their social environment behave toward vaccination.

To model this vaccination dilemma, researchers have studied vaccination games, which can predict the dynamics of (i) epidemic spread in complex social networks and (ii) decision making on whether to undergo vaccination depending on the status of the epidemic. Epidemic dynamics are predicted using mathematical epidemic models such as the susceptible–infected–recovered (SIR) model [5], and decision making is modeled on evolutionary game theory. Bauch *et al*. [6] and Fu *et al*. [7] published a pioneering works for a vaccination game. A significant number of researchers have studied various frameworks to quantitatively investigate multiple effects on vaccination behavior [8–12]. Most research on vaccination games relies on multi-agent simulation (MAS), which allows for a more flexible and realistic modeling approach. In addition to MAS approach, Fu *et al*. [7] proposed a mathematical framework for a mixed-population vaccination game that assumes complete vaccination. A theoretical approach based on a set of ordinary differential equations (ODEs) can be a powerful tool to explicitly demonstrate the dynamics of both epidemic spread and human decision making.

Most studies on the vaccination game have assumed that vaccinations provide perfect immunity to each vaccinator. In reality, vaccinations can only impart partial protection against many infectious diseases, such as measles, influenza, malaria, and HIV. In addition to vaccinations, there are other protective measures from infectious diseases, such as mask wearing, gargling, and hand washing, which are called intermediate protective measures. Although these protective measures come at a more

reasonable cost than vaccinations, they cannot block the transmission of infections to the body as effectively as vaccinations. Therefore, the stochastic effects of imperfect vaccination and intermediate protective measures need to be considered. On the basis of this background, Cardillo *et al*. [13] analyzed the effects of imperfect vaccination on immunization behavior in Erdős–Rényi random graph (ER–RG) [14] and Barabasi–Albert scale free (BA–SF) [15] networks by using the MAS approach. Iwamura *et al*. [16] and Ida and Tanimoto [17] used MAS to investigate the effect of intermediate protective measures on square lattice and BA–SF networks. Wu *et al*. [18] developed a new mathematical framework of the vaccination game that considered imperfect vaccination in an infinite and well-mixed population corresponding with a perfect graph by using mean-field approximation. Several studies have recently used the same concept and investigated the multiple effects of imperfect vaccination and other parameters on vaccination behavior [19–30]. Therefore, the modeling and analysis of the vaccination game can be enriched by the abundant quantity and quality of studies that have followed an MAS or theoretical approach.

2.2 Basic theoretical epidemic models

Theoretical epidemic models corresponding to the spread of diseases in some network topologies have developed. The epidemic dynamics in well-mixed population corresponding to the perfect graph are presented by the most fundamental epidemic model proposed by Kermack and McKendrick [5]. In terms of heterogeneous networks (i.e. Barabasi Albert Scale-free network and ER random graph), which have each degree distribution, Moreno et al. [31] developed the network model. Furthermore, for the more precise modeling of epidemic spreading on complex networks, Keeling [32] developed the pair approximation model. In this study, we focused on regular random graph. Figure 4.1 schematically presents the correspondence between epidemic spreading on the complex networks and the theoretical models. In this section, we reviewed the three theoretical models and determined epidemic parameters by solving the theoretical models.

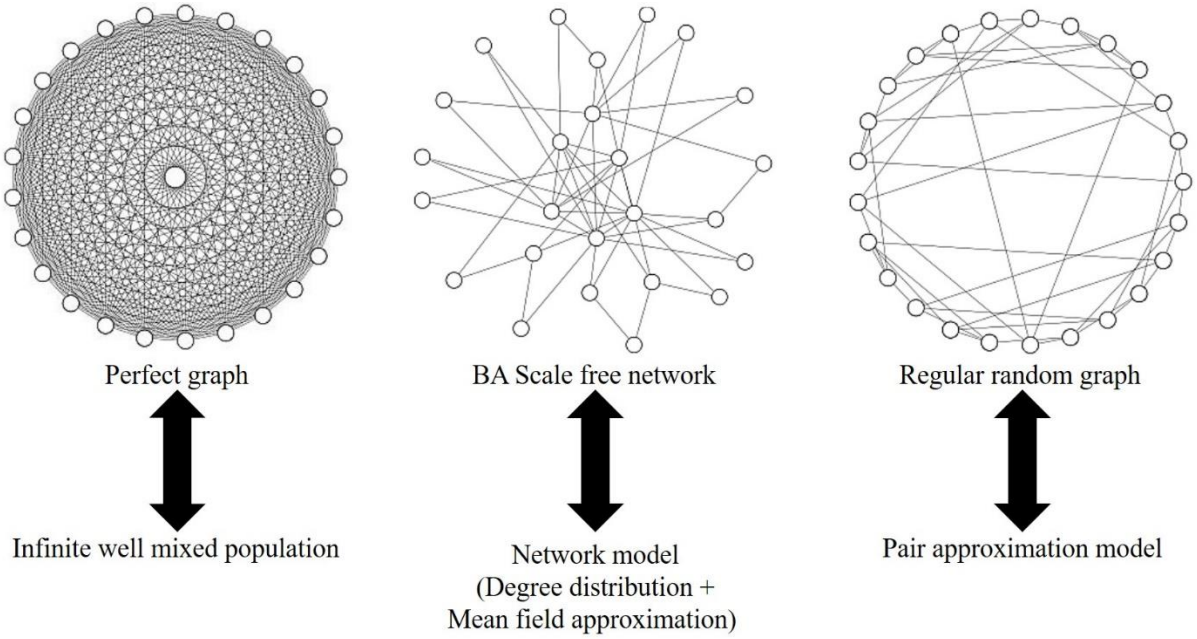

Figure 4.1. Schematic of correspondence between epidemic spreading on complex networks and theoretical models.

2.2.1 SIR model in well-mixed population

In general, the epidemic dynamics in well-mixed population are often described by susceptible-infected-recovered (SIR) model proposed by Kermack and McKendrick [5]. When the population dynamics due to birth and death are ignored, individuals in a population can be classified into susceptible (S), infected (I), recovered (R) states. A susceptible individual may become infected if he/she is exposed to infectious individuals at the disease transmission rate β (day^{-1} person^{-1}). An infected individual recovers at the recovery rate γ (day^{-1}). The SIR model is expressed as:

$$\frac{dS(t)}{dt} = -\beta S(t)I(t), \tag{2-1}$$

$$\frac{dI(t)}{dt} = \beta S(t)I(t) - \gamma I(t), \tag{2-2}$$

$$\frac{dR(t)}{dt} = \gamma I(t), \tag{2-3}$$

with the assumed set of initial values $S(0) = 1$, $I(0) \approx 0$, $R(0) = 0$. The following constraint is requisite:

$$S(t) + I(t) + R(t) = 1. \tag{2-4}$$

Dividing Eq. (2-1) by Eq. (2-3), we obtain

$$\frac{dS}{dR} = -R_0 S. \tag{2-5}$$

Here, $R_0 = \beta/\gamma$ is called the basic reproduction number, which is the number of secondary infections caused by a single infected individual. Integrating above equation from time 0 to ∞, the transcendental equation for the FES $R(\infty)$ are expressed as:

$$S(\infty) = \exp[-R_0 R(\infty)], \tag{2-6}$$

$$R(\infty) = 1 - S(\infty) = 1 - \exp[-R_0 R(\infty)]. \tag{2-7}$$

Fig 2.2 shows the FES as a function of the basic reproduction number R_0 in an infinite and well-mixed population. Differentiating both sides of Eq. (2-7) with respect to $R(\infty)$, we can see that the final size is positive if and only if $R_0 > 1$. If $R_0 < 1$, the disease does not spread. $S_k(t) = S_k(0)\exp[-\lambda k \phi(t)] = (1 - x_k)\exp[-\lambda k \phi(t)]$, Moreover, the basic reproduction numbers for representative diseases are summarized in Table 2.1. For example, the range of R_0 for Influenza is 2 to 3. If R_0 is set as 2.5 for Influenza, the FES in the well-mixed population will be approximately 0.9.

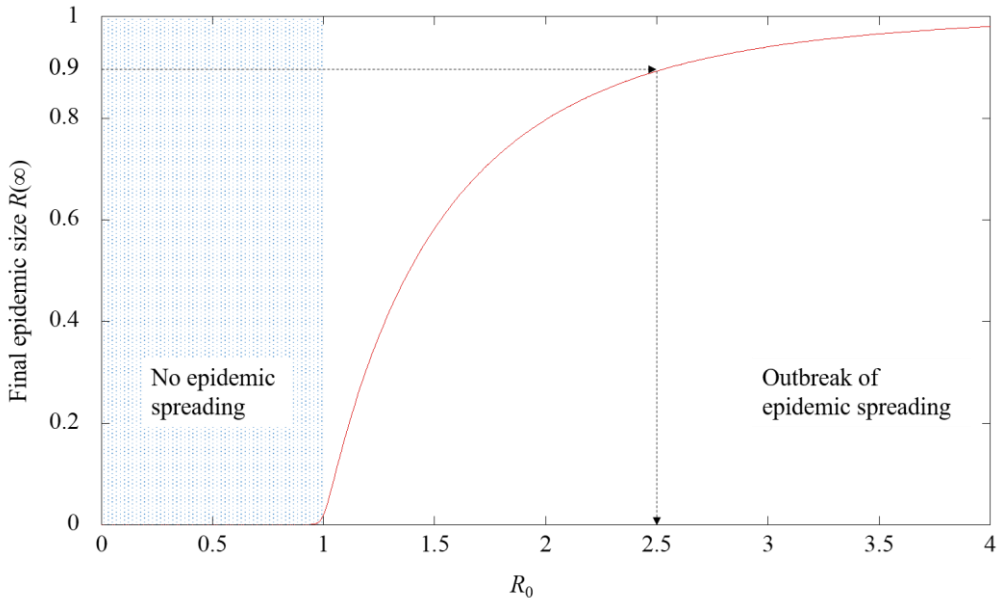

Figure 2.2. Final epidemic size as a function of the basic reproduction number R_0 in an infinite and well-mixed population.

2.2.2 Network model

At each time step, each node adopts one of the three possible states, and during one time-step, the susceptible node that is connected to the infected one is infected with a rate β. Meanwhile, the infected nodes are recovered with a rate γ. Defining the effective spreading rate $\lambda = \beta/\gamma$, without losing generality, we set $\gamma = 1$. To take into account the heterogeneity induced by the presence of nodes with different degrees, we consider the time evolution of the density of susceptible $S_k(t)$, as well as infected $I_k(t)$ and recovered $R_k(t)$, which are the infected and recovered nodes of degree k at time t, respectively. These variables are connected through normalization as follows:

$$S_k(t) + I_k(t) + R_k(t) = 1. \tag{2-8}$$

Using mean field approximation, we form the following set of coupled differential equations:

$$\frac{dS_k(t)}{dt} = -\lambda k S_k(t)\Theta(t), \tag{2-9}$$

$$\frac{dI_k(t)}{dt} = \lambda k S_k(t)\Theta(t) - I_k(t), \tag{2-10}$$

$$\frac{dR_k(t)}{dt} = I_k(t), \tag{2-11}$$

where $\Theta(t)$ represents the probability that any given link points to an infected site. This quantity can be computed in a self-consistent way. The probability that a link points to a node with s links is proportional to $sP(s)$. Thus, the probability that a randomly chosen link points to an infected node is given by [31,33];

$$\Theta(t) = \frac{\sum_k (k-1)P(k)I_k(t)}{\sum_s sP(s)} = \frac{\sum_k (k-1)P(k)I_k(t)}{\langle k \rangle}. \tag{2-12}$$

In this approximation, the connectivity correlations in the network were neglected, i.e., the probability that a link points to an infected node is considered independent of the connectivity of the node from which the link is emanating. Combined with the initial conditions, $S_k(0) = 1$, $I_k(0) \sim 0$, and $R_k(0) = 0$, we obtain

$$S_k(t) = S_k(0)\exp[-\lambda k \phi(t)] = \exp[-\lambda k \phi(t)], \tag{2-13}$$

where the auxiliary function $\phi(t)$ is defined as:

$$\phi(t) = \int_0^t \Theta(I(t'))dt' = \frac{1}{\langle k \rangle}\sum_{k=1}^{\infty}(k-1)P(k)\int_0^t I_k(t')dt' = \frac{1}{\langle k \rangle}\sum_{k=1}^{\infty}(k-1)P(k)R_k(t) \quad . \tag{2-14}$$

Focusing on the time evolution $\phi(t)$, we derive its time derivation as follows:

$$\begin{aligned}
\frac{d\phi(t)}{dt} &= \frac{1}{\langle k \rangle}\sum_{k=1}^{\infty}(k-1)P(k)\frac{dR_k(t)}{dt} \\
&= \frac{1}{\langle k \rangle}\sum_{k=1}^{\infty}(k-1)P(k)I_k(t) \\
&= \frac{1}{\langle k \rangle}\sum_{k=1}^{\infty}(k-1)P(k)(1-S_k(t)-R_k(t)) \\
&= \frac{1}{\langle k \rangle}\sum_{k=1}^{\infty}(k-1)P(k)\big(1-S_k(t)\big) - \phi(t) \\
&= \frac{1}{\langle k \rangle}\sum_{k=1}^{\infty}(k-1)P(k)\big(1-\exp[-\lambda k \phi(t)]\big) - \phi(t).
\end{aligned} \tag{2-15}$$

Since $I_k(\infty) = 0$ and $\lim_{t\to\infty} d\phi(t)/dt = 0$ are intuitively approved, we obtain from Eq. (2-15) the following self-consistent equation for $\phi(\infty)$:

$$\phi(\infty) = \frac{1}{\langle k \rangle}\sum_{k=1}^{\infty}(k-1)P(k)\big(1-\exp[-\lambda k \phi(\infty)]\big) = 1 - \frac{1}{\langle k \rangle} - \frac{1}{\langle k \rangle}\sum_{k=1}^{\infty}(k-1)P(k)\exp[-\lambda k \phi(\infty)]. \tag{2-16}$$

The final fractions are expressed as:

$$S_k(\infty) = S_k(0)\exp[-\lambda k \phi(\infty)] = \exp[-\lambda k \phi(\infty)]. \tag{2-17}$$

$$R_k(\infty) = 1 - S_k(\infty) = 1 - \exp[-\lambda k \phi(\infty)]. \tag{2-18}$$

With respect to Eq. (2-15), there is a trivial solution $\phi(\infty)=0$. To obtain a non-zero solution, the condition

$$\frac{d}{d\phi(\infty)}\left(1-\frac{1}{\langle k\rangle}-\frac{1}{\langle k\rangle}\sum_{k=1}^{\infty}(k-1)P(k)\exp[-\lambda k\phi(\infty)]\right)\Bigg|_{\phi(\infty)=0}>1, \tag{2-19}$$

must be satisfied, leading to

$$\lambda\frac{\langle k^2\rangle-\langle k\rangle}{\langle k\rangle}>1. \tag{2-20}$$

This inequality defines the epidemic threshold

$$\lambda_c=\frac{\langle k\rangle}{\langle k^2\rangle-\langle k\rangle}. \tag{2-21}$$

In this study, two of the most typical degree spatial structures were considered, the Poisson degree distribution and the power law degree distribution which are, respectively, associated with Erdős–Rényi random graph (ER-RG) [14] and Barabasi-Albert scale free (BA-SF) [15] networks. In Poisson's degree distribution $P(k)=\exp(-\langle k\rangle)\langle k\rangle^k/k!$, most of the modes have a connectivity k close to the mean value $\langle k\rangle=\sum_k kP(k)$. On the other hand, the power law degree distribution $P(k)\sim k^{-3}$ is often used for reproducing real-world networks observed in complex social networks. To reveal how different degree distribution patterns from a homogeneous distribution quantitatively affect disease spreading, these two degree distributions was focused on. Thus, for comparison, the average connectivity of the degree distributions is assimilated to <k> = 3, 4, 6, and 8 for actual numerical analysis. Assuming the approximation $P(k)=A/k(k+1)(k+2)$ (A is a normalized constant) derived by a master equation [34], and setting the minimum and maximum degrees, the power law degree distribution reproduced BA-SF with <k> = 4, 6, and 8.

Figure 2.3 shows the FES as a function of transmission rate λ when no individual is vaccinated on each network, following the power law degree distribution and Poisson's degree distribution. From this figure, we confirm that the epidemic threshold described by Eq. (2-21) is consistent with the critical point of transmission rate, which can lead to epidemic spreading. Moreover, we calibrate the transmission rate λ such that the final epidemic size across a network becomes 0.9 [7], which is 0.39 for Poisson's degree distribution and 0.48 for the power law degree distribution with <k> = 8.

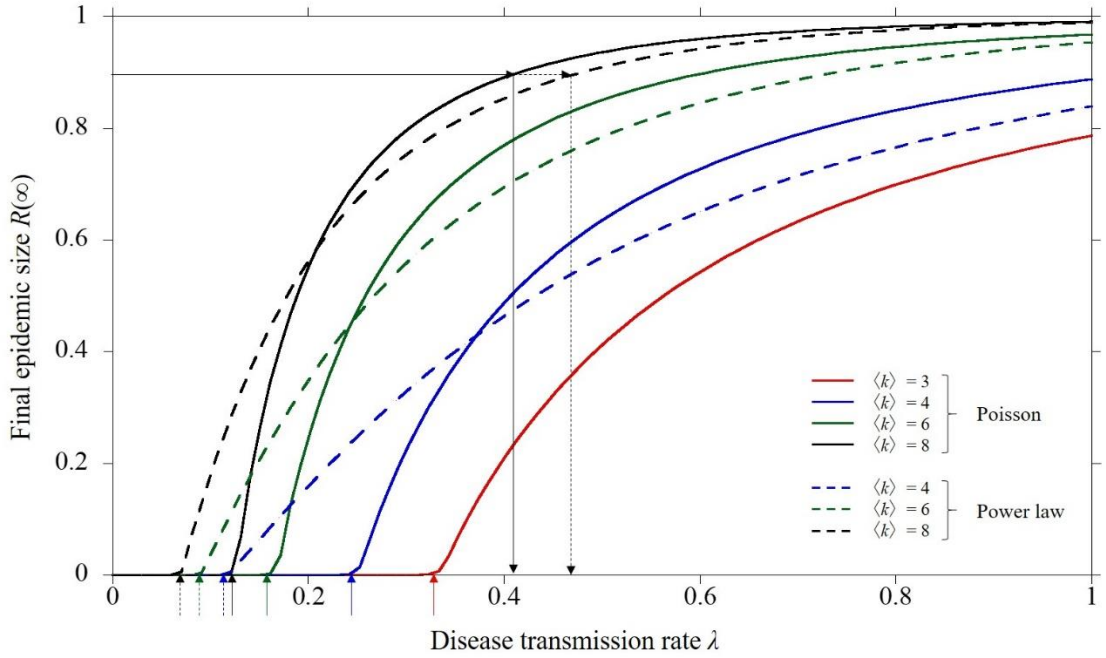

Figure 2.3. FES as a function of the transmission rate λ, when no individual is vaccinated on each network, following the power law degree distribution and Poisson's degree distribution, which have an average number of degrees of $\langle k \rangle$ = 3, 4, 6, and 8. The arrows point to the critical points of the transmission rate, which can lead to epidemic spreading, called the epidemic threshold.

2.2.3 Pair approximation SIR model

Through a brief review of the pair approximation SIR model [32,35], the dynamics of epidemic spreading on the regular random network with the number of degree k was determined. The fraction of individuals in state S, I, and R at time t are represented by $[S](t)$, $[I](t)$, and $[R](t)$, respectively. In addition, the pair $[XY](t)$ represents the number of $X-Y$ edges (pairs) linking a node in state X with a node in state Y on networks at time t. At each time step, each node adopts one of the three possible states: susceptible (S), infected (I), and recovered (R), and during one time step, the susceptible individual that is connected to the infected one is infected with an infection rate β per $S-I$ link. Meanwhile, the infected individuals are recovered with a recovery rate γ. Based on the above disease spreading mechanism of SIR model, we can represent the dynamics by the following ODEs:

$$\frac{d}{dt}[S](t) = -\beta[SI](t), \tag{2-22}$$

$$\frac{d}{dt}[I](t) = \beta[SI](t) - \gamma[I](t), \tag{2-23}$$

$$\frac{d}{dt}[R](t) = \gamma[I](t), \tag{2-24}$$

$$\frac{d}{dt}[SS](t) = -2\beta[SS](t)Q(I|SS), \tag{2-25}$$

$$\frac{d}{dt}[SI](t) = -\beta[SI](t)Q(I|SI) + \beta[SS](t)Q(I|SS) - \gamma[SI](t), \tag{2-26}$$

$$\frac{d}{dt}[SR](t) = -\beta[SR](t)Q(I|SR) + \gamma[SI](t), \tag{2-27}$$

$$\frac{d}{dt}[II](t) = 2\beta[SI](t)Q(I|SI) - 2\gamma[II](t), \tag{2-28}$$

$$\frac{d}{dt}[IR](t) = \beta[SR](t)Q(I|SR) + \gamma[II](t) - \gamma[IR](t), \tag{2-29}$$

$$\frac{d}{dt}[RR](t) = 2\gamma[IR](t), \tag{2-30}$$

where $Q(I|SS)$ is the average number of infected neighbors of a susceptible, given that the susceptible already has at least one susceptible neighbor, $Q(I|SI)$ is the average number of infected neighbors of a susceptible, given that the susceptible already has at least one infected neighbor, $Q(I|SR)$ is the average number of infected neighbors of a susceptible, given that the susceptible already has at least one recovered neighbor.

The set of initial conditions was assumed: $[S](0) = 1$, $[I](0) \sim 0$, $[R](0) = 0$, $[SS](0) \sim Q[S](0) = Q$ and $[SR](0) = 0$. The following constraints are requisite:

$$[S](t) + [I](t) + [R](t) = 1, \tag{2-31}$$

$$[SS](t) + [SI](t) + [SR](t) = Q[S](t), \tag{2-32}$$

$$[SI](t) + [II](t) + [IR](t) = Q[I](t), \tag{2-33}$$

$$[SR](t) + [IR](t) + [RR](t) = Q[R](t). \tag{2-34}$$

These equations are exact but unclosed. In order to close Eqs. (2-25) – (2-30), the third-order quantities $Q(I|SS)$, $Q(I|SI)$ and $Q(I|SR)$ must be expressed in terms of second-order state variables.

$$Q(I|SI) \approx 1 + \frac{Q-1}{Q}Q(I|S) = 1 + \frac{Q-1}{Q}\frac{[SI](t)}{[S](t)} = 1 + \mu\frac{[SI](t)}{[S](t)}, \tag{2-35}$$

$$Q(I|SS) = Q(I|SR) \approx \frac{Q-1}{Q}Q(I|S) = \frac{Q-1}{Q}\frac{[SI](t)}{[S](t)} = \mu\frac{[SI](t)}{[S](t)}. \tag{2-36}$$

Here, μ is defined as $(Q-1)/Q$.

To solve this set of equations, we started to substitute $[SI](t)$ from Eq. (2-22) into Eq. (2-25) with combination of Eq. (2-36) to obtain

$$\frac{d[SS](t)}{d[S](t)} = 2\mu\frac{[SS](t)}{[S](t)}. \tag{2-37}$$

By using the initial conditions, $[S](0) = 1$, $[SS](0) \sim Q[S](0) = Q$, integration leads to

$$[SS](t) = Q[S]^{2\mu}(t). \tag{2-38}$$

In addition, substituting $[SI](t)$from Eq. (2-22) into Eq. (2-27) with combination of Eq. (2-36) yields

$$\frac{d[SR](t)}{d[S](t)} = \mu \frac{[SR](t)}{[S](t)} - r\,, \tag{2-39}$$

where $r = \gamma/\beta$ is the relative recovery rate which means the inverse of basic reproduction number R_0.

By using the initial conditions, $[S](0) = 1$, $[SR](0) = 0$, integration leads to

$$[SR](t) = Qr([S]^{\mu}(t) - [S](t))\,. \tag{2-40}$$

At steady state ($t \to \infty$), there will be no infected individuals because they become recovered individuals spontaneously. Therefore, the constraints (2-31) – (2-34) can be rewritten as the following equations:

$$[S](\infty) + [R](\infty) = 1, \tag{2-41}$$

$$[SS](\infty) + [SR](\infty) = Q[S](\infty), \tag{2-42}$$

$$[SR](\infty) + [RR](\infty) = Q[R](\infty). \tag{2-43}$$

Substituting $[SS](\infty)$ and $[SR](\infty)$ from Eqs. (2-38) and (2-40) into Eq. (2-42) yields

$$[S]^{2\mu}(\infty) + r[S]^{\mu}(\infty) - (1+r)[S](\infty) = 0\,. \tag{2-44}$$

By defining $s = [S]^{1/Q}(t)$ and taking into account definition of μ, the following algebraic equation can written:

$$s^{Q-1} - (1+r)s + r = 0 \tag{2-45}$$

,which is equivalent to

$$(s-1)(s^{Q-2} + \cdots + s^2 + s - r) = 0\,. \tag{2-46}$$

The nontrivial solution is then given by

$$s^{Q-2} + \cdots + s^2 + s = r \tag{2-47}$$

In the interval $s > 0$, the polynomial on the left-hand side is an increasing function of s that vanishes at $s = 0$ and attains the value $Q-2$ at $s = 1$. Therefore, a real solution in the interval $0 < s < 1$ exists and is the only solution as long as $r < Q-2$. Therefore, there is a phase transition that occurs at the critical relative recovery rate

$$r_c = Q - 2 \tag{2-48}$$

The final fractions are expressed as

$$[S](\infty) = s^Q \tag{2-49}$$

$$[R](\infty) = 1 - [S](\infty) = 1 - s^Q \tag{2-50}$$

Figure 2.4 shows the FES as a function of the inverse of the relative recovery rate when no individual is vaccinated on each regular random network which have different degree Q. From this figure, we can confirm that the epidemic threshold described by Eq. (2-48) is consistent with the critical point of the relative recovery rate, which can lead to epidemic spread. Furthermore, we can calibrate the relative recovery rate r such that the FES across a network becomes 0.9 [7], but is 0.46, 0.87, 1.66, or

2.44 when Q is 3, 4, 6, or 8, respectively. To validate the theoretical results, we performed MAS on regular random graphs with a population size $N = 10^4$ averaged over 100 independent realizations. The MAS results are in fairly good agreement with the theoretical results. When the degree number was low (i.e., $Q = 3$), the discrepancy between the numerical simulation and the MAS approach was relatively high because of the effect of network topology.

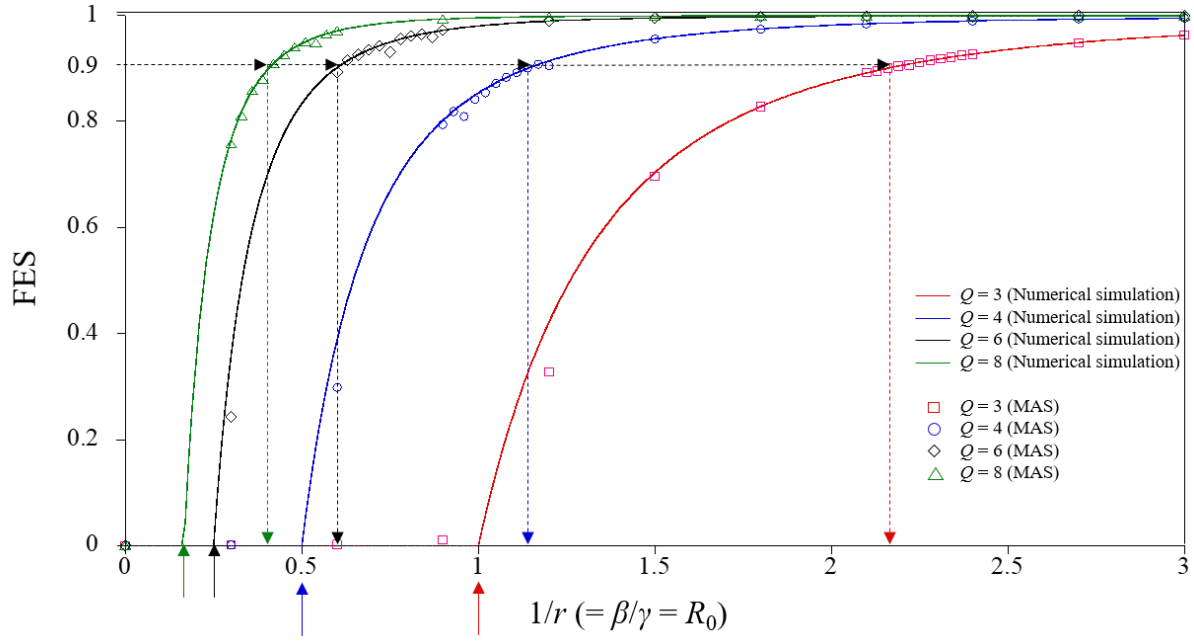

Figure 4.4. Final epidemic size as a function of the inverse of effective recovery rate $1/r$, which means the basic reproduction number R_0, when there is no vaccinated individual on regular random network with the number of degree $Q = 3, 4, 6, 8$. The arrows point to the critical points of the transmission rate, which can lead to epidemic spreading, called the epidemic threshold.

2.3 Impact of imperfect vaccination and intermediate protecting measure

Taking the SIR models described in Section 2.2 as the baseline, the Susceptible-Vaccinated-Infected-Recovered (SVIR) dynamics was developed. The SVIR model was modified to reproduce the two different scenarios, namely imperfect vaccination (the effectiveness model) and intermediate protective measure (the efficiency model). Figure 2.5 shows schematic of two types of concepts for avoiding infection. In the effectiveness scenario, a vaccinated population is separated into two classes: immune individuals obtaining perfect immunity and non-immune individuals failing to get immunity. Let the effectiveness of the vaccination and the vaccination coverage be e ($0 \le e \le 1$) and x, respectively. The fraction of vaccinated individuals with immunity must be ex, while the fraction of non-immune individuals is $(1 - ex)$. On the other hand, the efficiency model defined the efficiency of an intermediate protective measure to avoid infection as a parameter η ($0 \le \eta \le 1$), meaning how the defense measure can reduce the probability of being infected. While a non-vaccinated (more precisely, non-prepared with the defense against contagion) susceptible individual may become infected if he/she is exposed to

infectious individuals at the disease transmission rate β, an individual prepared with the intermediate protective measure who is in S may also become infectious at the rate $(1-\eta)\beta$.

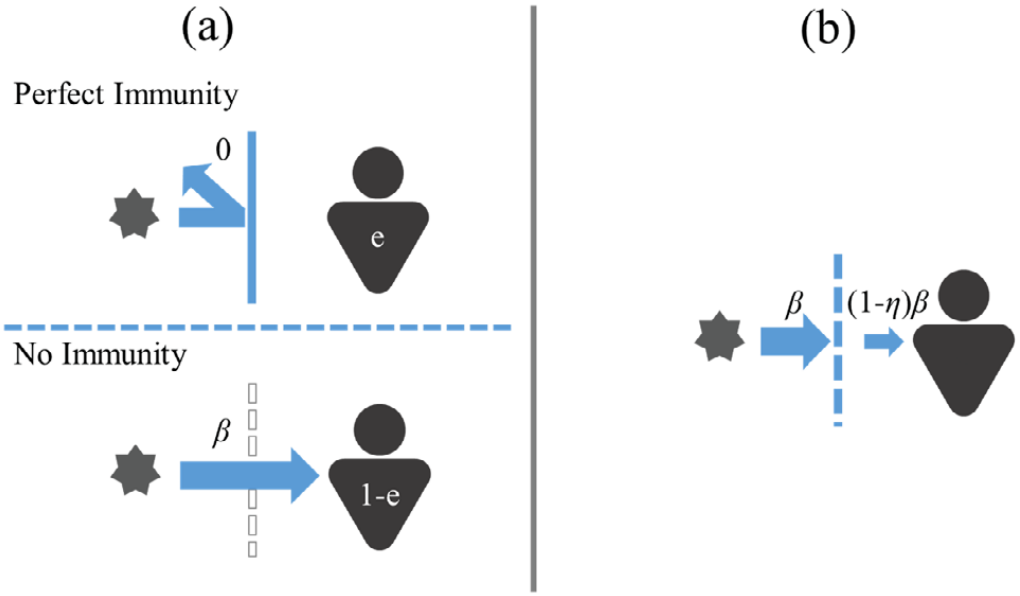

Figure 2.5. Schematic of two types of concepts for avoiding infection: (a) effectiveness model; (b) efficiency model.

2.3.1 Infinite and well-mixed population

In the effectiveness model, the SVIR model we use to describe such a condition is

$$\frac{dS(t)}{dt} = -\beta S(t)I(t), \tag{2-51}$$

$$\frac{dV(t)}{dt} = -\beta\big(V(t) - eV(0)\big)I(t), \tag{2-52}$$

$$\frac{dI(t)}{dt} = \beta S(t)I(t) + \beta\big(V(t) - eV(0)\big)I(t) - I(t), \tag{2-53}$$

$$\frac{dR(t)}{dt} = I(t). \tag{2-54}$$

with the assumed set of initial values $S(0) = 1 - x$, $V(0) = x$, $I(0) \approx 0$, $R(0) = 0$. The following constraint is requisite:

$$S(t) + V(t) + I(t) + R(t) = 1. \tag{2-55}$$

The final epidemic size $R(\infty)$ can be expressed in relation to both x and time t at equilibrium ($t = \infty$) as:

$$R(\infty) = (1 - ex)(1 - \exp[-R_0 R(\infty)]), \tag{2-56}$$

$R(\infty)$ gives the respective fractions of four different types of individual depending on whether they are vaccinated or non-vaccinated and whether they are healthy or infected as summarized in Table 2.1.

Table 2.1. Fractions of four types of individual using the effectiveness model.

Strategy/state	Healthy	Infected
Vaccinated	$x(e + (1 - e)\exp[-R_0R(\infty)])$	$x(1 - e)(1 - \exp[-R_0R(\infty)])$
Non-vaccinated	$(1 - x)\exp[-R_0R(\infty)]$	$(1 - x)(1 - \exp[-R_0R(\infty)])$

In the efficiency model, the SVIR model we use to describe such a condition is

$$\frac{dS(t)}{dt} = -\beta S(t)I(t), \tag{2-57}$$

$$\frac{dV(t)}{dt} = -(1-\eta)\beta V(t)I(t), \tag{2-58}$$

$$\frac{dI(t)}{dt} = \beta S(t)I(t) + (1-\eta)\beta V(t)I(t) - \gamma I(t), \tag{2-59}$$

$$\frac{dR(x,t)}{dt} = \gamma I(x,t), \tag{2-60}$$

with the assumed set of initial values $S(0) = 1 - x$, $V(0) = x$, $I(0) \approx 0$, $R(0) = 0$. The following constraint is requisite:

$$S(t) + V(t) + I(t) + R(t) = 1. \tag{2-61}$$

Because the population is not completely susceptible, it is accurate to use a control reproduction number R_c instead of the basic reproduction number R_0. In this case, R_c can be estimated as

$$R_c = R_0[S(0) + (1 - \eta)V(0)]. \tag{2-62}$$

The final epidemic size and other fractions can be expressed as

$$S(\infty) = (1 - x)\exp[-R_0R(\infty)], \tag{2-63}$$

$$V(\infty) = x\exp[-(1 - \eta)R_0R(\infty)], \tag{2-64}$$

$$R(\infty) = 1 - (1 - x)\exp[-R_0R(\infty)] - x\exp[-(1 - \eta)R_0R(\infty)]. \tag{2-65}$$

In the limit of this process, the respective fractions of the four different types of individual at equilibrium are as summarized in Table 2.2. Comparing Tables 2.1 and 2.2, it is worth noting that the "success probability of free-riding" is always given by $\exp[-R_0R(\infty)]$ irrespective of whether we assume a perfect vaccination, an imperfect one, or even a defense against contagion.

Table 2.2. Fractions of four types of individual using the efficiency model.

Strategy/state	Healthy	Infected
Vaccinated	$x\exp[-(1 - \eta)R_0R(\infty)]$	$x(1- \exp[-(1 - \eta)R_0R(\infty)])$
Non-vaccinated	$(1 - x)\exp[-R_0R(\infty)]$	$(1 - x)(1 - \exp[-R_0R(\infty)])$

Figure 2.5 shows the final epidemic size for different levels of vaccination coverage using the

effectiveness and efficiency models. From Figure 2.4, the so-called critical vaccination coverage that eradicates an epidemic spread can be read from the border of the extinct phase at which FES = 0. This border suggests the critical vaccination coverage for suppressing the spread of infection, which can be determined analytically as $x_c = (1-1/R_0)/\eta$ for the efficiency model and $x_c = (1-1/R_0)/e$ for the effectiveness model. Clearly, as long as a less-reliable defense measure is provided, say $\eta < 0.6$, we cannot avoid the breakout of an epidemic even if all individuals use that particular defense measure.

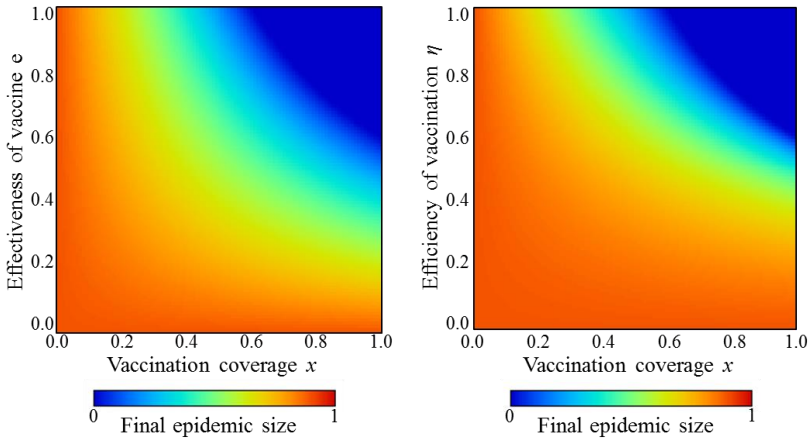

Figure 2.5. Final epidemic size according to vaccination coverage and (a) effectiveness e (effectiveness of a vaccination) or (b) efficiency η (efficiency of a defense against contagion). We assume $R_0 = 2.5$, which is applied consistently in this study.

2.3.2 Network model

Let the effectiveness of the vaccine, the density of a healthy vaccinated individual of degree k, and the vaccination coverage of that individual with degree k be e ($0 \le e \le 1$), V_k, and x_k, respectively. The fraction of vaccinated individuals with perfect immunity must be ex_k, while that of non-immune individuals is $(1 - ex_k)$. The differential equations of the SIR model under the vaccination policy presented by the effectiveness model are

$$\frac{dS_k(t)}{dt} = -\lambda k S_k(t)\Theta(t), \tag{2-66}$$

$$\frac{dV_k(t)}{dt} = -\lambda k\left(V_k(t) - eV_k(0)\right)\Theta(t), \tag{2-67}$$

$$\frac{dI_k(t)}{dt} = \lambda k S_k(t)\Theta(t) + \lambda k\left(V_k(t) - eV_k(0)\right)\Theta(t) - I_k(t), \tag{2-68}$$

$$\frac{dR_k(t)}{dt} = I_k(t), \tag{2-69}$$

with the assumed set of initial conditions: $S_k(0) = 1 - x_k$, $V_k(0) = x_k$, $I_k(0) \approx 0$, $R_k(0) = 0$. The following constraint is requisite:

$$S_k(t) + V_k(t) + I_k(t) + R_k(t) = 1. \tag{2-70}$$

Combined with these initial conditions and after normalization, we obtain

$$S_k(t) = S_k(0)\exp[-\lambda k\phi(t)] = (1-x_k)\exp[-\lambda k\phi(t)], \tag{2-71}$$

$$V_k(t) = V_k(0)(e+(1-e)\exp[-\lambda k\phi(t)]) = x_k(e+(1-e)\exp[-\lambda k\phi(t)]). \tag{2-72}$$

Focusing on the time evolution of $\phi(t)$, as depicted in Eq. (2-15), we modify it as

$$\begin{aligned}
\frac{d\phi(t)}{dt} &= \frac{1}{\langle k\rangle}\sum_{k=1}^{\infty}(k-1)\frac{dR_k(t)}{dt} \\
&= \frac{1}{\langle k\rangle}\sum_{k=1}^{\infty}(k-1)P(k)I_k(t) \\
&= \frac{1}{\langle k\rangle}\sum_{k=1}^{\infty}(k-1)P(k)(1-S_k(t)-V_k(t)-R_k(t)) \\
&= \frac{1}{\langle k\rangle}\sum_{k=1}^{\infty}(k-1)P(k)\left(1-S_k(t)-V_k(t)\right)-\phi(t) \\
&= \frac{1}{\langle k\rangle}\sum_{k=1}^{\infty}(k-1)P(k)\left(1-S_k(0)\exp[-\lambda k\phi(t)]-V_k(0)(e+(1-e)\exp[-\lambda k\phi(t)])\right)-\phi(t).
\end{aligned} \tag{2-73}$$

Because of $I_k(\infty) = 0$ and $\lim_{t\to\infty} d\phi(t)/dt = 0$, from Eq. (2-73) the following self-consistent equation for $\phi(\infty)$ can be obatined:

$$\begin{aligned}
\phi(\infty) &= \frac{1}{\langle k\rangle}\sum_{k=1}^{\infty}(k-1)P(k)\left(1-S_k(0)\exp[-\lambda k\phi(\infty)]-V_k(0)(e+(1-e)\exp[-\lambda k\phi(\infty)])\right) \\
&= 1-\frac{1}{\langle k\rangle}-\frac{1}{\langle k\rangle}\sum_{k=1}^{\infty}(k-1)P(k)\left(S_k(0)\exp[-\lambda k\phi(\infty)]+V_k(0)(e+(1-e)\exp[-\lambda k\phi(\infty)])\right) \\
&= 1-\frac{1}{\langle k\rangle}-\frac{1}{\langle k\rangle}\sum_{k=1}^{\infty}(k-1)P(k)\left((1-x_k)\exp[-\lambda k\phi(\infty)]+x_k(e+(1-e)\exp[-\lambda k\phi(\infty)])\right).
\end{aligned} \tag{2-74}$$

The final epidemic size and the other fractions can be expressed as

$$S_k(\infty) = S_k(0)\exp[-\lambda k\phi(\infty)] = (1-x_k)\exp[-\lambda k\phi(\infty)], \tag{2-75}$$

$$V_k(\infty) = V_k(0)(e+(1-e)\exp[-\lambda k\phi(\infty)]) = x_k(e+(1-e)\exp[-\lambda k\phi(\infty)]), \tag{2-76}$$

$$R_k(\infty) = (1-ex_k)(1-\exp[-\lambda k\phi(\infty)]). \tag{2-77}$$

As explained in the previous sub-section 2.2.2, the condition having a non-zero solution imposes the following inequality:

$$\frac{d}{d\phi(\infty)}\left(1-\frac{1}{\langle k\rangle}-\frac{1}{\langle k\rangle}\sum_{k=1}^{\infty}(k-1)P(k)\left((1-x_k)\exp[-\lambda k\phi(\infty)]+x_k(e+(1-e)\exp[-\lambda k\phi(t)])\right)\right)\Bigg|_{\phi(\infty)=0} > 1. \tag{2-78}$$

Assuming no dependence on degree *k* of the vaccinated individuals,

$$\lambda(1-ex)\frac{\langle k^2\rangle-\langle k\rangle}{\langle k\rangle} > 1. \tag{2-78}$$

This inequality defines the critical vaccination coverage, which can eradicate epidemic spreading

$$x_c = \left(1-\frac{\langle k\rangle}{\lambda(\langle k^2\rangle-\langle k\rangle)}\right)\Big/e. \tag{2-79}$$

The respective fractions of four different types of individuals, depending on whether they are vaccinated or non-vaccinated and whether they are healthy or infected, are summarized in Table 2.3.

Table 2.3. Fractions of four types of individuals in the effectiveness model

Strategy/state	Healthy	Infected
Vaccinated	$x_k(e+(1-e)\exp[-\lambda k\phi(\infty)])$	$x_k(1-e)(1-\exp[-\lambda k\phi(\infty)])$
Non-vaccinated	$(1-x_k)\exp[-\lambda k\phi(\infty)]$	$(1-x_k)(1-\exp[-\lambda k\phi(\infty)])$

Let the efficiency of a defense against contagion to avoid infection be η ($0 \le \eta \le 1$), meaning how much can the defense measure decrease the probability of infection. In the following formulation for the efficiency model, we temporarily regard the vaccinated state V as the state prepared with an intermediate defense measure, for comparison with the effectiveness model. A non-vaccinated (more precisely, non-prepared with defense against contagion) susceptible individual may become infected if he/she is exposed to infectious individuals with disease transmission rate λk. Vaccinated (that is, prepared) individuals by the intermediate defense measure, who are in S, may also become infectious with $(1-\eta)\lambda k$.

The SVIR model we use to describe such a condition is expressed as

$$\frac{dS_k(t)}{dt} = -\lambda k S_k(t)\Theta(t), \tag{2-80}$$

$$\frac{dV_k(t)}{dt} = -(1-\eta)\lambda k V_k(t)\Theta(t), \tag{2-81}$$

$$\frac{dI_k(t)}{dt} = \lambda k S_k(t)\Theta(t) + (1-\eta)\lambda k V_k(t)\Theta(t) - I_k(t), \tag{2-82}$$

$$\frac{dR_k(t)}{dt} = I_k(t), \tag{2-83}$$

with the assumed set of initial conditions $S_k(0) = 1 - x_k$, $V_k(0) = x_k$, $I_k(0) \approx 0$, $R_k(0) = 0$. The following constraint is requisite:

$$S_k(t) + V_k(t) + I_k(t) + R_k(t) = 1. \tag{2-84}$$

Combined with these initial conditions and through normalization, we obtain

$$S_k(t) = S_k(0)\exp[-\lambda k\phi(t)] = (1-x_k)\exp[-\lambda k\phi(t)], \tag{2-85}$$

$$V_k(t) = V_k(0)\exp[-(1-\eta)\lambda k\phi(t)] = x_k\exp[-(1-\eta)\lambda k\phi(t)]. \tag{2-86}$$

Focusing on the time evolution of $\phi(t)$, as depicted in Eq. (2-15), we modify it as

$$\begin{aligned}\frac{d\phi(t)}{dt} &= \frac{1}{\langle k\rangle}\sum_{k=1}^{\infty}(k-1)\frac{dR_k(t)}{dt} = \frac{1}{\langle k\rangle}\sum_{k=1}^{\infty}(k-1)P(k)I_k(t)\\ &= \frac{1}{\langle k\rangle}\sum_{k=1}^{\infty}(k-1)P(k)(1-S_k(t)-V_k(t)-R_k(t))\\ &= \frac{1}{\langle k\rangle}\sum_{k=1}^{\infty}(k-1)P(k)\big(1-S_k(t)-V_k(t)\big)-\phi(t)\\ &= \frac{1}{\langle k\rangle}\sum_{k=1}^{\infty}(k-1)P(k)\big(1-S_k(0)\exp[-\lambda k\phi(t)]-V_k(0)\exp[-(1-\eta)\lambda k\phi(t)]\big)-\phi(t).\end{aligned} \tag{2-87}$$

Because of $I_k(\infty) = 0$ and $\lim_{t\to\infty} d\phi(t)/dt = 0$, we obtain from Eq. (2-87) the following self-consistent equation for $\phi(\infty)$:

$$\begin{aligned}\phi(\infty) &= \frac{1}{\langle k\rangle}\sum_{k=1}^{\infty}(k-1)P(k)\big(1-S_k(0)\exp[-\lambda k\phi(\infty)]-V_k(0)\exp[-(1-\eta)\lambda k\phi(\infty)]\big)\\ &= 1-\frac{1}{\langle k\rangle}-\frac{1}{\langle k\rangle}\sum_{k=1}^{\infty}(k-1)P(k)\big(S_k(0)\exp[-\lambda k\phi(\infty)]+V_k(0)\exp[-(1-\eta)\lambda k\phi(\infty)]\big)\\ &= 1-\frac{1}{\langle k\rangle}-\frac{1}{\langle k\rangle}\sum_{k=1}^{\infty}(k-1)P(k)\big((1-x_k)\exp[-\lambda k\phi(\infty)]+x_k\exp[-(1-\eta)\lambda k\phi(\infty)]\big).\end{aligned} \tag{2-88}$$

The final epidemic size and other fractions can be expressed as:

$$S_k(\infty) = S_k(0)\exp[-\lambda k\phi(\infty)] = (1-x_k)\exp[-\lambda k\phi(\infty)]. \tag{2-89}$$

$$V_k(\infty) = V_k(0)\exp[-(1-\eta)\lambda k\phi(\infty)] = x_k\exp[-(1-\eta)\lambda k\phi(\infty)]. \tag{2-90}$$

$$R_k(\infty) = 1-(1-x_k)\exp[-\lambda k\phi(\infty)]) - x_k\exp[-(1-\eta)\lambda k\phi(\infty)]). \tag{2-91}$$

As in the previous sub-section 2.2.2, the condition having a non-zero solution imposes the following inequality:

$$\frac{d}{d\phi(\infty)}\left(1-\frac{1}{\langle k\rangle}-\frac{1}{\langle k\rangle}\sum_{k=1}^{\infty}(k-1)P(k)\big((1-x_k)\exp[-\lambda k\phi(\infty)]+x_k\exp[-(1-\eta)\lambda k\phi(\infty)]\big)\right)\Bigg|_{\phi(\infty)=0} > 1. \tag{2-92}$$

Assuming no dependence on the degree k of the vaccinated individuals,

$$\lambda(1-\eta x)\frac{\langle k^2\rangle-\langle k\rangle}{\langle k\rangle} > 1 \tag{2-93}$$

This inequality defines the critical vaccination coverage, which can eradicate the epidemic spreading

$$x_c = \left(1-\frac{\langle k\rangle}{\lambda(\langle k^2\rangle-\langle k\rangle)}\right)\Big/\eta \tag{2-94}$$

The respective fractions of the four individuals, depending on whether they are vaccinated or non-vaccinated and whether they are healthy or infected, are summarized in Table 2.4.

Figure 2.6 gives the final epidemic size depending on the vaccination level in both the effectiveness and efficiency models for three different population structures: power law degree distribution, Poisson's degree distribution, and well-mixed population. Although each vaccination coverage x_k depends on degree k in a real decision-making process on whether to take the vaccination,

as we discuss later, we hypothetically assume uniform vaccination coverage here. From Figure 2.5, the so-called critical vaccination coverage that eradicates an epidemic spreading can be read from the border of the extinct phase, where the final epidemic size is equal to zero. These borders suggest the critical vaccination coverage to oppress infection spreading, which can be analytically drawn as Eqs. (2-79) and (2-94), respectively. Notably, in power law degree distribution, infectious diseases can easily spread vis-à-vis the other two spatial structures, a result that is consistent with those of previous studies (e.g., [13]). Because of this, the protective effect of vaccination and defense against contagion in case of power law distribution is relatively low compared to that in Poisson's degree distribution and well-mixed population.

Table 2.4. Fractions of four individuals in case of the efficiency model

Strategy/state	Healthy	Infected
Vaccinated	$x_k \exp[-(1-\eta)\lambda k\phi(\infty)]$	$x_k(1-\exp[-(1-\eta)\lambda k\phi(\infty)])$
Non-vaccinated	$(1-x_k)\exp[-\lambda k\phi(\infty)]$	$(1-x_k)(1-\exp[-\lambda k\phi(\infty)])$

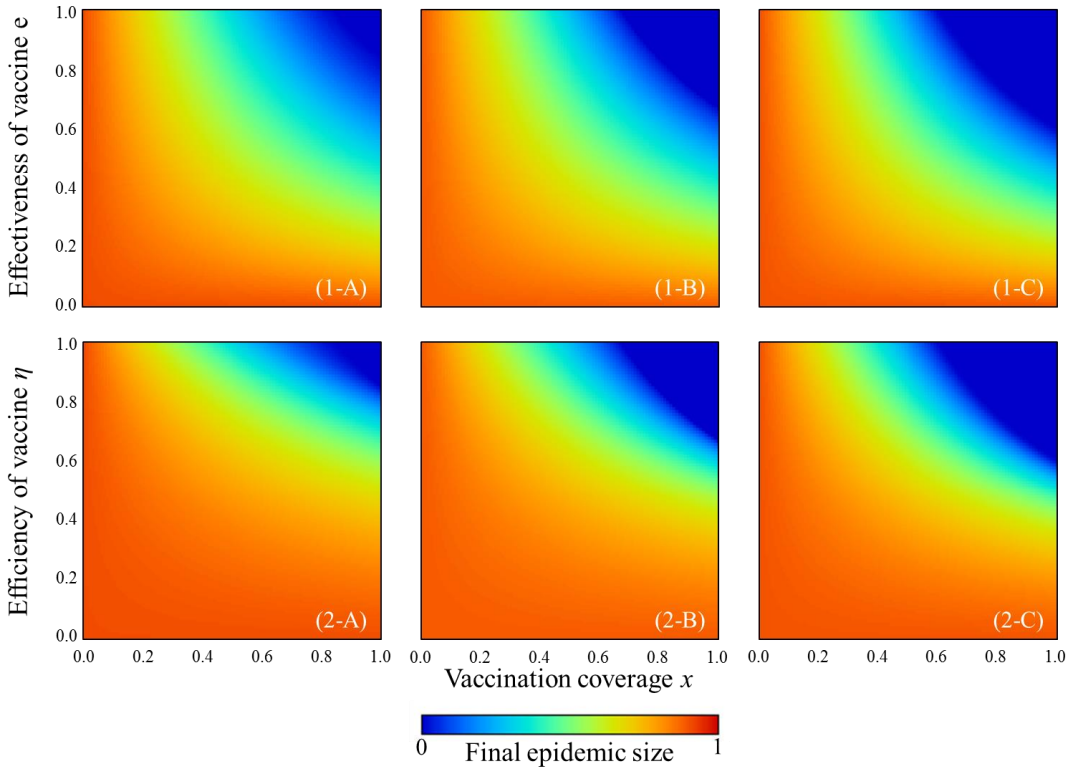

Figure 2.6. Final epidemic size according to vaccination coverage and (1-*) effectiveness e (effectiveness of a vaccination) or (2-*) efficiency η (efficiency of a defense against contagion) in three different population structures: (*-A) power law degree distribution, (*-B) Poisson's degree distribution, and (*-C) well-mixed population described in the Section 2.3.1. We assume $\lambda = 4.8$ and 3.9 for power law degree distribution and Poisson degree distribution, respectively. In the case of the well-mixed population, the reproduction number $R_0 = 2.5$ is applied.

2.3.3 Pair approximation model

In the effectiveness model, the population is subdivided into the following: nonvaccinated susceptible individual S_N, nonvaccinated infected individual I_N, nonvaccinated recovered individual R_N, vaccinated susceptible individual S_V, vaccinated infected individual I_V, vaccinated recovered individual R_V, and vaccinated individual with perfect immunity P_V. Let the effectiveness of the vaccination and the VC be e ($0 \le e \le 1$) and x, respectively. The fraction of vaccinated individuals with perfect immunity $[P_V](t)$ must be ex, whereas that of nonimmune individuals $[S_V](t) + [I_V](t) + [R_V](t)$ is $(1 - e)x$. On the basis of the above assumptions, the dynamics of the SVIR model with imperfect vaccination can be described by the following ODEs:

$$\frac{d}{dt}[S_N](t) = -\beta\left([S_N I_N](t) + [S_N I_V](t)\right), \tag{2-95}$$

$$\frac{d}{dt}[I_N](t) = \beta\left([S_N I_N](t) + [S_N I_V](t)\right) - \gamma[I_N](t), \tag{2-96}$$

$$\frac{d}{dt}[R_N](t) = \gamma[I_N](t), \tag{2-97}$$

$$\frac{d}{dt}[S_V](t) = -\beta\left([S_V I_N](t) + [S_V I_V](t)\right), \tag{2-98}$$

$$\frac{d}{dt}[I_V](t) = \beta\left([S_V I_N](t) + [S_V I_V](t)\right) - \gamma[I_V](t), \tag{2-99}$$

$$\frac{d}{dt}[R_V](t) = \gamma[I_V](t), \tag{2-100}$$

$$\frac{d}{dt}[P_V](t) = 0, \tag{2-101}$$

$$\frac{d}{dt}[S_N S_N](t) = -2\beta[S_N S_N](t)\left(Q(I_N \mid S_N S_N) + Q(I_V \mid S_N S_N)\right), \tag{2-102}$$

$$\begin{aligned}\frac{d}{dt}[S_N I_N](t) = {} & \beta[S_N S_N](t)\left(Q(I_N \mid S_N S_N) + Q(I_V \mid S_N S_N)\right) \\ & -\beta[S_N I_N](t)\left(Q(I_N \mid S_N I_N) + Q(I_V \mid S_N I_N)\right) - \gamma[S_N I_N](t)\end{aligned}, \tag{2-103}$$

$$\frac{d}{dt}[S_N R_N](t) = \gamma[S_N I_N](t) - \beta[S_N R_N](t)\left(Q(I_N \mid S_N R_N) + Q(I_V \mid S_N R_N)\right), \tag{2-104}$$

$$\frac{d}{dt}[I_N I_N](t) = 2\beta[S_N I_N](t)\left(Q(I_N \mid S_N I_N) + Q(I_V \mid S_N I_N)\right) - 2\gamma[I_N I_N](t), \tag{2-105}$$

$$\frac{d}{dt}[I_N R_N](t) = \beta[S_N R_N](t)\left(Q(I_N \mid S_N R_N) + Q(I_V \mid S_N R_N)\right) + \gamma[I_N I_N](t) - \gamma[I_N R_N](t), \tag{2-106}$$

$$\frac{d}{dt}[R_N R_N](t) = 2\gamma[I_N R_N](t), \tag{2-107}$$

$$\frac{d}{dt}[S_V S_V](t) = -2\beta[S_V S_V](t)\Big(Q(I_N|S_V S_V) + Q(I_V|S_V S_V)\Big), \tag{2-108}$$

$$\begin{aligned}\frac{d}{dt}[S_V I_V](t) &= \beta[S_V S_V](t)\Big(Q(I_N|S_V S_V) + Q(I_V|S_V S_V)\Big) \\ &\quad -\beta[S_V I_V](t)\Big(Q(I_N|S_V I_V) + Q(I_V|S_V I_V)\Big) - \gamma[S_V I_V](t)\end{aligned}, \tag{2-109}$$

$$\frac{d}{dt}[S_V R_V](t) = \gamma[S_V I_V](t) - \beta[S_V R_V](t)\Big(Q(I_N|S_V R_V) + Q(I_V|S_V R_V)\Big), \tag{2-110}$$

$$\frac{d}{dt}[S_V P_V](t) = -\beta[S_V P_V](t)\Big(Q(I_N|S_V P_V) + Q(I_V|S_V P_V)\Big), \tag{2-111}$$

$$\frac{d}{dt}[I_V I_V](t) = 2\beta[S_V I_V](t)\Big(Q(I_N|S_V I_V) + Q(I_V|S_V I_V)\Big) - 2\gamma[I_V I_V](t), \tag{2-112}$$

$$\frac{d}{dt}[I_V R_V](t) = \beta[S_V R_V](t)\Big(Q(I_N|S_V R_V) + Q(I_V|S_V R_V)\Big) + \gamma[I_V I_V](t) - \gamma[I_V R_V](t), \tag{2-113}$$

$$\frac{d}{dt}[I_V P_V](t) = \beta[S_V P_V](t)\Big(Q(I_N|S_V P_V) + Q(I_V|S_V P_V)\Big) - \gamma[I_V P_V](t), \tag{2-114}$$

$$\frac{d}{dt}[R_V R_V](t) = 2\gamma[I_V R_V](t), \tag{2-115}$$

$$\frac{d}{dt}[R_V P_V](t) = \gamma[I_V P_V](t), \tag{2-116}$$

$$\frac{d}{dt}[P_V P_V](t) = 0, \tag{2-117}$$

$$\begin{aligned}\frac{d}{dt}[S_N S_V](t) &= -\beta[S_N S_V](t)\Big(Q(I_N|S_N S_V) + Q(I_V|S_N S_V)\Big) \\ &\quad -\beta[S_N S_V](t)\Big(Q(I_N|S_V S_N) + Q(I_V|S_V S_N)\Big)\end{aligned}, \tag{2-118}$$

$$\begin{aligned}\frac{d}{dt}[S_N I_V](t) &= \beta[S_N S_V](t)\Big(Q(I_N|S_V S_N) + Q(I_V|S_V S_N)\Big) \\ &\quad -\beta[S_N I_V](t)\Big(Q(I_N|S_N I_V) + Q(I_V|S_N I_V)\Big) - \gamma[S_N I_V](t)\end{aligned}, \tag{2-119}$$

$$\begin{aligned}\frac{d}{dt}[S_V I_N](t) &= \beta[S_N S_V](t)\Big(Q(I_N|S_N S_V) + Q(I_V|S_N S_V)\Big) \\ &\quad -\beta[S_N I_V](t)\Big(Q(I_N|S_V I_N) + Q(I_V|S_V I_N)\Big) - \gamma[S_V I_N](t)\end{aligned}, \tag{2-120}$$

$$\frac{d}{dt}[S_N R_V](t) = \gamma[S_N I_V](t) - \beta[S_N R_V](t)\Big(Q(I_N|S_N R_V) + Q(I_V|S_N R_V)\Big), \tag{2-121}$$

$$\frac{d}{dt}[S_V R_N](t) = \gamma[S_V I_N](t) - \beta[S_V R_N](t)\Big(Q(I_N|S_V R_N) + Q(I_V|S_V R_N)\Big), \tag{2-122}$$

$$\frac{d}{dt}[S_N P_V](t) = -\beta[S_N P_V](t)\Big(Q(I_N|S_N P_V) + Q(I_V|S_N P_V)\Big), \tag{2-123}$$

$$\frac{d}{dt}[I_N I_V](t) = \beta[S_N I_V](t)\big(Q(I_N|S_N I_V) + Q(I_V|S_N I_V)\big) + \beta[S_N I_V](t)\big(Q(I_N|S_V I_N) + Q(I_V|S_V I_N)\big) - 2\gamma[I_N I_V](t) \quad (2\text{-}124)$$

$$\frac{d}{dt}[I_N R_V](t) = \gamma[I_N I_V](t) + \beta[S_N R_V](t)\big(Q(I_N|S_N R_V) + Q(I_V|S_N R_V)\big) - \gamma[I_N R_V](t), \quad (2\text{-}125)$$

$$\frac{d}{dt}[I_V R_N](t) = \gamma[I_N I_V](t) + \beta[S_V R_N](t)\big(Q(I_N|S_N R_V) + Q(I_V|S_N R_V)\big) - \gamma[I_V R_N](t), \quad (2\text{-}126)$$

$$\frac{d}{dt}[I_N P_V](t) = \beta[S_N P_V](t)\big(Q(I_N|S_N P_V) + Q(I_V|S_N P_V)\big) - \gamma[I_N P_V](t), \quad (2\text{-}127)$$

$$\frac{d}{dt}[R_N R_V](t) = \gamma[I_N R_V](t) + \gamma[I_V R_N](t), \quad (2\text{-}128)$$

$$\frac{d}{dt}[R_N P_V](t) = \gamma[I_N P_V](t). \quad (2\text{-}129)$$

The above set of dynamic equations should be assumed to have the following set of initial conditions:

$[S_N](0) = 1 - x$, $[S_V](0) = (1 - e)x$, $[P_V](0) = ex$, $[I_N](0) \sim 0$, $[I_V](0) \sim 0$, $[R_N](0) = 0$, $[R_V](0) = 0$,
$[S_N S_N](0) = Q(1 - x - \alpha)$, $[S_N S_V](0) = Q(1 - e)\alpha$, $[S_N P_V](0) = Qe\alpha$, $[S_V S_V](0) = Q(1 - e)^2(x - \alpha)$,
$[S_V P_V](0) = Qe(1 - e)(x - \alpha)$, $[P_V P_V](0) = Qe^2(x - \alpha)$.

Here, α is the vaccinator-nonvaccinator connection coefficient, which can be said dissortativity observed at initial moment of every season (time-evolved in repeating seasons), and is less than x and $1 - x$. If the homogeneous distribution of vaccinat or and nonvacciantor was assumed, $\alpha = x(1-x)$.

The following constraints are required:

$$[S_N](t) + [I_N](t) + [R_N](t) + [S_V](t) + [I_V](t) + [R_V](t) + [P_V](t) = 1, \quad (2\text{-}130)$$

$$[S_N S_N](t) + [S_N I_N](t) + [S_N R_N](t) + [S_N S_V](t) + [S_N I_V](t) + [S_N R_V](t) + [S_N P_V](t) = Q[S_N](t), \quad (2\text{-}131)$$

$$[S_N I_N](t) + [I_N I_N](t) + [I_N R_N](t) + [S_V I_N](t) + [I_N I_V](t) + [I_N R_V](t) + [I_N P_V](t) = Q[I_N](t), \quad (2\text{-}132)$$

$$[S_N R_N](t) + [I_N R_N](t) + [R_N R_N](t) + [S_V R_N](t) + [I_V R_N](t) + [R_N R_V](t) + [R_N P_V](t) = Q[R_N](t), \quad (2\text{-}133)$$

$$[S_N S_V](t) + [S_V I_N](t) + [S_V R_N](t) + [S_V S_V](t) + [S_V I_V](t) + [S_V R_V](t) + [S_V P_V](t) = Q[S_V](t), \quad (2\text{-}134)$$

$$[S_N I_V](t) + [I_N I_V](t) + [I_V R_N](t) + [S_V I_V](t) + [I_V I_V](t) + [I_V R_V](t) + [I_V P_V](t) = Q[I_V](t), \quad (2\text{-}135)$$

$$[S_N R_V](t) + [I_N R_V](t) + [R_N R_V](t) + [S_V R_V](t) + [I_V R_V](t) + [R_V R_V](t) + [R_V P_V](t) = Q[R_V](t), \quad (2\text{-}136)$$

$$[S_N P_V](t) + [I_N P_V](t) + [R_N P_V](t) + [S_V P_V](t) + [I_V P_V](t) + [R_V P_V](t) + [P_V P_V](t) = Q[P_V](t), \quad (2\text{-}137)$$

To solve the above set of equations, we add Eqs. (2-104) and (2-121), and the result is the following equation for the variable $[S_N I_N](t) + [S_N I_V](t)$:

$$\frac{d}{dt}\big([S_N R_N](t) + [S_N R_V](t)\big) = \gamma\big([S_N I_N](t) + [S_N I_V](t)\big) - \beta\mu\frac{\big([S_N I_N](t) + [S_N I_V](t)\big)\big([S_N R_N](t) + [S_N R_V](t)\big)}{[S_N](t)}. \quad (2\text{-}138)$$

By substituting $[S_N I_N](t) + [S_N I_V](t)$ from Eq. (2-95) into Eq. (2-138), we obtain the following:

$$\frac{d\left([S_N R_N](t)+[S_N R_V](t)\right)}{d[S_N](t)} = \mu \frac{\left([S_N R_N](t)+[S_N R_V](t)\right)}{[S_N](t)} - r \,. \tag{2-139}$$

By using the initial conditions $[S_N](0) = 1 - x$, $[S_N R_N](0) = 0$, and $[S_N R_V](0) = 0$, integration leads to the following:

$$[S_N R_N](t) + [S_N R_V](t) = Qr(1-x)\left(\left(\frac{[S_N](t)}{1-x}\right)^{\mu} - \frac{[S_N](t)}{1-x}\right). \tag{2-140}$$

Likewise, by adding Eqs. (2-110) and (2-122), we obtain the following equation for the variable $[S_V I_N](t) + [S_V I_V](t)$:

$$\begin{aligned}\frac{d}{dt}\left([S_V R_V](t)+[S_V R_N](t)\right) &= \gamma\left([S_V I_N](t)+[S_V I_V](t)\right) \\ &\quad -\beta\mu\frac{\left([S_V I_N](t)+[S_V I_V](t)\right)\left([S_V R_V](t)+[S_V R_N](t)\right)}{[S_V](t)}\end{aligned}. \tag{2-141}$$

By substituting $[S_V I_N](t) + [S_V I_V](t)$ from Eq. (2-98) into Eq. (2-141), the following is obtained:

$$\frac{d\left([S_V R_V](t)+[S_V R_N](t)\right)}{d[S_V](t)} = \mu \frac{\left([S_V R_V](t)+[S_V R_N](t)\right)}{[S_V](t)} - r \,. \tag{2-142}$$

By using the initial conditions $[S_V](0) = (1 - e)x$, $[S_V R_N](0) = 0$, and $[S_V R_V](0) = 0$, integration leads to the following:

$$[S_V R_N](t) + [S_V R_V](t) = Qr(1-e)x\left(\left(\frac{[S_V](t)}{(1-e)x}\right)^{\mu} - \frac{[S_V](t)}{(1-e)x}\right). \tag{2-143}$$

By taking the ratio between Eqs. (2-95) and (2-102), we obtain the following:

$$\frac{d[S_N S_N](t)}{d[S_N](t)} = 2\mu \frac{[S_N S_N](t)}{[S_N](t)} \,. \tag{2-144}$$

By using the initial conditions $[S_N](0) = 1 - x$ and $[S_N S_N](0) = Q(1 - x - \alpha)$, integration leads to the following:

$$[S_N S_N](t) = Q(1-x-\alpha)\left(\frac{[S_N](t)}{1-x}\right)^{2\mu} \,. \tag{2-145}$$

In the same way, by taking the ratio between Eqs. (2-98) and (2-108), we obtain the following:

$$\frac{d[S_V S_V](t)}{d[S_V](t)} = 2\mu \frac{[S_V S_V](t)}{[S_V](t)} \,. \tag{2-146}$$

By using the initial conditions $[S_V](0) = (1 - e)x$ and $[S_V S_V](0) = Q(1 - e)^2(x - \alpha)$, integration leads to the following:

$$[S_V S_V](t) = Q(1-e)^2(x-\alpha)\left(\frac{[S_V](t)}{(1-e)x}\right)^{2\mu} \,. \tag{2-147}$$

By substituting $[S_N I_N](t) + [S_N I_V](t)$ and $[S_V I_N](t) + [S_V I_V](t)$ from Eqs. (2-95) and (2-98) into Eq. (2-118), we obtain the following:

$$\frac{1}{[S_N S_V](t)}\frac{d[S_N S_V](t)}{dt} = \frac{\mu}{[S_N](t)}\frac{d}{dt}[S_N](t) + \frac{\mu}{[S_V](t)}\frac{d}{dt}[S_V](t)\,. \tag{2-148}$$

By using the initial conditions $[S_N](0) = 1 - x$, $[S_V](0) = (1 - e)x$, and $[S_N S_V](0) = Q(1 - e)\,\alpha$, integration leads to the following:

$$[S_N S_V](t) = Q(1-e)\alpha\left(\frac{[S_N](t)}{1-x}\right)^{\mu}\left(\frac{[S_V](t)}{(1-e)x}\right)^{\mu}\,. \tag{2-149}$$

By substituting $[S_N I_N](t) + [S_N I_V](t)$ from Eq. (2-95) into Eq. (2-123), we obtain the following:

$$\frac{d[S_N P_V](t)}{d[S_N](t)} = \mu\frac{[S_N P_V](t)}{[S_N](t)}\,. \tag{2-150}$$

By using the initial conditions $[S_N](0) = 1 - x$ and $[S_N P_V](0) = Qe\alpha$, integration leads to the following:

$$[S_N P_V](t) = Qe\alpha\left(\frac{[S_N](t)}{1-x}\right)^{\mu}\,. \tag{4-151}$$

By substituting $[S_V I_N](t) + [S_V I_V](t)$ from Eq. (2-98) into Eq. (2-111), we obtain the following:

$$\frac{d[S_V P_V](t)}{d[S_V](t)} = \mu\frac{[S_V P_V](t)}{[S_V](t)}\,. \tag{2-152}$$

By using the initial conditions $[S_V](0) = (1 - e)x$ and $[S_V P_V](0) = Qe(1 - e)(x - \alpha)$, integration leads to the following:

$$[S_V P_V](t) = Qe(1-e)(x-\alpha)\left(\frac{[S_V](t)}{(1-e)x}\right)^{\mu}\,. \tag{2-153}$$

At the steady state ($t \to \infty$), the constraints in Eq. (4-130) to (4-137) can be rewritten as follows:

$$[S_N](\infty) + [R_N](\infty) + [S_V](\infty) + [R_V](\infty) + [P_V](\infty) = 1, \tag{2-154}$$

$$[S_N S_N](\infty) + [S_N R_N](\infty) + [S_N S_V](\infty) + [S_N R_V](\infty) + [S_N P_V](\infty) = Q[S_N](\infty), \tag{2-155}$$

$$[S_N R_N](\infty) + [R_N R_N](\infty) + [S_V R_N](\infty) + [R_N R_V](\infty) + [R_N P_V](\infty) = Q[R_N](\infty), \tag{2-156}$$

$$[S_N S_V](\infty) + [S_V R_N](\infty) + [S_V S_V](\infty) + [S_V R_V](\infty) + [S_V P_V](\infty) = Q[S_V](\infty), \tag{2-157}$$

$$[S_N R_V](\infty) + [R_N R_V](\infty) + [S_V R_V](\infty) + [R_V R_V](\infty) + [R_V P_V](\infty) = Q[R_V](\infty), \tag{2-158}$$

$$[S_N P_V](\infty) + [R_N P_V](\infty) + [S_V P_V](\infty) + [R_V P_V](\infty) + [P_V P_V](\infty) = Q[P_V](\infty), \tag{2-159}$$

Substituting $[S_N R_N](\infty) + [S_N R_V](\infty)$, $[S_N S_N](\infty)$, $[S_N S_V](\infty)$, and $[S_N P_V](\infty)$ from Eqs. (2-140), (2-145), (2-149), and (2-151) into Eq. (2-155) yields:

$$\begin{aligned}&(1-x-\alpha)\left(\frac{[S_N](\infty)}{1-x}\right)^{2\mu} + (1-e)\alpha\left(\frac{[S_N](\infty)}{1-x}\right)^{\mu}\left(\frac{[S_V](\infty)}{(1-e)x}\right)^{\mu}\\ &+r(1-x)\left(\left(\frac{[S_N](\infty)}{1-x}\right)^{\mu} - \frac{[S_N](\infty)}{1-x}\right) + e\alpha\left(\frac{[S_N](\infty)}{1-x}\right)^{\mu}\\ &= (1-x)\frac{[S_N](\infty)}{1-x}\end{aligned}\,. \tag{2-160}$$

Substituting $[S_I R_N](\infty) + [S_I R_V](\infty)$, $[S_I S_V](\infty)$, $[S_N S_V](\infty)$, and $[S_I P_V](\infty)$ from Eqs. (2-143), (2-147), (2-149) and (2-153) into Eq. (2-157) yields:

$$\begin{aligned}&\alpha\left(\frac{[S_N](t)}{1-x}\right)^{\mu}\left(\frac{[S_V](t)}{(1-e)x}\right)^{\mu}+rx\left(\left(\frac{[S_V](t)}{(1-e)x}\right)^{\mu}-\frac{[S_V](t)}{(1-e)x}\right)\\&+(1-e)(x-\alpha)\left(\frac{[S_V](t)}{(1-e)x}\right)^{2\mu}+e(x-\alpha)\left(\frac{[S_V](t)}{(1-e)x}\right)^{\mu}\\&=x\frac{[S_V](t)}{(1-e)x}\end{aligned} \quad . \tag{2-161}$$

By defining $p=\left(\frac{[S_N](\infty)}{1-x}\right)^{1/Q}$, $q=\left(\frac{[S_V](\infty)}{(1-e)x}\right)^{1/Q}$ and taking into account the definition of μ, we can write Eqs. (2-160) and (2-161) as follows:

$$(1-x-\alpha)p^{Q-1}-(1+r)(1-x)p+r(1-x)+e\alpha+(1-e)\alpha q^{Q-1}=0\,, \tag{2-162}$$

$$(1-e)(x-\alpha)q^{Q-1}-(1+r)xq+rx+e(x-\alpha)+\alpha p^{Q-1}=0\,. \tag{2-163}$$

If we assumed a homogeneous distribution of vaccinators and nonvaccinators, $\alpha=x(1-x)$ and $p=q$, the following equation is obtained:

$$(1-ex)p^{Q-1}-(1+r)p+r+ex=0\,, \tag{2-164}$$

which is equivalent to

$$(p-1)\left\{(1-ex)(p^{Q-2}+\cdots+p^2+p)-ex-r\right\}=0\,. \tag{2-165}$$

The nontrivial solution is then given by the following:

$$(1-ex)(p^{Q-2}+\cdots+p^2+p)=ex+r\,. \tag{2-166}$$

When the epidemic spread is eradicated, $p=1$ is satisfied. Therefore, the critical vaccination coverage is represented by the following:

$$x_c=\frac{Q-2-r}{(Q-1)e}\,. \tag{2-167}$$

The final fractions are expressed as follows:

$$[S_N](\infty)=(1-x)p^Q\,, \tag{2-168}$$

$$[S_V](\infty)=(1-e)xq^Q\,, \tag{2-169}$$

$$[P_V](\infty)=ex\,, \tag{2-170}$$

$$[R_N](\infty)=1-x-[S_N](\infty)=(1-x)(1-p^Q)\,, \tag{2-171}$$

$$[R_V](\infty)=(1-e)x-[S_V](\infty)=(1-e)x(1-q^Q)\,. \tag{2-172}$$

The other final pairs are hypothetically calculated as follows:

$$[S_N R_N](\infty)=Qr(1-x)(p^{Q-1}-p^Q)\frac{[R_N](\infty)}{[R_N](\infty)+[R_V](\infty)}\,, \tag{2-173}$$

$$[S_N R_N](\infty) = Qr(1-x)(p^{Q-1} - p^Q)\frac{[R_V](\infty)}{[R_N](\infty)+[R_V](\infty)}, \tag{2-174}$$

$$[S_V R_N](\infty) = Qr(1-e)x(q^{Q-1} - q^Q)\frac{[R_N](\infty)}{[R_N](\infty)+[R_V](\infty)}, \tag{2-175}$$

$$[S_V R_N](\infty) = Qr(1-e)x(q^{Q-1} - q^Q)\frac{[R_V](\infty)}{[R_N](\infty)+[R_V](\infty)}, \tag{2-176}$$

$$[R_N R_N](\infty) = [S_N S_N](0) - [S_N S_N](\infty) - 2[S_N R_N](\infty), \tag{2-177}$$

$$[R_V R_V](\infty) = [S_V S_V](0) - [S_V S_V](\infty) - 2[S_V R_V](\infty), \tag{2-178}$$

$$[R_N R_V](\infty) = [S_N S_V](0) - [S_N S_V](\infty) - [S_N R_V](\infty) - [S_V R_N](\infty), \tag{2-179}$$

$$[R_N P_V](\infty) = [S_N P_V](0) - [S_N P_V](\infty) = Qex(1-x)(1-p^{Q-1}), \tag{2-180}$$

$$[R_V P_V](\infty) = [S_V P_V](0) - [S_V P_V](\infty) = Qe(1-e)x^2(1-q^{Q-1}). \tag{2-181}$$

In the efficiency model, the population is subdivided into the following: nonvaccinated susceptible individual S_N, nonvaccinated infected individual I_N, nonvaccinated recovered individual R_N, vaccinated susceptible individual S_V, vaccinated infected individual I_V, and vaccinated recovered individual R_V. A nonvaccinated susceptible individual S_N (more precisely, an individual not prepared with intermediate protective measures) may become infected if he/she is exposed to infectious individuals with a disease transmission rate of β (day^{-1} person^{-1}). A vaccinated (i.e., prepared) individual S_V who is taking intermediate protective measures may also become infectious with (1–η) β. On the basis of the above assumptions, the dynamics of the SVIR model with intermediate protective measure can be described by the following ODEs:

$$\frac{d}{dt}[S_N](t) = -\beta\left([S_N I_N](t) + [S_N I_V](t)\right), \tag{2-182}$$

$$\frac{d}{dt}[I_N](t) = \beta\left([S_N I_N](t) + [S_N I_V](t)\right) - \gamma[I_N](t), \tag{2-183}$$

$$\frac{d}{dt}[R_N](t) = \gamma[I_N](t), \tag{2-184}$$

$$\frac{d}{dt}[S_V](t) = -(1-\eta)\beta\left([S_V I_N](t) + [S_V I_V](t)\right), \tag{2-185}$$

$$\frac{d}{dt}[I_V](t) = (1-\eta)\beta\left([S_V I_N](t) + [S_V I_V](t)\right) - \gamma[I_V](t), \tag{2-186}$$

$$\frac{d}{dt}[R_V](t) = \gamma[I_V](t), \tag{2-187}$$

$$\frac{d}{dt}[S_N S_N](t) = -2\beta[S_N S_N](t)\left(Q(I_N \mid S_N S_N) + Q(I_V \mid S_N S_N)\right), \tag{2-188}$$

$$\frac{d}{dt}[S_N I_N](t) = \beta[S_N S_N](t)\left(Q(I_N|S_N S_N) + Q(I_V|S_N S_N)\right) - \beta[S_N I_N](t)\left(Q(I_N|S_N I_N) + Q(I_V|S_N I_N)\right) - \gamma[S_N I_N](t), \tag{2-189}$$

$$\frac{d}{dt}[S_N R_N](t) = \gamma[S_N I_N](t) - \beta[S_N R_N](t)\left(Q(I_N|S_N R_N) + Q(I_V|S_N R_N)\right), \tag{2-190}$$

$$\frac{d}{dt}[I_N I_N](t) = 2\beta[S_N I_N](t)\left(Q(I_N|S_N I_N) + Q(I_V|S_N I_N)\right) - 2\gamma[I_N I_N](t), \tag{2-191}$$

$$\frac{d}{dt}[I_N R_N](t) = \beta[S_N R_N](t)\left(Q(I_N|S_N R_N) + Q(I_V|S_N R_N)\right) + \gamma[I_N I_N](t) - \gamma[I_N R_N](t), \tag{2-192}$$

$$\frac{d}{dt}[R_N R_N](t) = 2\gamma[I_N R_N](t), \tag{2-193}$$

$$\frac{d}{dt}[S_V S_V](t) = -2(1-\eta)\beta[S_V S_V](t)\left(Q(I_N|S_V S_V) + Q(I_V|S_V S_V)\right), \tag{2-194}$$

$$\frac{d[S_V I_V](t)}{dt} = (1-\eta)\beta[S_V S_V](t)\left(Q(I_N|S_V S_V) + Q(I_V|S_V S_V)\right) - (1-\eta)\beta[S_V I_V](t)\left(Q(I_N|S_V I_V) + Q(I_V|S_V I_V)\right) - \gamma[S_V I_V](t), \tag{2-195}$$

$$\frac{d}{dt}[S_V R_V](t) = \gamma[S_V I_V](t) - (1-\eta)\beta[S_V R_V](t)\left(Q(I_N|S_V R_V) + Q(I_V|S_V R_V)\right), \tag{2-196}$$

$$\frac{d}{dt}[I_V I_V](t) = 2(1-\eta)\beta[S_V I_V](t)\left(Q(I_N|S_V I_V) + Q(I_V|S_V I_V)\right) - 2\gamma[I_V I_V](t), \tag{2-197}$$

$$\frac{d}{dt}[I_V R_V](t) = (1-\eta)\beta[S_V R_V](t)\left(Q(I_N|S_V R_V) + Q(I_V|S_V R_V)\right) + \gamma[I_V I_V](t) - \gamma[I_V R_V](t), \tag{2-198}$$

$$\frac{d}{dt}[R_V R_V](t) = 2\gamma[I_V R_V](t), \tag{2-199}$$

$$\frac{d}{dt}[S_N S_V](t) = -\beta[S_N S_V](t)\left(Q(I_N|S_N S_V) + Q(I_V|S_N S_V)\right) - (1-\eta)\beta[S_N S_V](t)\left(Q(I_N|S_V S_N) + Q(I_V|S_V S_N)\right), \tag{2-200}$$

$$\frac{d}{dt}[S_N I_V](t) = (1-\eta)\beta[S_N S_V](t)\left(Q(I_N|S_V S_N) + Q(I_V|S_V S_N)\right) - \beta[S_N I_V](t)\left(Q(I_N|S_N I_V) + Q(I_V|S_N I_V)\right) - \gamma[S_N I_V](t), \tag{2-201}$$

$$\frac{d}{dt}[S_V I_N](t) = \beta[S_N S_V](t)\left(Q(I_N|S_N S_V) + Q(I_V|S_N S_V)\right) - (1-\eta)\beta[S_N I_V](t)\left(Q(I_N|S_V I_N) + Q(I_V|S_V I_N)\right) - \gamma[S_V I_N](t), \tag{2-202}$$

$$\frac{d}{dt}[S_N R_V](t) = \gamma[S_N I_V](t) - \beta[S_N R_V](t)\left(Q(I_N|S_N R_V) + Q(I_V|S_N R_V)\right), \tag{2-203}$$

$$\frac{d}{dt}[S_V R_N](t) = \gamma[S_V I_N](t) - (1-\eta)\beta[S_V R_N](t)\left(Q(I_N|S_V R_N) + Q(I_V|S_V R_N)\right), \tag{2-204}$$

$$\frac{d}{dt}[I_N I_V](t) = \beta[S_N I_V](t)\left(Q(I_N|S_N I_V) + Q(I_V|S_N I_V)\right) + (1-\eta)\beta[S_N I_V](t)\left(Q(I_N|S_V I_N) + Q(I_V|S_V I_N)\right) - 2\gamma[I_N I_V](t) \quad (2\text{-}205)$$

$$\frac{d}{dt}[I_N R_V](t) = \gamma[I_N I_V](t) + \beta[S_N R_V](t)\left(Q(I_N|S_N R_V) + Q(I_V|S_N R_V)\right) - \gamma[I_N R_V](t), \quad (2\text{-}206)$$

$$\frac{d}{dt}[I_V R_N](t) = \gamma[I_N I_V](t) + (1-\eta)\beta[S_V R_N](t)\left(Q(I_N|S_N R_V) + Q(I_V|S_N R_V)\right) - \gamma[I_V R_N](t), \quad (2\text{-}207)$$

$$\frac{d}{dt}[R_N R_V](t) = \gamma[I_N R_V](t) + \gamma[I_V R_N](t). \quad (2\text{-}208)$$

The above set of equations are assumed to have the following initial conditions: $[S_N](0) = 1 - x$, $[S_V](0) = x$, $[I_N](0) \sim 0$, $[I_V](0) \sim 0$, $[R_N](0) = 0$, $[R_V](0) = 0$, $[S_N S_N](0) = Q(1 - x - \alpha)$, $[S_N S_V](0) = Q\alpha$, and $[S_V S_V](0) = Q(x - \alpha)$.

The following constraints are required:

$$[S_N](t) + [I_N](t) + [R_N](t) + [S_V](t) + [I_V](t) + [R_V](t) = 1, \quad (2\text{-}209)$$

$$[S_N S_N](t) + [S_N I_N](t) + [S_N R_N](t) + [S_N S_V](t) + [S_N I_V](t) + [S_N R_V](t) = Q[S_N](t), \quad (2\text{-}210)$$

$$[S_N I_N](t) + [I_N I_N](t) + [I_N R_N](t) + [S_V I_N](t) + [I_N I_V](t) + [I_N R_V](t) = Q[I_N](t), \quad (2\text{-}211)$$

$$[S_N R_N](t) + [I_N R_N](t) + [R_N R_N](t) + [S_V R_N](t) + [I_V R_N](t) + [R_N R_V](t) = Q[R_N](t), \quad (2\text{-}212)$$

$$[S_N S_V](t) + [S_V I_N](t) + [S_V R_N](t) + [S_V S_V](t) + [S_V I_V](t) + [S_V R_V](t) = Q[S_V](t), \quad (2\text{-}213)$$

$$[S_N I_V](t) + [I_N I_V](t) + [I_V R_N](t) + [S_V I_V](t) + [I_V I_V](t) + [I_V R_V](t) = Q[I_V](t), \quad (2\text{-}214)$$

$$[S_N R_V](t) + [I_N R_V](t) + [R_N R_V](t) + [S_V R_V](t) + [I_V R_V](t) + [R_V R_V](t) = Q[R_V](t), \quad (2\text{-}215)$$

To solve the above set of equations, we add Eqs. (2-190) and (2-203) to obtain the following equation for the variable $[S_N I_N](t) + [S_N I_V](t)$:

$$\frac{d}{dt}\left([S_N R_N](t) + [S_N R_V](t)\right) = \gamma\left([S_N I_N](t) + [S_N I_V](t)\right) - \beta\mu\frac{\left([S_N I_N](t) + [S_N I_V](t)\right)\left([S_N R_N](t) + [S_N R_V](t)\right)}{[S_N](t)}. \quad (2\text{-}216)$$

By substituting $[S_N I_N](t) + [S_N I_V](t)$ from Eq. (2-182) into Eq. (2-216), we obtain the following:

$$\frac{d\left([S_N R_N](t) + [S_N R_V](t)\right)}{d[S_N](t)} = \mu\frac{\left([S_N R_N](t) + [S_N R_V](t)\right)}{[S_N](t)} - r. \quad (2\text{-}217)$$

By using the initial conditions $[S_N](0) = 1 - x$, $[S_N R_N](0) = 0$, and $[S_N R_V](0) = 0$, integration leads to the following:

$$[S_N R_N](t) + [S_N R_V](t) = Qr(1-x)\left(\left(\frac{[S_N](t)}{1-x}\right)^{\mu} - \frac{[S_N](t)}{1-x}\right). \quad (2\text{-}218)$$

Likewise, adding Eqs. (2-196) and (2-204) yields the following equation for the variable of $[S_V I_N](t) + [S_V I_V](t)$:

$$\frac{d}{dt}\left([S_V R_V](t)+[S_V R_N](t)\right)=\gamma\left([S_V I_N](t)+[S_V I_V](t)\right) \\ -(1-\eta)\beta\mu\frac{\left([S_V I_N](t)+[S_V I_V](t)\right)\left([S_V R_V](t)+[S_V R_N](t)\right)}{[S_V](t)}. \tag{2-219}$$

By substituting $[S_V I_N](t) + [S_V I_V](t)$ from Eq. (2-185) into Eq. (2-219), we obtain the following:

$$\frac{d\left([S_V R_V](t)+[S_V R_N](t)\right)}{d[S_V](t)}=\mu\frac{\left([S_V R_V](t)+[S_V R_N](t)\right)}{[S_V](t)}-\frac{r}{1-\eta}. \tag{2-220}$$

By using the initial conditions $[S_V](0) = x$, $[S_V R_N](0) = 0$, and $[S_V R_V](0) = 0$, integration leads to the following:

$$[S_V R_N](t)+[S_V R_V](t)=\frac{Qrx}{1-\eta}\left(\left(\frac{[S_V](t)}{x}\right)^{\mu}-\frac{[S_V](t)}{x}\right). \tag{2-221}$$

By taking the ratio between Eqs. (2-182) and (4-188), we obtain the following:

$$\frac{d[S_N S_N](t)}{d[S_N](t)}=2\mu\frac{[S_N S_N](t)}{[S_N](t)}. \tag{2-222}$$

By using the initial conditions $[S_N](0) = 1 - x$ and $[S_N S_N](0) = Q(1 - x)^2$, integration leads to the following:

$$[S_N S_N](t)=Q(1-x)^2\left(\frac{[S_N](t)}{1-x}\right)^{2\mu}. \tag{2-223}$$

In the same way, by taking the ratio between Eqs. (2-185) and (2-194), we obtain the following:

$$\frac{d[S_V S_V](t)}{d[S_V](t)}=2\mu\frac{[S_V S_V](t)}{[S_V](t)}. \tag{2-224}$$

By using the initial conditions $[S_V](0) = x$ and $[S_V S_V](0) = Qx^2$, integration leads to the following:

$$[S_V S_V](t)=Qx^2\left(\frac{[S_V](t)}{x}\right)^{2\mu}. \tag{2-225}$$

By substituting $[S_N I_N](t) + [S_N I_V](t)$ and $[S_V I_N](t) + [S_V I_V](t)$ from Eqs. (2-182) and (2-185) into Eq. (2-200), we obtain the following:

$$\frac{1}{[S_N S_V](t)}\frac{d[S_N S_V](t)}{dt}=\frac{\mu}{[S_N](t)}\frac{d}{dt}[S_N](t)+\frac{\mu}{[S_V](t)}\frac{d}{dt}[S_V](t). \tag{2-226}$$

By using the initial conditions $[S_N](0) = 1 - x$, $[S_V](0) = x$, and $[S_N S_V](0) = Qx(1 - x)$, integration leads to the following:

$$[S_N S_V](t)=Qx(1-x)\left(\frac{[S_N](t)}{1-x}\right)^{\mu}\left(\frac{[S_V](t)}{x}\right)^{\mu}. \tag{2-227}$$

At the steady state ($t \to \infty$), the constraints in Eqs. (2-209) to (2-215) can be rewritten as follows:

$$[S_N](\infty) + [R_N](\infty) + [S_V](\infty) + [R_V](\infty) = 1, \tag{2-228}$$

$$[S_N S_N](\infty) + [S_N R_N](\infty) + [S_N S_V](\infty) + [S_N R_V](\infty) = Q[S_N](\infty), \tag{2-229}$$

$$[S_N R_N](\infty) + [R_N R_N](\infty) + [S_V R_N](\infty) + [R_N R_V](\infty) = Q[R_N](\infty), \tag{2-230}$$

$$[S_N S_V](\infty) + [S_V R_N](\infty) + [S_V S_V](\infty) + [S_V R_V](\infty) = Q[S_V](\infty), \tag{2-231}$$

$$[S_N R_V](\infty) + [R_N R_V](\infty) + [S_V R_V](\infty) + [R_V R_V](\infty) = Q[R_V](\infty), \tag{2-232}$$

Substituting $[S_N S_N](\infty)$, $[S_N S_V](\infty)$, and $[S_N R_N](\infty) + [S_N R_V](\infty)$ from Eqs. (2-218), (2-223), and (2-227) into Eq. (2-229) yields the following:

$$Q(1-x-\alpha)\left(\frac{[S_N](\infty)}{1-x}\right)^{2\mu} + Qr(1-x)\left(\left(\frac{[S_N](\infty)}{1-x}\right)^{\mu} - \frac{[S_N](\infty)}{1-x}\right) + Q\alpha\left(\frac{[S_N](\infty)}{1-x}\right)^{\mu}\left(\frac{[S_V](\infty)}{x}\right)^{\mu} = Q(1-x)\frac{[S_N](\infty)}{1-x}. \tag{2-233}$$

Substituting $[S_V S_V](\infty)$, $[S_N S_V](\infty)$, and $[S_N R_N](\infty)+[S_N R_V](\infty)$ from Eqs. (2-221), (2-225), and (2-227) into Eq. (2-231) yields the following:

$$Q(x-\alpha)\left(\frac{[S_V](\infty)}{x}\right)^{2\mu} + \frac{Qrx}{1-\eta}\left(\left(\frac{[S_V](\infty)}{x}\right)^{\mu} - \frac{[S_V](\infty)}{x}\right) + Q\alpha\left(\frac{[S_N](\infty)}{1-x}\right)^{\mu}\left(\frac{[S_V](\infty)}{x}\right)^{\mu} = Qx\frac{[S_V](\infty)}{x}. \tag{2-234}$$

By defining $p = \left(\frac{[S_N](\infty)}{1-x}\right)^{1/Q}$ and $q = \left(\frac{[S_V](\infty)}{x}\right)^{1/Q}$ and by taking into account the definition of μ, we can write Eqs. (2-233) and (2-234) as follows:

$$(1-x-\alpha)p^{Q-1} - (1+r)(1-x)p + r(1-x) + \alpha q^{Q-1} = 0, \tag{2-235}$$

$$(x-\alpha)q^{Q-1} - \left(1+\frac{r}{1-\eta}\right)xq + \frac{rx}{1-\eta} + \alpha p^{Q-1} = 0. \tag{2-236}$$

By assuming a homogeneous distribution of vaccinated and non-vaccinated individuals, $\alpha = x(1-x)$, and taking away Eq. (2-235) from Eq. (2-236), we obtain the following equation:

$$q = Ap + B. \tag{2-237}$$

Here, $A = \frac{(1-\eta)(1+r)}{1-\eta+r}$, $B = \frac{r\eta}{1-\eta+r}$.

By inserting Eq. (2-237) to Eq. (2-235), we can obtain the following algebraic equation of p:

$$(1-x)p^{Q-1} - (1+r)p + r + x(Ap+B)^{Q-1} = 0, \tag{2-238}$$

which is equivalent to

$$(p-1)\left[\left\{(1-x) + A^{Q-1}x\right\}p^{Q-2} + \left\{(1-x) + A^{Q-1}x + (Q-1)A^{Q-2}B\right\}p^{Q-3}\cdots\right] = 0. \tag{2-239}$$

The nontrivial solution is then given by the following:

$$\left\{(1-x) + A^{Q-1}x\right\}p^{Q-2} + \left\{(1-x) + A^{Q-1}x + (Q-1)A^{Q-2}B\right\}p^{Q-3}\cdots = 0. \tag{2-240}$$

Given that $p = 1$ is also satisfied, the critical VC is represented by the following:

$$x_c = \frac{(Q-1)-(1+r)}{(Q-1) - \sum_{k=1}^{Q-2} k\binom{Q-1}{k}A^k B^{Q-1-k}}. \tag{2-241}$$

The final fractions are expressed as follows:

$$[S_N](\infty) = (1-x)p^Q, \tag{2-242}$$

$$[S_V](\infty) = xq^Q, \tag{2-243}$$

$$[R_N](\infty) = 1 - x - [S_N](\infty) = (1-x)(1-p^Q), \tag{2-244}$$

$$[R_V](\infty) = x - [S_V](\infty) = x(1-q^Q). \tag{2-245}$$

The other final pairs are hypothetically calculated as follows:

$$[S_N R_N](\infty) = Qr(1-x)\left(\left(\frac{[S_N](\infty)}{1-x}\right)^{\mu} - \frac{[S_N](\infty)}{1-x}\right)\frac{[R_N](\infty)}{[R_N](\infty)+[R_V](\infty)}, \tag{2-246}$$

$$[S_N R_V](\infty) = Qr(1-x)\left(\left(\frac{[S_N](\infty)}{1-x}\right)^{\mu} - \frac{[S_N](\infty)}{1-x}\right)\frac{[R_V](\infty)}{[R_N](\infty)+[R_V](\infty)}, \tag{2-247}$$

$$[S_V R_N](\infty) = Qr(1-e)x\left(\left(\frac{[S_V](\infty)}{(1-e)x}\right)^{\mu} - \frac{[S_V](\infty)}{(1-e)x}\right)\frac{[R_N](\infty)}{[R_N](\infty)+[R_V](\infty)}, \tag{2-248}$$

$$[S_V R_V](\infty) = Qr(1-e)x\left(\left(\frac{[S_V](\infty)}{(1-e)x}\right)^{\mu} - \frac{[S_V](\infty)}{(1-e)x}\right)\frac{[R_V](\infty)}{[R_N](\infty)+[R_V](\infty)}, \tag{2-249}$$

$$[R_N R_N](\infty) = [S_N S_N](0) - [S_N S_N](\infty) - 2[S_N R_N](\infty), \tag{2-250}$$

$$[R_V R_V](\infty) = [S_V S_V](0) - [S_V S_V](\infty) - 2[S_V R_V](\infty), \tag{2-251}$$

$$[R_N R_V](\infty) = [S_N S_V](0) - [S_N S_V](\infty) - [S_N R_V](\infty) - [S_V R_N](\infty). \tag{2-252}$$

Figure 2.7 shows the FES as a function of vaccination level in both the effectiveness and efficiency models shown above for the four different degrees. The figure also shows that the critical VC that eradicates an epidemic spread can be read from the border of the extinct phase, where FES = 0. These borders suggest the critical VC for preventing the spread of infection, which can be analytically drawn as Eqs. (2-167) and (2-241). These relationships were also confirmed in the MAS approach. Despite subtle discrepancies between the theoretical and MAS approaches, the simulation assumes a finite population size of $N = 10^4$ as opposed to infinity in pair approximation; in contrast to the deterministic approach of pair approximation, it assumes a stochastic process.

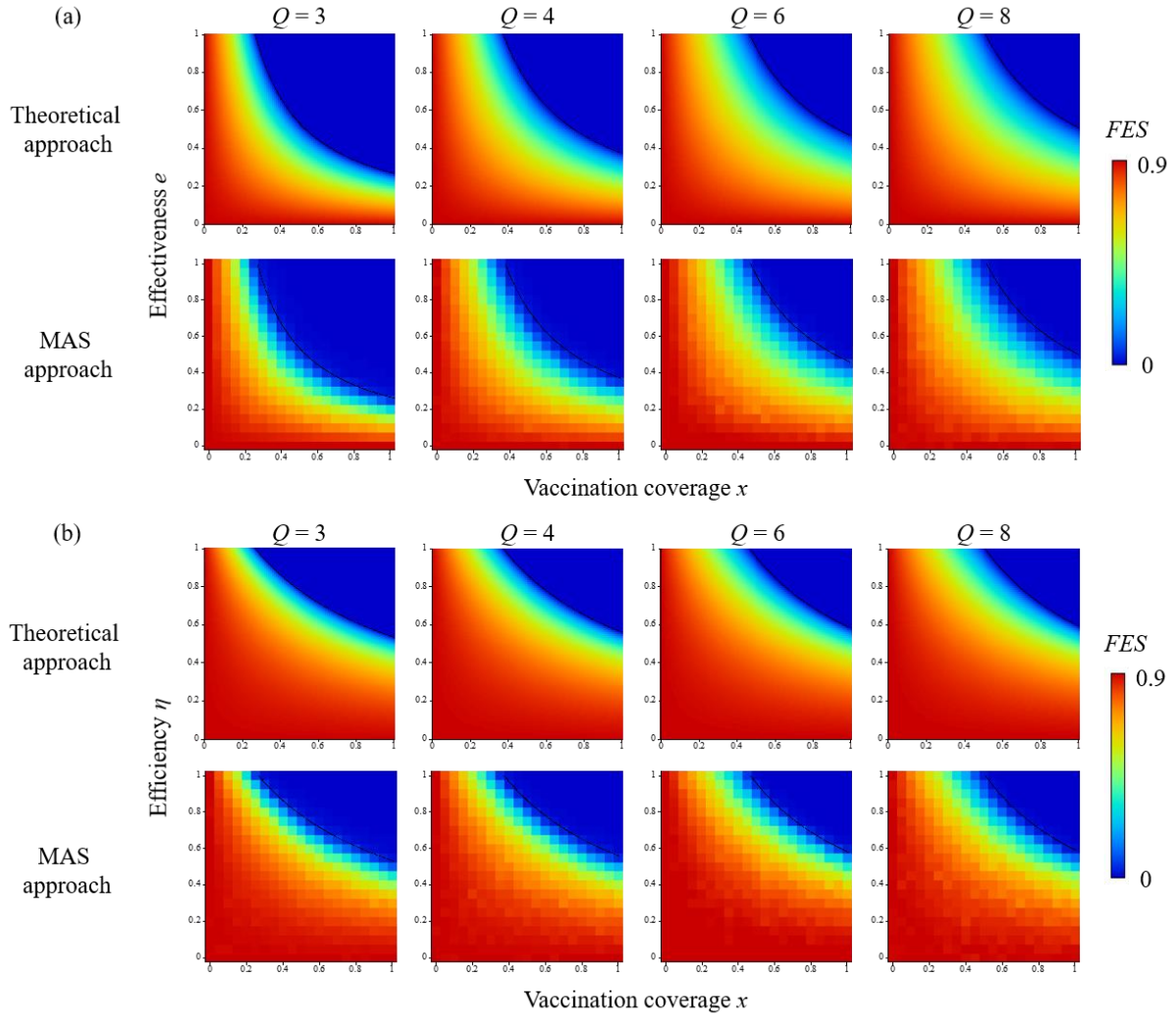

Figure 2.7. FES according to VC and the (a) effectiveness e and (b) efficiency η in four different degrees (Q = 3, 4, 6, 8). The upper panels represent the results of the theoretical approach, and the bottom panels represent the results of the MAS approach.

2.4 Vaccination game model

The underlying vaccination game model used throughout this study based on the original by Fu *et al*. [7]. In this model, each individual is placed in a social network and decides whether to get vaccinated or not. A seasonal infectious disease (e.g., influenza) spreads through such a population. The protective efficacy of the vaccine persists for less than a year because of waning antibodies and year-to-year changes in the circulating virus strain. Therefore, under a voluntary vaccination policy, individuals must make their mind regarding vaccination every year. The model captured this dynamics in two stages: an epidemic season and a vaccination campaign. Running until reaching a social equilibrium, the model observed the following performance measures: vaccination coverage (VC), the final epidemic size (FES), and the average social payoff (ASP). Figure 2.8 schematically shows the outline of vaccination game model.

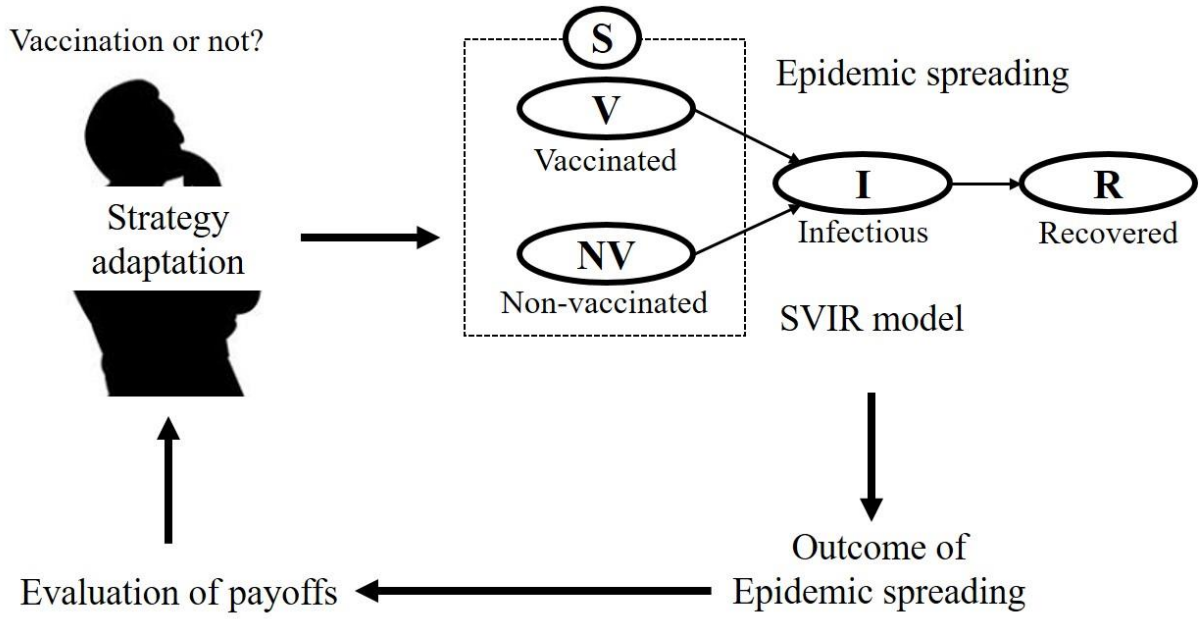

Figure 2.8. Schematic of vaccination game model

2.4.1 Payoff structure

An epidemic season continues until all infected individuals recover, meaning that the number of infected individuals is zero. If non-vaccinated individuals are infected, they incur the cost C_i of infection. By contrast, non-vaccinated individuals that fortunately remain healthy can avoid any cost burden. Moreover, individuals who unfortunately are infected despite taking either the vaccination or the defense against contagion are assigned the cost $C_v + C_i$ of vaccination and infection. To simplify the evaluation of each individual's payoff, without loss of generality, we rescale the cost by defining a relative cost of vaccination, namely $C_r = C_v / C_i$ ($0 \leq C_r \leq 1$; $C_i = 1$). Consequently, the payoff of each individual at the end of an epidemic season depends on his/her final state. Table 2.5 summarizes the payoff whether committing to a provision (either vaccination or defense against contagion) or not and whether having been healthy or infected.

Table 2.5. Payoff structure determined at the end of an epidemic season.

Strategy/state	Healthy	Infected
Vaccinated	$-C_r$	$-C_r-1$
Non-vaccinated	0	-1

We can now evaluate the expected payoffs in the form of the average social payoff $<\pi>$, the average corporative (vaccinated) payoff $<\pi_C>$, and the average defective (non-vaccinated) payoff $<\pi_D>$ for the respective provisions, namely imperfect vaccination and the defense against contagion:

2.4.1.1 Infinite and well-mixed population

These payoffs are calculated by the following equations:

Effectiveness model

$$\begin{aligned}\langle \pi \rangle = &-C_r x(e+(1-e)\exp[-R_0 R(\infty)]) - (C_r+1)x(1-e)(1-\exp[-R_0 R(\infty)]) \\ &-(1-x)(1-\exp[-R_0 R(\infty)])\end{aligned}, \tag{2-253}$$

$$\langle \pi_C \rangle = -C_r (e+(1-e)\exp[-R_0 R(\infty)]) - (C_r+1)(1-e)(1-\exp[-R_0 R(\infty)]), \tag{2-254}$$

$$\langle \pi_D \rangle = -(1-\exp[-R_0 R(\infty)]). \tag{2-255}$$

Efficiency model

$$\begin{aligned}\langle \pi \rangle = &-C_r x\exp[-(1-\eta)R_0 R(\infty)] - (C_r+1)x(1-\exp[-(1-\eta)R_0 R(\infty)]) \\ &-(1-x)(1-\exp[-R_0 R(\infty)])\end{aligned}, \tag{2-256}$$

$$\langle \pi_C \rangle = -C_r \exp[-(1-\eta)R_0 R(\infty)] - (C_r+1)(1-\exp[-(1-\eta)R_0 R(\infty)]), \tag{2-257}$$

$$\langle \pi_D \rangle = -(1-\exp[-R_0 R(\infty)]). \tag{2-258}$$

2.4.1.2 Network model

In the network model, these payoffs are calculated by the following equations:

Effectiveness model

$$\begin{aligned}\langle \pi \rangle = &-C_r \textstyle\sum_k P(k)x_k(e+(1-e)\exp[-(\lambda k\phi(\infty)]) - (C_r+1)\sum_k P(k)x_k(1-e)(1-\exp[-\lambda k\phi(\infty)]) \\ &-\textstyle\sum_k P(k)(1-x_k)(1-\exp[-\lambda k\phi(\infty)])\end{aligned}, \tag{2-259}$$

$$\langle \pi_C \rangle = -C_r \textstyle\sum_k P(k)x_k(e+(1-e)\exp[-(\lambda k\phi(\infty)]) - (C_r+1)\sum_k P(k)x_k(1-e)(1-\exp[-\lambda k\phi(\infty)]), \tag{2-260}$$

$$\langle \pi_D \rangle = -\textstyle\sum_k P(k)(1-x_k)(1-\exp[-\lambda k\phi(\infty)]). \tag{2-261}$$

Efficiency model

$$\begin{aligned}\langle \pi \rangle = &-C_r \textstyle\sum_k P(k)x_k \exp[-(1-\eta)\lambda k\phi(\infty)] - (C_r+1)\sum_k P(k)x_k(1-\exp[-(1-\eta)\lambda k\phi(\infty)]) \\ &-\textstyle\sum_k P(k)(1-x_k)(1-\exp[-\lambda k\phi(\infty)])\end{aligned}, \tag{2-262}$$

$$\langle \pi_C \rangle = -C_r \textstyle\sum_k P(k)x_k \exp[-(1-\eta)\lambda k\phi(\infty)] - (C_r+1)\sum_k P(k)x_k(1-\exp[-(1-\eta)\lambda k\phi(\infty)]), \tag{2-263}$$

$$\langle \pi_D \rangle = -\textstyle\sum_k P(k)(1-x_k)(1-\exp[-\lambda k\phi(\infty)]). \tag{2-264}$$

2.4.1.3 Pair approximation model

In the pair approximation model, these payoffs are calculated by the following equations:

Effectiveness model

$$\begin{aligned}\langle \pi \rangle &= -C_r\left([S_V](\infty)+[P_V](\infty)\right) - (C_r+1)[R_V](\infty) - [R_N](\infty) \\ &= -C_r\left((1-e)xp^Q + ex\right) - (C_r+1)(1-e)x(1-p^Q) - (1-x)(1-p^Q)\end{aligned}, \tag{2-265}$$

Efficiency model

$$\langle \pi \rangle = -C_r[S_V](\infty) - (C_r+1)[R_V](\infty) - [R_N](\infty) = -C_r xq^Q - (C_r+1)x(1-q^Q) - (1-x)(1-p^Q). \tag{2-266}$$

2.4.2 Strategy adaptation

In the framework of the vaccination game, when an epidemic season ends, an individual is allowed to alter his/her strategy whether using a provision or not by reflecting on what happened in the previous epidemic season. In the present study, we consider the following three types of strategy updating proposed respectively by Fu et al. [7], Fukuda et al. [9], and Iwamura et al. [12]. Those studies, based on a multi-agent simulation (MAS) approach, assumed a spatial structure among individuals by introducing a certain underlying network connecting individual agents. The present study does not consider any spatial structure. Hence, we rely on the so-called mean field approximation to evaluate a neighbor's payoff.

2.4.2.1 Individual-based risk assessment (IB-RA)

As with arguably the most accepted stochastic strategy-updating rule among the usual two-strategy and two-player (2×2) games, namely pairwise Fermi updating, every individual updates his/her strategy by imitating his/her neighborhood. An individual randomly selects one neighbor and then decides whether to adopt that neighbor's strategy. That is, individual i will adopt the selected neighbor j's strategy with probability

$$P(s_i \leftarrow s_j) = \frac{1}{1+\exp[-(\pi_j - \pi_i)/\kappa]}, \tag{2-267}$$

where s_i means the strategy of i, π_i is i's payoff in the previous season, and the parameter $\kappa > 0$ characterizes the strength of selection (the sensitivity of individuals to differences in their payoffs); smaller κ means that an individual is more sensitive to a payoff difference. We set $\kappa = 0.1$. Following Ref. [9], we call this updating rule individual-based risk assessment (IB-RA).

In the present framework, there are four classes of individual in relation to cost burden: (i) a successful free-rider (SFR) who pays nothing, (ii) a failed free-rider (FFR) who pays −1, (iii) an infected vaccinator (IV) who pays $-C_r-1$, and (iv) a healthy vaccinator (HV) who pays $-C_r$. While the strategies and individual can choose are two: using vaccination (V) and not using vaccination (NV). Thus, the transition probability that affects the time transition of x, which should be considered in the IB-RA rule, is covered by one of the following eight cases:

$$P(HV \leftarrow SFR) = \frac{1}{1+\exp\left[-(0-(-C_r))/\kappa\right]}, \tag{2-268-1}$$

$$P(HV \leftarrow FFR) = \frac{1}{1+\exp\left[-(-1-(-C_r))/\kappa\right]}, \tag{2-268-2}$$

$$P(IV \leftarrow SFR) = \frac{1}{1+\exp\left[-(0-(-C_r-1))/\kappa\right]}, \tag{2-268-3}$$

$$P(IV \leftarrow FFR) = \frac{1}{1+\exp\left[-(-1-(-C_r-1))/\kappa\right]}, \tag{2-268-4}$$

$$P(SFR \leftarrow HV) = \frac{1}{1+\exp\left[-\left(-C_r - 0\right)/\kappa\right]}, \tag{2-268-5}$$

$$P(SFR \leftarrow IV) = \frac{1}{1+\exp\left[-\left(-C_r - 1 - 0\right)/\kappa\right]}, \tag{2-268-6}$$

$$P(FFR \leftarrow HV) = \frac{1}{1+\exp\left[-\left(-C_r - (-1)\right)/\kappa\right]}, \tag{2-268-7}$$

$$P(FFR \leftarrow IV) = \frac{1}{1+\exp\left[-\left(-C_r - 1 - (-1)\right)/\kappa\right]}, \tag{2-268-8}$$

2.4.2.2 Strategy-based risk assessment (SB-RA)

Fukuda et al. [9] modified the imitation probability (IB-RA) to reflect the situation in which an individual tends to assess the risk based on a socially averaged payoff because of the prevalence of information about epidemics (probably given by the media). The modified probability is

$$P(s_i \leftarrow s_j) = \frac{1}{1+\exp[-(\langle \pi_j \rangle - \pi_i)/\kappa]}, \tag{2-269}$$

where $\langle \pi_j \rangle$ is the average payoff obtained by averaging the collective payoff over individuals who adopt the same strategy as that of a randomly selected neighbor *j* of individual *i*. Following Ref. [9], we call this updating rule strategy-based risk assessment (SB-RA).

The transition probability that we must consider now is one of the following:

$$P(HV \leftarrow NV) = \frac{1}{1+\exp\left[-\left(\langle \pi_D \rangle - (-C_r)\right)/\kappa\right]}, \tag{2-270-1}$$

$$P(IV \leftarrow NV) = \frac{1}{1+\exp\left[-\left(\langle \pi_D \rangle - (-C_r - 1)\right)/\kappa\right]}, \tag{2-270-2}$$

$$P(SFR \leftarrow V) = \frac{1}{1+\exp\left[-\left(\langle \pi_C \rangle - 0\right)/\kappa\right]}, \tag{2-270-3}$$

$$P(FFR \leftarrow V) = \frac{1}{1+\exp\left[-\left(\langle \pi_C \rangle - (-1)\right)/\kappa\right]}. \tag{2-270-4}$$

2.4.2.3 Direct commitment (DC)

Iwamura et al. [12] proposed a new updating rule that directly gives an individual's "probability of using vaccination," namely $P_{S=V}$, triggered by his/her consciousness of how dangerous trying to be a free-rider would be. This probability is evaluated by comparing the average payoffs of using and not using vaccination as observed in this agent's neighborhood:

$$P_{S=V} = \frac{1}{1+\exp\left[-\left(\langle \pi_{S=V} \rangle - \langle \pi_{s=NV} \rangle\right)/\kappa\right]}, \quad P_{S=NV} = 1 - P_{S=V}, \tag{2-271}$$

where $\langle \pi_{S=V} \rangle$ and $\langle \pi_{S=NV} \rangle$ are the mean average payoffs of vaccinators and non-vaccinators, respectively, as observed in the agent's neighborhood; taken alone, $P_{S=NV}$ is the probability of not using

vaccination. In the present model, the mean field approximation gives that those two can be alternated by $\langle \pi_C \rangle$ and $\langle \pi_D \rangle$, respectively. We call this updating rule direct commitment (DC).

The transition probability that we must consider now is one of the following:

$$P(V \leftarrow NV) = \frac{1}{1+\exp\left[-\left(\langle \pi_D \rangle - \langle \pi_C \rangle\right)/\kappa\right]}, \tag{2-272-1}$$

$$P(NV \leftarrow V) = \frac{1}{1+\exp\left[-\left(\langle \pi_C \rangle - \langle \pi_D \rangle\right)/\kappa\right]}. \tag{2-272-2}$$

2.4.3 Evolutionary system

Strategy updating takes place after each epidemic season as defined above, thereby inevitably increasing or decreasing vaccination coverage x.

2.4.3.1 Infinite and well-mixed population

Effectiveness model + IB-RA:

$$\begin{aligned}\frac{dx}{dt} = {} & x(1-x)(e+(1-e)\exp[-R_0R(\infty)])\exp[-R_0R(\infty)]\left(P(SFR \leftarrow HV) - P(HV \leftarrow SFR)\right) \\ & + x(1-x)(e+(1-e)\exp[-R_0R(\infty)])(1-\exp[-R_0R(\infty)])\left(P(FFR \leftarrow HV) - P(HV \leftarrow FFR)\right) \\ & + x(1-x)(1-e)(1-\exp[-R_0R(\infty)])\exp[-R_0R(\infty)]\left(P(SFR \leftarrow IV) - P(IV \leftarrow SFR)\right) \\ & + x(1-x)(1-e)(1-\exp[-R_0R(\infty)])^2\left(P(FFR \leftarrow IV) - P(IV \leftarrow FFR)\right)\end{aligned}, \tag{2-273}$$

Efficiency model + IB-RA:

$$\begin{aligned}\frac{dx}{dt} = {} & x(1-x)\exp[-(1-\eta)R_0R(\infty)]\exp[-R_0R(\infty)]\left(P(SFR \leftarrow HV) - P(HV \leftarrow SFR)\right) \\ & + x(1-x)\exp[-(1-\eta)R_0R(\infty)](1-\exp[-R_0R(\infty)])\left(P(FFR \leftarrow HV) - P(HV \leftarrow FFR)\right) \\ & + x(1-x)(1-\exp[-(1-\eta)R_0R(\infty)])\exp[-R_0R(\infty)]\left(P(SFR \leftarrow IV) - P(IV \leftarrow SFR)\right) \\ & + x(1-x)(1-\exp[-(1-\eta)R_0R(\infty)])(1-\exp[-R_0R(\infty)])\left(P(FFR \leftarrow IV) - P(IV \leftarrow FFR)\right)\end{aligned}, \tag{2-274}$$

Effectiveness model + SB-RA:

$$\begin{aligned}\frac{dx}{dt} = {} & -x(1-x)(e+(1-e)\exp[-R_0R(\infty)])P(HV \leftarrow NV) \\ & - x(1-x)(1-e)(1-\exp[-R_0R(\infty)])P(IV \leftarrow NV) \\ & + x(1-x)\exp[-R_0R(\infty)]P(SFR \leftarrow V) \\ & + x(1-x)(1-\exp[-R_0R(\infty)])P(FFR \leftarrow V)\end{aligned}, \tag{2-275}$$

Efficiency model + SB-RA:

$$\begin{aligned}\frac{dx}{dt} = {} & -x(1-x)\exp[-(1-\eta)R_0R(\infty)]P(HV \leftarrow NV) \\ & - x(1-x)(1-\exp[-(1-\eta)R_0R(\infty)])P(IV \leftarrow NV) \\ & + x(1-x)\exp[-R_0R(\infty)]P(SFR \leftarrow V) \\ & + x(1-x)(1-\exp[-R_0R(\infty)])P(FFR \leftarrow NV)\end{aligned}, \tag{2-276}$$

Effectiveness or efficiency model + DC:

$$\frac{dx}{dt} = -xP\left(V \leftarrow NV\right) + (1-x)P\left(NV \leftarrow V\right). \tag{2-277}$$

Something worth noting is that Eq. (2-277) is qualitatively consistent with what are called replicator dynamics, one of the most common concepts in evolutionary game theory for expressing a system's dynamics (e.g., [3]). All the above dynamical equations can be solved numerically. We introduce a so-called explicit scheme for the time-varying terms to obtain a numerical solution; a vaccination coverage at equilibrium.

2.4.3.2 Network model

IB-RA + effectiveness model

$$\begin{aligned}
\frac{dx_k}{dt} = & -x_k\left(e+(1-e)\exp[-\lambda k\phi(\infty)]\right)\frac{1}{\langle k\rangle}\sum_k kp(k)(1-x_k)\exp[-\lambda k\phi(\infty)]P\left(HV \leftarrow SFR\right) \\
& - x_k\left(e+(1-e)\exp[-\lambda k\phi(\infty)]\right)\frac{1}{\langle k\rangle}\sum_k kp(k)(1-x_k)(1-\exp[-\lambda k\phi(\infty)])P\left(HV \leftarrow FFR\right) \\
& - x_k(1-e)(1-\exp[-\lambda k\phi(\infty)])\frac{1}{\langle k\rangle}\sum_k kp(k)(1-x_k)\exp[-\lambda k\phi(\infty)]P\left(IV \leftarrow SFR\right) \\
& - x_k(1-e)(1-\exp[-\lambda k\phi(\infty)])\frac{1}{\langle k\rangle}\sum_k kp(k)(1-x_k)(1-\exp[-\lambda k\phi(\infty)])P\left(IV \leftarrow FFR\right) \\
& + (1-x_k)\exp[-\lambda k\phi(\infty)]\frac{1}{\langle k\rangle}\sum_k kp(k)x_k\left(e+(1-e)\exp[-\lambda k\phi(\infty)]\right)P\left(SFR \leftarrow HV\right) \\
& + (1-x_k)\exp[-\lambda k\phi(\infty)]\frac{1}{\langle k\rangle}\sum_k kp(k)x_k(1-e)(1-\exp[-\lambda k\phi(\infty)])P\left(SFR \leftarrow IV\right) \\
& + (1-x_k)(1-\exp[-\lambda k\phi(\infty)])\frac{1}{\langle k\rangle}\sum_k kp(k)x_k\left(e+(1-e)\exp[-\lambda k\phi(\infty)]\right)P\left(FFR \leftarrow HV\right) \\
& + (1-x_k)(1-\exp[-\lambda k\phi(\infty)])\frac{1}{\langle k\rangle}\sum_k kp(k)x_k(1-e)(1-\exp[-\lambda k\phi(\infty)])P\left(FFR \leftarrow IV\right)
\end{aligned}, \tag{2-278}$$

IB-RA + efficiency model

$$\begin{aligned}\frac{dx_k}{dt} = &-x_k \exp[-(1-\eta)\lambda k\phi(\infty)]\frac{1}{\langle k\rangle}\sum_k kp(k)(1-x_k)\exp[-\lambda k\phi(\infty)]P\left(HV \leftarrow SFR\right)\\ &- x_k \exp[-(1-\eta)\lambda k\phi(\infty)]\frac{1}{\langle k\rangle}\sum_k kp(k)(1-x_k)(1-\exp[-\lambda k\phi(\infty)])P\left(HV \leftarrow FFR\right)\\ &- x_k (1-\exp[-(1-\eta)\lambda k\phi(\infty)])\frac{1}{\langle k\rangle}\sum_k kp(k)(1-x_k)\exp[-\lambda k\phi(\infty)]P\left(IV \leftarrow SFR\right)\\ &- x_k (1-\exp[-(1-\eta)\lambda k\phi(\infty)])\frac{1}{\langle k\rangle}\sum_k kp(k)(1-x_k)(1-\exp[-\lambda k\phi(\infty)])P\left(IV \leftarrow FFR\right)\\ &+ (1-x_k)\exp[-\lambda k\phi(\infty)]\frac{1}{\langle k\rangle}\sum_k kp(k)x_k \exp[-(1-\eta)\lambda k\phi(\infty)]P\left(SFR \leftarrow HV\right)\\ &+ (1-x_k)\exp[-\lambda k\phi(\infty)]\frac{1}{\langle k\rangle}\sum_k kp(k)x_k (1-\exp[-(1-\eta)\lambda k\phi(\infty)])P\left(SFR \leftarrow IV\right)\\ &+ (1-x_k)(1-\exp[-\lambda k\phi(\infty)])\frac{1}{\langle k\rangle}\sum_k kp(k)x_k \exp[-(1-\eta)\lambda k\phi(\infty)]P\left(FFR \leftarrow HV\right)\\ &+ (1-x_k)(1-\exp[-\lambda k\phi(\infty)])\frac{1}{\langle k\rangle}\sum_k kp(k)x_k (1-\exp[-(1-\eta)\lambda k\phi(\infty)])P\left(FFR \leftarrow IV\right)\end{aligned}, \quad (2\text{-}279)$$

SB-RA + effectiveness model

$$\begin{aligned}\frac{dx_k}{dt} = &-x_k (e+(1-e)\exp[-\lambda k\phi(\infty)])\frac{1}{\langle k\rangle}\sum_k kp(k)(1-x_k)P\left(HV \leftarrow NV\right)\\ &- x_k (1-e)(1-\exp[-\lambda k\phi(\infty)])\frac{1}{\langle k\rangle}\sum_k kp(k)(1-x_k)P\left(IV \leftarrow NV\right)\\ &+ (1-x_k)\exp[-\lambda k\phi(\infty)]\frac{1}{\langle k\rangle}\sum_k kp(k)x_k P\left(SFR \leftarrow V\right)\\ &+ (1-x_k)(1-\exp[-\lambda k\phi(\infty)])\frac{1}{\langle k\rangle}\sum_k kp(k)x_k P\left(FFR \leftarrow V\right)\end{aligned}, \quad (2\text{-}280)$$

SB-RA + efficiency model

$$\begin{aligned}\frac{dx_k}{dt} = &-x_k \exp[-(1-\eta)\lambda k\phi(\infty)]\frac{1}{\langle k\rangle}\sum_k kp(k)(1-x_k)P\left(HV \leftarrow NV\right)\\ &- x_k (1-\exp[-(1-\eta)\lambda k\phi(\infty)])\frac{1}{\langle k\rangle}\sum_k kp(k)(1-x_k)P\left(IV \leftarrow NV\right)\\ &+ (1-x_k)\exp[-\lambda k\phi(\infty)]\frac{1}{\langle k\rangle}\sum_k kp(k)x_k P\left(SFR \leftarrow V\right)\\ &+ (1-x_k)(1-\exp[-\lambda k\phi(\infty)])\frac{1}{\langle k\rangle}\sum_k kp(k)x_k P\left(FFR \leftarrow V\right)\end{aligned}. \quad (2\text{-}281)$$

All the above dynamical equations, Eqs. (2-278)–(2-281), can be solved numerically. Thus, the final result is affected by the two-stage process: SIR dynamics in a single season and the strategy adaptation process. We rely on an explicit scheme. We evaluate how this specific dynamic system evolves. Therefore, we observe the FES, VC, and ASP at a social equilibrium.

2.4.3.3 Pair approximation model

After the end of every epidemic season, the vaccination coverage x will increase or decrease.

Here, we applied the IB-RA model. To quantify this evolutionary process, we obtain the following equation for the dynamic system:

Effectiveness model

$$\frac{dx}{dt}=\frac{[S_NS_V](\infty)+[S_NP_V](\infty)}{Q}\left(P(SFR\leftarrow HV)-P(HV\leftarrow SFR)\right)+\frac{[S_NR_V](\infty)}{Q}\left(P(SFR\leftarrow IV)-P(IV\leftarrow SFR)\right)$$
$$+\frac{[S_VR_N](\infty)+[P_VR_N](\infty)}{Q}\left(P(FFR\leftarrow HV)-P(HV\leftarrow FFR)\right)+\frac{[R_NR_V](\infty)}{Q}\left(P(FFR\leftarrow IV)-P(IV\leftarrow FFR)\right) \quad (2\text{-}282)$$

Efficiency model

$$\frac{dx}{dt}=\frac{[S_NS_V](\infty)}{Q}\left(P(SFR\leftarrow HV)-P(HV\leftarrow SFR)\right)+\frac{[S_NR_V](\infty)}{Q}\left(P(SFR\leftarrow IV)-P(IV\leftarrow SFR)\right)$$
$$+\frac{[S_VR_N](\infty)}{Q}\left(P(FFR\leftarrow HV)-P(HV\leftarrow FFR)\right)+\frac{[R_NR_V](\infty)}{Q}\left(P(FFR\leftarrow IV)-P(IV\leftarrow FFR)\right) \quad (2\text{-}283)$$

As a result of changing the strategy, the vaccinator-nonvaccinator connection coefficient α will also change. To quantify this evolutionary process, we obtain the following equation for the dynamic system:

Effectiveness model

$$\begin{aligned}
Q\frac{d\alpha}{dt}=&[S_NS_N](\infty)P(S_N\to V|S_NS_N)\left(1-P(S_N\to V|S_NS_N)\right)\\
&+[S_NR_N](\infty)\left\{P(S_N\to V|S_NR_N)\left(1-P(R_N\to V|S_NR_N)\right)+P(R_N\to V|S_NR_N)\left(1-P(S_N\to V|S_NR_N)\right)\right\}\\
&+[R_NR_N](\infty)P\left(R_N\to V|R_NR_N\right)\left(1-P(R_N\to V|R_NR_N)\right)\\
&+[S_VS_V](\infty)P\left(S_V\to NV|S_VS_V\right)\left(1-P(S_V\to NV|S_VS_V)\right)\\
&+[S_VR_V](\infty)\left\{P(S_V\to NV|S_VR_V)\left(1-P(R_V\to NV|S_VR_V)\right)+P(R_V\to NV|S_VR_V)\left(1-P(S_V\to NV|S_VR_V)\right)\right\}\\
&+[R_VR_V](\infty)P\left(R_V\to NV|R_VR_V\right)\left(1-P(R_V\to NV|R_VR_V)\right)\\
&+[S_VP_V](\infty)\left\{P(S_V\to NV|S_VP_V)\left(1-P(P_V\to NV|S_VP_V)\right)+P(P_V\to NV|S_VP_V)\left(1-P(S_V\to NV|S_VP_V)\right)\right\}\\
&+[R_VP_V](\infty)\left\{P(R_V\to NV|S_VP_V)\left(1-P(P_V\to NV|R_VP_V)\right)+P(P_V\to NV|R_VP_V)\left(1-P(S_V\to NV|R_VP_V)\right)\right\}\\
&-[S_NS_V](\infty)\left\{P(S_N\to V|S_NS_V)\left(1-P(S_V\to NV|S_NS_V)\right)+P(S_V\to NV|S_NS_V)\left(1-P(S_N\to V|S_NS_V)\right)\right\}\\
&-[S_NR_V](\infty)\left\{P(S_N\to V|S_NR_V)\left(1-P(R_V\to NV|S_NR_V)\right)+P(R_V\to NV|S_NR_V)\left(1-P(S_N\to V|S_NR_V)\right)\right\}\\
&-[S_VR_N](\infty)\left\{P(R_N\to V|S_VR_N)\left(1-P(S_V\to NV|S_VR_N)\right)+P(S_V\to NV|S_VR_N)\left(1-P(R_N\to V|S_VR_N)\right)\right\}\\
&-[R_NR_V](\infty)\left\{P(R_N\to V|R_NR_V)\left(1-P(R_V\to NV|R_NR_V)\right)+P(R_V\to NV|R_NR_V)\left(1-P(R_N\to V|R_NS_V)\right)\right\}\\
&-[S_NP_V](\infty)\left\{P(S_N\to V|S_NP_V)\left(1-P(P_V\to NV|S_NP_V)\right)+P(P_V\to NV|S_NP_V)\left(1-P(S_N\to V|S_NP_V)\right)\right\}\\
&-[R_NP_V](\infty)\left\{P(R_N\to V|R_NP_V)\left(1-P(P_V\to NV|R_NP_V)\right)+P(P_V\to NV|R_NP_V)\left(1-P(R_N\to V|R_NP_V)\right)\right\}
\end{aligned} \quad (2\text{-}284)$$

Here, $P(A\to V \text{ or } NV|AB)$ is a transition probability that the focal A of pair AB change to the opposite strategy (vaccinator or nonvaccinator). These transition probabilities were calculated as the following equations:

$$P(S_N \to V \mid S_N S_N) = P(S_N \to V \mid S_N R_N)$$
$$= \frac{Q-1}{Q}\left(\frac{[S_N S_V](\infty)+[S_N P_V](\infty)}{Q[S_N]} P(SFR \leftarrow HV) + \frac{[S_N R_V](\infty)}{Q[S_N]} P(SFR \leftarrow IV)\right) \quad (2\text{-}285\text{-}1)$$

$$P(R_N \to V \mid S_N R_N) = P(R_N \to V \mid R_N R_N)$$
$$= \frac{Q-1}{Q}\left(\frac{[S_V R_N](\infty)+[R_N P_V](\infty)}{Q[R_N]} P(FFR \leftarrow HV) + \frac{[R_N R_V](\infty)}{Q[R_N]} P(FFR \leftarrow IV)\right) \quad (2\text{-}285\text{-}2)$$

$$P(S_V \to NV \mid S_V S_V) = P(S_V \to NV \mid S_V R_V) = P(S_V \to NV \mid S_V P_V)$$
$$= \frac{Q-1}{Q}\left(\frac{[S_N S_V](\infty)}{Q[S_V]} P(HV \leftarrow SFR) + \frac{[S_V R_N](\infty)}{Q[S_V]} P(HV \leftarrow FFR)\right) \quad (2\text{-}285\text{-}3)$$

$$P(R_V \to NV \mid S_V R_V) = P(R_V \to NV \mid R_V R_V) = P(R_V \to NV \mid R_V P_V)$$
$$= \frac{Q-1}{Q}\left(\frac{[S_N R_V](\infty)}{Q[R_V]} P(IV \leftarrow SFR) + \frac{[R_N R_V](\infty)}{Q[R_V]} P(IV \leftarrow FFR)\right) \quad (2\text{-}285\text{-}4)$$

$$P(P_V \to NV \mid P_V P_V) = P(P_V \to NV \mid S_V P_V) = P(P_V \to NV \mid R_V P_V)$$
$$= \frac{Q-1}{Q}\left(\frac{[S_N P_V](\infty)}{Q[P_V]} P(HV \leftarrow SFR) + \frac{[R_N P_V](\infty)}{Q[P_V]} P(HV \leftarrow FFR)\right) \quad (2\text{-}285\text{-}5)$$

$$P(S_N \to V \mid S_N S_V) = P(S_N \to V \mid S_N P_V)$$
$$= \frac{1}{Q} P(SFR \leftarrow HV) + \frac{Q-1}{Q}\left(\frac{[S_N S_V](\infty)+[S_N P_V](\infty)}{Q[S_N]} P(SFR \leftarrow HV) + \frac{[S_N R_V](\infty)}{Q[S_N]} P(SFR \leftarrow IV)\right)$$
$$(2\text{-}285\text{-}6)$$

$$P(S_V \to NV \mid S_N S_V)$$
$$= \frac{1}{Q} P(HV \leftarrow SFR) + \frac{Q-1}{Q}\left(\frac{[S_N S_V](\infty)}{Q[S_V]} P(HV \leftarrow SFR) + \frac{[S_V R_N](\infty)}{Q[S_V]} P(HV \leftarrow FFR)\right) \quad (2\text{-}285\text{-}7)$$

$$P(P_V \to NV \mid S_N P_V)$$
$$= \frac{1}{Q} P(HV \leftarrow SFR) + \frac{Q-1}{Q}\left(\frac{[S_N P_V](\infty)}{Q[P_V]} P(HV \leftarrow SFR) + \frac{[R_N P_V](\infty)}{Q[P_V]} P(HV \leftarrow FFR)\right) \quad (2\text{-}285\text{-}8)$$

$$P(S_N \to V \mid S_N R_V)$$
$$= \frac{1}{Q} P(SFR \leftarrow IV) + \frac{Q-1}{Q}\left(\frac{[S_N S_V](\infty)+[S_N P_V](\infty)}{Q[S_N]} P(SFR \leftarrow HV) + \frac{[S_N R_V](\infty)}{Q[S_N]} P(SFR \leftarrow IV)\right)$$
$$(2\text{-}285\text{-}9)$$

$$P(R_V \to NV \mid S_N R_V)$$
$$= \frac{1}{Q} P(IV \leftarrow SFR) + \frac{Q-1}{Q}\left(\frac{[S_N R_V](\infty)}{Q[R_V]} P(IV \leftarrow SFR) + \frac{[R_N R_V](\infty)}{Q[R_V]} P(IV \leftarrow FFR)\right) \quad (2\text{-}285\text{-}10)$$

$$P(R_N \to V \mid S_V R_N) = P(R_N \to V \mid R_N P_V)$$
$$= \frac{1}{Q} P(FFR \leftarrow HV) + \frac{Q-1}{Q}\left(\frac{[S_V R_N](\infty)+[R_N P_V](\infty)}{Q[R_N]} P(FFR \leftarrow HV) + \frac{[R_N R_V](\infty)}{Q[R_N]} P(FFR \leftarrow IV)\right)$$
$$(2\text{-}285\text{-}11)$$

$$P(S_V \to NV \,|\, S_V R_N)$$
$$= \frac{1}{Q} P(HV \leftarrow FFR) + \frac{Q-1}{Q}\left(\frac{[S_N S_V](\infty)}{Q[S_V]} P(HV \leftarrow SFR) + \frac{[S_V R_N](\infty)}{Q[S_V]} P(HV \leftarrow FFR) \right) \quad (2\text{-}285\text{-}12)$$

$$P(P_V \to NV \,|\, R_N P_V)$$
$$= \frac{1}{Q} P(HV \leftarrow FFR) + \frac{Q-1}{Q}\left(\frac{[S_N P_V](\infty)}{Q[P_V]} P(HV \leftarrow SFR) + \frac{[R_N P_V](\infty)}{Q[P_V]} P(HV \leftarrow FFR) \right) \quad (2\text{-}285\text{-}13)$$

$$P(R_N \to V \,|\, R_N R_V)$$
$$= \frac{1}{Q} P(FFR \leftarrow IV) + \frac{Q-1}{Q}\left(\frac{[S_V R_N](\infty) + [R_N P_V](\infty)}{Q[R_N]} P(FFR \leftarrow HV) + \frac{[R_N R_V](\infty)}{Q[R_N]} P(FFR \leftarrow IV) \right)$$

(2-285-14)

$$P(R_V \to NV \,|\, R_N R_V)$$
$$= \frac{1}{Q} P(IV \leftarrow FFR) + \frac{Q-1}{Q}\left(\frac{[S_N R_V](\infty)}{Q[R_V]} P(IV \leftarrow SFR) + \frac{[R_N R_V](\infty)}{Q[R_V]} P(IV \leftarrow FFR) \right) \quad (2\text{-}285\text{-}15)$$

Efficiency model

$$\begin{aligned}
Q\frac{d\alpha}{dt} &= [S_N S_N](\infty) P(S_N \to V \,|\, S_N S_N)\left(1 - P(S_N \to V \,|\, S_N S_N)\right) \\
&+ [S_N R_N](\infty)\left\{ P(S_N \to V \,|\, S_N R_N)\left(1 - P(R_N \to V \,|\, S_N R_N)\right) + P(R_N \to V \,|\, S_N R_N)\left(1 - P(S_N \to V \,|\, S_N R_N)\right) \right\} \\
&+ [R_N R_N](\infty) P\left(R_N \to V \,|\, R_N R_N\right)\left(1 - P(R_N \to V \,|\, R_N R_N)\right) \\
&+ [S_V S_V](\infty) P\left(S_V \to NV \,|\, S_V S_V\right)\left(1 - P(S_V \to NV \,|\, S_V S_V)\right) \\
&+ [S_V R_V](\infty)\left\{ P(S_V \to NV \,|\, S_V R_V)\left(1 - P(R_V \to NV \,|\, S_V R_V)\right) + P(R_V \to NV \,|\, S_V R_V)\left(1 - P(S_V \to NV \,|\, S_V R_V)\right) \right\} \\
&+ [R_V R_V](\infty) P\left(R_V \to NV \,|\, R_V R_V\right)\left(1 - P(R_V \to NV \,|\, R_V R_V)\right) \\
&- [S_N S_V](\infty)\left\{ P(S_N \to V \,|\, S_N S_V)\left(1 - P(S_V \to NV \,|\, S_N S_V)\right) + P(S_V \to NV \,|\, S_N S_V)\left(1 - P(S_N \to NV \,|\, S_N S_V)\right) \right\} \\
&- [S_N R_V](\infty)\left\{ P(S_N \to V \,|\, S_N R_V)\left(1 - P(R_V \to NV \,|\, S_N R_V)\right) + P(R_V \to NV \,|\, S_N R_V)\left(1 - P(S_N \to NV \,|\, S_N R_V)\right) \right\} \\
&- [S_V R_N](\infty)\left\{ P(R_N \to V \,|\, S_V R_N)\left(1 - P(S_V \to NV \,|\, S_V R_N)\right) + P(S_V \to NV \,|\, S_V R_N)\left(1 - P(R_N \to NV \,|\, S_V R_N)\right) \right\} \\
&- [R_N R_V](\infty)\left\{ P(R_N \to V \,|\, R_N R_V)\left(1 - P(R_V \to NV \,|\, R_N R_V)\right) + P(R_V \to NV \,|\, R_N R_V)\left(1 - P(R_N \to NV \,|\, R_N S_V)\right) \right\}
\end{aligned}$$

(2-286)

The transition probabilities for efficiency model were calculated as the following equations:

$$P(S_N \to V \,|\, S_N S_N) = P(S_N \to V \,|\, S_N R_N)$$
$$= \frac{Q-1}{Q}\left(\frac{[S_N S_V](\infty)}{Q[S_N]} P(SFR \leftarrow HV) + \frac{[S_N R_V](\infty)}{Q[S_N]} P(SFR \leftarrow IV) \right) \quad (2\text{-}287\text{-}1)$$

$$P(R_N \to V \,|\, S_N R_N) = P(R_N \to V \,|\, R_N R_N)$$
$$= \frac{Q-1}{Q}\left(\frac{[S_V R_N](\infty)}{Q[R_N]} P(FFR \leftarrow HV) + \frac{[R_N R_V](\infty)}{Q[R_N]} P(FFR \leftarrow IV) \right) \quad (2\text{-}287\text{-}2)$$

$$P(S_V \to NV \,|\, S_V S_V) = P(S_V \to NV \,|\, S_V R_V)$$
$$= \frac{Q-1}{Q}\left(\frac{[S_N S_V](\infty)}{Q[S_V]} P(HV \leftarrow SFR) + \frac{[S_V R_N](\infty)}{Q[S_V]} P(HV \leftarrow FFR) \right) \quad (2\text{-}287\text{-}3)$$

$$P(R_V \to NV \,|\, S_V R_V) = P(R_V \to NV \,|\, R_V R_V)$$
$$= \frac{Q-1}{Q}\left(\frac{[S_N R_V](\infty)}{Q[R_V]} P(IV \leftarrow SFR) + \frac{[R_N R_V](\infty)}{Q[R_V]} P(IV \leftarrow FFR) \right) \quad (2\text{-}287\text{-}4)$$

$$P(S_N \to V \,|\, S_N S_V)$$
$$= \frac{1}{Q} P(SFR \leftarrow HV) + \frac{Q-1}{Q}\left(\frac{[S_N S_V](\infty)}{Q[S_N]} P(SFR \leftarrow HV) + \frac{[S_N R_V](\infty)}{Q[S_N]} P(SFR \leftarrow IV) \right) \quad (2\text{-}287\text{-}5)$$

$$P(S_V \to NV \,|\, S_N S_V)$$
$$= \frac{1}{Q} P(HV \leftarrow SFR) + \frac{Q-1}{Q}\left(\frac{[S_N S_V](\infty)}{Q[S_V]} P(HV \leftarrow SFR) + \frac{[S_V R_N](\infty)}{Q[S_V]} P(HV \leftarrow FFR) \right) \quad (2\text{-}287\text{-}6)$$

$$P(S_N \to V \,|\, S_N R_V)$$
$$= \frac{1}{Q} P(SFR \leftarrow IV) + \frac{Q-1}{Q}\left(\frac{[S_N S_V](\infty)}{Q[S_N]} P(SFR \leftarrow HV) + \frac{[S_N R_V](\infty)}{Q[S_N]} P(SFR \leftarrow IV) \right) \quad (2\text{-}287\text{-}7)$$

$$P(R_V \to NV \,|\, S_N R_V)$$
$$= \frac{1}{Q} P(IV \leftarrow SFR) + \frac{Q-1}{Q}\left(\frac{[S_N R_V](\infty)}{Q[R_V]} P(IV \leftarrow SFR) + \frac{[R_N R_V](\infty)}{Q[R_V]} P(IV \leftarrow FFR) \right) \quad (2\text{-}287\text{-}8)$$

$$P(R_N \to V \,|\, S_V R_N)$$
$$= \frac{1}{Q} P(FFR \leftarrow HV) + \frac{Q-1}{Q}\left(\frac{[S_V R_N](\infty)}{Q[R_N]} P(FFR \leftarrow HV) + \frac{[R_N R_V](\infty)}{Q[R_N]} P(FFR \leftarrow IV) \right) \quad (2\text{-}287\text{-}9)$$

$$P(S_V \to NV \,|\, S_V R_N)$$
$$= \frac{1}{Q} P(HV \leftarrow FFR) + \frac{Q-1}{Q}\left(\frac{[S_N S_V](\infty)}{Q[S_V]} P(HV \leftarrow SFR) + \frac{[S_V R_N](\infty)}{Q[S_V]} P(HV \leftarrow FFR) \right) \quad (2\text{-}287\text{-}10)$$

$$P(P_V \to NV \,|\, R_N P_V)$$
$$= \frac{1}{Q} P(HV \leftarrow FFR) + \frac{Q-1}{Q}\left(\frac{[S_N P_V](\infty)}{Q[P_V]} P(HV \leftarrow SFR) + \frac{[R_N P_V](\infty)}{Q[P_V]} P(HV \leftarrow FFR) \right) \quad (2\text{-}287\text{-}11)$$

$$P(R_N \to V \,|\, R_N R_V)$$
$$= \frac{1}{Q} P(FFR \leftarrow IV) + \frac{Q-1}{Q}\left(\frac{[S_V R_N](\infty)}{Q[R_N]} P(FFR \leftarrow HV) + \frac{[R_N R_V](\infty)}{Q[R_N]} P(FFR \leftarrow IV) \right) \quad (2\text{-}287\text{-}12)$$

$$P(R_V \to NV \,|\, R_N R_V)$$
$$= \frac{1}{Q} P(IV \leftarrow FFR) + \frac{Q-1}{Q}\left(\frac{[S_N R_V](\infty)}{Q[R_V]} P(IV \leftarrow SFR) + \frac{[R_N R_V](\infty)}{Q[R_V]} P(IV \leftarrow FFR) \right) \quad (2\text{-}287\text{-}13)$$

All of the above dynamic equations can be solved numerically. Therefore, the final result is affected by a two-stage process: single-season SIR dynamics and the strategy adaptation process. We rely on an explicit scheme, and we evaluate how this specific dynamic system evolves. Therefore, we can observe the final epidemic size, vaccination coverage, and average social payoff in social equilibrium.

2.4.4 Results and discussions

2.4.4.1 The infinite and well-mixed population

Figures 2.9 and 2.10 relating to the effectiveness model and efficiency model, respectively, give the FES (left-hand panels), VC (central panels), and ASP (right-hand panels) for the various strategy-updating rules, namely IB-RA (upper panels), SB-RA (middle panels), and DC (lower panels).

The regions colored uniformly by light red (FES), dark blue (VC), and light blue (ASP) indicate a pandemic taking place, in which most individuals do not use vaccination (precisely speaking, not using either imperfect vaccination or a defense against contagion); thus, almost full-scale spread of infection occurs. Roughly speaking, these regions emerge when a smaller effectiveness (efficiency) is assumed or a larger cost is imposed. This seems quite natural because most individuals tend to shy away from vaccination if it is less reliable and/or too expensive. The border between each of these monotone regions and the remaining region implies a combination of critical effectiveness (efficiency) and critical vaccination cost to control the spread of an epidemic, bringing an obvious phase change (between pandemic phase and controlled phase). As far as the controlled phase is concerned, interestingly, lower effectiveness (efficiency) can realize higher vaccination coverage, which is also helped by the effect of lower cost. Even if a large fraction of individuals use vaccination, the epidemic cannot be eradicated because of the lower reliability of vaccination.

Comparing the three updating rules, their detailed tendencies differ although the overall tendency is the same to some extent. Comparing the effectiveness model and the efficiency model, the latter has a wider pandemic phase at first glance. This implies that a defense against contagion with a certain η is less effective at suppressing the spread of an epidemic compared to imperfect vaccination, with e being defined as having the same numerical value as η.

To validate our theoretical framework, we conducted a series of numerical simulations based on the MAS approach [7,9]. Because we assumed a well-mixed population, we assumed a perfect graph as the underlying network connecting the agents. Following previous studies, we set $\beta = 0.00088$, which was determined as the minimum transition rate β that exceeds the pre-defined [7,9] threshold final epidemic size of 0.9 without vaccination. The results are shown in Figs. 2.11–2.13 for effectiveness model, and in Figs. 2.14-2.16 for efficiency model. Generally, all six results are consistent with Fig. 2.9(1-*), (2-*), (3-*), Fig.4.10(1-*), (2-*), and (3-*), although subtle discrepancies arise from the fact that the simulation assumed a finite population size of N = 1000.

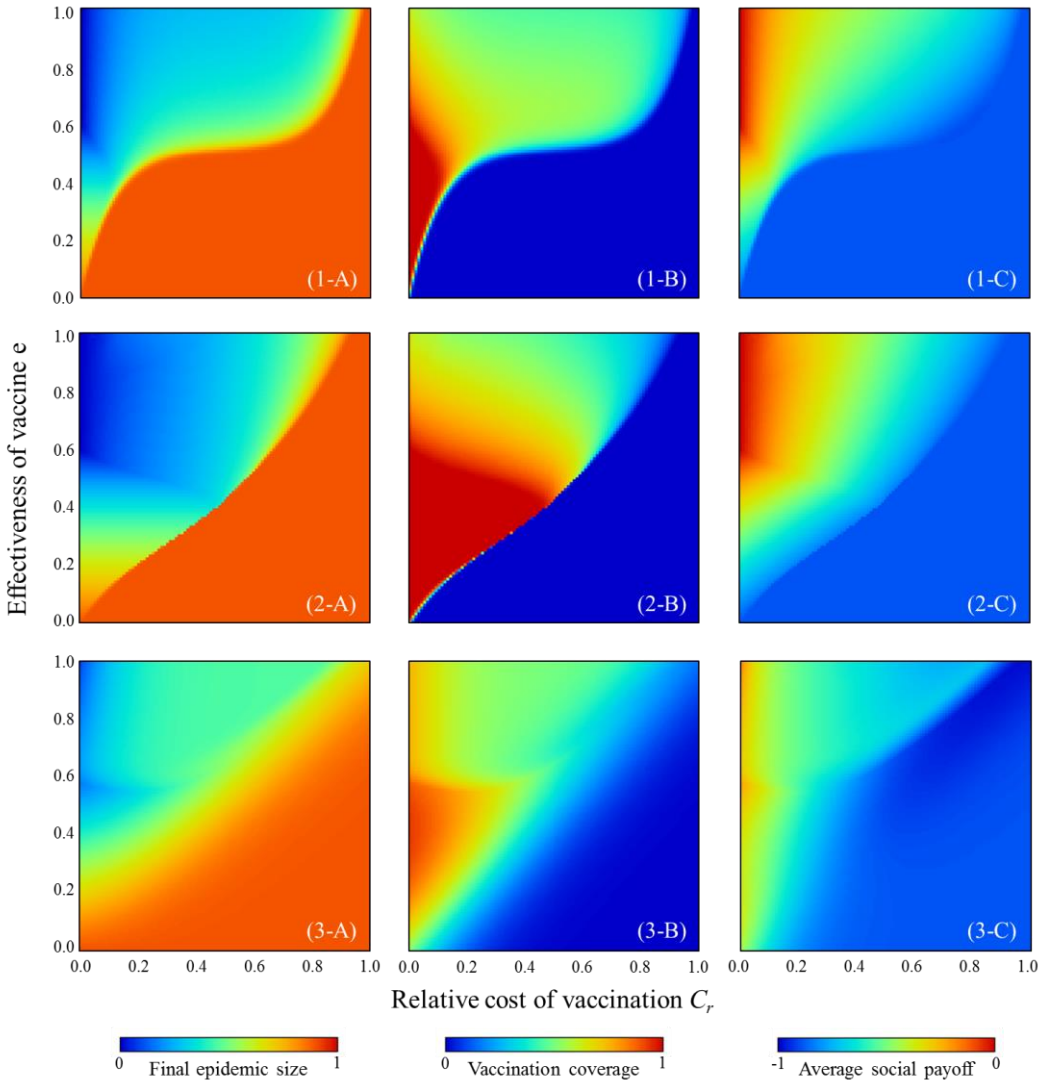

Figure 2.9. FES (left-hand panels; *-A), VC (central panels; *-B), and ASP (right-hand panels; *-C) for strategy-updating rule IB-RA (upper panels; 1-*), SB-RA (middle panels; 2-*), and DC (lower panels; 3-*). Effectiveness model is applied.

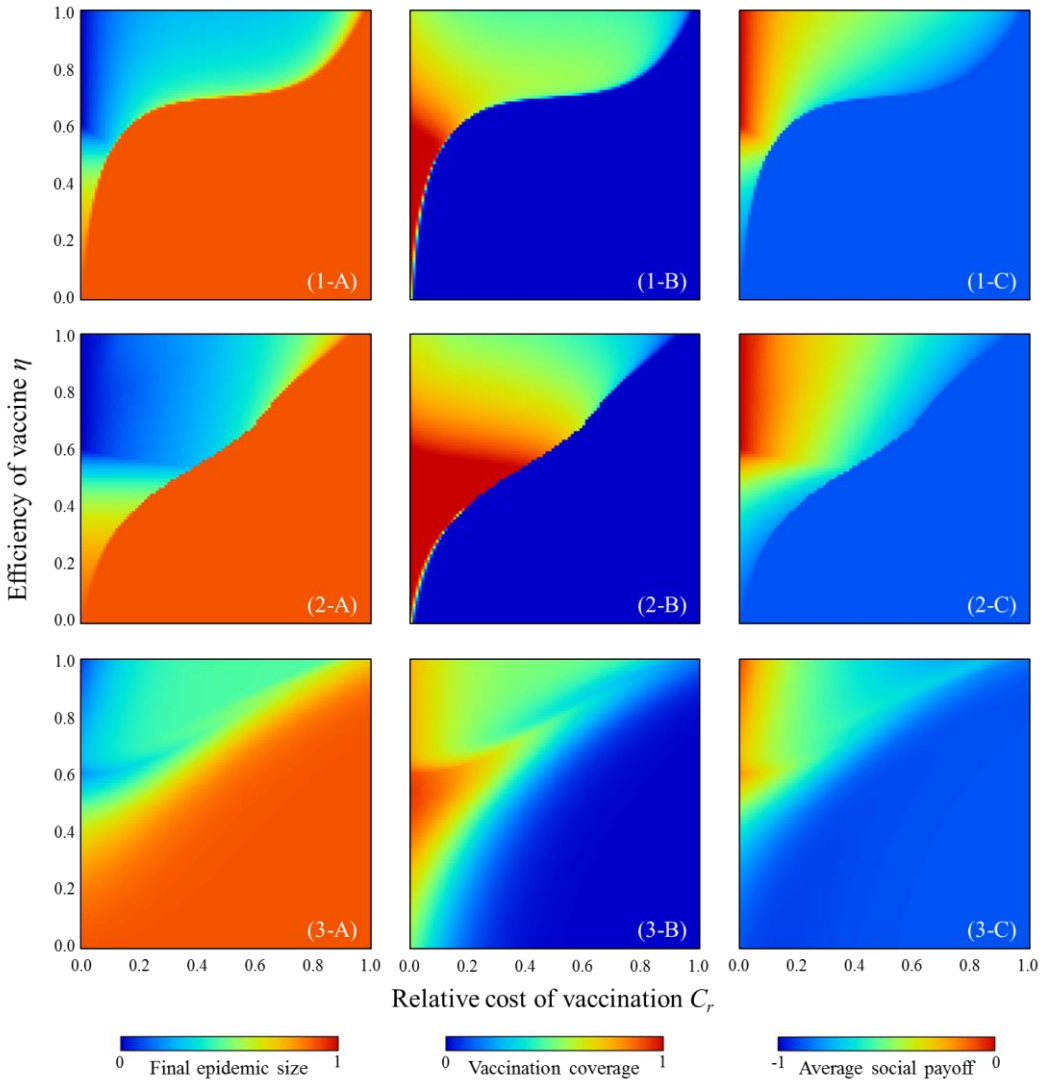

Figure 2.10. FES (left-hand panels; *-A), VC (central panels; *-B), and ASP (right-hand panels; *-C) for strategy-updating rule IB-RA (upper panels; 1-*), SB-RA (middle panels; 2-*), and DC (bottom panels; 3-*). Efficiency model is applied.

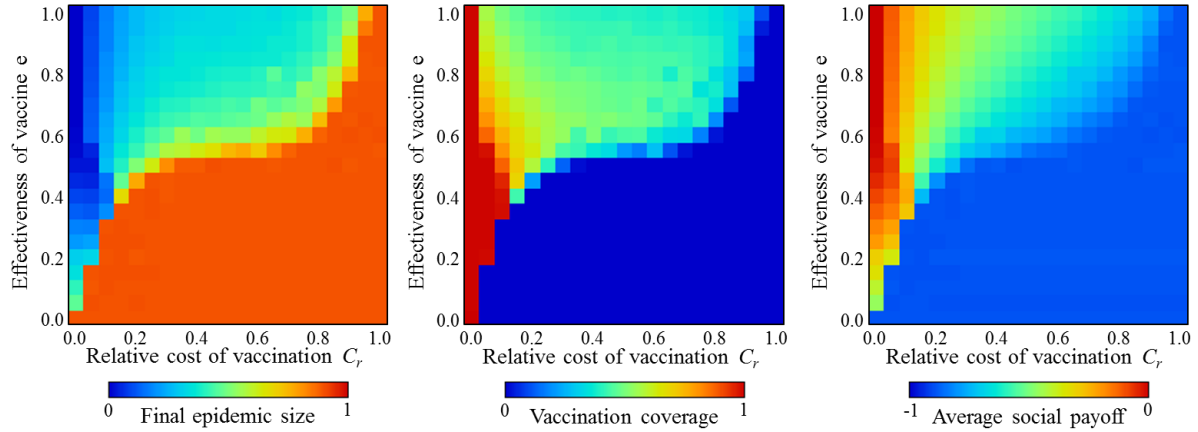

Figure 2.11. Simulation results for FES (left-hand panel), VC (central panel), and ASP (right-hand panel) assuming IB-RA when effectiveness model is applied. We assumed a perfect graph with N=1000,

β= 0.00088, and γ= 1/3.

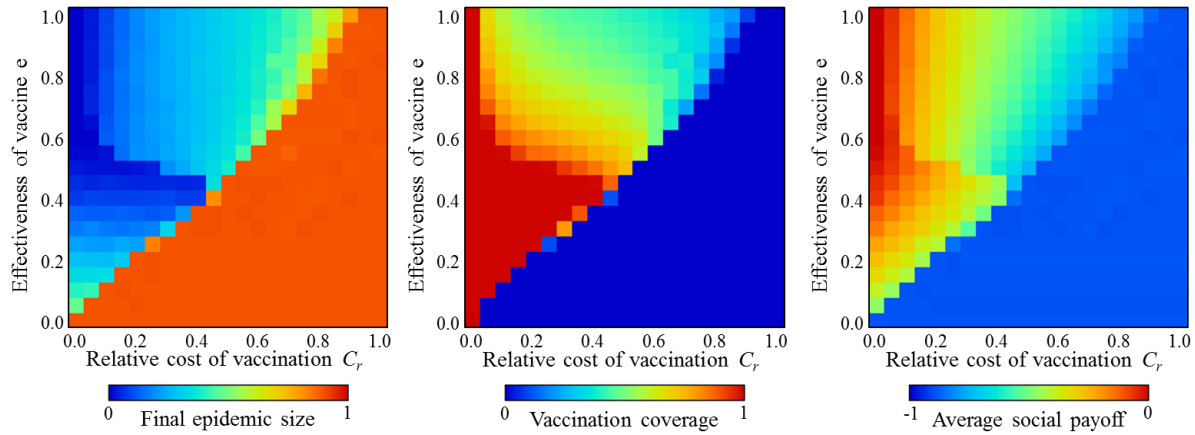

Figure 2.12. Counterpart result with Fig.4.9 (1-B), (2-B) and (3-B), assuming SB-RA. Other settings are all consistent with Fig. 2.11.

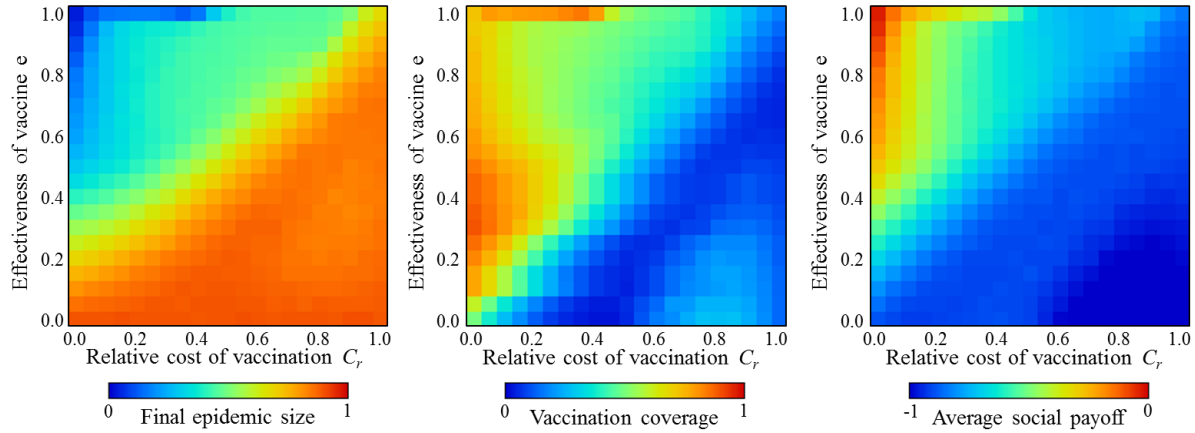

Figure 2.13. Counterpart result with Fig.4.9 (1-C), (2-C) and (3-C), assuming DC Other settings are all consistent with Fig. 2.11.

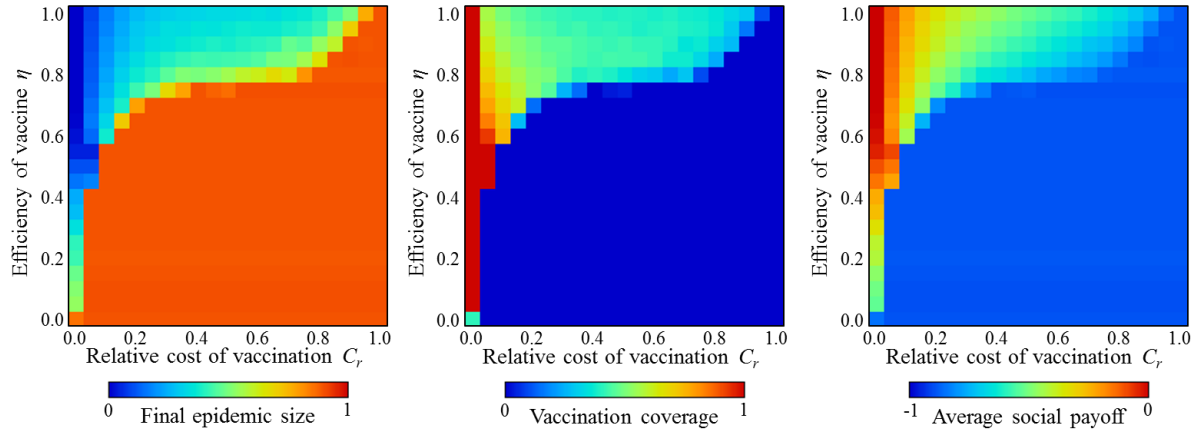

Figure 2.14. Simulation results for final epidemic size (left-hand panel), vaccination coverage (central panel), and average social payoff (right-hand panel) assuming IB-RA when efficiency model is applied. We assumed a perfect graph with N =1000, β = 0.00088, and γ = 1/3.

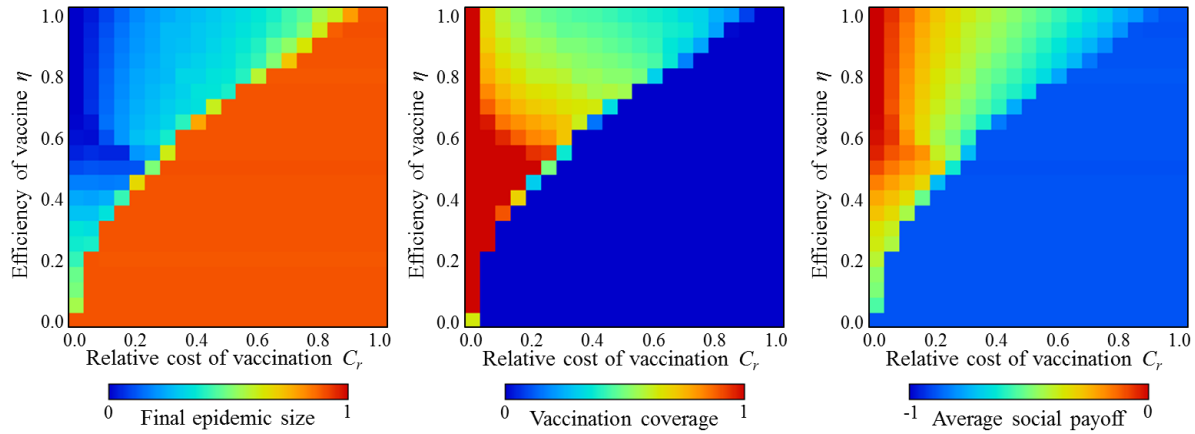

Figure 2.15. Counterpart result with Fig.5 (1-B), (2-B) and (3-B), assuming SB-RA. Other settings are all consistent with Fig. 2.14.

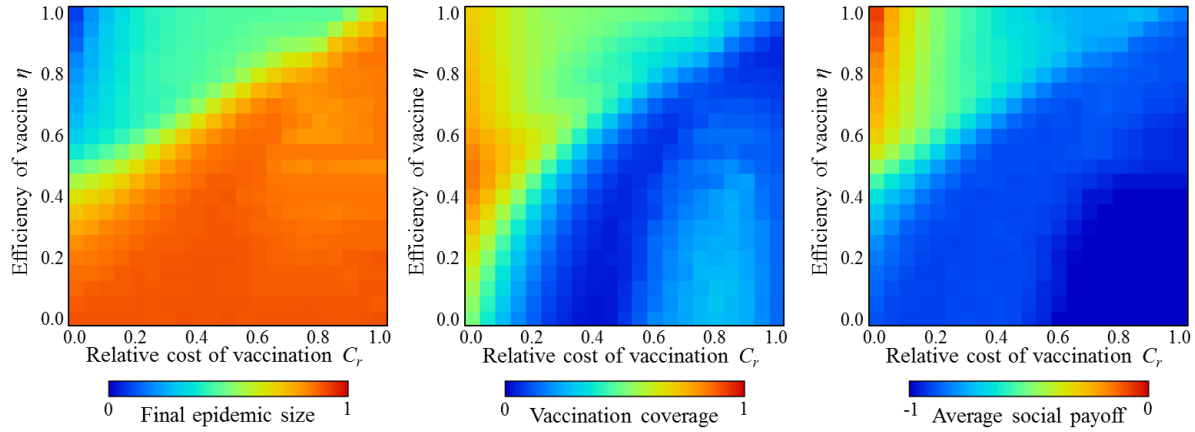

Figure 2.16. Counterpart result with Fig.5 (1-C), (2-C) and (3-C), assuming DC. Other settings are all consistent with Fig. 2.14.

2.4.4.2 Network model

Figures 2.17–2.20 show the FES (left-hand panels), VC (central panels), and ASP, respectively. In addition, they show ASP (right-hand panels) drawn on the 2D plane of either relative vaccination cost vs. effectiveness (Figs. 2.17 and 2.19) or relative vaccination cost vs. efficiency (Figs. 2.18 and 2.20) for three different degree distributions: the power law degree distribution (upper panels), Poisson's degree distribution (middle panels), and a well-mixed population (lower panels). Figures 2.17 and 2.18 show results considering IB-RA, while Figs. 2.19 and 2.20 show those considering SB-RA as the strategy-updating rule. In all figures, light red in FES, dark blue in VC, and light red in ASP indicate a pandemic taking palace, in which most individuals do not rely on vaccination (more precisely, not taking either imperfect vaccination or defense against contagion). Thus, almost full-scale spread of infection is inevitable. Roughly speaking, these regions emerge when a smaller effectiveness (or efficiency) is assumed or a larger cost is imposed. This seems quite natural because most individuals tend to avoid

committing vaccination (or defense against contagion).

The border between each of these monotone regions and the remaining area implies a critical line suggesting the combination of critical effectiveness (efficiency) and critical vaccination cost to appropriately control spreading of an epidemic, which implies a phase change between the pandemic and controlled phases. As long as the controlled phase is concerned, interestingly, a lower effectiveness (or efficiency) can realize higher vaccination coverage. Such an ironic situation can be justified by the following point. Namely, the lower reliability of the protecting measure (by either vaccination or defense against contagion) makes more individuals commit to the measure due to its uncertainty. From an opposite viewpoint, even if a large fraction of the individuals takes a measure (vaccination or defense against contagion), an epidemic cannot be eradicated because of the lower reliability of the vaccination itself.

Comparing the different network topologies, the power law distribution shows the largest, followed by Poisson's degree distribution, and the well-mixed population has the smallest VC in the region of the controlled phase. This tendency, more precisely the order of those three topologies, seems acceptable. It is because the more heterogeneous the degree distribution becomes, the more degree agents exist. Specifically, the power law distribution lets a hub agent work as a so-called super spreader. The tendency can be observed more or less in all cases regardless of the employed strategy update rule or whether the efficiency or effectiveness model is assumed, although the case presuming SB-RA with the effectiveness model (Fig. 2.19 (*-B)) seems subtle. The above-mentioned tendency concerning VC implies that the power law distribution brings less ASP than Poisson's degree distribution does, which is less than the well-mixed population shows.

To validate our theoretical result, we conducted a series of numerical simulations based on the MAS approach. To compare the power law degree distribution, we assumed a BA-SF network with an average degree $\langle k \rangle = 8$ as the underlying network connection of the agents. Following previous studies, we set $\beta = 0.19$, which was determined as the minimum transition rate β that exceeded a pre-defined threshold FES of 0.9 without vaccinated individuals. The shown result is obtained by an assemble average of 10 independent realizations starting from different initial conditions. Figures 2.21 and 2.22 show the results for the effectiveness and efficiency models, respectively. Generally, all four results are consistent with Figs. 2.17 (1-*), 2.18 (1-*), 2.19 (1-*), and 2.20 (1-*), although subtle discrepancies arise from the fact that the simulation assumed a finite population size of $N = 10000$.

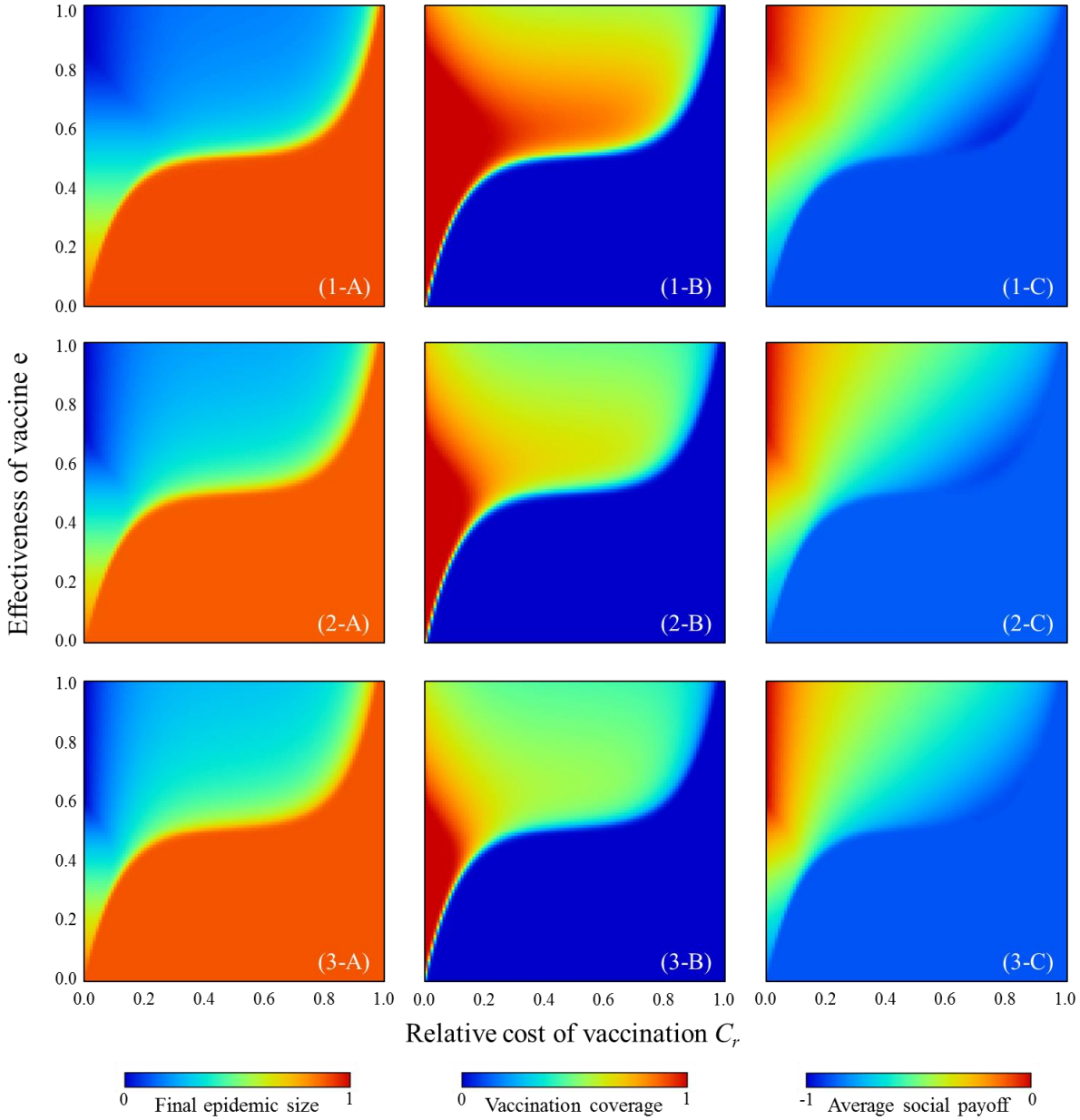

Figure 2.17. FES (left-hand panels; *-A), VC (central panels; *-B), and ASP (right-hand panels; *-C) in population structure: power law degree distribution (upper panels; 1-*), Poisson's degree distribution (middle panels; 2-*), and well-mixed population (lower panels; 3-*) [6]. Effectiveness model is applied. IB-RA is applied for strategy-updating rule.

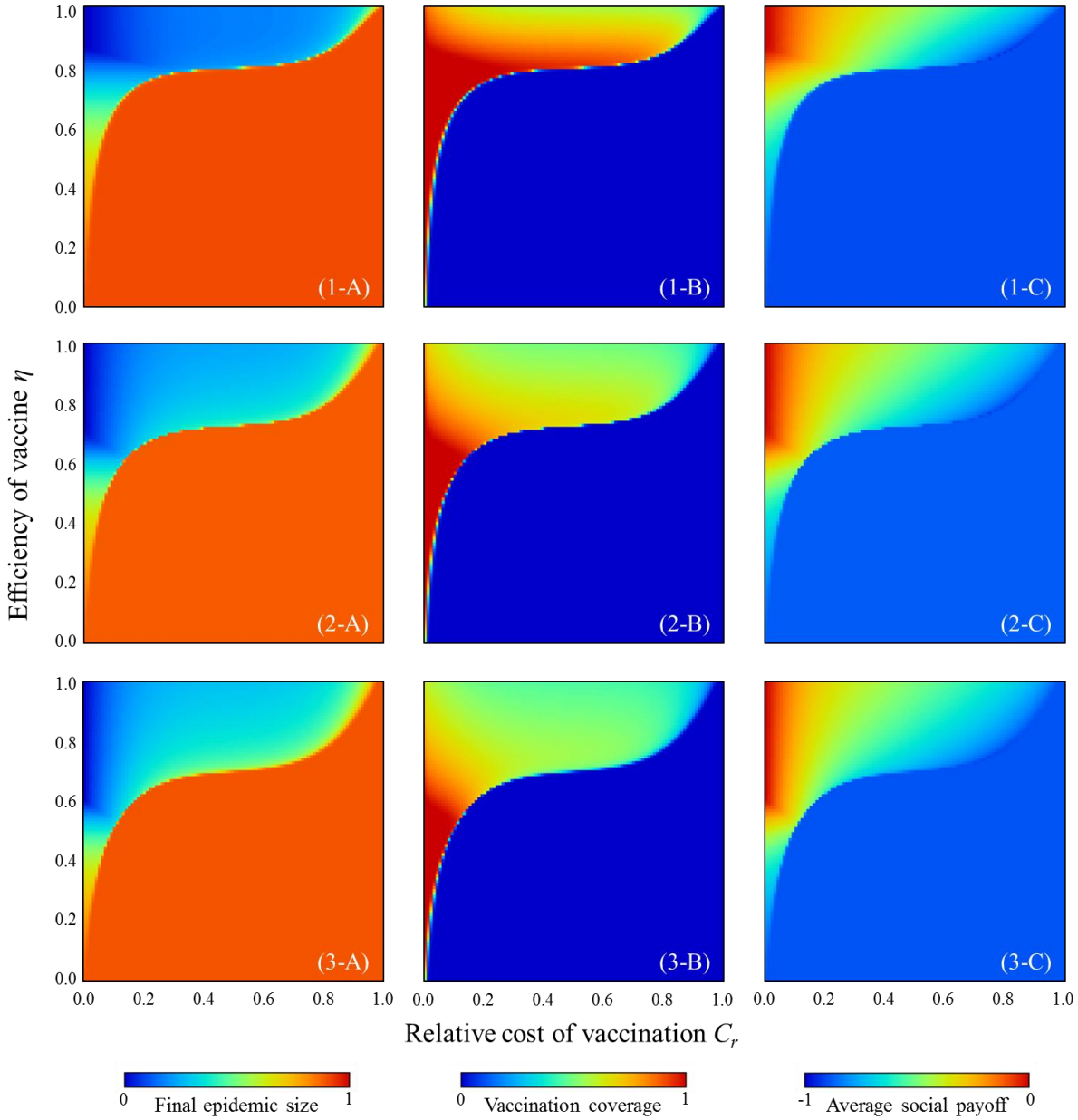

Figure 2.18. FES (left-hand panels; *-A), VC (central panels; *-B), and ASP (right-hand panels; *-C) in population structure: power law degree distribution (upper panels; 1-*), Poisson's degree distribution (middle panels; 2-*), and well-mixed population (lower panels; 3-*) [6]. Efficiency model is applied. IB-RA is applied for strategy-updating rule.

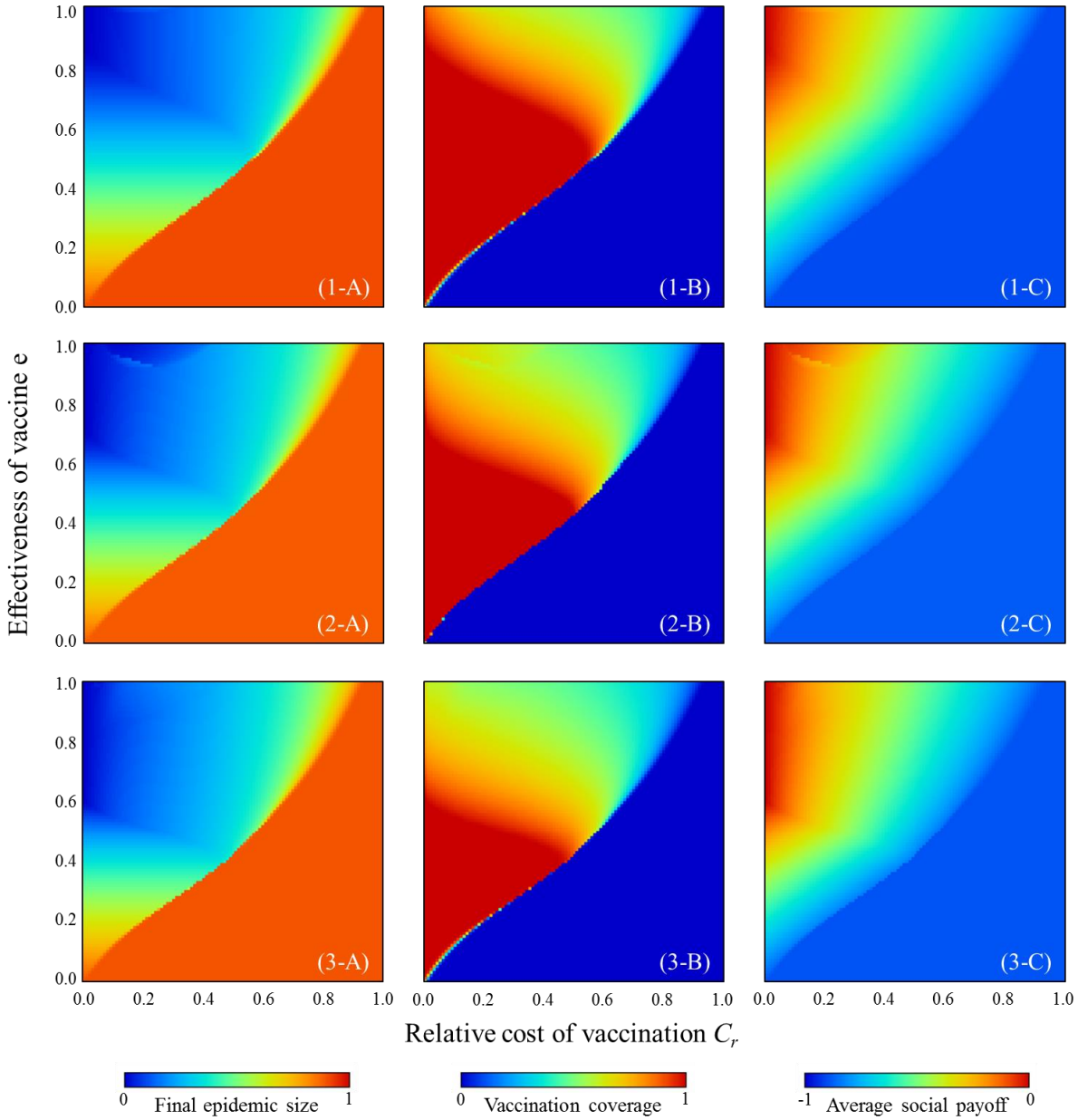

Figure 2.19. FES (left-hand panels; *-A), VC (central panels; *-B), and ASP (right-hand panels; *-C) in population structure: power law degree distribution (upper panels; 1-*), Poisson's degree distribution (middle panels; 2-*), and well-mixed population (lower panels; 3-*) [6]. Effectiveness model is applied. SB-RA is applied for strategy-updating rule.

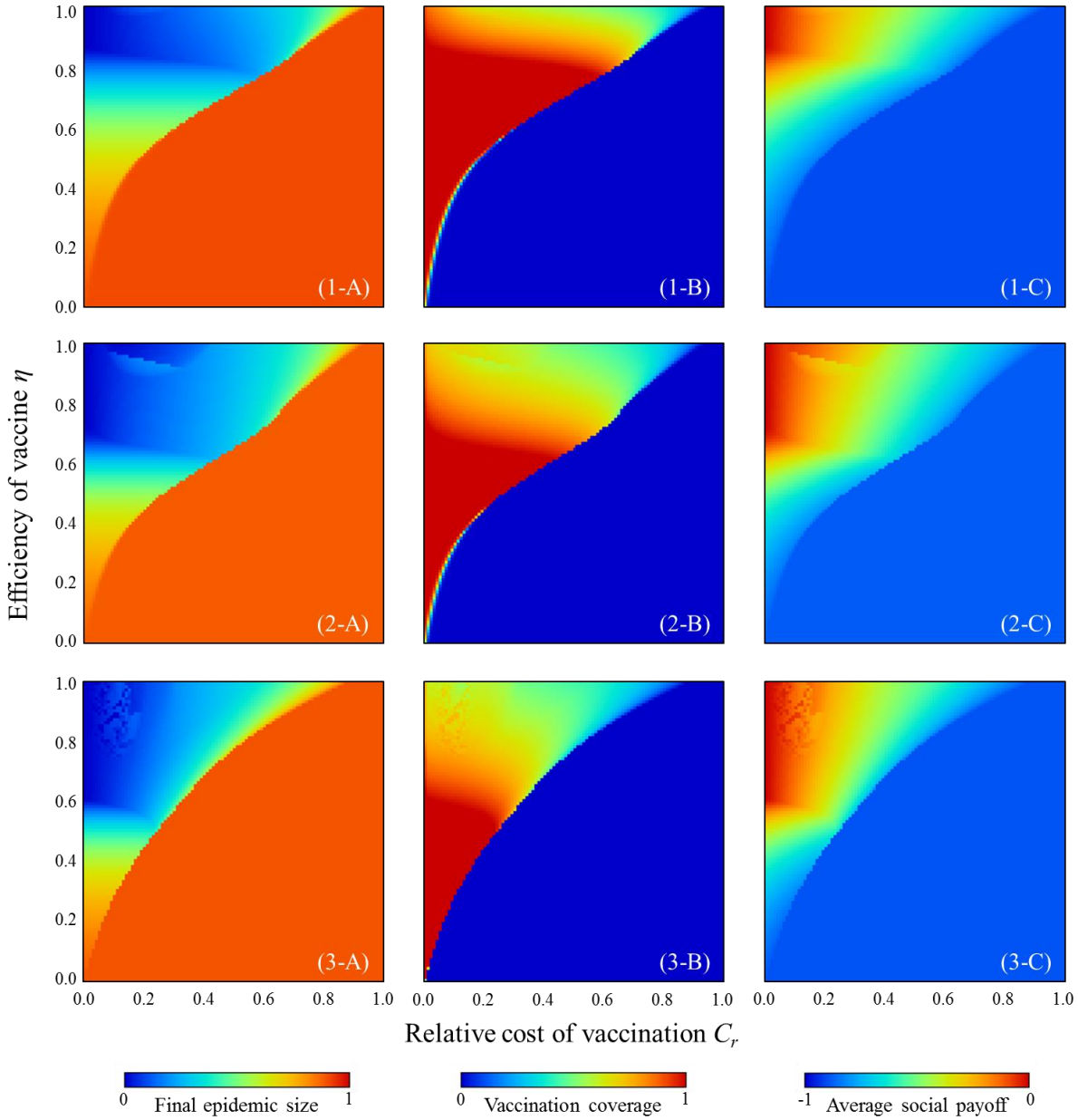

Figure 2.20. FES (left-hand panels; *-A), VC (central panels; *-B), and ASP (right-hand panels; *-C) in population structure: power law degree distribution (upper panels; 1-*), Poisson's degree distribution (middle panels; 2-*), and well-mixed population (lower panels; 3-*) [6]. Efficiency model is applied. SB-RA is applied for strategy-updating rule.

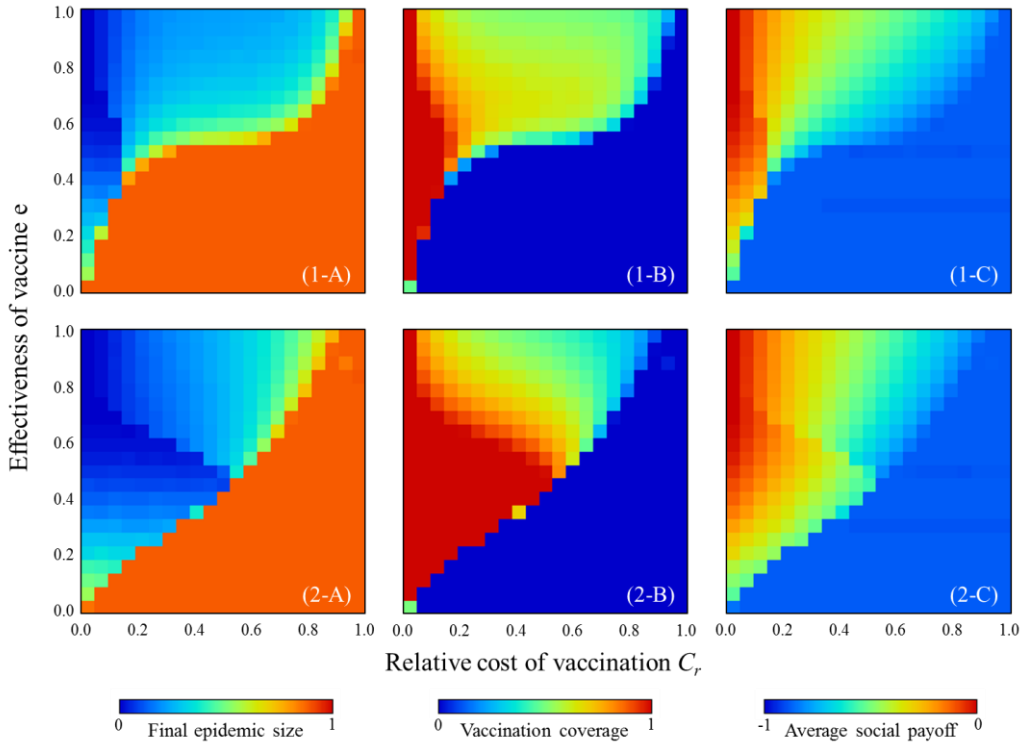

Figure 2.21. FES (left-hand panels; *-A), VC (central panels; *-B), and ASP (right-hand panels; *-C) for strategy-updating rules IB-RA (upper panels; 1-*) and SB-RA (lower panels; 2-*). Effectiveness model is applied. We assumed a BA-SF network with N = 10000, $\langle k \rangle = 8$, β= 0.19, and γ= 1/3.

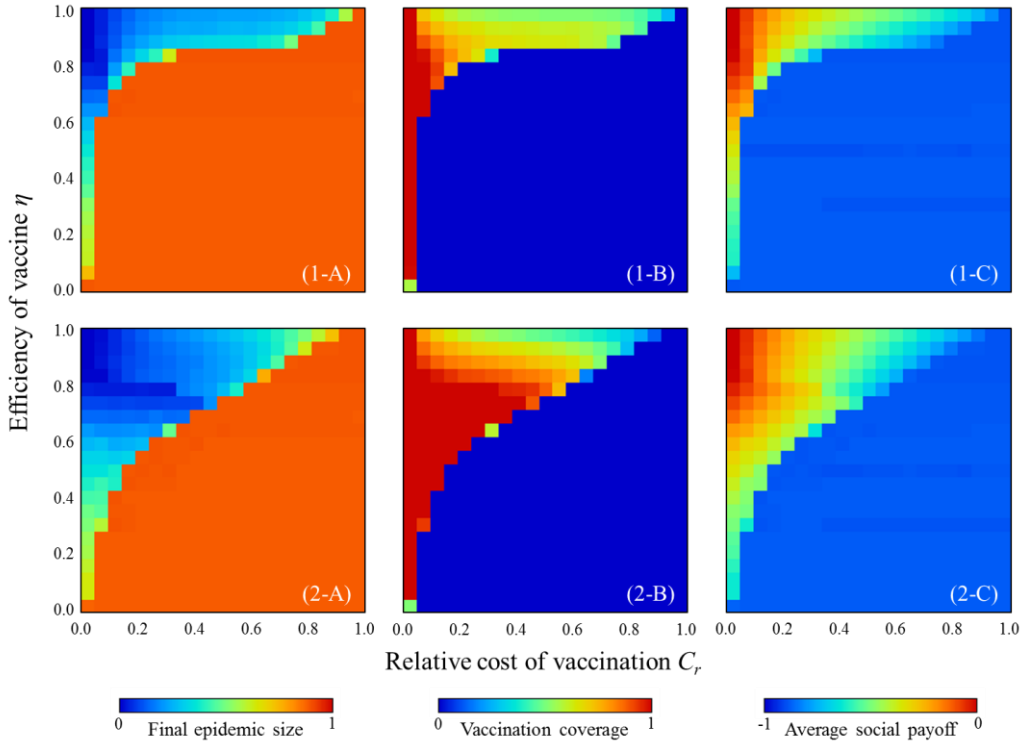

Figure 2.22. FES (left-hand panels; *-A), VC (central panels; *-B), and ASP (right-hand panels; *-C) for strategy-updating rules IB-RA (upper panels; 1-*) and SB-RA (lower panels; 2-*). Efficiency model is applied. We assumed a BA-SF network with N = 10000, $\langle k \rangle = 8$, β= 0.19, and γ= 1/3.

2.4.4.3 Pair approximation model

Figures 2.23 and 2.24 show the FES (top panels), VC (middle panels), and ASP (bottom panels) corresponding to the relative vaccination cost C_r and the effectiveness e or efficiency η, under a different number of links; degree Q. The panels on the far-right show previous results based on mean-field approximation (denoted "well mixed"). First, the present result with a lower degree shows a significantly different picture from the mean-field approximation prediction. A lower degree generally implies a robust environment for disease spreading and ironically leads to an individual shunning protective measures. In line with this justification, with an increase in degree, the present model's prediction gets close to the prediction of the mean-field approximation. A random regular graph with infinite degree is quite possible because it literally means "well mixed." Keeping this in mind, we were able to see how meaningful the present model is over conventional analytical approaches that rely on mean-field approximation.

In all figures, the red color in FES, blue color in VC, and red color in ASP indicate a pandemic state, in which most individuals rely on neither vaccination nor intermediate protective measures. Therefore, an almost full-scale spread of infection is inevitable. Generally speaking, these regions emerge when the reliability of vaccinations or intermediate protective measure is low or when the cost is high. The border between each of these monotone regions and the remaining area represents a threshold that suggests a combination of critical effectiveness (efficiency) and critical cost to appropriately control the epidemic spread. Therefore, under a voluntary vaccination policy, we can confirm how the relationship between the reliability of protective measures and the cost of protection is an important factor in controlling the damage caused by epidemic spread. Figure 2.25 shows the relationship between cost and critical effectiveness (efficiency) under which no individual takes vaccination (or intermediate protective measures). It clearly suggests that a higher cost requires a higher effectiveness (efficiency) to enable individuals to commit because individuals have no incentive to take protective measures unless there is a sufficiently high counterbalancing effect to the high cost. An observation of the differences in the degree Q shows that a lower degree requires greater effectiveness (efficiency), i.e., lower level social networks are more robust against disease spreading than those at a higher level. This ironically results in a reduced incentive for individuals to vaccinate (or take intermediate protective measures) because of the temptation to take a free ride on herd immunity.

A lower effectiveness (or efficiency) corresponds with a higher vaccination rate as long as the costs imposed are acceptable. This ironic situation can be explained as follows: when a protective measure is less reliable, it will create more uncertainty and fear, and more individuals will commit to the measure. However, even if a large proportion of individuals take protective measures, the epidemic cannot be eradicated if the vaccination is unreliable.

A comparison of the effectiveness and efficiency models in Figures 2.23 and 2.24 show that the latter has a wider pandemic phase at first glance. This implies that intermediate protective measures

with certain η are less effective for suppressing an epidemic than imperfect vaccination, and this finding is consistent with our previous results based on mean-field approximation.

Figure 2.26 shows the isograms of the relative vaccination cost C_r drawn on a 2D plane of VC and effectiveness (efficiency). The gray arrows indicate the direction of the rising slope of C_r, thus indicating that VC (the rate of intermediate protective measures) decreases with increasing effectiveness (efficiency) when the costs are kept the same. This finding confirms what we have discussed above and is consistent with the reports by Chen *et al*. [13] and Wu *et al*. [18].

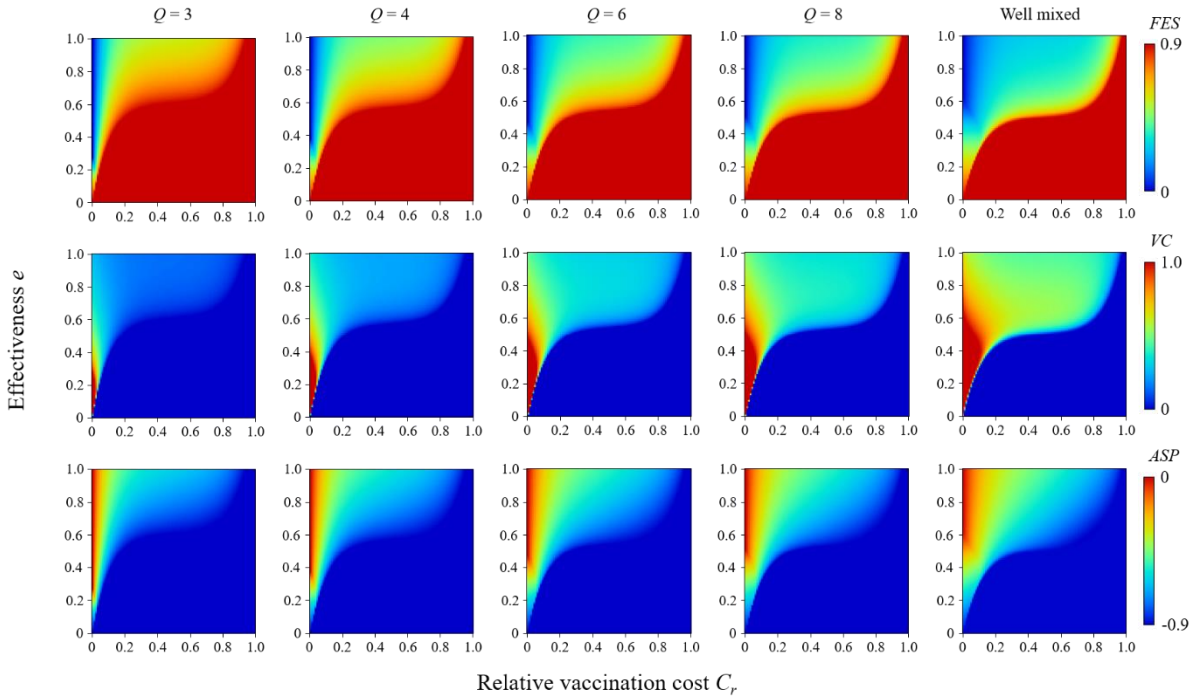

Figure 2.23. FES (upper panels), VC (middle panels), and ASP (right-hand panels) for different numbers of degrees Q. The effectiveness model is applied.

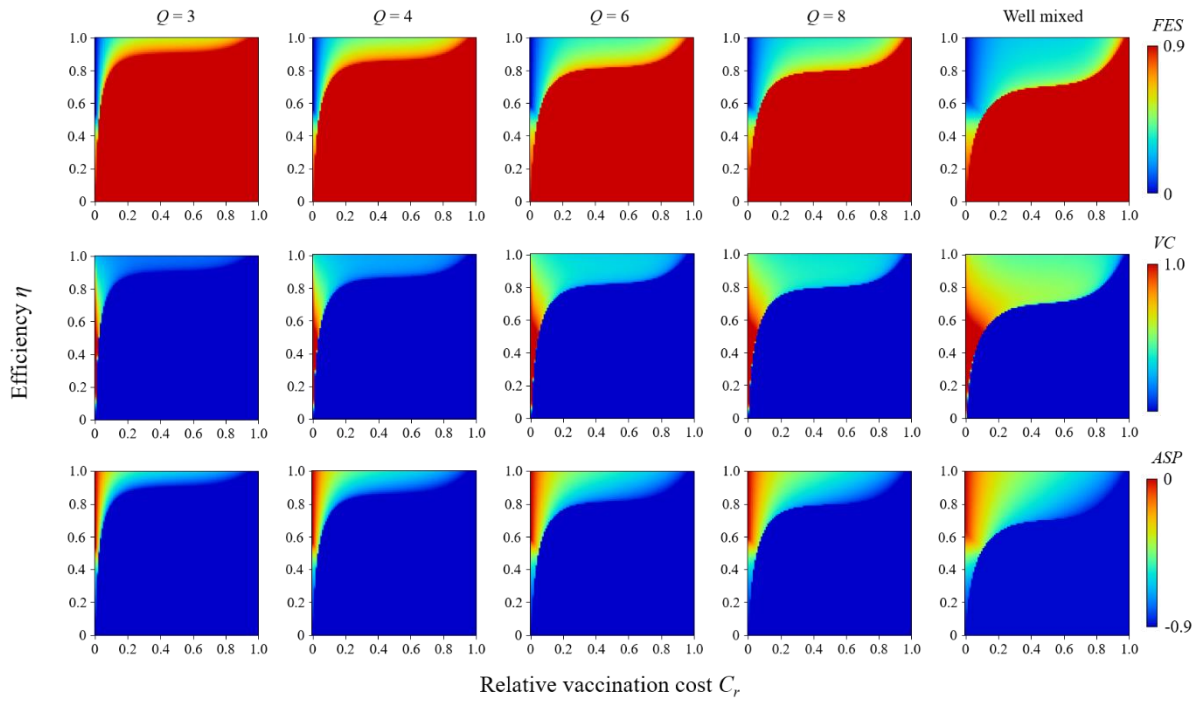

Figure 2.24. FES (upper panels), VC (middle panels), and ASP (right-hand panels) for different numbers of degrees Q. The efficiency model is applied.

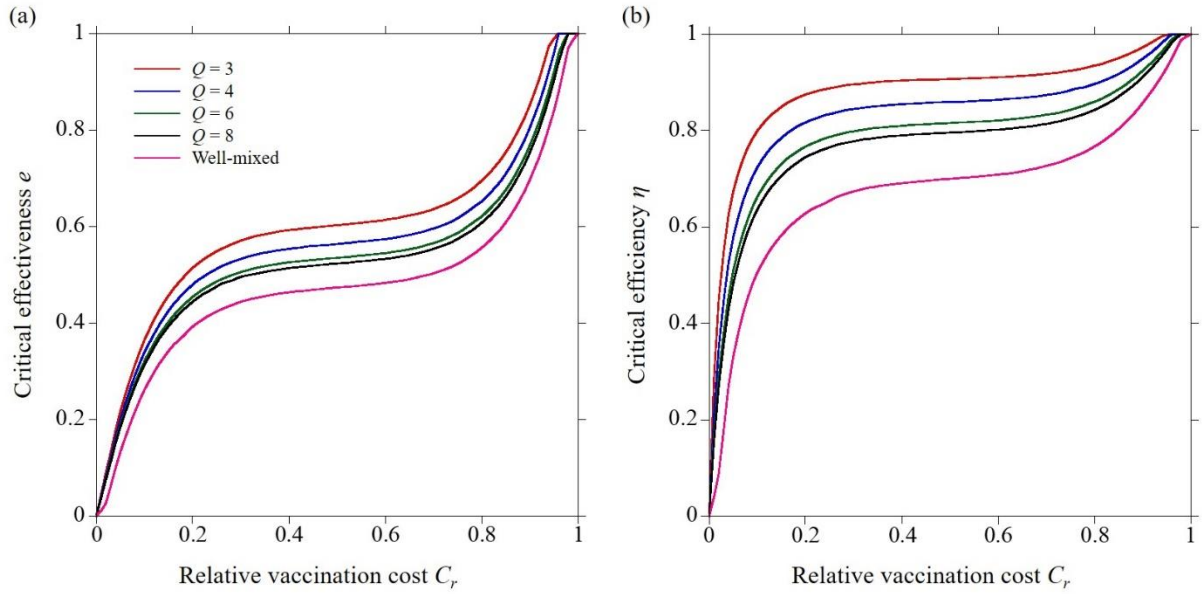

Figure 2.25. Critical effectiveness (a) and critical efficiency (b) vs. relative vaccination cost C_r under different numbers of degrees Q.

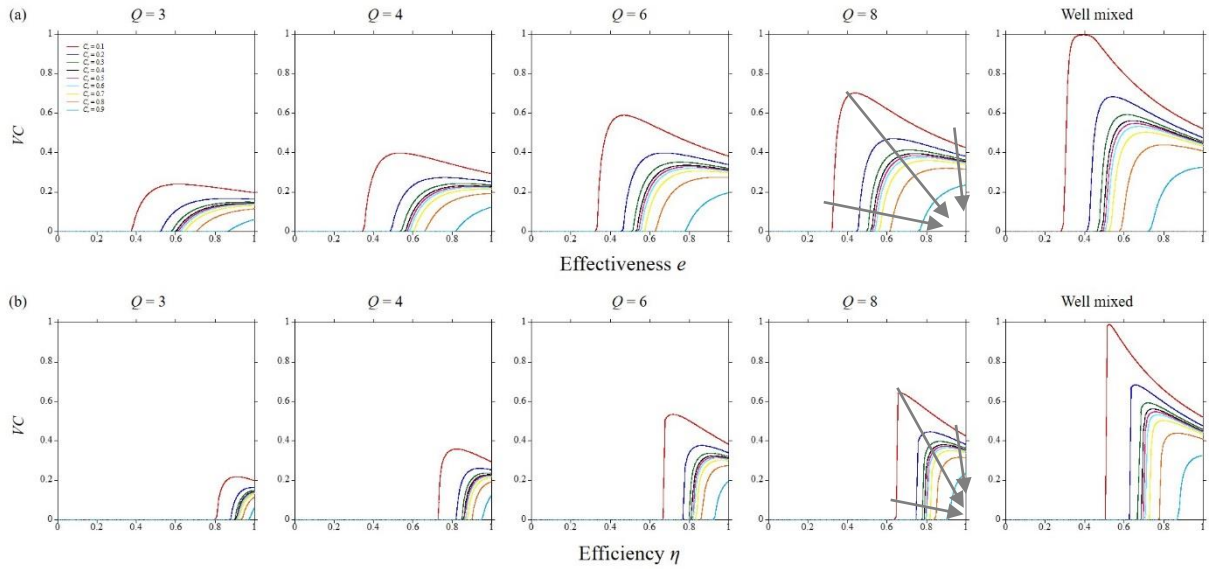

Figure 2.26. Isogram of relative vaccination cost C_r drawn on a 2D plane of VC vs. effectiveness (a) or efficiency (b). The gray arrows indicate the direction of the slope.

To validate the theoretical results, a series of numerical simulations based on the MAS approach was performed. Following the procedure in previous studies [7,9], we set β as the point at which FES exceeds the predefined threshold (i.e., 0.9) without any vaccinated individuals. The results shown below were obtained by a collective average of 100 independent realizations starting from various initial conditions. Figures 2.27 and 2.28 show the results for the effectiveness and efficiency models, respectively. Generally, all results are consistent with Figures 2.23 and 2.24, although there are subtle discrepancies arising from the fact that the above simulation assumed a finite population size of $N = 10^4$.

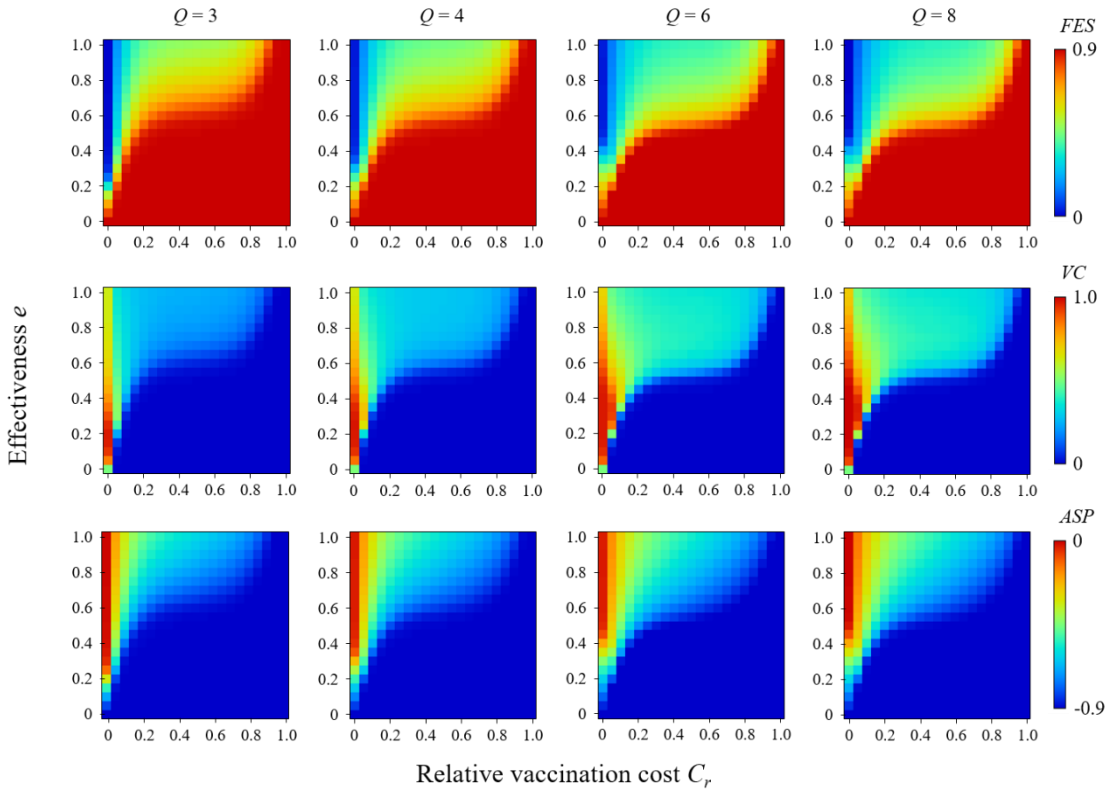

Figure 2.27. FES (upper panels), VC (middle panels), and ASP (right-hand panels) for different numbers of degrees Q. The efficiency model is applied.

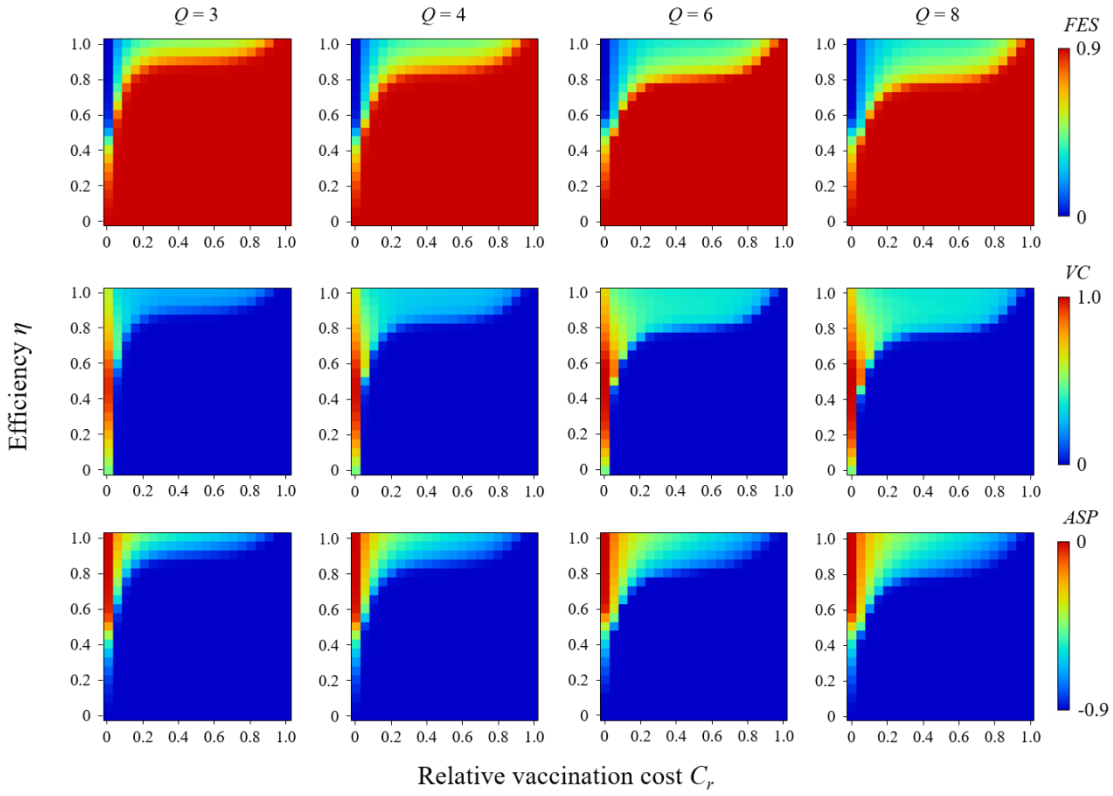

Figure 2.28. FES (upper panels), VC (middle panels), and ASP (right-hand panels) for different numbers of degrees Q. The efficiency model is applied.

To characterize the effect of infection rates on vaccination behavior, FES and VC were shown as a function of the inverse of the effective recovery rate $1/r$ and the protection quality: (a) effectiveness e and (b) efficiency η in Figure 2.29. We fixed the relative vaccination cost $C_r = 0.1$. Looking at the effect of the degree of Q on vaccination behavior, individuals do not vaccinate until the relative recovery rate r is less than the critical relative recovery rate r_c, as expressed in Eq. (2-48), because the epidemic does not spread. Furthermore, VC increases with an increase in Q, both in terms of effectiveness and efficiency. This implies that a high number of degrees promote not only the epidemic spread but also the (cooperative) vaccination behavior. The critical value of effectiveness, below which no individual will be vaccinated, does not show sensitivity to the relative cost, which is expressed as $e = 0.35$ in this case. On the other hand, the critical value of efficiency, below which no individual will be vaccinated, increases monotonically with an increase in the relative recovery rate. This result is consistent with results by Cardillo *et al*. [12].

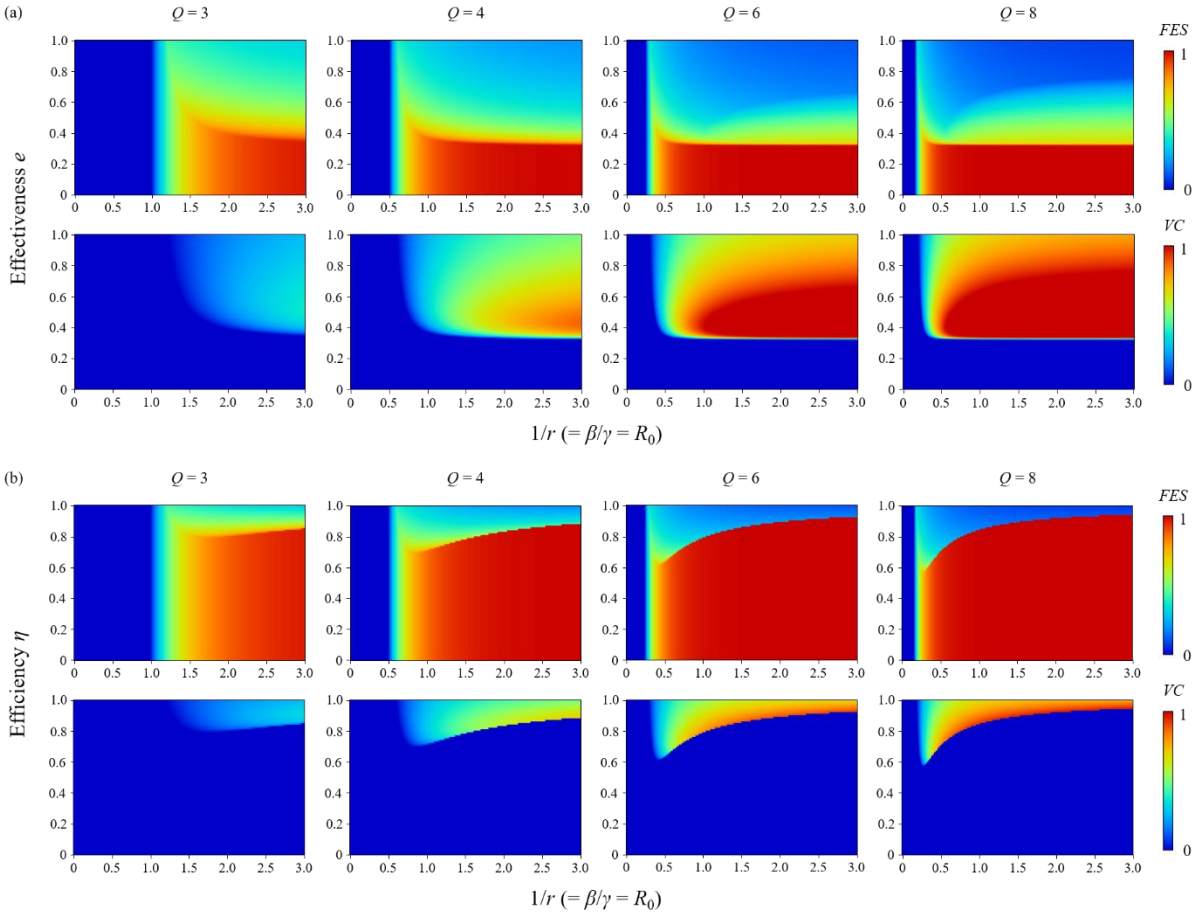

Figure 2.29. FES and VC as a function of the inverse of the relative recovery rate $1/r$ and the protection quality: (a) effectiveness e and (b) efficiency η for regular random networks with different numbers of degrees Q. We assumed $C_r = 0.1$.

In general, most of theoretical vaccination game model using mean-field approximation ignored the local correlations between vaccinators and nonvaccinators and assumed a homogeneous distribution

of vaccinator and nonvaccinator. On the other hand, pair approximation can capture the evolution of heterogeneous distribution of vaccinator and nonvaccinatior caused from strategy adaptation. In the model formulation, we introduced new parameter; α, meaning disassortativity at the beginning of every season, that can be time-evolved according to Eqs. (2-284) and (2-286) when we digress from the mean-filed approximation abovementioned. Let us name this setting 'heterogeneous' case. Contrariwise, when we follow to the conventional idea; taking mean-field approximation, α is always frozen at $\alpha = x(1-x)$, which is called 'homogeneous' case. As shown in Figure 2.30, when heterogeneous setting was imposed, vaccination coverage is relatively high and final epidemic size is relatively low compared to the homogeneous one ($\alpha = x(1-x)$). Regardless of C_r, we confirmed that α is always lower than that the homogeneous case; $x(1-x)$, because of the existence of the cluster of vaccinators and nonvacciantors. The existence of nonvaccinators cluster with high frequency pushes up the risk of disease spreading shared amid nonvaccinators, which makes defectors commit vaccination. This subsequently enables less final epidemic size when the heterogeneous case is presumed.

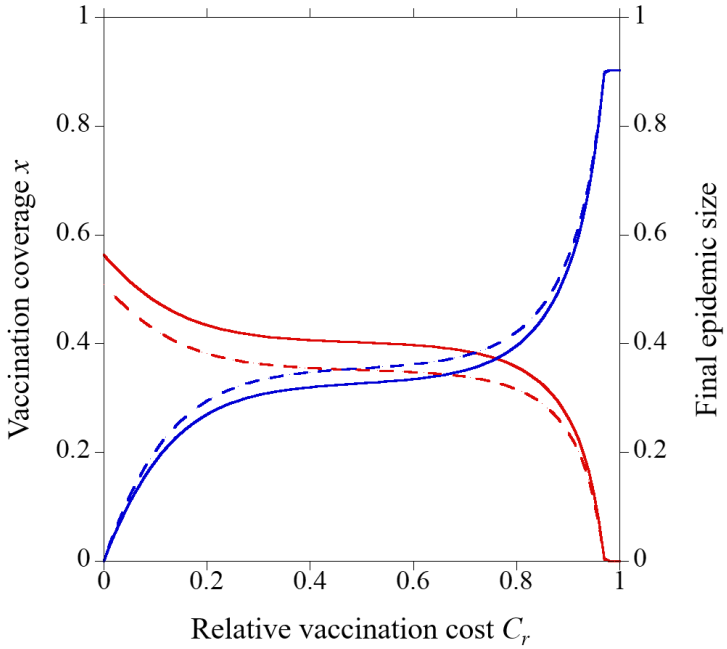

Figure 2-30. Differences of vaccination coverage and final epidemic size caused from whether to assume homogeneous or evolutionary heterogeneous distribution of vaccinator and nonvacciantior. Red lines present vaccination coverage and blue lines present final epidemic size. In the solid lines, we assumed the evolutionary heterogeneous distribution and the parameter α varied every strategy adaptation. On the other hand, in dash line, we assumed the homogeneous distribution ($\alpha = x(1-x)$). We assumed perfect vaccination.

2.5 Conclusions

In this chapter, we presented three theoretical framework of the vaccination game that considers imperfect vaccination and intermediate protective measures corresponding to (i) an infinite and well-mixed population using mean field approximation, (ii) Complex networks using mean field approximation with different degree distributions (Poisson's degree distribution and power law distribution), and (iii) Regular random graph using pair approximation. For expressing the stochastic effect of imperfect vaccination and intermediate protective measure on epidemic dynamics, we developed two scenarios: effectiveness model and efficiency model. The exact mathematical formulas for both dynamic processes, namely, epidemic spreading and strategy updating, are explicitly discussed. When solving the ODEs for three epidemic models, the critical vaccination coverage and the final fractions for each individual were derived. We validated our frameworks by comparing its predictions with simulation results. As long as the same coefficient values, namely effectiveness and efficiency, are assumed, an intermediate protective measure is marginally inferior to an imperfect vaccination

In terms of possible applications from our contribution of the study, we would like to mention two points as below. First, our framework relying on mathematical approach may call other extended models; for example, where we can consider not only either committing vaccination or intermediate protective measure to control a disease spreading but also both vaccination and intermediate protective measure being applied at the same time. As the second, with respect to the standpoint of meaning implications to a real world, our model, which is able to deal with the framework of 'vaccination game' with consideration of vaccination effectiveness or efficiency as well as the underlying topology effect resulting from degree distribution, can be easily extended to a more practical situation, struck many people; public-health officials as well as medical doctors, as interesting, where a subsidy for helping vaccination to certain individuals (senior people or poor people, for example) can be quantitatively discussed. Those may be our future works.

References

1. Reluga TC, Bauch CT, Galvani AP. 2006. Evolving public perceptions and stability in vaccine uptake. Mathematical biosciences, 204(2), 185-198.
2. Mbah MLN, Liu J, Bauch CT, Tekel YI, Medlock J, Meyers LA, Galvani AP. 2012. The impact of imitation on vaccination behavior in social contact networks. PLoS computational biology, 8(4).
3. Tanimoto J. 2015. Fundamentals of evolutionary game theory and its applications. Springer Japan.
4. Tanimoto J. 2019. Evolutionary Games With Sociophysics. Tokyo: Springer.
5. Kermack WO, McKendrick AG. 1927. A contribution to the mathematical theory of epidemics. Proceedings of the royal society of london. Series A, Containing papers of a mathematical and physical character, 115(772), 700-721.
6. Bauch CT, Galvani AP, Earn DJD. 2003. Group interest versus self-interest in smallpox vaccination policy. Proceedings of the National Academy of Sciences of the United States of America 100,

10564.
7. Fu F, Rosenbloom DI, Wang L, Nowak MA. 2011. Imitation dynamics of vaccination behavior on social networks. Proceedings of the Royal Society B 278, 42.
8. Liu XT, Wu ZX, Zhang L. 2012. Impact of committed individuals on vaccination behavior. Physical Review E, 86(5), 051132.
9. Fukuda E, Kokubo S, Tanimoto J, Wang Z, Hagishima A, Ikegaya N. 2014. Risk assessment for infectious disease and its impact on voluntary vaccination behaviour in social networks. Chaos, Solitons & Fractals, 68, 1-9.
10. Fukuda E, Tanimoto J, Akimoto M. 2015. Influence of breaking the symmetry between disease transmission and information propagation networks on stepwise decisions concerning vaccination. Chaos, Solitons & Fractals, 80, 47-55.
11. Fukuda E, Tanimoto J. 2016. Effects of stubborn decision-makers on vaccination and disease propagation in social networks. International Journal of Automation and Logistics, 2, 78-92.
12. Iwamura Y, Tanimoto J. 2018. Realistic decision-making processes in a vaccination game. Physica A: Statistical Mechanics and its Applications, 494 (15), 236-241.
13. Cardillo A, Reyes-Suárez C, Naranjo F, Gómez-Gardeñes J. 2013. Evolutionary vaccination dilemma in complex networks. Physical Review E, 88(3), 032803
14. Erdős P, Rényi A. 1960. On the evolution of random graphs. Publ. Math. Inst. Hung. Acad. Sci, 5(1), 17-60.
15. Barabási AL, Albert R. 1999. Emergence of scaling in random networks. science, 286(5439), 509-512.
16. Iwamura Y, Tanimoto J, Fukuda E. 2016. Effect of intermediate defense measures in voluntary vaccination games. Journal of Statistical Mechanics: Theory and Experiment, 2016(9), 093501.
17. Ida Y, Tanimoto J. 2018. Effect of noise-perturbing intermediate defense measures in voluntary vaccination games. Chaos, Solitons & Fractals, 106, 337-341.
18. Wu B, Fu F, Wang L. 2011. Imperfect vaccine aggravates the long-standing dilemma of voluntary vaccination. PloS one, 6(6), e20577.
19. Chen X, Fu F. 2019. Imperfect vaccine and hysteresis. Proceedings of the Royal Society, B 286(1894), 20182406.
20. Alam M, Tanaka M, Tanimoto J. 2019. A game theoretic approach to discuss the positive secondary effect of vaccination scheme in an infinite and well-mixed population. Chaos, Solitons & Fractals, 125, 201-213.
21. Alam M, Kuga K, Tanimoto J. 2019. Three-strategy and four-strategy model of vaccination game introducing an intermediate protecting measure. Applied Mathematics and Computation, 346, 408-422.
22. Kabir KA, Tanimoto J. 2019. Analysis of epidemic outbreaks in two-layer networks with different

structures for information spreading and disease diffusion. Communications in Nonlinear Science and Numerical Simulation, 72, 565-574.

23. Kabir KA, Tanimoto J. 2019. Evolutionary vaccination game approach in metapopulation migration model with information spreading on different graphs. Chaos, Solitons & Fractals, 120, 41-55.
24. Kabir KA, Tanimoto J. 2019. Vaccination strategies in a two-layer SIR/V–UA epidemic model with costly information and buzz effect. Communications in Nonlinear Science and Numerical Simulation, 76, 92-108.
25. Kabir KA, Tanimoto J. 2019. Modelling and analysing the coexistence of dual dilemmas in the proactive vaccination game and retroactive treatment game in epidemic viral dynamics. Proceedings of the Royal Society A, 475(2232), 20190484.
26. Kabir KA, Jusup M, Tanimoto J. 2019. Behavioral incentives in a vaccination-dilemma setting with optional treatment. Physical Review E, 100(6), 062402.
27. Kabir KA, Kuga K, Tanimoto J. 2019. Effect of information spreading to suppress the disease contagion on the epidemic vaccination game. Chaos, Solitons & Fractals, 119, 180-187.
28. Kabir KA, Kuga K, Tanimoto J. 2020. The impact of information spreading on epidemic vaccination game dynamics in a heterogeneous complex network-A theoretical approach. Chaos, Solitons & Fractals, 132, 109548.
29. Kabir KA, Tanimoto J. 2019. Dynamical behaviors for vaccination can suppress infectious disease–A game theoretical approach. Chaos, Solitons & Fractals, 123, 229-239.
30. Kabir KA, Tanimoto J. 2019. Evolutionary vaccination game approach in metapopulation migration model with information spreading on different graphs. Chaos, Solitons & Fractals, 120, 41-55.
31. Moreno Y, Pastor-Satorras R, Vespignani A. 2002. Epidemic outbreaks in complex heterogeneous networks. *The European Physical Journal B-Condensed Matter and Complex Systems*, *26*(4), 521-529.
32. Keeling MJ. 1999. The effects of local spatial structure on epidemiological invasions. Proceedings of the Royal Society of London B: Biological Sciences, 266(1421), 859-867.
33. Pastor-Satorras R, Rubi M, Diaz-Guilera A. 2003. *Statistical mechanics of complex networks* (Vol. 625). Springer Science & Business Media.
34. Albert R, Barabási AL. 2002. Statistical mechanics of complex networks. *Reviews of modern physics*, *74*(1), 47.
35. Tomé T, De Oliveira MJ. 2011. Susceptible-infected-recovered and susceptible-exposed-infected models. Journal of Physics A: Mathematical and Theoretical, 44(9), 095005.

[Previously published documents related to this chapter]

1. Kuga K, Tanimoto J. 2018. Which is more effective for suppressing an infectious disease: imperfect vaccination or defense against contagion?. Journal of Statistical Mechanics: Theory and Experiment, 2018(2), 023407.

2. Kuga K, Tanimoto J. 2018. Impact of imperfect vaccination and defense against contagion on vaccination behavior in complex networks. Journal of Statistical Mechanics: Theory and Experiment, 2018(11), 113402.

Chapter 3: A comprehensive study of vaccination-subsidizing policies with multi-agent simulations and mean-field modeling

3.1 Introduction and literature review

Attempts to resolve or relax the vaccination dilemma have often assumed the availability of subsidies from central and/or municipal governments. In Japan, in fact, people over certain age and other critical groups are subsidized to vaccinate against seasonal influenza. Such subsidies have, in turn, widened the Japanese government's budget deficit due to the increasing costs of medical care for a rapidly aging population. However, if a subsidy is implemented in a way that secures herd immunity, then the burden imposed by the infectious disease may drastically reduce or disappear altogether, thus fully justifying a vaccination-subsidizing policy. It is for this reason that examining various vaccination subsidies represents an important research subject.

Gavious and Yamin [1] firstly examined vaccination-subsidizing policies. Based on a macro model with SIR dynamics included, which was validated on a dataset of field observations, these authors insist that a sufficiently large subsidy is needed to contain prolonged epidemics. Interestingly, subsidizing young and middle-aged population is favored over subsidizing the elderly.

A comprehensive study by Zhang et al. [2] compared two policies: (i) distributing free-tickets as long as the budget allows (hereafter, called the free-ticket policy) and (ii) distributing a discount coupon to all individuals (originally referred to as the partial-offset policy, but hereafter simply the discount policy). The total social cost was defined as a sum of infection-related costs and vaccination-related costs paid individually, meaning that the subsidy was externalized as a ‘gift of nature’. A couple of follow-up studies [3, 4] additionally examined the performance of the free-ticket policy against the discount policy in various situations, as well as the performance of random subsidies against targeted ones. Further studies explored the viability of mutual support between neighbors instead of a central government [5], the effects of renewed infections by replacing an SIR model with an SIRS model [6], and the benefits of a free-ticket subsidy to hub agents in scale-free networks [7].

It is plausible that a vaccinator who is given a free-ticket may motivate neighboring agents to vaccinate voluntarily. This is somewhat analogous to the role of ‘stubborn vaccinators’ [8] or ‘zealot cooperators’ in spatial 2-strategy, 2-player (i.e., 2×2) games [9]. One important difference, however, is that a stubborn vaccinator's spatial location is determined by agent mobility, whereas a free-ticket can be administered where needed the most by the policy maker.

In view of the described background, we set out to quantitatively answer whether a subsidized vaccination policy can really reduce the total social cost. Unlike the gift-of-nature approaches, we

include all relevant costs: vaccination-related, infection-related, as well as the tax burden to implement the subsidy. We also make a step further to examine which policy is the most suitable (free tickets vs. discount coupons).

3.2 Vaccination game model

The underlying vaccination game model used throughout this study closely resembles the original by Fu *et al*. [10] (but see also [11,12]). To this underlying model, we attached several plausible vaccination policies and examined their performance in terms of disease prevention and the total social cost.

3.2.1. Basic assumptions

We considered a population of size N in which each individual is placed in a social network and decides whether to get vaccinated or not. We assumed that a seasonal infectious disease, e.g., influenza, spreads through such a population. The protective efficacy of the vaccine persists for less than a year because of waning antibodies and year-to-year changes in the circulating virus strain. Accordingly, under a voluntary vaccination program, individuals must make their mind regarding vaccination every year. Our model captured this dynamics in two stages: an epidemic season and a vaccination campaign. These two stages comprise one model period. The model runs until reaching a social equilibrium in which we observed the following performance measures: vaccination coverage (VC; the fraction of vaccinators in the population), the final epidemic size (FES; the fraction recovered individuals), and the total social payoff (TSP; formally defined in Section 3.2.3).

The epidemic season. At the beginning of this stage, I_0 randomly selected susceptible individuals are identified as the initial infection carriers. Subsequently, the epidemic spreads according to SIR/V dynamics, which considers each individual's one-way state-transition from a susceptible (S) via an infected (I) to a recovered (R) state. The parameters characterizing the disease are the transmission rate per day per person, β, and the recovery rate per day, γ. We set γ=1/3 throughout. A susceptible individual who commits to vaccination avoids the infected state for one model period. In MAS approach, we made a simplifying assumption that vaccination provides perfect immunity. We subsequently relaxed this assumption in the mean-field approach. An epidemic season lasts until the infected state disappears from the population. Each individual who gets infected during the epidemic season incurs the cost of infection, C_i. Free riding is costless for individuals who avoid infection despite refusing to vaccinate.

The vaccination campaign. In this stage, each individual makes a decision whether to vaccinate or not. The decision was assumed to take place at the end of the epidemic season at which point agents reassess how they fared with respect to the disease spread: remained healthy, H, or suffered an infection, I. Adopting the game-theoretic terminology, hereafter we refer to this decision-making process as 'strategy updating'. Committing to vaccination introduces another dimension of agent states (beside H

and I). We denoted voluntary vaccinators with C for cooperation and non-vaccinators with D for defection. Voluntary vaccinators bear full vaccination cost C_v in each model period when they decide to vaccinate. Here, we assumed that C_v includes not only the monetary cost, but also other perceived risks, such as adverse side effects. We simplified the analysis by renormalizing this cost to reflect the relative cost of vaccination, $C_r=C_v/C_i$ ($0<C_r<1$). Finally, we assumed that subsidy can be given to voluntary vaccinators to alleviate the vaccination burden (denoted SC), but also to non-vaccinators to reverse their decision and commit to vaccination despite their initial opposition (denoted SD).

At the end of the model period, agents are assigned a payoff depending on how the epidemic affected them (healthy H or infected I), and depending on their strategic choice in conjunction with the subsidy (voluntary vaccinator C, non-vaccinator D, subsidized vaccinator SC, and subsidized non-vaccinator SD). According to these definitions, under the free-ticket subsidy, HC agents pay cost $-C_r$, HD, HSC, and HSD agents pay no cost, and ID agents pay the cost of infection set to -1. In addition, when the vaccine efficacy is imperfect, IC agents pay cost $-C_r-1$, while ISC and ISD pay -1. Under the discount subsidy, all vaccinators are subsidized (no HC and IC agents), while non-vaccinators receive nothing (no HSD and ISD agents), meaning that HSC agents pay reduced cost $-C_r'$, $C_r'<C_r$, while ISC pay $-C_r'-1$.

3.2.2. Strategy updating

We examined two different strategy updating rules appearing in literature [10,11]. Individual-based risk assessment (IB-RA) [10] is analogous to the Pairwise Fermi rule [13,14], which plays a prominent role in game-theoretic studies. Here, an individual randomly selects one neighbor and then decides whether to adopt that neighbor's strategy. That is, if agent i selects neighbor j for comparison, i will copy j's strategy ($s_i \leftarrow s_j$) with probability

$$P(s_i \leftarrow s_j) = \frac{1}{1+\exp[-(\pi_j - \pi_i)/\kappa]}, \tag{3-1}$$

where π_i is i's payoff in the previous model period, while parameter $\kappa > 0$ characterizes the strength of selection, i.e., the sensitivity of individuals to differences in their payoffs. Smaller κ means that agents are more sensitive to the payoff difference. We set κ=0.1.

Strategy-based risk assessment (SB-RA) [11] is a modification of the IB-RA rule to reflect the situation in which agents tend to assess the risk based on a socially averaged payoff because of the prevalence of information about the epidemic. Such information could be circulated by the media, for instance. The probability of copying a neighbor's strategy becomes

$$P(s_i \leftarrow s_j) = \frac{1}{1+\exp[-(\langle\pi_j\rangle - \pi_i)/\kappa]}, \tag{3-2}$$

where $<\pi_j>$ is the average collective payoff of neighbors who adopted the same strategy as i's randomly selected neighbor j.

3.2.3. Vaccination-subsidizing policies

Four different vaccination subsidizing policies were considered from a policy design perspective. These differ by the type of subsidy (free-ticket vs. discount) and the presumed target individuals (voluntary vaccinators vs. non-vaccinators vs. both). Specifically:

- Model A-1 combines the free-ticket subsidy with random target selection to spread the reach of the vaccination-subsidizing policy as much as the budget allows.
- Model A-2 also implements the free-ticket subsidy, but targets (randomly) only non-vaccinators from the previous model period. Tickets are again distributed as widely as the subsidy budget allows.
- Model A-3 is another implementation of the free-ticket subsidy, but targets (randomly) vaccinators from the previous model period. Tickets are still distributed as widely as possible given the subsidy budget.
- Model B implements a discount subsidy distributed to all vaccinators. Non-vaccinators receive nothing. The vaccination cost is reduced, but not entirely eliminated.

Figure 3.1 offers a schematic summary of the models listed above.

Subsidies represent a tax burden for society. If σ denotes the population fraction to be subsidized, this tax burden per capita, *TAX*, is given by

$$TAX = C_r \sigma. \tag{3-3}$$

From here we can define the total social payoff per capita due to an epidemic as:

$$TSP = -C_r (VC - \sigma) - FES - TAX = -C_r \cdot VC - 1 \cdot FES < 0\,, \tag{3-4}$$

where VC is vaccination coverage and FES is the final epidemic size. The TSP is negative because it quantifies how much a society is burdened by an epidemic. Furthermore, TAX does not play an explicit role on the right-hand side of Eq. (3-4) because taxes simply redistribute the cost from those who vaccinate to everyone. Without such redistribution, the VC would be lower meaning that there truly is an extra cost associated with taxation. If a vaccination strategy is successful, however, this taxation cost is more than offset by a lower FES. In this sense, subsidies can be considered a 'catalyst' to facilitate a social change that makes society more resilient to infectious disease outbreaks.

Hereafter, we made an additional assumption that the tax burden to subsidize vaccination does not affect an individual's decision whether to commit to vaccination or not. This is because, in reality, it is exceedingly difficult to recognize the exact part of one's taxes that ends up supporting subsidized vaccination programs. Taxes are for practical purposes levied in terms of general categories such as income tax, sales tax, property tax, etc., while a detailed breakdown remains invisible. By contrast, a subsidy via a free ticket or a discount coupon is manifestly visible to the subsidized individual, and thus relevant to decision making. That an assumption like this is reasonable is perhaps more clearly seen by considering the politics of 'populism' and its tendency to ride on various subsidies because these are generally favored and even enthusiastically accepted be the general population.

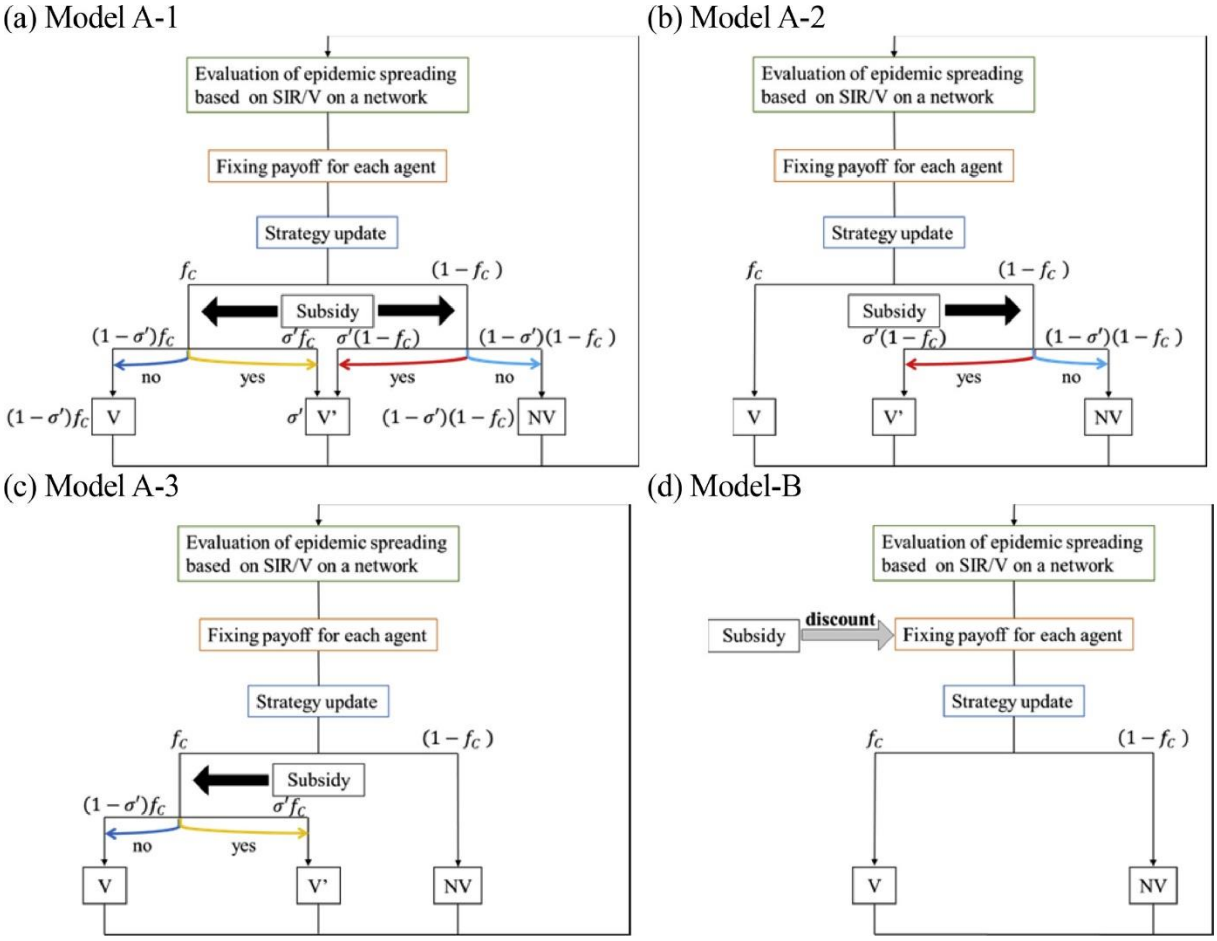

Figure 3.1. Schematic representation of four subsidy models. (a) In Model A-1 both voluntary vaccinators (V) and non-vaccinators (NV) may receive a subsidy, thus becoming subsidized vaccinators (V'). The free-ticket subsidy completely removes the vaccination cost. (b) Model A-2 is another implementation of the free-ticket subsidy, but targeted are only non-vaccinators from the previous model period. (c) Model A-3 also implements the free ticket subsidy, but in this case voluntary vaccinators from the previous model period are the only targets. (d) Model-B is an instance of the discount subsidy, whereby every vaccinator from the previous model period pays a reduced vaccination cost.

3.3 MAS approach

3.3.1. Model setup

For the MAS approach, we chose to work with a finite population containing $N=10^4$ individuals connected into an underlying network with average degree <k>=8. Three network topologies were explored: lattice, random regular, and scale-free [15]. The disease transmission rate, β, was differently set for each topology, but in such a way that the disease without any vaccinators spreads through up to 90% of the total population (i.e., FES=0.9) [10,11]. Because the SIR/V dynamics in spatially structured populations cannot be specified by a system of differential equations, we numerically simulated epidemic spreading using the Gillespie algorithm [16]. We started each simulation with $I_0=5$.

All simulation results presented hereafter are an ensemble average of 100 independent realizations. We expressed the performance of a given subsidy policy by measuring vaccination coverage (VC), the final epidemic size (FES), and the total social payoff (TSP) as a function of the vaccination cost, C_r, and the subsidized population fraction, σ. To highlight how subsidies affect the social equilibrium, we calculated the difference from the 'default' situation. A natural default herein are the results without any subsidy implemented.

3.3.2. Results and discussion

Fig. 3.2 shows the results of Model A-1 for the subsidy policy in conjunction with the IB-RA strategy updating rule. Combining the free-ticket subsidy to both voluntary vaccinators and non-vaccinators with the individual-based risk assessment mostly improves the TSP (blue color in Fig. 3.2(c)), but there are two instances in which the TSP is worse than in the default case (red color in Fig. 3.2(c)).

The first of those two instances appears when the vaccination cost is low and the subsidized population fraction are small. Here, the low vaccination cost ensures that the VC is relatively high even in the default situation, meaning that the only effect of a subsidy with limited reach is to turn some voluntary vaccinators into non-vaccinators in hope of receiving the subsidy the next time around. This negative effect manifests itself in a decreased VC (Fig. 3.2(a)), and consequently an increased FES (Fig. 3.2(b)) relative to the default setting. Interestingly, when the vaccination cost increases, even the limited subsidy reach has a positive effect because the VC is low in the default case.

The second instance in which the TSP is worse than in the default case is when the vaccination cost is high and the subsidized population fraction is large. Here, the high vaccination cost presents a barrier to having a large VC in the default case, but from a societal perspective the difference between an agent getting infected or not is almost negligible. Therefore, even a considerable increase in the VC (Fig. 3.2(a)), and a consequent decrease in FES (Fig. 3.2(b)) fail to justify introducing a vaccination-subsidizing policy. These results stress the need for a carefully optimized budget that is neither too small nor too large. Interestingly, directing the subsidy solely to non-vaccinators (Model A-2) changes nothing

in a qualitative sense (Fig. 3.3; cf. Fig. 3.2).

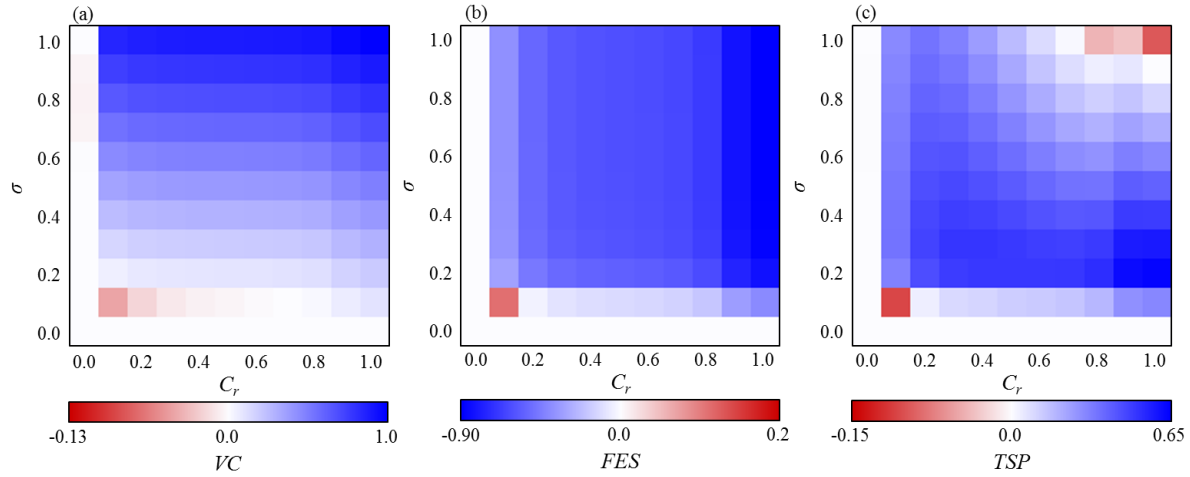

Figure 3.2. MAS simulations on a lattice with Model A-1 and the IB-RA strategy updating rule. Color indicates the difference between the case in which vaccination is subsidized (σ>0) and the default case without subsidy (σ=0). Blue indicates better, white neutral, and red worse performance than the default. Panel (a) displays VC, panel (b) FES, and panel (c) TSP.

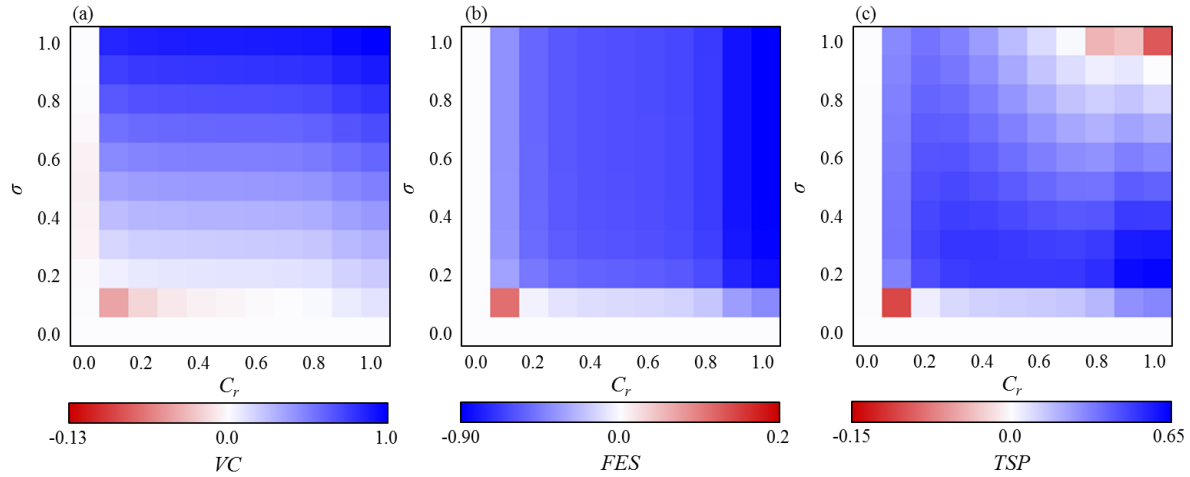

Figure 3.3. MAS simulations on a lattice with Model A-2 and the IB-RA strategy updating rule. Color indicates the difference between the case in which vaccination is subsidized (σ>0) and the default case without subsidy (σ=0). Blue indicates better, white neutral, and red worse performance than the default. Panel (a) displays VC, panel (b) FES, and panel (c) TSP.

Model A-3 reveals how a vaccination-subsidizing policy can improve the TSP in the limit of a low vaccination cost and a small subsidized population fraction (Fig. 3.4). Here, 'heaven helps those who help themselves' because non-vaccinators gain very little by refusing cheap vaccination in the first place, and the subsidy potentially erases this tiny gain. However, as evidenced by a decreased TSP relative to the default case, having a subsidy with wide reach when the cost of vaccination is high cannot be justified even if the subsidy is directed only towards voluntary vaccinators.

Model B implements the discount policy such that the cost of vaccination is reduced for all

voluntary vaccinators. The results of this model and Model A-3 are qualitatively similar (Fig. 3.5; cf. Fig. 3.4). Such a similarity is intuitively understood by considering that the subsidy in both models is reserved solely for voluntary vaccinators. Therefore, as long as the sole purpose of a vaccination-subsidizing policy is to increase the VC, putting in place a 'priority system' with free-tickets to a select group of voluntary vaccinators or an 'egalitarian system' with discount for all voluntary vaccinators makes little difference.

Turning attention to the effects of strategy updating rules, we replaced the IB-RA rule in Model A-1 with a more globally oriented SB-RA rule. In the limit of low (high) vaccination cost and a small (large) subsidized population fraction, the area in which the model underperforms the default setting increases (decreases) compared to when the IB-RA rule is implemented. The overall impact on the TSP turns out to be small, however (Fig. 3.6; cf. Fig. 3.2).

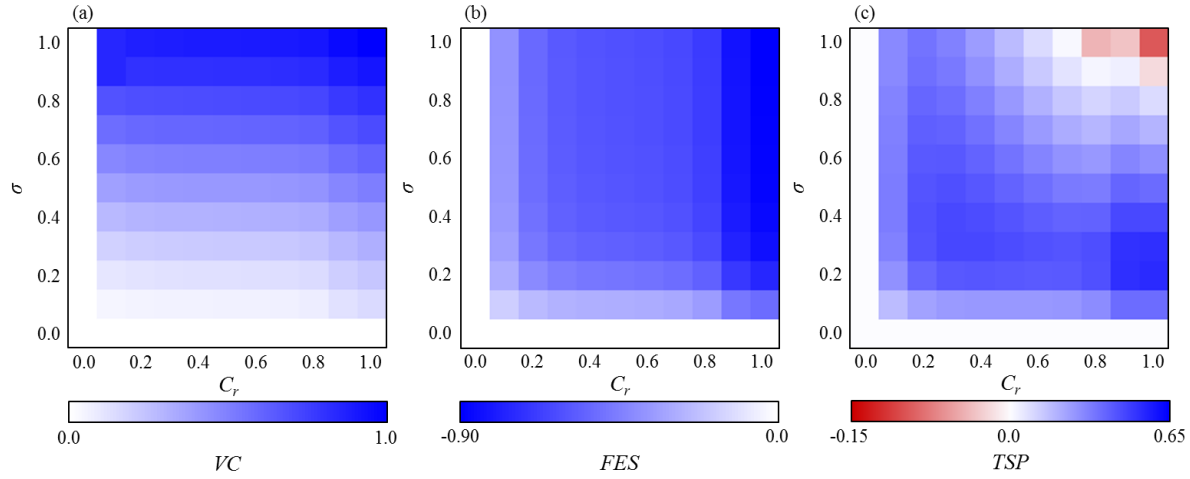

Figure 3.4. MAS simulations on a lattice with Model A-3 and the IB-RA strategy updating rule. Color indicates the difference between the case in which vaccination is subsidized (σ>0) and the default case without subsidy (σ=0). Blue indicates better, white neutral, and red worse performance than the default. Panel (a) displays VC, panel (b) FES, and panel (c) TSP.

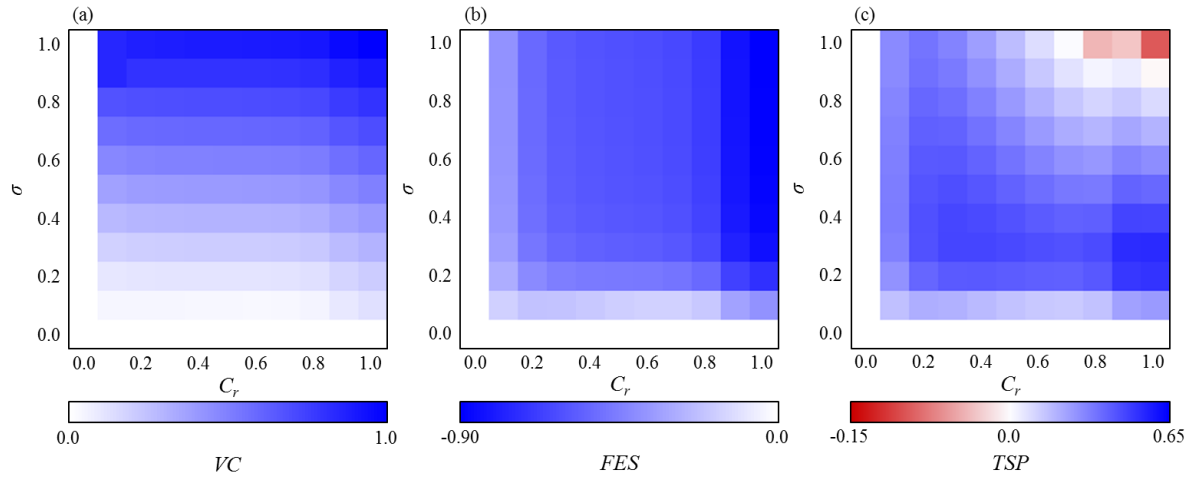

Figure 3.5. MAS simulations on a lattice with Model B and the IB-RA strategy updating rule. Color indicates the difference between the case in which vaccination is subsidized (σ>0) and the default case without subsidy (σ=0). Blue indicates better, white neutral, and red worse performance than the default.

Panel (a) displays VC, panel (b) FES, and panel (c) TSP.

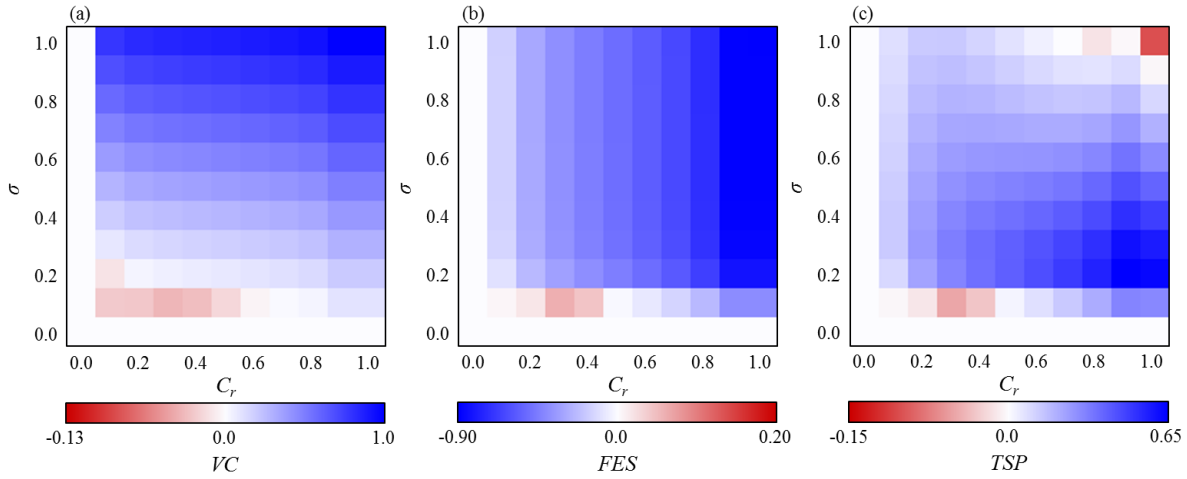

Figure 3.6. MAS simulations on a lattice with Model A-1 and the SB-RA strategy updating rule. Color indicates the difference between the case in which vaccination is subsidized (σ>0) and the default case without subsidy (σ=0). Blue indicates better, white neutral, and red worse performance than the default. Panel (a) displays VC, panel (b) FES, and panel (c) TSP.

Network topology exerts a much stronger effect on the performance of vaccination subsidies than the strategy updating rule. Replacing the lattice in Model A-1 with a regular random network considerably increases the domain of the phase space where the model performs worse than in the default case (Fig. 3.7; cf. Fig. 3.2). This is particularly true in the zone where the vaccination cost is relatively low and the subsidized population fraction relatively small. When the random regular network is further replaced with a scale-free network, the model performance worsens even more (Fig. 3.8; cf. Fig. 3.7). We thus see that randomizing links between agents disrupts the free-ticket vaccination policy if this policy fails to prioritize voluntary vaccinators over non-vaccinators. Heterogeneity in node degree exacerbates this disruptive effect. Given that human social networks, in addition to the small-world property, often exhibit the scale-free property [17], it is important that the results in Fig. 3.8(c) point to societal burden above the default setting. In fact, such additional burden arises almost irrespective of the vaccination cost (C_r<0.9), as well as for any feasible subsidized population fraction (σ<0.5) within the realistic limitations on budget size.

Because of the disruptive effect that the scale-free topology has on Model A-1 with the IB-RA strategy updating rule, we tested whether the SB-RA rule improves the model's performance. The results remain qualitatively similar, but unlike in the regular lattice, here the more global strategy updating rule helps alleviate some of the burden in terms of the TSP (Fig. 3.9; cf. Fig. 3.8). Particularly, the model's performance improves in the zone where the vaccination cost is relatively low and the subsidized population fraction relatively small.

Finally, we checked whether subsidizing only voluntary vaccinators, either via a free-ticket (Model A-3) or a discount (Model B) policy, suffers from the same disruptive effect caused by the scale-

free topology as when the subsidy is distributed non-preferentially (Model A-1). Here, we imposed the IB-RA strategy updating rule once again. The results of Model A-3 (Fig. 3.10), just as with agents arranged in a lattice, show no qualitative differences from the results of Model B (Fig. 3.11). More importantly, the disruptive effect of the scale-free topology disappears in the limit of a low vaccination cost and a small fraction of subsidized population. The overall performance of the subsidy is not as convincing as before, but there is a considerable range of vaccination costs and subsidy reaches in which the TSP improves relative to the default case. Governments should thus be guided by the 'heaven helps those who help themselves' principle, whereby either free tickets or discount coupons should be distributed to individuals who voluntarily commit to vaccination.

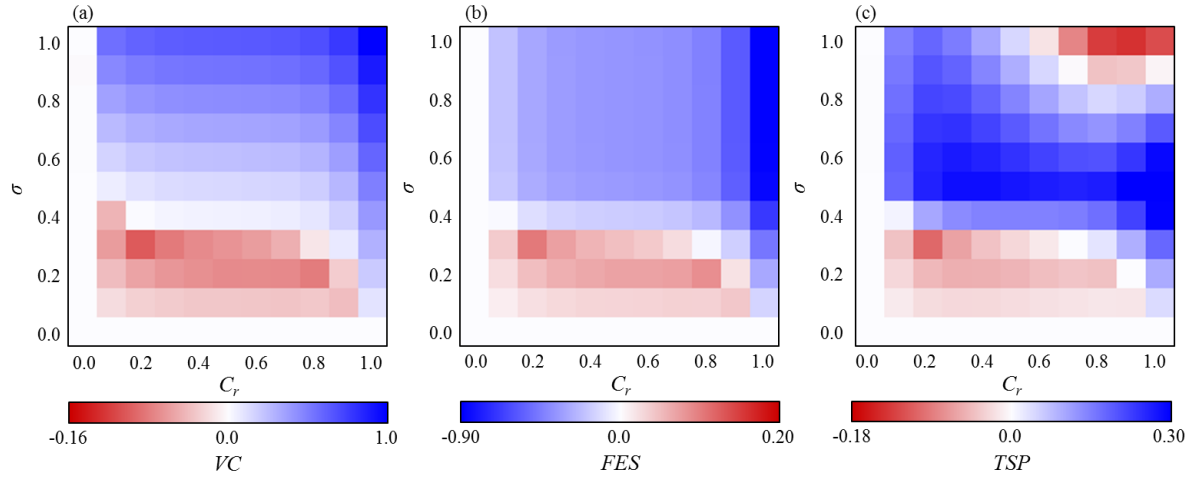

Figure 3.7. MAS simulations on random regular networks with Model A-1 and the IB-RA strategy updating rule. Color indicates the difference between the case in which vaccination is subsidized (σ>0) and the default case without subsidy (σ=0). Blue indicates better, white neutral, and red worse performance than the default. Panel (a) displays VC, panel (b) FES, and panel (c) TSP.

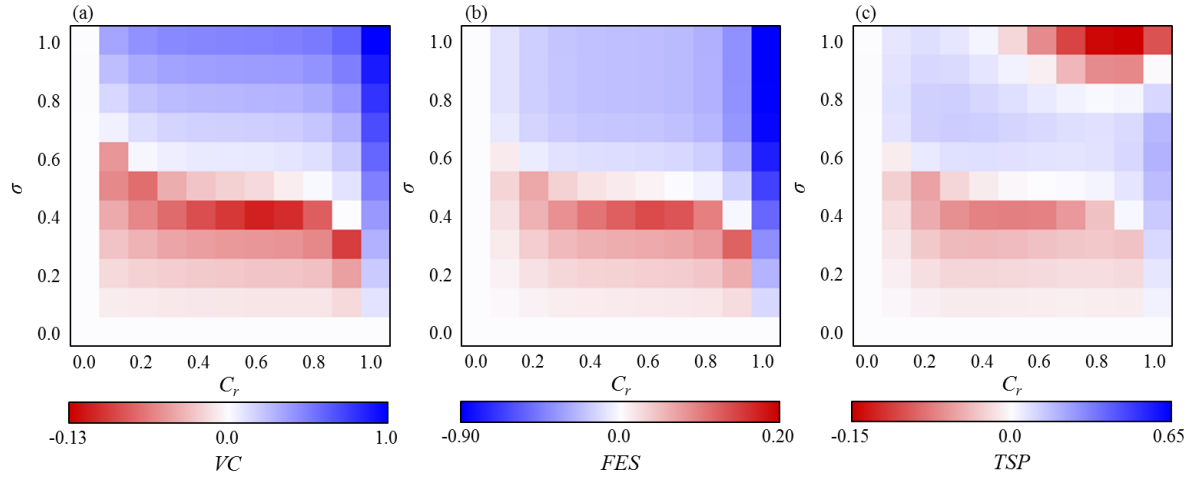

Figure 3.8. MAS simulations on scale-free networks with Model A-1 and the IB-RA strategy updating rule. Color indicates the difference between the case in which vaccination is subsidized (σ>0) and the default case without subsidy (σ=0). Blue indicates better, white neutral, and red worse performance than the default. Panel (a) displays VC, panel (b) FES, and panel (c) TSP.

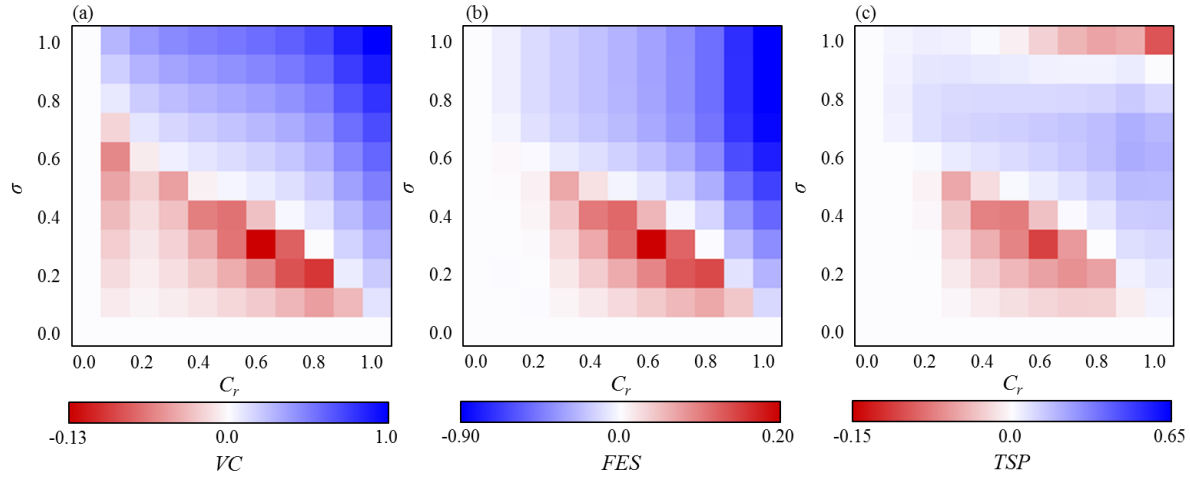

Figure 3.9. MAS simulations on scale-free networks with Model A-1 and the SB-RA strategy updating rule. Color indicates the difference between the case in which vaccination is subsidized (σ>0) and the default case without subsidy (σ=0). Blue indicates better, white neutral, and red worse performance than the default. Panel (a) displays VC, panel (b) FES, and panel (c) TSP.

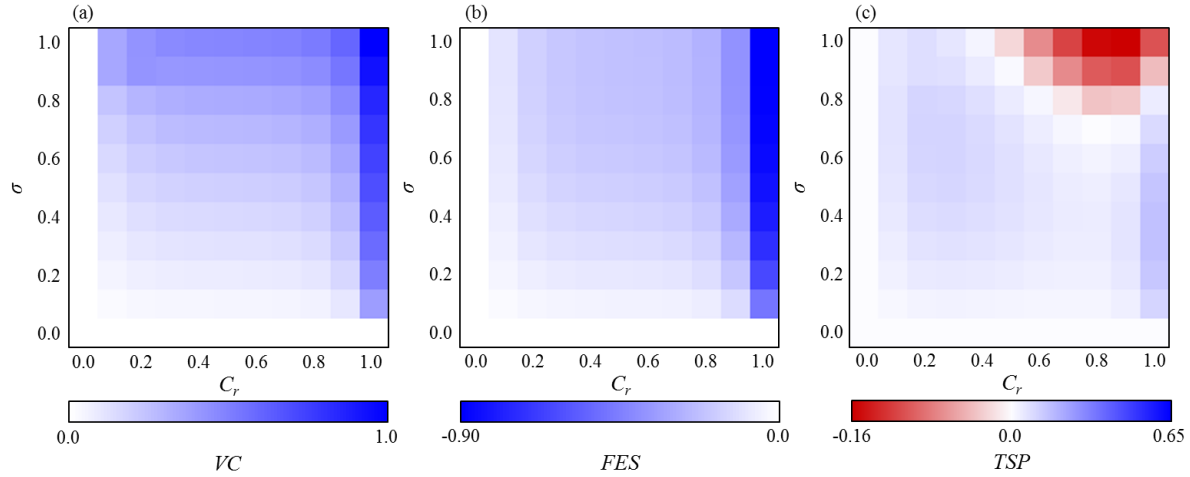

Figure 3.10. MAS simulations on scale-free networks with Model A-3 and the IB-RA strategy updating rule. Color indicates the difference between the case in which vaccination is subsidized (σ>0) and the default case without subsidy (σ=0). Blue indicates better, white neutral, and red worse performance than the default. Panel (a) displays VC, panel (b) FES, and panel (c) TSP.

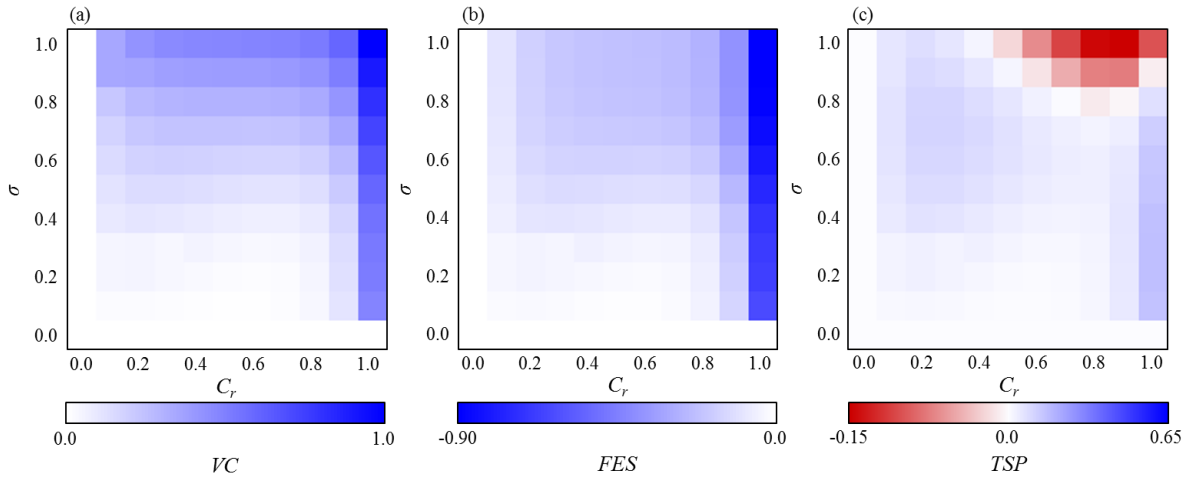

Figure 3.11. MAS simulations on scale-free networks with Model B and the IB-RA strategy updating rule. Color indicates the difference between the case in which vaccination is subsidized (σ>0) and the default case without subsidy (σ=0). Blue indicates better, white neutral, and red worse performance than the default. Panel (a) displays VC, panel (b) FES, and panel (c) TSP.

3.4 Mean field approach

There are two main differences between the MAS approach described heretofore and the mean-field approach that follows hereafter. First, we assumed that the population of agents is infinite and ideally well mixed. Because under this assumption references to any particular part of the population are quantified in terms of fractions, the population size is said to be normalized to N=1. It is therefore also appropriate to consider the per capita tax burden, TAX, equivalent to the total subsidy budget, SB. Namely, we have TAX=$C_r{\cdot}\sigma$=$C_r{\cdot}\sigma{\cdot}1$=$C_r{\cdot}\sigma{\cdot}N$=SB. The second assumption was that immunity after vaccination is not guaranteed. This assumption means that a vaccinated agent becomes immune to the disease with some probability e, $0 \leq e \leq 1$, because vaccines in the real world are imperfect more often than not. This is nicely exemplified by seasonal influenza too [18]. With remaining probability $1-e$ the agent fails to attain immunity. Apart from these two assumptions, the mean-field approach is analogous to the MAS approach, with the main advantage of providing generalized insights beyond what is possible purely by running numerical simulations.

3.4.1. Epidemic dynamics

Herein, we adopted an epidemic dynamics model described in Chapter 4. Denoting with x vaccination coverage (i.e., the fraction of all vaccinators, voluntary or otherwise), the fraction of immune individuals in the population is ex. The fraction of non-immune individuals is by extension $1-ex$. Because we are interested only in the equilibrium state, a single relevant equation of the epidemic dynamics model is that for the final epidemic size, FPS. Further denoting the FPS with $R(\infty)$ to emphasize that this is the fraction of recovered agents conditional on the current vaccination coverage (x) and reached in the equilibrium state (t=∞), we have

$$R(\infty) = (1-ex)(1-\exp[-R_0 R(\infty)]), \quad (3\text{-}5)$$

where R_0 is the basic reproduction number of the infectious disease. We presume R_0 = 2.5, which is applied consistently in this study. In this transcendental equation quantity $R(\infty)$ appears on both sides, indicating the necessity to solve the equation numerically in every model period. Once quantity $R(\infty)$ was calculated, we used it to express the fractions of four types of individuals appearing in the default model without a subsidy policy: healthy vaccinators HC, healthy non-vaccinators HD, infected vaccinators IC, and infected non-vaccinators ID. We afterwards used the same quantity in more complex models with a vaccination-subsidizing policy included.

3.4.2. Payoffs

As described in Chapter 2, agents are assigned a payoff at the end of the model period depending on how the epidemic season affected them, and depending on their strategic choice with respect to vaccination. In the default model without subsidy, infected non-vaccinators ID incur a cost of −1, while healthy non-vaccinators HD avoid paying any cost. Furthermore, infected vaccinators IC pay both the cost of vaccination and the cost of infection, $-C_r-1$, while healthy vaccinators HC incur only vaccination cost $-C_r$. In more complex models with a vaccination-subsidizing policy included, we considered additional player types whose payoffs depend on the specifics of the subsidy.

3.4.3. Vaccination-subsidizing policies

As in the MAS approach, we examined the performance of four subsidy models: Model A-1, Model A-2, Model A-3, and Model B. In the former three models, the limited subsidy is randomly distributed after each agent makes a decision whether to vaccinate or not (Fig. 3.1). The main difference between these models is that in Model A-1 subsidy recipients can be both voluntary vaccinators and non-vaccinators, in Model A-2 only non-vaccinators can receive the subsidy, while in Model A-3 only voluntary vaccinators have the right to receive the subsidy. In all these models, a subsidized agent always gets vaccinated; a voluntary vaccinator simply offsets the cost of vaccination with a free ticket, whereas a non-vaccinator reverses their initial decision because the obstacle to vaccination (i.e., the vaccination cost) disappears. In Model B with the discount policy, all voluntary vaccinators partially offset the vaccination cost by receiving discount coupons. Here, the amount of subsidy per vaccinator depends on the current vaccination coverage and thus changes in time.

Model A-1. In this model, the subsidy is distributed to a certain population fraction comprising both voluntary vaccinators and non-vaccinators. If we let this fraction be σ', then by definition σ=TAX/C_r=SB/C_r=σ' (cf. Eq. (3-4)). Furthermore, if the fraction of voluntary vaccinators is f_C and non-vaccinators is f_D=1−f_C, then the vaccination coverage becomes x=f_C+σ'(1−f_C), where subsidized voluntary vaccinators σ'f_C and subsidized non-vaccinators σ'(1−f_C) alike get vaccinated at no personal

cost. During the epidemic season these player types can either stay healthy or get infected, producing eight possible outcomes (in shorthand notation HC, HSC, HSD, HD, IC, ISC, ISD, and ID). Each outcome occupies a certain fraction of the population (Table 3.1) and earns a certain payoff (Table 3.2). These considerations lead to expected per-capita social payoff $\langle\pi\rangle$, cooperative payoff $\langle\pi_C\rangle$, and defecting payoff $\langle\pi_D\rangle$ in the case of imperfect vaccination:

$$\begin{aligned}\langle\pi\rangle = &-C_r(1-\sigma')f_C(e+(1-e)\exp[-R_0R(\infty)]) - (C_r+1)(1-\sigma')f_C(1-e)(1-\exp[-R_0R(\infty)]) \\ &-\sigma' f_C(1-e)(1-\exp[-R_0R(\infty)]) - (1-\sigma')(1-f_C)(1-\exp[-R_0R(\infty)]) \\ &-\sigma'(1-f_C)(1-e)(1-\exp[-R_0R(\infty)]) - SB\end{aligned}, \qquad (3\text{-}6)$$

$$\begin{aligned}\langle\pi_C\rangle = &-C_r(1-\sigma')(e+(1-e)\exp[-R_0R(\infty)]) - (C_r+1)(1-\sigma')(1-e)(1-\exp[-R_0R(\infty)]) \\ &-\sigma'(1-e)(1-\exp[-R_0R(\infty)])\end{aligned}, \qquad (3\text{-}7)$$

$$\langle\pi_D\rangle = -(1-\sigma')(1-\exp[-R_0R(\infty)]) - \sigma'(1-e)(1-\exp[-R_0R(\infty)])\,. \qquad (3\text{-}8)$$

From these equations, identity $\langle\pi\rangle=f_C\langle\pi_C\rangle+f_D\langle\pi_D\rangle-$SB holds, indicating that the expected social payoff is not only a weighted average of cooperative and defecting payoffs, but also the subsidy, as a burden to society, must be subtracted. The expected per-capita social payoff, $\langle\pi\rangle$, is thus equivalent to the total social payoff, TSP, as defined in Section 3.2.3. The reason why Eq. (3-6) explicitly contains the subsidy term, −SB, is the premise in Section 3.2.3 that the tax burden does not affect decision-making of an individual.

Table 3.1. Fractions of the eight types of agents appearing in Model A-1 of the analytical approach.

		Healthy	Infected
C	Vaccinated	$(1-\sigma')f_C(e+(1-e)\exp[-R_0R(\infty)])$	$(1-\sigma')f_C(1-e)(1-\exp[-R_0R(\infty)])$
	Subsidized	$\sigma' f_C(e+(1-e)\exp[-R_0R(\infty)])$	$\sigma' f_C(1-e)(1-\exp[-R_0R(\infty)])$
D	Non-vaccinated	$(1-\sigma')(1-f_C)\exp[-R_0R(\infty)]$	$(1-\sigma')(1-f_C)(1-\exp[-R_0R(\infty)])$
	Subsidized	$\sigma'(1-f_C)(e+(1-e)\exp[-R_0R(\infty)])$	$\sigma'(1-f_C)(1-e)(1-\exp[-R_0R(\infty)])$

Table 3.2. Payoffs at the end of the model period depending on an agent's state and the strategic choice with respect to vaccination in Model A-1.

		Healthy	Infected
C	Vaccinated	$-C_r$	$-C_r-1$
	Subsidized	0	−1
D	Non-vaccinated	0	−1
	Subsidized	0	−1

Model A-2. Here, the subsidy is distributed to a certain fraction of non-vaccinators. If we let this fraction be σ', then σ=TAX/C_r=SB/C_r=σ'(1−f_C). Accordingly, the subsidized population fraction, $\sigma=\sigma'(1-f_C)$, comprises only non-vaccinators who get vaccinated at no personal cost. The corresponding vaccination coverage is $x=f_C+\sigma'(1-f_C)$. Similarly as before, during the epidemic season voluntary

vaccinators, subsidized non-vaccinators, and non-vaccinators can either stay healthy or get infected, producing a total of six possible outcomes (in shorthand notation HC, HSD, HD, IC, ISD, and ID). Each outcome occupies a certain population fraction (Table 3.3) and earns a certain payoff (Table 3.4). The resulting expected per-capita social payoff $\langle\pi\rangle$, cooperative payoff $\langle\pi_C\rangle$, and defecting payoff $\langle\pi_D\rangle$ in the case of imperfect vaccination are:

$$\begin{aligned}\langle\pi\rangle = &-C_r f_C(e+(1-e)\exp[-R_0R(\infty)]) - (C_r+1) f_C(1-e)(1-\exp[-R_0R(\infty)]) \\ &-(1-\sigma')(1-f_C)(1-\exp[-R_0R(\infty)]) - \sigma'(1-f_C)(1-e)(1-\exp[-R_0R(\infty)]) - SB\end{aligned}, \tag{3-9}$$

$$\langle\pi_C\rangle = -C_r(e+(1-e)\exp[-R_0R(\infty)]) - (C_r+1)(1-e)(1-\exp[-R_0R(\infty)]), \tag{3-10}$$

$$\langle\pi_D\rangle = -(1-\sigma')(1-\exp[-R_0R(\infty)]) - \sigma'(1-e)(1-\exp[-R_0R(\infty)]). \tag{3-11}$$

Table 3.3. Fractions of the six types of agents appearing in Model A-2 of the analytical approach.

		Healthy	Infected
C	Vaccinated	$f_C(e+(1-e)\exp[-R_0R(\infty)])$	$f_C(1-e)(1-\exp[-R_0R(\infty)])$
D	Non-vaccinated	$(1-\sigma')(1-f_C)\exp[-R_0R(\infty)]$	$(1-\sigma')(1-f_C)(1-\exp[-R_0R(\infty)])$
	Subsidized	$\sigma'(1-f_C)(e+(1-e)\exp[-R_0R(\infty)])$	$\sigma'(1-f_C)(1-e)(1-\exp[-R_0R(\infty)])$

Table 3.4. Payoffs at the end of the model period depending on an agent's state and the strategic choice with respect to vaccination in Model A-2 of the analytical approach.

		Healthy	Infected
C	Vaccinated	$-C_r$	$-C_r-1$
D	Non-vaccinated	0	-1
	Subsidized	0	-1

Model A-3. In this model, the subsidy is distributed to a certain fraction of voluntary vaccinators. If we let this fraction be σ', then σ=TAX/C_r=SB/C_r=$\sigma' f_C$. Accordingly, the subsidized population fraction, $\sigma=\sigma' f_C$, comprises only voluntary vaccinators who get vaccinated at no personal cost. During the epidemic season voluntary vaccinators, subsidized or not, and non-vaccinators can either stay healthy or get infected, producing a total of six possible outcomes (in shorthand notation HC, HSC, HD, IC, ISC, and ID). Each outcome occupies a certain population fraction (Table 3.5) and earns a certain payoff (Table 3.6). The resulting expected per-capita social payoff $\langle\pi\rangle$, cooperative payoff $\langle\pi_C\rangle$, and defecting payoff $\langle\pi_D\rangle$ in the case of imperfect vaccination are:

$$\begin{aligned}\langle\pi\rangle = &-C_r(1-\sigma') f_C(e+(1-e)\exp[-R_0R(\infty)]) - (C_r+1)(1-\sigma') f_C(1-e)(1-\exp[-R_0R(\infty)]) \\ &-\sigma' f_C(1-e)(1-\exp[-R_0R(\infty)]) - (1-f_C)(1-\exp[-R_0R(\infty)]) - SB\end{aligned}, \tag{5-12}$$

$$\begin{aligned}\langle\pi_C\rangle = &-C_r(1-\sigma')(e+(1-e)\exp[-R_0R(\infty)]) - (C_r+1)(1-\sigma')(1-e)(1-\exp[-R_0R(\infty)]) \\ &-\sigma'(1-e)(1-\exp[-R_0R(\infty)])\end{aligned}, \tag{5-13}$$

$$\langle\pi_D\rangle = -(1-\exp[-R_0R(\infty)]). \tag{5-14}$$

Table 3.5. Fractions of the six types of agents appearing in Model A-3 of the analytical approach.

		Healthy	Infected
C	Vaccinated	$(1-\sigma')\,f_C\,(e+(1-e)\exp[-R_0R(\infty)])$	$(1-\sigma')\,f_C\,(1-e)(1-\exp[-R_0R(\infty)])$
	Subsidized	$\sigma' f_C\,(e+(1-e)\exp[-R_0R(\infty)])$	$\sigma' f_C\,(1-e)(1-\exp[-R_0R(\infty)])$
D	Non-vaccinated	$(1-f_C)(e+(1-e)\exp[-R_0R(\infty)])$	$(1-f_C)(1-e)(1-\exp[-R_0R(\infty)])$

Table 3.6. Payoffs at the end of the model period depending on an agent's state and the strategic choice with respect to vaccination in Model A-3 of the analytical approach.

		Healthy	Infected
C	Vaccinated	$-C_r$	$-C_r-1$
	Subsidized	0	-1
D	Non-vaccinated	0	-1

Model B. Under the discount policy, vaccination coverage equals the voluntary vaccination rate by definition, i.e., $x=f_C$. Accordingly, with the passage of an epidemic season there are only four outcomes (shorthand notation HSC, HD, ISC, and ID). Each outcome occupies the population fraction as in the default setting (Table 1), where the HSC (ISC) type takes the role of the HC (IC) type. Because the subsidy is equally distributed equally among all voluntary vaccinators, their vaccination cost is reduced by SB/f_C, leading to a similar but somewhat modified payoff structure (Table 3.7) relative to the default setting. The resulting expected per-capita social payoff $\langle\pi\rangle$, cooperative payoff $\langle\pi_C\rangle$, and defecting payoff $\langle\pi_D\rangle$ in the case of imperfect vaccination are:

$$\langle\pi\rangle=\left(-C_r+\frac{SB}{f_C}\right)f_C\,(e+(1-e)\exp[-R_0R(\infty)])+\left(-C_r-1+\frac{SB}{f_C}\right)f_C\,(1-e)(1-\exp[-R_0R(\infty)]) \\ -(1-f_CS)(1-\exp[-R_0R(\infty)])-SB, \tag{3-15}$$

$$\langle\pi_C\rangle=\left(-C_r+\frac{SB}{f_C}\right)(e+(1-e)\exp[-R_0R(\infty)])+\left(-C_r-1+\frac{SB}{f_C}\right)(1-e)(1-\exp[-R_0R(\infty)]), \tag{3-16}$$

$$\langle\pi_D\rangle=-(1-\exp[-R_0R(\infty)])\,. \tag{3-17}$$

Table 3.7. Payoff structure under the cooperator preferential subsidy policy.

		Healthy	Infected
C	Subsidized	$-C_r+\frac{SB}{f_C}$	$-C_r-1+\frac{SB}{f_C}$
D	Non-vaccinated	0	-1

3.4.4. Strategy updating

Strategy updates in our analytical approach are analogous to the rules already established in the MAS approach. Specifically, we rewrote the IB-RA equation (Eq. (5-3-1)) and the SB-RA equation

(Eq. (5-3-2)) in a form suitable for use in a mean-field approximation.

IB-RA rule. Ultimately, our interest was in the fraction of voluntary vaccinators, f_C, from which we could calculate the vaccination coverage, x. We have so far mentioned eight agent types depending on their decision to vaccinate or not, and depending on how they fare during an epidemic season. Summarizing these agent types using the shorthand notation (and the corresponding cost) gives: HC ($-C_r$), HD (0), HSC (0), HSD (0), IC ($-C_r-1$), ID (-1), ISC (-1), and ISD (-1). Voluntary vaccinators are HC, HSC, IC, and ISC, meaning that a total of 16 transitions to any of these four types from the remaining four types (HD, HSD, ID, and ISD) increase f_C. The probabilities of these transitions are:

$$P(HD \leftarrow HC) = P(HSD \leftarrow HC) = \frac{1}{1+\exp\left[-(-C_r - 0)/\kappa\right]}, \tag{3-18-1}$$

$$P(HD \leftarrow IC) = P(HSD \leftarrow IC) = \frac{1}{1+\exp\left[-((-C_r - 1) - 0)/\kappa\right]}, \tag{3-18-2}$$

$$P(HD \leftarrow HCS) = P(HSD \leftarrow HCS) = \frac{1}{1+\exp\left[-(0 - 0)/\kappa\right]}, \tag{3-18-3}$$

$$P(HD \leftarrow ICS) = P(HSD \leftarrow ICS) = \frac{1}{1+\exp\left[-((-1) - 0)/\kappa\right]}, \tag{3-18-4}$$

$$P(ID \leftarrow HC) = P(ISD \leftarrow HC) = \frac{1}{1+\exp\left[-(-C_r - (-1))/\kappa\right]}, \tag{3-18-5}$$

$$P(ID \leftarrow IC) = P(ISD \leftarrow IC) = \frac{1}{1+\exp\left[-((-C_r - 1) - (-1))/\kappa\right]}, \tag{3-18-6}$$

$$P(ID \leftarrow HCS) = P(ISD \leftarrow HCS) = \frac{1}{1+\exp\left[-(0 - (-1))/\kappa\right]}, \text{ and} \tag{3-18-7}$$

$$P(ID \leftarrow ICS) = P(ISD \leftarrow ICS) = \frac{1}{1+\exp\left[-((-1) - (-1))/\kappa\right]}. \tag{3-18-8}$$

There are also 16 transition probabilities from any of the types HC, HSC, IC, and ISC to any of the types HD, HSD, ID, and ISD, which cause decreases in f_C. These transition probabilities are:

$$P(HC \leftarrow HD) = P(HC \leftarrow HSD) = \frac{1}{1+\exp\left[-(0 - (-C_r))/\kappa\right]}, \tag{3-19-1}$$

$$P(HC \leftarrow ID) = P(HC \leftarrow ISD) = \frac{1}{1+\exp\left[-(-1 - (-C_r))/\kappa\right]}, \tag{3-19-2}$$

$$P(IC \leftarrow HD) = P(IC \leftarrow HSD) = \frac{1}{1+\exp\left[-(0 - (-C_r - 1))/\kappa\right]}, \tag{3-19-3}$$

$$P(IC \leftarrow ID) = P(IC \leftarrow ISD) = \frac{1}{1+\exp\left[-(-1 - (-C_r - 1))/\kappa\right]}, \tag{3-19-4}$$

$$P(HCS \leftarrow HD) = P(HCS \leftarrow HSD) = \frac{1}{1+\exp\left[-(0 - 0)/\kappa\right]}, \tag{3-19-5}$$

$$P(HCS \leftarrow ID) = P(HCS \leftarrow ISD) = \frac{1}{1+\exp\left[-(-1 - 0)/\kappa\right]}, \tag{3-19-6}$$

$$P(ICS \leftarrow HD) = P(ICS \leftarrow HSD) = \frac{1}{1+\exp\left[-(0-(-1))/\kappa\right]}, \text{ and} \quad (3\text{-}19\text{-}7)$$

$$P(ICS \leftarrow ID) = P(ICS \leftarrow ISD) = \frac{1}{1+\exp\left[-(-1-(-1))/\kappa\right]}. \quad (3\text{-}19\text{-}8)$$

In Model B, agent types HC, IC, HSD, and ISD are impossible, leading to a reduced set of transition probabilities. Those transition probabilities that increase f_C are:

$$P(HD \leftarrow HSC) = \frac{1}{1+\exp\left[-(-C_r + SB/f_C - 0)/\kappa\right]}, \quad (3\text{-}20\text{-}1)$$

$$P(HD \leftarrow ISC) = \frac{1}{1+\exp\left[-(-C_r - 1 + SB/f_C - 0)/\kappa\right]}, \quad (3\text{-}20\text{-}2)$$

$$P(ID \leftarrow HSC) = \frac{1}{1+\exp\left[-(-C_r + SB/f_C - (-1))/\kappa\right]}, \text{ and} \quad (3\text{-}20\text{-}3)$$

$$P(ID \leftarrow ISC) = \frac{1}{1+\exp\left[-(-C_r - 1 + SB/f_C - (-1))/\kappa\right]}. \quad (3\text{-}20\text{-}4)$$

Transition probabilities decreasing f_C are:

$$P(HSC \leftarrow HD) = \frac{1}{1+\exp\left[-(0-(-C_r + SB/f_C))/\kappa\right]}, \quad (3\text{-}21\text{-}1)$$

$$P(HSC \leftarrow ID) = \frac{1}{1+\exp\left[-(-1-(-C_r + SB/f_C))/\kappa\right]}, \quad (3\text{-}21\text{-}2)$$

$$P(ISC \leftarrow HD) = \frac{1}{1+\exp\left[-(0-(-C_r - 1 + SB/f_C))/\kappa\right]}, \text{ and} \quad (3\text{-}21\text{-}3)$$

$$P(ISC \leftarrow ID) = \frac{1}{1+\exp\left[-(-1-(-C_r - 1 + SB/f_C))/\kappa\right]}. \quad (3\text{-}21\text{-}4)$$

SB-RA rule. Here, the assumption was that agents compare their own payoff with the expected per-capita payoff of everyone else. This assumption in all variants of Model A leads to a total of eight transition probabilities. The probabilities with a positive effect on voluntary vaccination, i.e., those increasing f_C, are:

$$P(HD \leftarrow C) = \frac{1}{1+\exp[-(\langle \pi_C \rangle - 0)/\kappa]}, \quad (3\text{-}22\text{-}1)$$

$$P(ID \leftarrow C) = \frac{1}{1+\exp[-(\langle \pi_C \rangle - (-1))/\kappa]}, \quad (3\text{-}22\text{-}2)$$

$$P(HSD \leftarrow C) = \frac{1}{1+\exp[-(\langle \pi_C \rangle - 0)/\kappa]}, \text{ and} \quad (3\text{-}22\text{-}3)$$

$$P(ISD \leftarrow C) = \frac{1}{1+\exp[-(\langle \pi_C \rangle - (-1))/\kappa]}. \quad (3\text{-}22\text{-}4)$$

By contrast, transition probabilities that decrease f_C are:

$$P(HC \leftarrow D) = \frac{1}{1+\exp[-(\langle \pi_D \rangle - (-C_r))/\kappa]}, \tag{3-23-1}$$

$$P(IC \leftarrow D) = \frac{1}{1+\exp[-(\langle \pi_D \rangle - (-C_r - 1))/\kappa]}, \tag{3-23-2}$$

$$P(HSC \leftarrow D) = \frac{1}{1+\exp[-(\langle \pi_D \rangle - 0)/\kappa]}, \text{ and} \tag{3-23-3}$$

$$P(ISC \leftarrow D) = \frac{1}{1+\exp[-(\langle \pi_D \rangle - (-1))/\kappa]}. \tag{3-23-4}$$

Finally, the fact that Model B does not contain certain agent types by definition, produces a total of only four transition probabilities. The two transition probabilities increasing f_C are:

$$P(HD \leftarrow C) = \frac{1}{1+\exp\left[-(\langle \pi_C \rangle - 0)/\kappa\right]} \quad \text{and} \tag{3-24-1}$$

$$P(ID \leftarrow C) = \frac{1}{1+\exp\left[-(\langle \pi_C \rangle - (-1))/\kappa\right]}, \tag{3-24-2}$$

while the two remaining transition probabilities that decrease f_C are:

$$P(HSC \leftarrow D) = \frac{1}{1+\exp\left[-(\langle \pi_D \rangle - (-C_r + SB/f_C))/\kappa\right]} \quad \text{and} \tag{3-25-1}$$

$$P(ISC \leftarrow D) = \frac{1}{1+\exp\left[-(\langle \pi_D \rangle - (-C_r - 1 + SB/f_C))/\kappa\right]}. \tag{3-25-2}$$

Herewith we have listed all the equations that serve as a backbone of our mean-field approach. The last remaining step is to specify the equations for global time evolution.

3.4.5. Global time evolution

As described previously, a vaccination campaign follows after every epidemic season (Fig. 3.1). During the vaccination campaign, willingness to voluntarily get vaccinated changes among the population (i.e., f_C increases or decreases), thus affecting the total vaccination coverage (i.e., x also increases or decreases in response to the change in f_C). There are in total eight different dynamical equations for f_C because we have devised four different vaccination-subsidizing policies (Models A-1, A-2, A-3, and B) and envisioned two different strategy updating rules (IB-RA and SB-RA). Each of these equations comes with a time derivative of f_C on the left-hand side and a sum of terms on the right-hand side consisting of two elements. These two elements depend on the implemented strategy updating rule. With the IB-RA rule, the first element represents the interaction of a cooperative (i.e., committing) with a non-cooperative (i.e., abstaining) agent type in the form of a product of their fractions in the population, while the second term is a difference of transition probabilities that one agent type will copy the other and vice versa. With the SB-RA rule, the first element is a given agent type's fraction in the population, while the second element is this agent's transition probability to switch from a cooperative to a non-cooperative action or vice versa.

In Model A-1 equipped with the IB-RA rule, there are four cooperative and four non-cooperative agent types, and thus 16 possible bidirectional interactions. The dynamical equation becomes

$$
\begin{aligned}
\frac{df_C}{dt} = {} & f_C(1-f_C)(1-\sigma')^2(e+(1-e)\exp[-R_0R(\infty)])\exp[-R_0R(\infty)]\big(P(HD \leftarrow HC)-P(HC \leftarrow HD)\big) \\
& + f_C(1-f_C)(1-\sigma')^2(e+(1-e)\exp[-R_0R(\infty)])(1-\exp[-R_0R(\infty)])\big(P(ID \leftarrow HC)-P(HC \leftarrow ID)\big) \\
& + f_C(1-f_C)\sigma'(1-\sigma')(e+(1-e)\exp[-R_0R(\infty)])^2\big(P(HSD \leftarrow HC)-P(HC \leftarrow HSD)\big) \\
& + f_C(1-f_C)\sigma'(1-\sigma')(1-e)(e+(1-e)\exp[-R_0R(\infty)])(1-\exp[-R_0R(\infty)])\big(P(ISD \leftarrow HC)-P(HC \leftarrow ISD)\big) \\
& + f_C(1-f_C)(1-\sigma')^2(1-e)(1-\exp[-R_0R(\infty)])\exp[-R_0R(\infty)]\big(P(HD \leftarrow IC)-P(IC \leftarrow HD)\big) \\
& + f_C(1-f_C)(1-\sigma')^2(1-e)(1-\exp[-R_0R(\infty)])^2\big(P(ID \leftarrow IC)-P(IC \leftarrow ID)\big) \\
& + f_C(1-f_C)\sigma'(1-\sigma')(1-e)(e+(1-e)\exp[-R_0R(\infty)])(1-\exp[-R_0R(\infty)])\big(P(HSD \leftarrow IC)-P(IC \leftarrow HSD)\big) \\
& + f_C(1-f_C)\sigma'(1-\sigma')(1-e)^2(1-\exp[-R_0R(\infty)])^2\big(P(ISD \leftarrow IC)-P(IC \leftarrow ISD)\big) \\
& + f_C(1-f_C)\sigma'(1-\sigma')(e+(1-e)\exp[-R_0R(\infty)])\exp[-R_0R(\infty)]\big(P(HD \leftarrow HSC)-P(HSC \leftarrow HD)\big) \\
& + f_C(1-f_C)\sigma'(1-\sigma')(e+(1-e)\exp[-R_0R(\infty)])(1-\exp[-R_0R(\infty)])\big(P(ID \leftarrow HSC)-P(HSC \leftarrow ID)\big) \\
& + f_C(1-f_C)\sigma'^2(e+(1-e)\exp[-R_0R(\infty)])^2\big(P(HSD \leftarrow HSC)-P(HCS \leftarrow HSD)\big) \\
& + f_C(1-f_C)\sigma'^2(1-e)(e+(1-e)\exp[-R_0R(\infty)])(1-\exp[-R_0R(\infty)])\big(P(IDS \leftarrow HSC)-P(HCS \leftarrow ISD)\big) \\
& + f_C(1-f_C)\sigma'(1-\sigma')(1-e)(1-\exp[-R_0R(\infty)])\exp[-R_0R(\infty)]\big(P(HD \leftarrow ISC)-P(ISC \leftarrow HD)\big) \\
& + f_C(1-f_C)\sigma'(1-\sigma')(1-e)(1-\exp[-R_0R(\infty)])^2\big(P(ID \leftarrow ISC)-P(ISC \leftarrow ID)\big) \\
& + f_C(1-f_C)\sigma'^2(1-e)(e+(1-e)\exp[-R_0R(\infty)])(1-\exp[-R_0R(\infty)])\big(P(HDS \leftarrow ISC)-P(ICS \leftarrow HSD)\big) \\
& + f_C(1-f_C)\sigma'^2(1-e)^2(1-\exp[-R_0R(\infty)])^2\big(P(ISD \leftarrow ISC)-P(ISC \leftarrow ISD)\big)
\end{aligned}
$$

. (3-26)

In Model A-1 equipped with the SB-RA rule, four cooperative agent types can transition to a non-cooperative type and four non-cooperative agent types can transition to a cooperative type. The corresponding dynamical equation is

$$
\begin{aligned}
\frac{df_C}{dt} = {} & -f_C(1-f_C)(1-\sigma')(e+(1-e)\exp[-R_0R(\infty)])P(HC \leftarrow D) \\
& - f_C(1-f_C)(1-\sigma')(1-e)(1-\exp[-R_0R(\infty)])P(IC \leftarrow D) \\
& - f_C(1-f_C)\sigma'(1-e)\exp[-R_0R(\infty)]P(HSC \leftarrow D) \\
& - f_C(1-f_C)\sigma'(1-e)(1-\exp[-R_0R(\infty)])P(ISC \leftarrow D) \\
& + f_C(1-f_C)(1-\sigma')\exp[-R_0R(\infty)]P(HD \leftarrow C) \\
& + f_C(1-f_C)(1-\sigma')(1-\exp[-R_0R(\infty)])P(ID \leftarrow C) \\
& + f_C(1-f_C)\sigma'(e+(1-e)\exp[-R_0R(\infty)])P(HSD \leftarrow C) \\
& + f_C(1-f_C)\sigma'(1-e)(1-\exp[-R_0R(\infty)])P(ISD \leftarrow C)
\end{aligned}
$$

. (3-27)

In Model A-2 equipped with the IB-RA rule, there are two cooperative and four non-cooperative agent types for a total of eight bidirectional interactions. The dynamical model equation is

$$
\begin{aligned}
\frac{df_C}{dt} = {} & f_C(1-f_C)(1-\sigma')(e+(1-e)\exp[-R_0R(\infty)])\exp[-R_0R(\infty)]\big(P(HD \leftarrow HC) - P(HC \leftarrow HD)\big) \\
& + f_C(1-f_C)(1-\sigma')(e+(1-e)\exp[-R_0R(\infty)])(1-\exp[-R_0R(\infty)])\big(P(ID \leftarrow HC) - P(HC \leftarrow ID)\big) \\
& + f_C(1-f_C)\sigma'(e+(1-e)\exp[-R_0R(\infty)])^2\big(P(HSD \leftarrow HC) - P(HC \leftarrow HSD)\big) \\
& + f_C(1-f_C)\sigma'(e+(1-e)\exp[-R_0R(\infty)])(1-e)(1-\exp[-R_0R(\infty)])\big(P(ISD \leftarrow HC) - P(HC \leftarrow ISD)\big) \\
& + f_C(1-f_C)(1-\sigma')(1-e)(1-\exp[-R_0R(\infty)])\exp[-R_0R(\infty)]\big(P(HD \leftarrow IC) - P(IC \leftarrow HD)\big) \\
& + f_C(1-f_C)(1-\sigma')(1-e)(1-\exp[-R_0R(\infty)])(1-\exp[-R_0R(\infty)])\big(P(ID \leftarrow IC) - P(IC \leftarrow ID)\big) \\
& + f_C(1-f_C)\sigma'(1-e)(1-\exp[-R_0R(\infty)])(e+(1-e)\exp[-R_0R(\infty)])\big(P(ID \leftarrow IC) - P(IC \leftarrow ID)\big) \\
& + f_C(1-f_C)\sigma'(1-e)^2(1-\exp[-R_0R(\infty)])^2\big(P(ID \leftarrow IC) - P(IC \leftarrow ID)\big)
\end{aligned}
\tag{3-28}
$$

In Model A-2 equipped with the SB-RA rule, there are two cooperative agent types who can transition to a non-cooperative type and four non-cooperative agent types who can transition to a cooperative type. Accordingly, the dynamical equation is

$$
\begin{aligned}
\frac{df_C}{dt} = {} & -f_C(1-f_C)(e+(1-e)\exp[-R_0R(\infty)])P(HC \leftarrow D) \\
& - f_C(1-f_C)(1-e)(1-\exp[-R_0R(\infty)])P(IC \leftarrow D) \\
& + f_C(1-f_C)(1-\sigma')\exp[-R_0R(\infty)]P(HD \leftarrow C) \\
& + f_C(1-f_C)(1-\sigma')(1-\exp[-R_0R(\infty)])P(ID \leftarrow C) \\
& + f_C(1-f_C)\sigma'(e+(1-e)\exp[-R_0R(\infty)])P(HSD \leftarrow C) \\
& + f_C(1-f_C)\sigma'(1-e)(1-\exp[-R_0R(\infty)])P(ISD \leftarrow C)
\end{aligned}
\tag{3-29}
$$

In Model A-3 equipped with the IB-RA rule, there are four cooperative and two non-cooperative agent types, again giving rise to eight bidirectional interactions. The dynamical equation is

$$
\begin{aligned}
\frac{df_C}{dt} = {} & f_C(1-f_C)(1-\sigma')(e+(1-e)\exp[-R_0R(\infty)])\exp[-R_0R(\infty)]\big(P(HD \leftarrow HC) - P(HC \leftarrow HD)\big) \\
& + f_C(1-f_C)(1-\sigma')(e+(1-e)\exp[-R_0R(\infty)])(1-\exp[-R_0R(\infty)])\big(P(ID \leftarrow HC) - P(HC \leftarrow ID)\big) \\
& + f_C(1-f_C)(1-\sigma')(1-e)(1-\exp[-R_0R(\infty)])\exp[-R_0R(\infty)]\big(P(HD \leftarrow IC) - P(IC \leftarrow HD)\big) \\
& + f_C(1-f_C)(1-\sigma')(1-e)(1-\exp[-R_0R(\infty)])(1-\exp[-R_0R(\infty)])\big(P(ID \leftarrow IC) - P(IC \leftarrow ID)\big) \\
& + f_C(1-f_C)\sigma'(e+(1-e)\exp[-R_0R(\infty)])\exp[-R_0R(\infty)]\big(P(HD \leftarrow HSC) - P(HSC \leftarrow HD)\big) \\
& + f_C(1-f_C)\sigma'(e+(1-e)\exp[-R_0R(\infty)])(1-\exp[-R_0R(\infty)])\big(P(ID \leftarrow HSC) - P(HSC \leftarrow ID)\big) \\
& + f_C(1-f_C)\sigma'(1-e)(1-\exp[-R_0R(\infty)])\exp[-R_0R(\infty)]\big(P(HD \leftarrow ISC) - P(ISC \leftarrow HD)\big) \\
& + f_C(1-f_C)\sigma'(1-e)(1-\exp[-R_0R(\infty)])(1-\exp[-R_0R(\infty)])\big(P(ID \leftarrow ISC) - P(ISC \leftarrow ID)\big)
\end{aligned}
\tag{3-30}
$$

In Model A-3 equipped with the SB-RA rule, there are four cooperative agent types who can transition to a non-cooperative type and two non-cooperative agent types who can transition to a cooperative type. The corresponding dynamical equation is

$$\begin{aligned}\frac{df_C}{dt} = &-f_C(1-f_C)(1-\sigma')(e+(1-e)\exp[-R_0R(\infty)])P\left(HC \leftarrow D\right)\\ &-f_C(1-f_C)(1-\sigma')(1-e)(1-\exp[-R_0R(\infty)])P\left(IC \leftarrow D\right)\\ &-f_C(1-f_C)\sigma'(e+(1-e)\exp[-R_0R(\infty)])P\left(HSC \leftarrow D\right)\\ &-f_C(1-f_C)\sigma'(1-e)(1-\exp[-R_0R(\infty)])P\left(ISC \leftarrow D\right)\\ &+f_C(1-f_C)\exp[-R_0R(\infty)]P\left(HD \leftarrow C\right)\\ &+f_C(1-f_C)(1-\exp[-R_0R(\infty)])P\left(ID \leftarrow C\right)\end{aligned} \quad . \tag{3-31}$$

In Model B equipped with the IB-RA rule, there are two cooperative and two non-cooperative agent types for a total of four bidirectional interactions. The dynamical equation becomes

$$\begin{aligned}\frac{df_C}{dt} = &f_C(1-f_C)(e+(1-e)\exp[-R_0R(\infty)])\exp[-R_0R(\infty)]\left(P\left(HD \leftarrow HSC\right)-P\left(HSC \leftarrow HD\right)\right)\\ &+f_C(1-f_C)(e+(1-e)\exp[-R_0R(\infty)])(1-\exp[-R_0R(\infty)])\left(P\left(ID \leftarrow HSC\right)-P\left(HSC \leftarrow ID\right)\right)\\ &+f_C(1-f_C)(1-e)(1-\exp[-R_0R(\infty)])\exp[-R_0R(\infty)]\left(P\left(HD \leftarrow ISC\right)-P\left(ISC \leftarrow HD\right)\right)\\ &+f_C(1-f_C)(1-e)(1-\exp[-R_0R(\infty)])^2\left(P\left(ID \leftarrow ISC\right)-P\left(ISC \leftarrow ID\right)\right)\end{aligned} \quad . \tag{3-32}$$

Finally, in Model B equipped with the SB-RA rule, two cooperative agent types can transition to a non-cooperative type and two non-cooperative agent types can transition to a cooperative type. The dynamical equation is

$$\begin{aligned}\frac{df_C}{dt} = &-f_C(1-f_C)(e+(1-e)\exp[-R_0R(\infty)])P\left(HSC \leftarrow D\right)\\ &-f_C(1-f_C)(1-e)(1-\exp[-R_0R(\infty)])P\left(ISC \leftarrow D\right)\\ &+f_C(1-f_C)\exp[-R_0R(\infty)]P\left(HD \leftarrow C\right)\\ &+f_C(1-f_C)(1-\exp[-R_0R(\infty)])P\left(ID \leftarrow VC\right)\end{aligned} \quad . \tag{3-33}$$

All these dynamical equations can be solved numerically. We implemented an explicit scheme to obtain a numerical solution, and ultimately the total vaccination coverage at equilibrium.

3.4.6. Results and discussion

Before focusing on the effects of imperfect vaccine (i.e., situations with e<1), we examined the performance of the mean-field approximation relative to MAS simulations. Taking, for example, Model A-1 equipped with the IB-RA rule, the mean-field results should be comparable with the MAS results obtained with the random regular network (Fig. 3.12, top row; cf. Fig. 3.7). The results are indeed qualitatively similar. The MAS approach yields coarser images than the mean-field approach due to finite population, finite node degree, and finite resolution (i.e., number of simulations), but the same patterns are present in both cases. Namely, subsidies worsen the total social payoff (TSP) relative to the default case of no subsidy (i) when the vaccination cost is relatively low and the subsidized population fraction is relatively small or (ii) in the limit of a high vaccination cost and a large subsidized population fraction. This latter result is understandable because it becomes a lesser burden for society to have a few

more infected individuals than to secure vaccination for a sufficient number of individuals to avoid these infections. The former result, however, is easier to understand in the context of Model A-2.

Subsidizing only non-vaccinators, as assumed in Model A-2, does not change the results qualitatively, but worsens the negative effect of subsidies in a quantitative sense (Fig. 3.12, second row). Specifically, vaccination coverage (VC) is lower, the final epidemic size (FES) is larger, and the TSP is more negative than in a comparable scenario executed with Model A-1, i.e., when the subsidy is distributed to both voluntary vaccinators and non-vaccinators. The reason for this dismal outcome is similar to what we have seen in MAS simulations. By directing subsidies to non-vaccinators, there is an incentive for voluntary vaccinators to abstain in hope that they can receive the subsidy and offset the cost of vaccination. This incentive causes harm by increasing the presence of non-vaccinators as long as the subsidy covers a relatively small fraction of the population. The effect is stronger with a lower vaccination cost because in that case, even without any subsidy, the fraction of voluntary vaccinators is relatively large.

If subsidizing non-vaccinators worsens the TSP, should only voluntary vaccinators be the recipients of subsidies? Models A-3 and B offer a similar, positive answer to this question (Fig. 3.12, third and last rows, respectively). Here, the incentive for voluntary vaccinators to abstain in hope of receiving the subsidy completely disappears. This improves the TSP in almost all scenarios, except in the limit of a high vaccination cost and a large fraction of subsidized vaccinators. Once again, 'heaven helps those who help themselves'. When it comes to distinguishing between the performance of Models A-3 and B, the former is slightly better. This is due to the fact that the IB-RA strategy updating rule depends on the payoff difference between alternative actions, and the free-ticket policy increases this difference relative to the discount-coupon policy. However, any performance improvement of Model A-3 over Model B is quantitatively small.

By changing the strategy updating rule from the IB-RA rule to the SB-RA rule, the results are qualitatively still the same, but there is a noticeable size increase of the zone in which subsidizing vaccination is justifiable (Fig. 3.13). This is particularly true in the limit of a high vaccination cost and a large vaccination coverage. Such a result is possible because under the SB-RA rule there are more voluntary vaccinators than in the same scenario under the IB-RA rule, meaning that a given subsidy secures a higher VC, reduces the FES, and finally is less burdensome to society.

Turning attention to an imperfect vaccine ($e<1$), one of the most striking features is that the dependence on the subsidized population fraction (i.e., parameter σ) almost vanishes, while the relative cost of vaccination almost entirely controls the final outcome (Fig. 3.14). If $C_r<0.2$ then the subsidy in Models A-1 and A-2 slightly deteriorates the TSP regardless of the reach (i.e., budget size), while in Models A-3 and B, the subsidy's effect is neutral. Even worse, if $C_r>0.6$ then the subsidy grossly deteriorates the TSP in all models regardless of the subsidy's reach. Introducing the SB-RA rule deteriorates the subsidy's performance even further (Fig. 3.15). The margin for justifying the subsidy in

terms of the TSP becomes extremely narrow; the maximum improvement relative to the default case is only 0.06 compared to 0.37 with the IB-RA rule.

Multiple reasons conspire to produce these results. First, when relative vaccination cost C_r is low, the fraction of voluntary vaccinators is reasonably large even in the default case. In this situation, giving subsidies to non-vaccinators only creates a negative incentive to forgo vaccination in order to perhaps receive the subsidy next time around. If, in addition, the subsidized population fraction, σ, is small, the aggregate result will be a decrease in vaccination coverage compared to the default. The subsidy's reach as expressed by parameter σ needs to become sufficiently large to overcome the said negative incentive, which is what we have seen with the perfect vaccine in Models A-1 and A-2. An imperfect vaccine, however, nullifies the positive effect of increasing σ, thus making the outcomes almost insensitive to the value of this parameter. Even when the negative incentive of subsidizing non-vaccinators is removed, as is the case in Models A-3 and B, there is no substantial improvement over the default because the subsidy brings little benefit in view of the low values of parameters C_r and e. Introducing the SB-RA rule, which increases the fraction of voluntary vaccinators, only narrows the window for the subsidy to improve the situation. Finally, with high relative vaccination cost C_r and the insensitivity of the results to increasing subsidy reach as expressed by parameter σ, it simply becomes less burdensome for society to let the infection take its natural course than to try to increase the VC beyond voluntary vaccinators that would be present anyway.

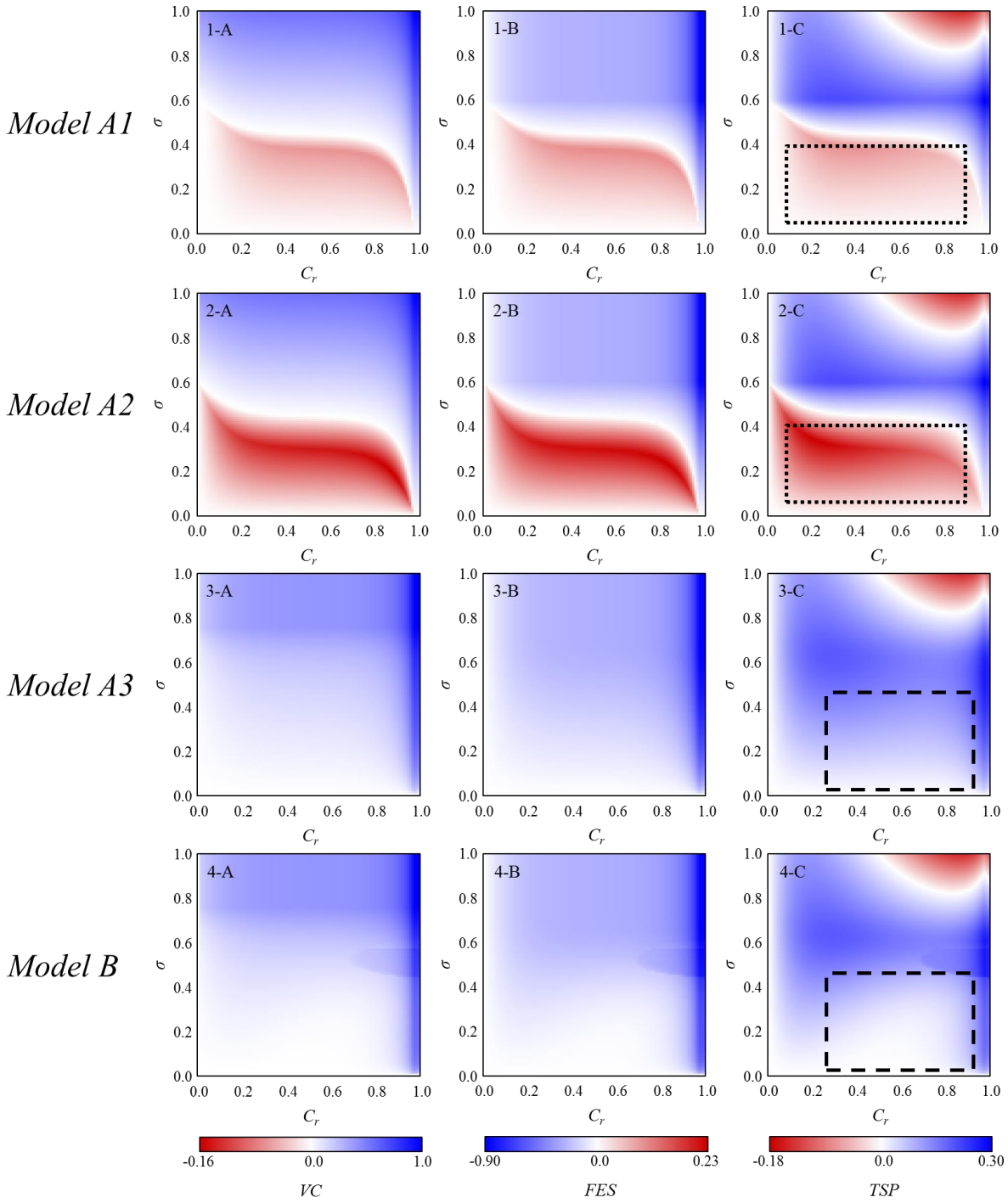

Figure 3.12. Mean-field approximation with the IB-RA rule and a perfect vaccine (e=1). Color indicates the difference between the case in which vaccination is subsidized (σ>0) and the default case without subsidy (σ=0). Blue indicates better, white neutral, and red worse performance than the default. Panel rows display the performance of Model A-1 (top row), Model A-2 (second row), Model A-3 (third row), and Model B (bottom row). Panel columns display VC (left column), FES (middle column), and TSP (right column). Dotted rectangles emphasize the zone in which Model A-1 quantitatively outperforms Model A-2. Similarly, dashed rectangles single out the zone in which Model A-3 outperforms Model B.

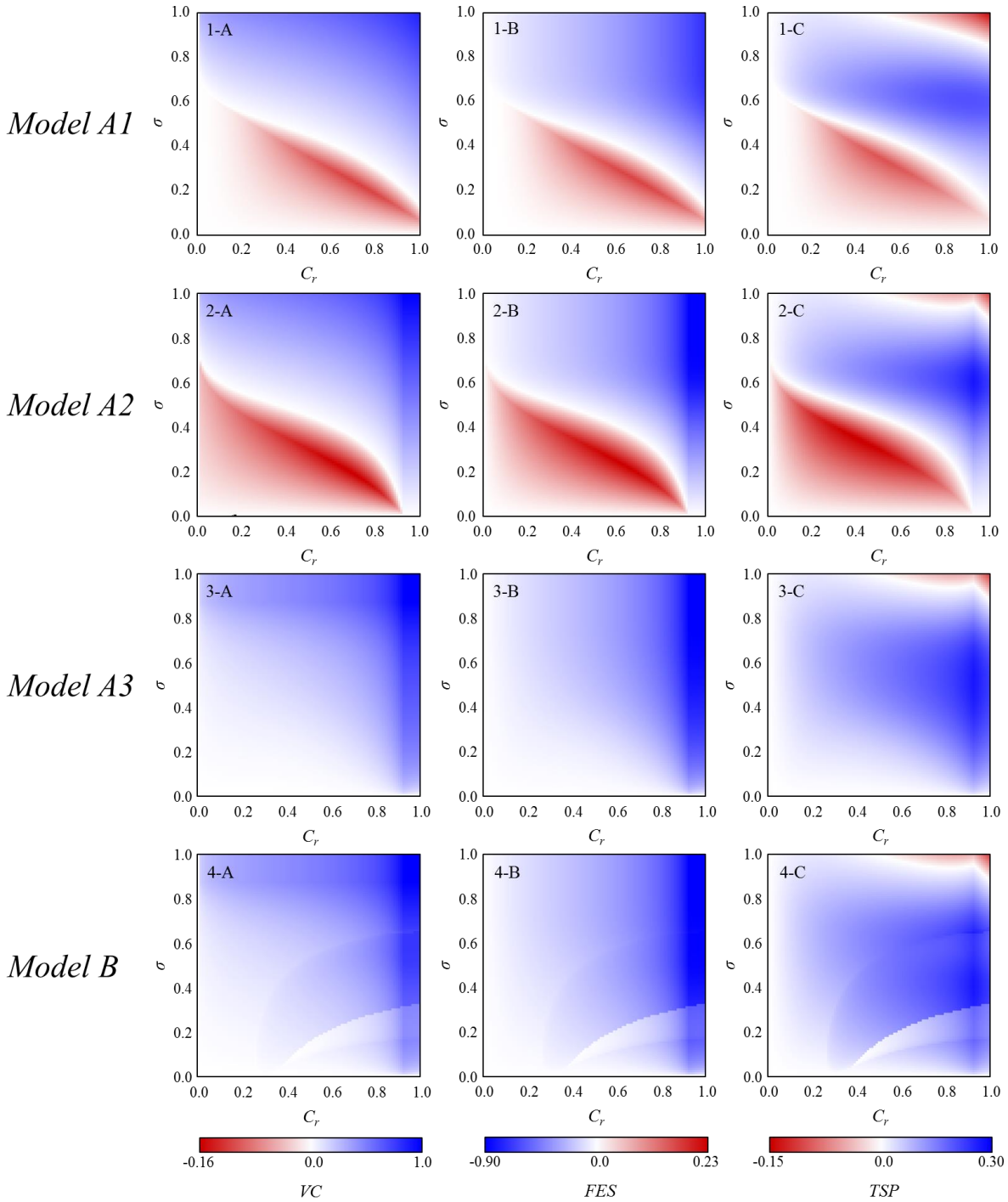

Figure 3.13. Mean-field approximation with the SB-RA rule and a perfect vaccine (e=1). Color indicates the difference between the case in which vaccination is subsidized (σ>0) and the default case without subsidy (σ=0). Blue indicates better, white neutral, and red worse performance than the default. Panel rows display the performance of Model A-1 (top row), Model A-2 (second row), Model A-3 (third row), and Model B (bottom row). Panel columns display VC (left column), FES (middle column), and TSP (right column).

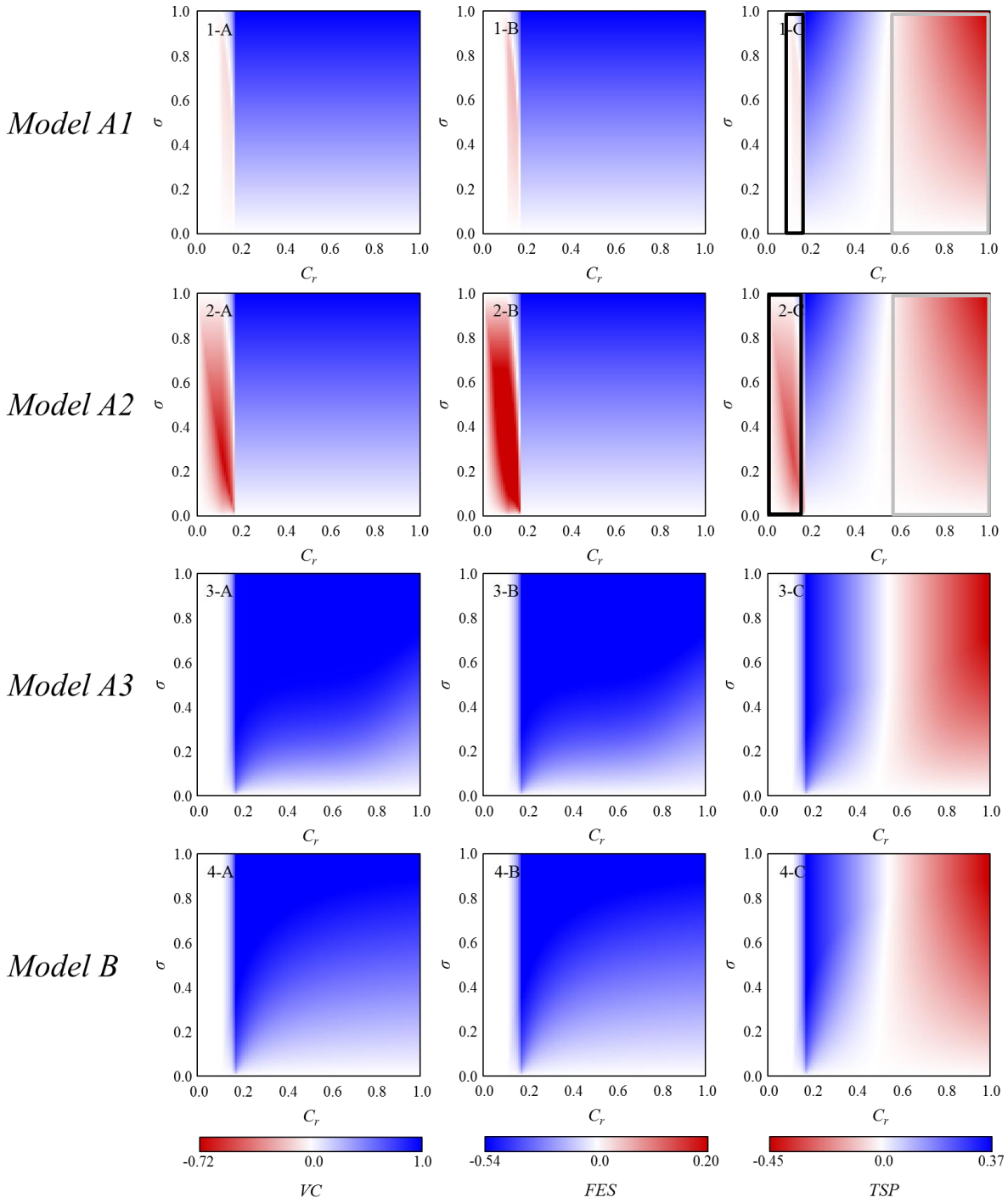

Figure 3.14. Mean-field approximation with the IB-RA rule and an imperfect vaccine (e<1). Color indicates the difference between the case in which vaccination is subsidized (σ>0) and the default case without subsidy (σ=0). Blue indicates better, white neutral, and red worse performance than the default. Panel rows display the performance of Model A-1 (top row), Model A-2 (second row), Model A-3 (third row), and Model B (bottom row). Panel columns display VC (left column), FES (middle column), and TSP (right column). Black (gray) rectangles emphasize the zone of a negative TSP in Models A-1 and A-2 when the relative vaccination cost is low (high).

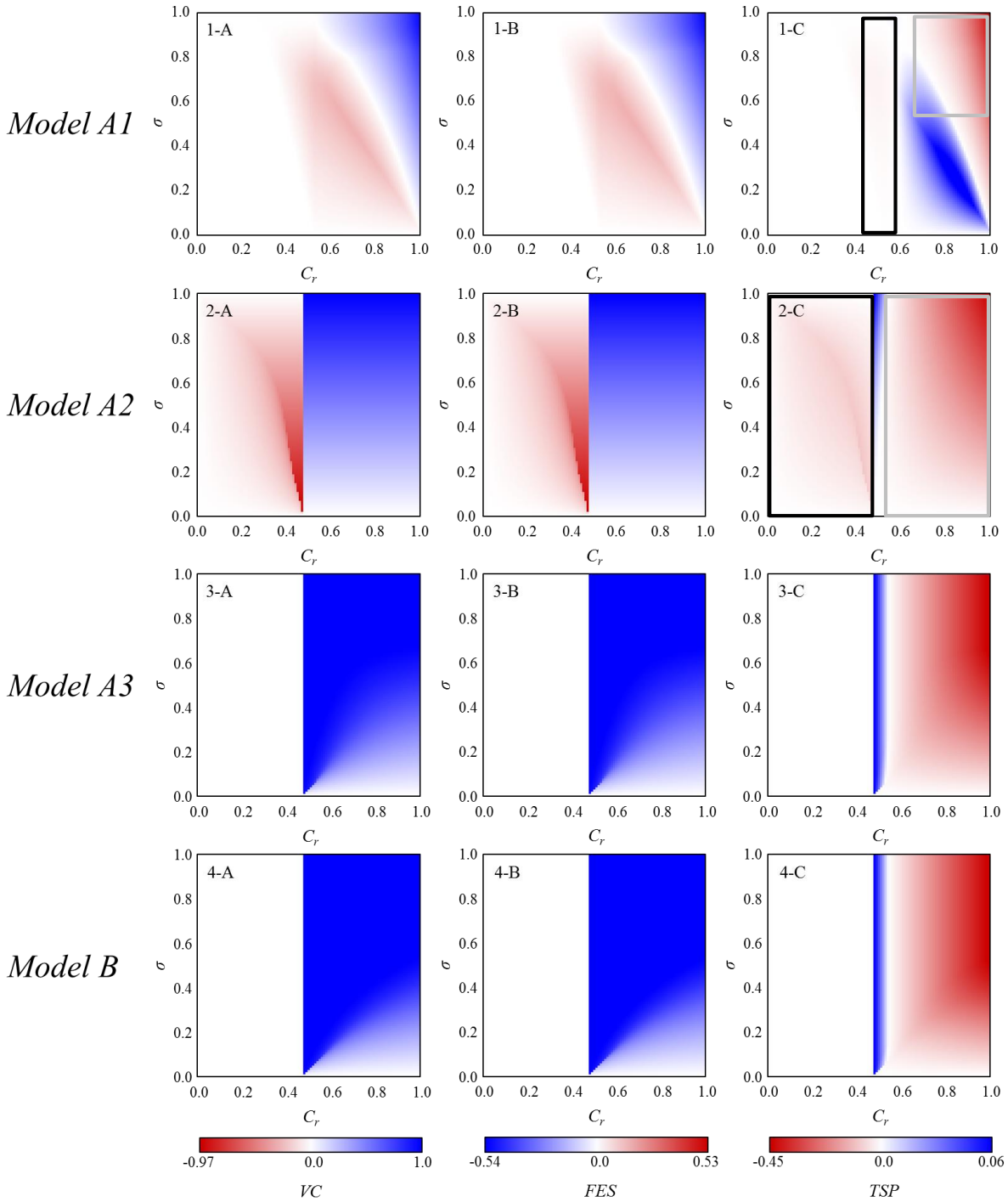

Figure 3.15. Mean-field approximation with the SB-RA rule and an imperfect vaccine (e<1). Color indicates the difference between the case in which vaccination is subsidized (σ>0) and the default case without subsidy (σ=0). Blue indicates better, white neutral, and red worse performance than the default. Panel rows display the performance of Model A-1 (top row), Model A-2 (second row), Model A-3 (third row), and Model B (bottom row). Panel columns display VC (left column), FES (middle column), and TSP (right column). Black (gray) rectangles emphasize the zone of a negative TSP in Models A-1 and A-2 when the relative vaccination cost is low (high).

3.5 Conclusions

To examine how societies could combat seasonal epidemics with vaccination-subsidizing policies, we devised a comprehensive 'vaccination game' with intertwined decision-making dynamics and epidemic dynamics. We based the former on evolutionary game theory and the latter on a typical SIR/V setup. In addition, we considered four subsidy variants; three free-ticket subsidies targeting different individuals (voluntary vaccinators, non-vaccinators, or both) and a discount subsidy aimed exclusively at voluntary vaccinators to partly offset their vaccination cost. We implemented these games as multi-agent simulations (MAS) and a mean-field approximation. The MAS approach allowed us to investigate how the underlying topologies of the social network affect the performance of subsidized vaccination. The mean-field approach helped us to independently confirm some of the key the results obtained using the MAS approach, and to better understand the effects of an imperfect vaccine. We evaluated the performance of different subsidies by tracking three quantities: vaccination coverage (VC), the final epidemic size (FES), and the total social payoff (TSP). The TSP in particular was an aggregate measure taking into account the vaccination cost, the cost of an epidemic, and the tax burden to subsidize vaccination.

Our results suggest that there are two situations in which subsidies act counterproductively. First, subsidizing non-vaccinators creates a negative incentive for voluntary vaccinators to abstain in hope of receiving a subsidy. If the subsidy has a relatively small reach due to a limited budget, then this negative incentive may cause more people to forgo vaccination than the subsidy can motivate to vaccinate. Second is the situation in which overspending causes that the marginal cost of increasing the VC becomes higher than the marginal cost of infections that this increased coverage prevents. Taken together, these two situations emphasize the need for carefully targeting and budgeting vaccination campaigns.

MAS simulations deepen our understanding of how the topology of the underlying social networks affects a subsidy's performance. Both random and heterogeneous connections increase the domain of the phase space in which the subsidy's performance is worse than in the default case of no-subsidy policy. The mean-field approximation, on the other hand, provides an additional insight into the effects of an imperfect vaccine. Here, the dependence of the subsidy's performance on its reach (i.e., budget size) almost entirely disappears, making the relative vaccination cost the key determinant of success. Subsidizing a cheap, but unreliable vaccine has an overall neutral effect at best because any gain from an increased coverage is usually nullified by the vaccine's unreliability. Subsidizing an expensive, but unreliable vaccine, in addition to overcoming the vaccine's unreliability, also has to overcome its high cost, which turns out to be too much in almost all circumstances. Imperfect vaccines, depending on how reliable they are, may leave a very narrow margin for improving the TSP by means of a vaccination-subsidizing policy.

When it comes to whom a subsidy should target, our results clearly indicate that the guiding

principle is ‘heaven helps those who help themselves’. By trying to motivate non-vaccinators to commit to vaccination, society actually creates the aforementioned negative incentive whereby someone who would normally get vaccinated at their own cost, now waits for the subsidy to offset that cost. Such a negative incentive is most simply avoided by distributing subsidies only to voluntary vaccinators. Once this decision is reached, it is less important whether the subsidy is implemented in the form of free tickets to a certain fraction of voluntary vaccinators or discount coupons to all voluntary vaccinators. There is only a minor difference in the performance of these two approaches, which arises due to a clearer benefit from receiving a free ticket (fully offsets the cost) than a discount coupon (partly offsets the cost).

References

1. Yamin D, Gavious A. 2013. Incentives' effect in influenza vaccination policy. *Management Science*, *59*(12), 2667-2686.
2. Zhang HF, Wu ZX, Xu XK, Small M, Wang L, Wang BH. 2013. Impacts of subsidy policies on vaccination decisions in contact networks. *Physical Review E*, *88*(1), 012813.
3. Zhang HF, Wu ZX, Tang M, Lai YC. 2014. Effects of behavioral response and vaccination policy on epidemic spreading-an approach based on evolutionary-game dynamics. *Scientific reports*, *4*, 5666.
4. Zhang HF, Shu PP, Wang Z, Tang M, Small M. 2017. Preferential imitation can invalidate targeted subsidy policies on seasonal-influenza diseases. *Applied Mathematics and Computation*, *294*, 332-342.
5. Tang GM, Cai CR, Wu ZX. 2017. Evolutionary vaccination dynamics with internal support mechanisms. Physica A: Statistical Mechanics and its Applications, 473, 135-143.
6. Li Q, Li M, Lv L, Guo C, Lu K. 2017. A new prediction model of infectious diseases with vaccination strategies based on evolutionary game theory. Chaos, Solitons & Fractals, 104, 51-60.
7. Ding H, Xu JH, Wang Z, Ren YZ, Cui GH. 2018. Subsidy strategy based on history information can stimulate voluntary vaccination behaviors on seasonal diseases. Physica A: Statistical Mechanics and its Applications, 503, 390-399.
8. Fukuda E, Tanimoto J. 2016. Effects of stubborn decision-makers on vaccination and disease propagation in social networks. International Journal of Automation and Logistics, 2(1-2), 78-92.
9. Matsuzawa R, Tanimoto J, Fukuda E. 2016. Spatial prisoner's dilemma games with zealous cooperators. Physical Review E, 94(2), 022114.
10. Fu F, Rosenbloom DI, Wang L, Nowak MA. 2011. Imitation dynamics of vaccination behaviour on social networks. Proceedings of the Royal Society B: Biological Sciences, 278(1702), 42-49.
11. Fukuda E, Kokubo S, Tanimoto J, Wang Z, Hagishima A, Ikegaya N. 2014. Risk assessment for infectious disease and its impact on voluntary vaccination behavior in social networks. Chaos, Solitons & Fractals, 68, 1-9.

12. Cardillo A, Reyes-Suárez C, Naranjo F, Gómez-Gardenes J. 2013. Evolutionary vaccination dilemma in complex networks. Physical Review E, 88(3), 032803.
13. Tanimoto J. 2015. Fundamentals of evolutionary game theory and its applications. Springer Japan.
14. Wang Z, Kokubo S, Jusup M, Tanimoto J. 2015. Universal scaling for the dilemma strength in evolutionary games. Physics of life reviews, 14, 1-30.
15. Barabási AL, Albert R. 1999. Emergence of scaling in random networks. science, 286(5439), 509-512.
16. Gillespie DT. 1977. Exact stochastic simulation of coupled chemical reactions. The journal of physical chemistry, 81(25), 2340-2361.
17. Masuda N, Holme P. 2017. Temporal network epidemiology. Berlin, Germany: Springer.
18. Osterholm MT, Kelley NS, Sommer A, Belongia EA. 2012. Efficacy and effectiveness of influenza vaccines: a systematic review and meta-analysis. The Lancet infectious diseases, 12(1), 36-44.

[Previously published documents related to this chapter]

Kuga K, Tanimoto J, Jusup M. 2019. To vaccinate or not to vaccinate: A comprehensive study of vaccination-subsidizing policies with multi-agent simulations and mean-field modeling. Journal of theoretical biology, 469, 107-126.

Chapter 4: Fundamental analyses of heat and mass transfer in animal upper airways

4.1 Introduction and literature review

The respiratory system is one of the most essential processes in the human body. The basic functions of the respiratory system are gas exchange (supply oxygen from ambient air and remove carbon dioxide from the blood) and air conditioning via the exchange of heat and moisture through the mucous surfaces of the airway. Furthermore, the respiratory system is also the primary interface between the human body and indoor environment, in which various contaminants exist. Hence, indoor air quality has a crucial impact on human health. To understand the transfer of heat, moisture, and contaminants inside the respiratory tract and to predict toxic inhalation risks, a number of researchers conducted in vivo studies involving human volunteers and/or mammal surrogate models, such as rats and monkey [1–4]. Although in inhalation toxicological studies and the development of respiratory drug delivery systems (DDS), animal and biological testing will always be needed, in vivo studies are restricted in terms of animal protection and ethical problems. From this viewpoint, computer simulation models (i.e., in silico respiratory tract models) have great potential to contribute to the essential understanding of heat and contaminant transfer phenomena in the respiratory tract, in place of in vivo and in vitro studies. From this background, various types of numerical respiratory tract models have been developed.

The human respiratory tract consists of the nasal cavity, oral cavity, pharynx, larynx, trachea, bronchiole, and alveoli, and can be classified into three domains: (i) the upper airway from the nasal cavity and oral cavity to the trachea, (ii) the lower airway from the trachea to the terminal bronchioles, and (iii) the alveolar region. Generally, numerical respiratory tract models do not reproduce the geometry of the whole airway from the nasal or oral cavity to the alveolar region because of limitations in computer resources. Researchers select the reproduced airway region depending on the purpose of their simulation.

4.1.1. Upper airway models (nasal and oral airway)

The nose and mouth openings are the primary entrance and exit of various gases and particle matter between the human airway and the indoor environment by respiration. Thus, the study of airflow and contaminant transport and exposure in the upper airway is considerably important compared to that of the lower airway and alveolar region. This pathway of airflow is classified as the nasal airway and oral airway in terms of breathing methods (nasal breathing and oral breathing). The nasal cavity is composed of two narrow passages that are separated by the nasal septum. Each nasal passage is a complicated geometry divided by three curved fin-like airway protrusions known as the superior, middle,

and inferior meatus. This complexity of the nasal cavity promotes the transfer of heat and moisture, and the nasal cavity plays a role in the conditioning of inhaled air. Most researchers have developed realistic nasal cavity models by using high-resolution computed tomography (CT) and magnetic resonance imaging (MRI) [5–9]. On the other hand, the geometry of the oral cavity, excluding the teeth, is relatively simple compared to that of the nasal cavity. The geometry of the oral cavity is usually modeled by excluding the teeth. Xi and Longest [10] used surface geometries for the oral cavity based on measurements of a dental impression with an approximate half-mouth opening. For this cast, Cheng et al. [11] provided a complete mathematical description of the geometric parameters along the axial direction in terms of cross-sectional shapes, areas, perimeters and hydraulic diameters. Furthermore, the flow pattern in the airway is also affected by laryngeal geometry associated with a pipe with sudden contraction. Thus, the laryngeal geometries were also extracted by CT or MRI [12].

From viewpoint of the interaction between the human body (nasal cavity and oral cavity) and indoor environment, the streamline from the indoors to the nasal and oral cavities, namely, the flow profile in the openings of the nose and mouth, strongly affect the flow pattern in the airway. To account for this, Corley et al. [13,14] developed airway models attached to a cylinder that reproduced the space of the indoor environment. Tian et al. [14] also reproduced the external space in front of the human face.

The geometry of the upper airway is diverse because of individual differences. Therefore, it is difficult to develop a numerical respiratory tract model that is average in terms of air permeability and contaminant deposition. We must accumulate studies on the respiratory tract using various airway models and report the properties of each model.

4.1.2. Lower airway models (bronchial tree)

The small bronchus flows are low-Reynolds-number flows, with values that are usually less than 1000 [16]. However, the existence of secondary currents due to vortices makes these flows quite complicated. These vortices are generated as an effect of the complex bronchial tube geometry. Some of the properties of the bronchial tube geometry are multiple bifurcations, asymmetry, and non-planarity. The complexity of the geometry of the bronchial tree is attributed to the bifurcations that produce multiple generations with asymmetric and non-planar branching. A bifurcation is defined as the location where two daughter tubes diverge from a parent tube. Typically, there are a total of 23 generations of airways in the human bronchopulmonary tree, which consists of 222 distinct tubes [17].

In the early stages of development of the bronchial tube geometry, mathematical and theoretical models have been morphologically proposed based on the anatomical measurement of the bronchial tube. Weibel [18] first introduced a symmetric model of morphological descriptions of the human bronchial tubes. After that, Horsfield et al. [19,20] proposed a more realistic model that represents lung asymmetry from the measurement of the lung cast of a young male. Moreover, there have been various analytical and mathematical models proposed for defining bronchial tube geometry

[21–23]. Calay et al. [24] studied the flow patterns in a single first-generation bifurcation to the trachea and in a multiple-bifurcation model, with its three generations based on the anatomical data provided by Horsfield [20]. Lee and Lee [25] generated a three-dimensional network model with four generations, which conformed closely to the Weibel model [18], in order to study aerosol dispersion.

On the other hand, realistic detailed lung airway models have recently been developed by using CT or MRI techniques [26–28]. Tawhai et al. [26,27] developed a three-dimensional tree growing algorithm specific to a given host geometry derived from MRI. Schmidt et al. [28] developed a 17-generation anatomical model that was extracted from CT data. Gemci et al. [29] and Islam et al. [30,31] analyzed the flow pattern and aerosol deposition in the lungs using the 17-generation anatomical model [29].

4.1.3. Alveolar airway models

The mechanisms of airflow and contaminant exposure in the alveolar (pulmonary) region are different from those of the upper airways in various aspects. The upper airways do not expand and contract in response to inhalation and exhalation, and hence are considered fixed geometry. On the other hand, the lower airway, especially the alveolar region, changes shape during respiration. Thus, the boundary condition of the alveolar region is treated as a moving wall in transient flow conditions. Furthermore, because of the continuous expansion and contraction of the alveolar airway, it is difficult to develop an accurate geometric model for the alveolar region using current technology such as CT and MRI. The size and air velocity in the alveolar region are considerably small compared to those of the upper airway. Hence, laminar flow is dominant in the flow field of the alveolar airway and the residence (exposure) time is greater than that in the upper airway.

Various geometric models have been designed for alveolar studies. Kitaoka et al. [32] developed a four-dimensional alveolar model, corresponding to elastin fibers at alveolar mouths and junctions of alveolar septa to simulate alveolar deformation. Kumar et al. [33] considered honeycomb shapes for acinar geometries to investigate particle transport in the acinar region. Other studies also considered a polyhedral shape for alveoli models [34–36]. The other types of alveolar airway models were assumed as a cylinder surrounded by spherical caps [37–39].

In recent years, high-resolution micro-CT imaging (e.g., synchrotron-based imaging) of the acinar region has advanced considerably, and the number of airflow studies on the acinar region using imaging-based geometry has been increasing. Sera et al. [40,41] used an alveolar airway (acinar) model obtained from synchrotron micro-CT in a mouse and reported nanoparticle deposition in the alveolar region. Henry et al. [42] used image-based alveoli geometry obtained using synchrotron radiation-based X-ray tomographic microscopy and reported the 3D re-circulatory flow in the alveolar region. Sznitman et al. [43] also used synchrotron radiation-based X-ray tomographic microscopy images of the pulmonary acinus of a mouse to reconstruct 3D alveolar airspaces and conduct CFD simulations

mimicking rhythmic breathing motion.

4.1.4. Animal surrogate models

For deep understanding of heat and mass transfer and air-conditioning in the respiratory system of animals, development of drug delivery system (DDS), and reducing the sacrifice of laboratory animals, the numerical animal airway models need to be developed. Various types of numerical animal airway models have been developed based on the geometrical data extracted by CT or MRI for Rat [13,14,44-46], dog [47-50], monkey [13,51], rabbit [52-55].

4.1.5. Objectives

In this study, we developed computer models of the upper respiratory airway of a rat, a dog, a monkey and two humans encompassing the nose/mouth to the pharynx/larynx. Here, these computer models are referred to as virtual airways. As a numerical simulation for predicting the airflow characteristics, CFD has been used to provide an understanding of the air flow patterns as well as heat transfer. A steady inhalation flow through the nose was assumed, using a low-Reynolds-number (Re) k-ε model. In this study, five airflow conditions in each virtual airway model, i.e., the transitions from a laminar to a turbulent flow regime, were considered. Further, the convective heat transfer phenomena in the virtual airway models were analyzed by estimating the convective heat transfer coefficients (h_c) and segment under various breathing airflow conditions. The respiratory h_c is a phenomenological constant relating the heat flux to the temperature difference between the free airstream and airway walls. Considering the similarities between heat and mass transfer, h_c is a good indicator of mass transfer from the mucosal tissue surface to the lumen or vice versa in the respiratory tract. The calculated h_c values will contribute to the understanding of heat and mass transfer phenomenon in respiratory systems and to quantify the differences in heat and mass transfer efficiency between species.

4.2 Materials and Methods

4.2.1. Development of in silico animal airway models

Rat: A geometrical respiratory data from the nose through to the larynx of a Sprague-Dawley rat (400 g weight) was extracted by a micro-CT scan at 140 μm resolution. The model included both left and right nasal cavities, and the nasopharyngeal duct. The computational model was meshed using ICEM-CFD (ANSYS Inc.) with unstructured tetrahedral elements. To provide accurate predictions in the boundary layer, prism layers were applied in the vicinity of wall surfaces into the viscous sublayer. To accurately reproduce the flow patterns at and around the nostril inlets, the external nares, facial features, and the surrounding environmental space near the face were included [56-60]. The number of independent mesh elements for this rat model was 5.34 million [61]. Details of the rat's geometric information are given in Table 4.1 and Figure 4.1.

Table 4.1 Details of rat virtual airway

Total inner surface area	3.62×10^{-6} [m^2]
Total length	55.10 [mm]
Maximum height	18.30 [mm]
Maximum width	16.00 [mm]
Area of naris (right)/ Equivalent diameter	3.72×10^{-7} [m^2]/ 6.89×10^{-4} [m]
Area of naris (left)/ Equivalent diameter	3.08×10^{-7} [m^2]/ 6.27×10^{-4} [m]
Total meshes	5.34 million (unstructured)

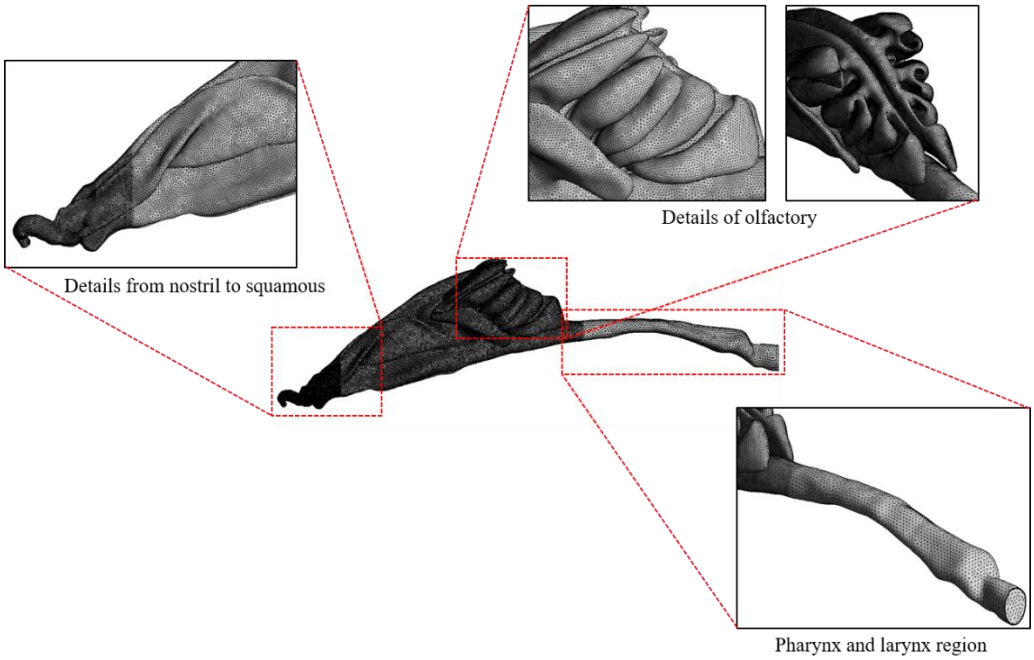

Figure 2.1 Computational geometry and mesh of the rat virtual airway

Dog: A geometrical respiratory data from the nose through to the larynx of an 8-month-old male beagle (11 kg weight) was extracted by a CT scan. CT examinations were carried out using an eight-detector-row computed tomography system (ECLOS 8; Hitachi Medical Corporation). Scans were obtained with a collimation of 8 × 1.25 mm, a table pitch of 0.875, a tube voltage of 120 kV and a tube current of 350 mA [62]. The computational model of the dog was discretized and meshed using ICEM-CFD (ANSYS Inc.) with unstructured tetrahedral elements. The number of independent mesh elements for this dog model was 6.49 million. Details of the dog's geometric information are shown in Table 4.2 and Figure 4.2.

Table 4.2 Details of dog virtual airway

Total inner surface area	1.29×10^{-4} [m^2]
Total length	1.45×10^{-1} [m]
Maximum height	7.16×10^{-2} [m]
Maximum width	4.97×10^{-2} [m]
Area of naris (right)/ Equivalent diameter	6.00×10^{-5} [m^2]/ 8.74×10^{-3} [m]
Area of naris (left)/ Equivalent diameter	5.28×10^{-5} [m^2]/ 8.20×10^{-3} [m]
Total meshes	6.49 million (unstructured)

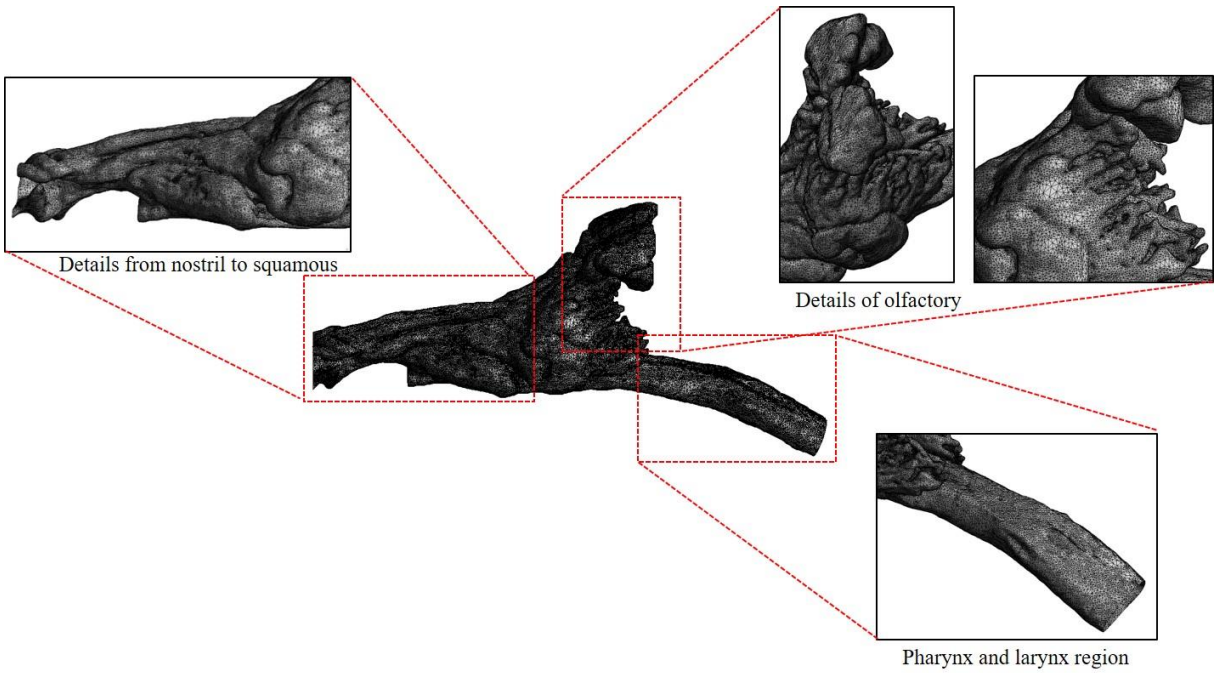

Figure 4.2 Computational geometry and mesh of the dog virtual airway

Monkey: A geometrical respiratory data from the nose/mouth through to the larynx of a 6-month-old male monkey (*Macaca fascicularis*) (1.2 kg weight) was extracted by a micro-CT (computer tomography) scan at 200 μm resolution. The computational model was discretized and meshed using ICEM-CFD (ANSYS Inc.) with unstructured tetrahedral elements. The number of independent mesh elements for this monkey model was 7.03 million. Details of the monkey's geometry are given in Table 4.3 and Figure 4.3.

Table 4.3 Details of monkey virtual airway

Total inner surface area	2.81×10^{-5} [m^2]
Total length	1.05×10^{-1} [m]
Maximum height	4.32×10^{-2} [m]
Maximum width	2.8110^{-2} [m]
Area of naris (right)/ Equivalent diameter	5.48×10^{-6} [m^2]/ 2.64×10^{-3} [m]
Area of naris (left)/ Equivalent diameter	5.46×10^{-6} [m^2]/ 2.64×10^{-3} [m]
Total meshes	7.03 million (unstructured)

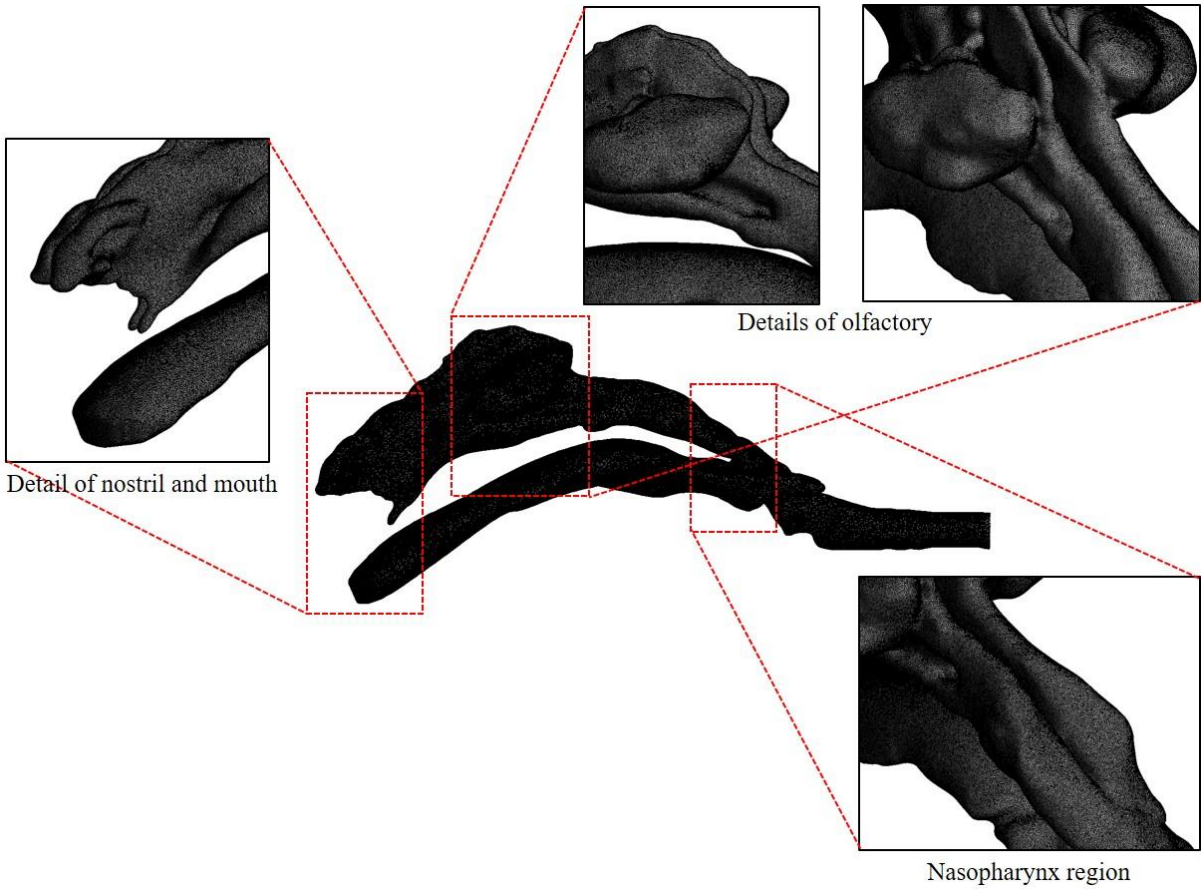

Figure 4.3 Computational geometry and mesh of the monkey virtual airway

Human: Two human respiratory tract models (Model A and Model B) were created. Original geometrical respiratory tract data were obtained using a Toshiba 64 multi-detector row computed tomography (MDCT) scanner. The subjects were Asian and European male who were non-smoker and have a body mass index (BMI) of approximately 22. The CT scans produced 785 slices of the respiratory tract. The original set of CT images was converted into a file format compatible with Mimics® (Materialise NV). Generation of a surface model from the 2D contour data began with the translation of the segmented, modified, and smoothed contour points into a data series that was loaded into ICEM-

CFD (ANSYS Inc.) and TGrid, which were used to modify the surface mesh and then create a volume mesh of the model, respectively. Surface geometries of the respiratory tracts were also exported in STL (stereo lithography) format. Table 4.4 shows the detailed geometric information for the two human upper airway models. Figure 4.4 shows views of the human airway models after going through this process. These respiratory tract models are composed of an upper airway, including the nasal and oral cavities, the pharynx, and the larynx [63,64].

The present human airway model (Model A) has been validated with experimental data sets from laminar to turbulent flows [63,64]. In a previously reported study, a realistic replica model made from transparent acrylic material was created and a particle image velocimetry (PIV) technique was applied to measure flow patterns in the human upper airway model (Model A). In this PIV experiment, a three-dimensional respiratory tract model was created with a 3D printer by using identical geometry data of CFD model and flow patterns in respiratory tract were precisely measured as a function of flow rate (from 7.5L/min to 30L/min). Further, CFD simulations correspond with the experimental scenarios were also conducted with the four different turbulent flow models (two low Reynolds number type k-ε models (Abe-Kondoh-Nagano model and Launder-Sharma model), an RNG type k-ε model, and an SST k-ω model). Finally, CFD simulation results with the low-Reynolds-number k–ε model reasonably agreed with the results measured by PIV [63].

Table 4.4 Details of human virtual airways

Total inner surface area	2.19×10^{-4} [m^2] for Model A, 2.14×10^{-4} [m^2] for Model B
Total length	2.39×10^{-1} [m] for Model A, 1.95×10^{-1} [m^2] for Model B
Maximum height	1.46×10^{-1} [m] for Model A, 1.34×10^{-1} [m] for Model B
Maximum width	6.21×10^{-2} [m] for Model A, 6.21×10^{-2} [m] for Model B
Area of naris (right)/ Equivalent diameter	8.00×10^{-5} [m2]/1.00×10^{-2} [m] for Model A 8.00×10^{-5} [m2]/1.00×10^{-2} [m] for Model B
Area of naris (left)/ Equivalent diameter	8.00×10^{-5} [m2]/1.00×10^{-2} [m] for Model A 8.00×10^{-5} [m2]/1.00×10^{-2} [m] for Model B
Total meshes	7.25 million (unstructured) for Model A 3.82 million (unstructured) for Model B

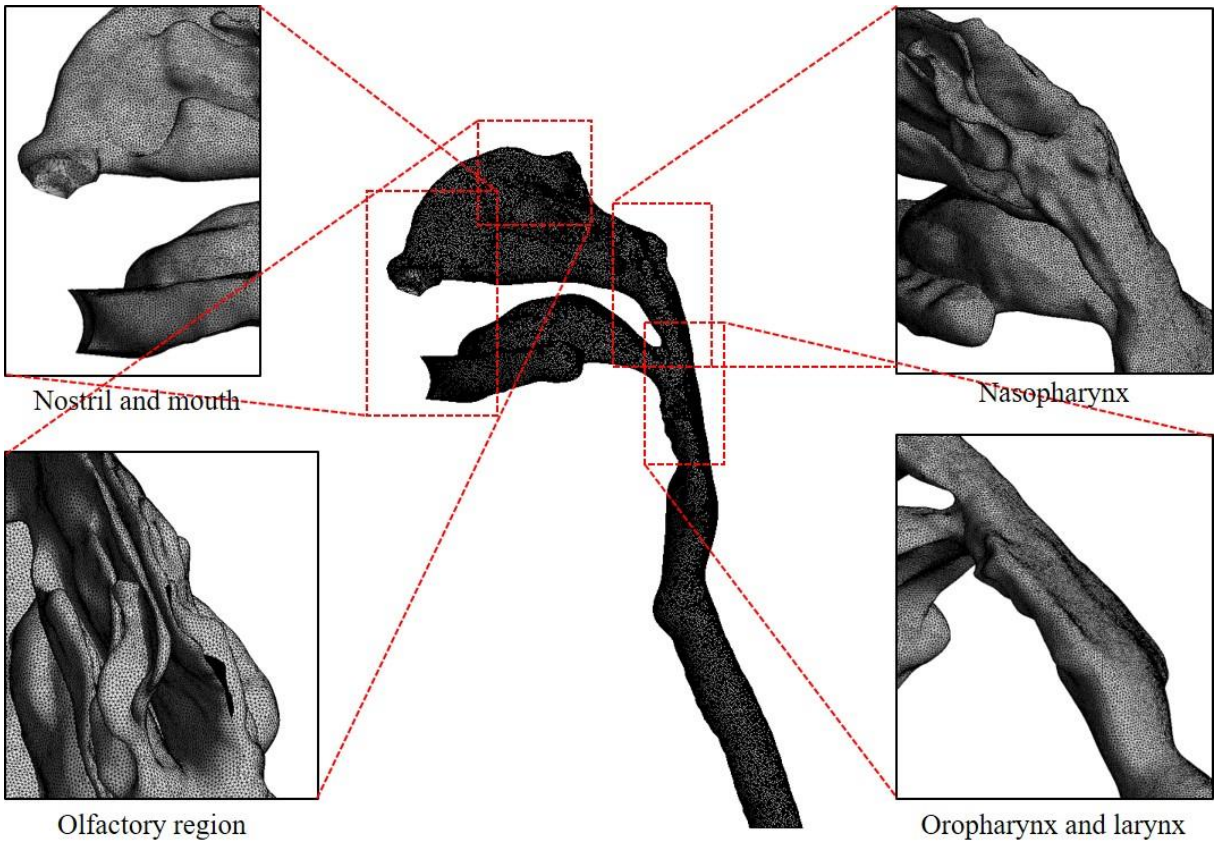

(1) Model A – Asian male

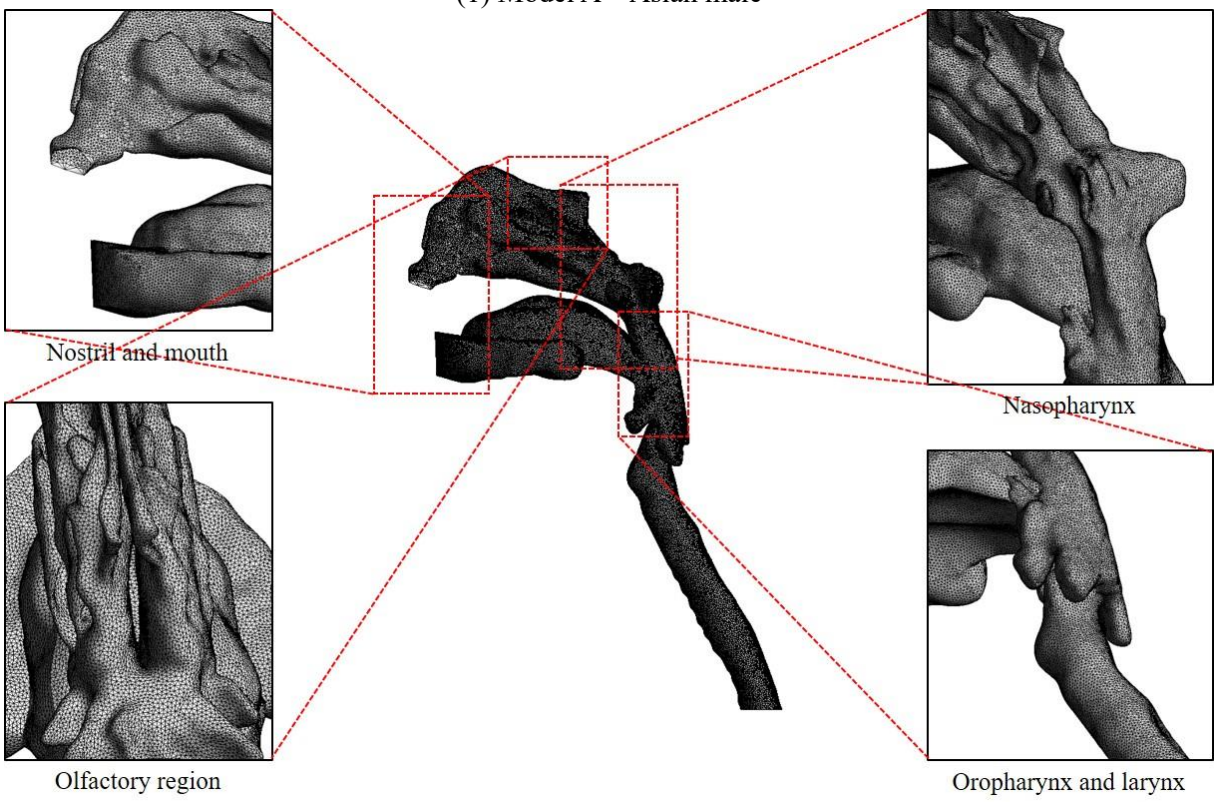

(2) Model B – European male

Figure 4.4 Computational geometry and mesh of the human virtual airway

4.2.2. Airflow simulations

The inner geometry of the animal and human upper airways were precisely reproduced by a CFD mesh. To resolve the flow profile in the viscous sub-layer of airways, a fine mesh (approximately 0.1 mm or less for human models) was used as the first layer of mesh on the inner wall surface. The number of cells was set to approximately 4–7 million or more for each upper airway model. For all cases, the wall unit y^+ was ≤1 in all areas, where $y^+ = u * y_1/\nu$; y_1 is the distance normal to the wall surface, ν is the kinematic viscosity, and $u^* = \sqrt{\tau_w/\rho}$ is the friction velocity (ρ is the air density and τ_w is the wall shear stress). In the CFD simulation, a grid independence check was performed and a minimum mesh size in the vicinity of wall surface, skewness, and size ratio of adjoining meshes were created.

The entire flow fields in the upper airways were analyzed using a low-Reynolds-number k–ε model (Abe–Kondoh–Nagano model) [65]. Generally, the low-Reynolds-number k–ε model was designed to account for damping and echo effects in the near-wall region. It is also applied to quasi-laminarized flow fields existing within stable stratifications. The model implements damping and model functions, and performs low-Reynolds-number corrections for the production and dissipation terms of the eddy viscosity μ_t and ε equations. The model reproduces turbulence phenomena around walls that results from trying to solve adequately refined mesh partitions under no-slip conditions in the region around the wall. The model (Abe-Kondoh-Nagano model) has been adopted for the various types of flow field analysis (from laminar to turbulent) and has confirmed the good prediction accuracy for flow field analysis intended for enclosed spaces [66-69].

A steady and constant breathing airflow rate was used for the breathing condition as a function of metabolic rate and was set at the end of trachea outlet for each model. The turbulent kinetic energy at the inlet, i.e., at the nostril, was specified with a 10% turbulence intensity. The SIMPLE algorithm was used for the pressure-velocity coupling, and a second-order upwind difference scheme was used for the convection terms and a central difference scheme was used for the other terms. The simulation was conducted under isothermal and non-isothermal conditions. A summary of the numerical conditions are given in Table 4.5.

4.2.3. Heat transfer simulations

A constant inlet air temperature of 293K (20°C) was used for the inhaled ambient air, and the inner walls, which are covered by a layer of mucus, were assumed a constant temperature; 311 K (38°C) for the rat, dog and monkey and 309.8 K (36.8°C) for the human model. The respiratory convective heat transfer coefficient (h_c) relates the heat flux to the temperature difference between the free airstream and body surface or airway walls (in this research). The widely accepted expression for the h_c is as follows:

$$h_c = \frac{Q_c}{(T_w - T_{air})} \tag{4-1}$$

Here, the heat flux unit for Q_c is W/m^2, and T_w and T_{air} are the constant wall and inhaled air

temperatures in Kelvin. The Nusselt (*Nu)* number is a commonly used dimensionless parameter that is defined as the ratio of convection heat transfer to conduction heat transfer for a given reference length. The *Nu* number can be expressed as

$$Nu = \frac{h_c D_T}{\lambda} \tag{4-2}$$

where λ is the thermal conductivity of the air (W/m-K), and D_T is the representative diameter (m); the diameters in the trachea were used to calculate the *Nu* number for upper airway model. The *Nu* number is often used to correlate experimental data with the convective heat transfer.

Details of numerical and boundary conditions are summarized in Table 4.5.

Table 4.5 Numerical and boundary conditions of CFD

	Rat	Dog	Monkey	Human A	Human B
Turbulence Model	Low Reynolds Number Type k-ε model(Abe- Kondoh- Nagano Model, 3D Cal.)				
Mesh	5.34M mesh (Unstructured, Tetra)	6.49M mesh (Unstructured, Tetra)	7.03M mesh (Unstructured, Tetra)	7.25M mesh (Unstructured, Tetra)	3.81M mesh (Unstructured, Tetra)
Outflow boundary (Trachea opening)	Case 1: Q= 0.11L/min Case 2: (basic case) Q= 0.275 L/min Case 3: Q= 0.55 L/min Case 4: Q= 1.1 L/min	Case 1: Q= 1.75L/min Case 2: (basic case) Q= 3.5 L/min Case 3: Q= 7.0 L/min Case 4: Q= 10.5 L/min	Case 1: Q= 1.0 L/min Case 2: (basic case) Q= 2.0 L/min Case 3: Q= 4.0 L/min Case 4: Q= 6.0 L/min	Case 1: Q= 3.75 L/min Case 2: (basic case) Q= 7.5 L/min Case 3: Q= 15 L/min Case 4: Q= 30 L/min	Case 1: Q= 3.75 L/min Case 2: (basic case) Q= 7.5 L/min Case 3: Q= 15 L/min Case 4: Q= 30L/min
	TI=10 % $k_{out}=3/2\,(U_{in}\times 0.1)^2$ $\varepsilon_{out}=C_\mu^{3/4} k_{out}^{3/2} l_{out}$				
Inflow boundary	Nasal opening ; U_{in}=Free slip, k_{in}=Free slip, ε_{in}=Free slip, Inflow temperature:293 K				
Wall treatment	Temperature : 311 K Velocity: no slip	Temperature : 311 K Velocity: no slip	Temperature : 310.8 K Velocity: no slip	Temperature : 309.8 K Velocity: no slip	Temperature : 309.8 K Velocity: no slip

4.3 Results

Results from our numerical simulations for different airway geometries and inspiratory flow rates are given below. Scalar velocity and temperature distributions at representative sections in the nasal cavity are shown in Figure 4.5. In these analyses, exhaust flow rates (from within the virtual airway) were set at the trachea outlet based on respiratory flow rate. Non-uniform and complicated air flow patterns in nasal cavities were confirmed in all virtual airway models. Scalar air velocities were normalized with representative air velocities at the outlet (at the trachea). Because of the asymmetries of left and right nasal cavities, different air flow rates and varying air velocity distributions were found

in both nasal chambers. Figure 4.5 also shows the temperature distribution in terms of non-dimensional temperature profiles, i.e., $\bar{T} = (T - T_{wall}) / (T_{in} - T_{wall})$. Non-uniform temperature distributions were also observed in the nasal cavities. The inhaled air temperature rapidly heated to approximately the tissue surface temperature within the distance up to Slice B. This was due to the turbulent mixing in the narrow cross-section.

The local convective heat flux distributions for each virtual airway model are shown in Figures 4.6, 4.7, 4.8, 4.9 and 4.10. Relatively high local convective heat flux was observed in the nostril area in all cases. These phenomena were caused by the large temperature difference between respiratory air (indoor air) and the surface tissue. The average convective heat transfer coefficient (h_c) as a function of respiratory airflow rate (normalized by the flow rate velocity) are shown in Figure 4.11. With all analytical cases, a near linear relationship between airflow rate and h_c was confirmed. The h_c for the human model was estimated higher than those of the other animal models.

The relationship between the Nusselt (Nu) number and the product of the Reynolds (Re) and Prandtl (Pr) numbers for the upper airway is depicted in Figure 4.12 where the Reynolds (Re) and Prandtl (Pr) numbers are defined as follows;

$$\mathrm{Re} = \frac{uD_T}{\nu} \tag{4-3}$$

$$\mathrm{Pr} = \frac{\nu}{\alpha} \tag{4-4}$$

Here, u is the representative axial velocity, ν is the kinetic molecular viscosity and α is the thermal diffusivity. Based on the CFD simulation results, the correlations between Nusselt (Nu) number and the product of the Reynolds (Re) and Prandtl (Pr) numbers are summarized in Table 4.6. The type of correlation function was selected according to previously reported studies [70-72]. The trivial discrepancy between human models (A and B) may be due to the differences of airway geometries and this will represent individual differences. The heat transfer efficiency (order of h_c and correlation of Nu and $RePr$) in the upper airway of the dog seems to match those of the human models. On the other hand, the results for the rat and monkey showed clear differences compared with those of human models.

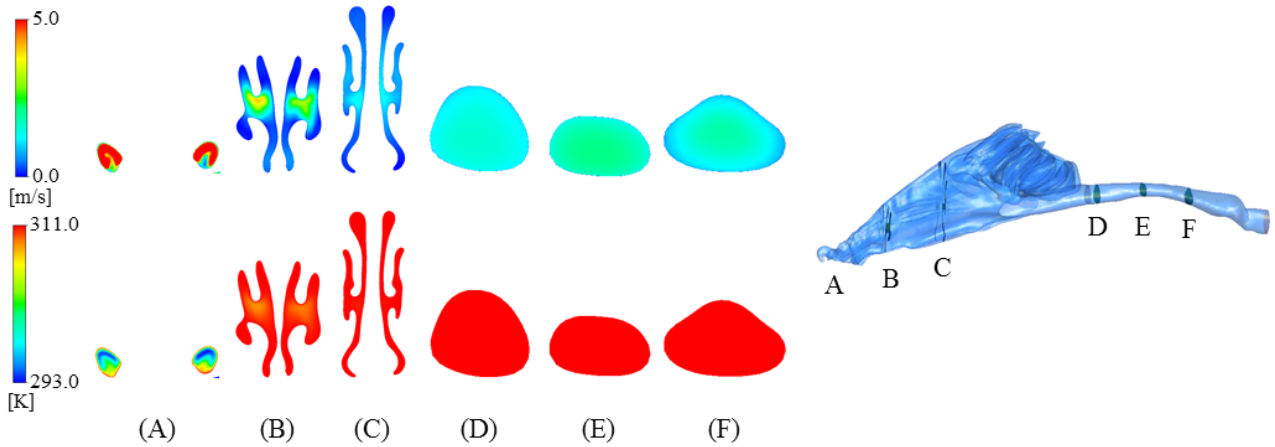

(1) Rat

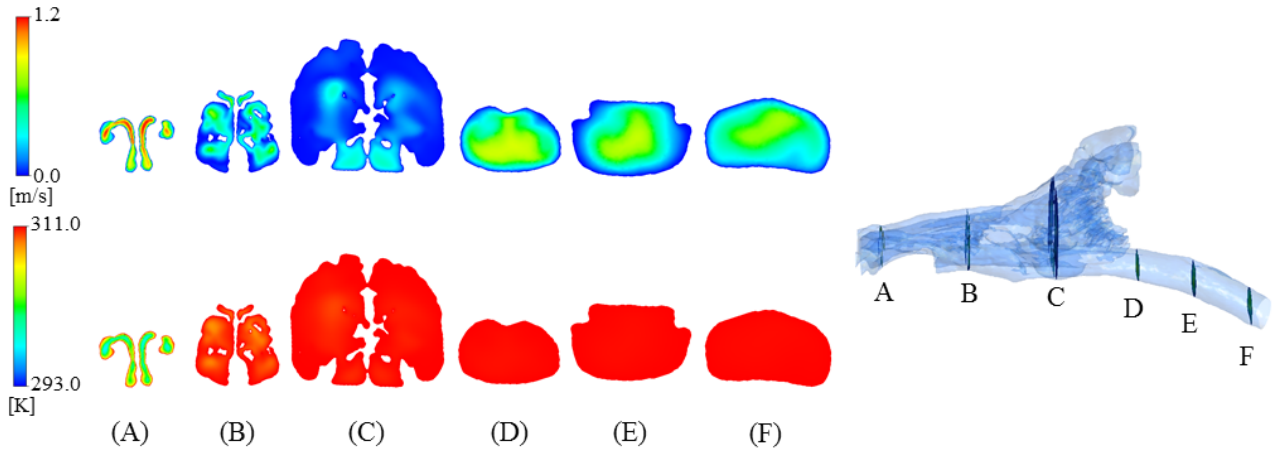

(2) Dog

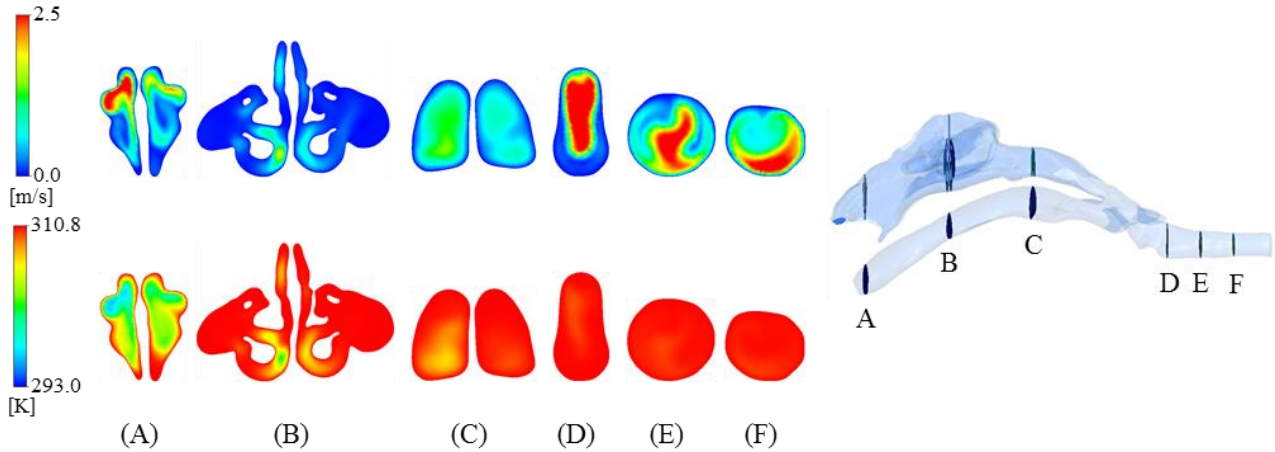

(3) Monkey

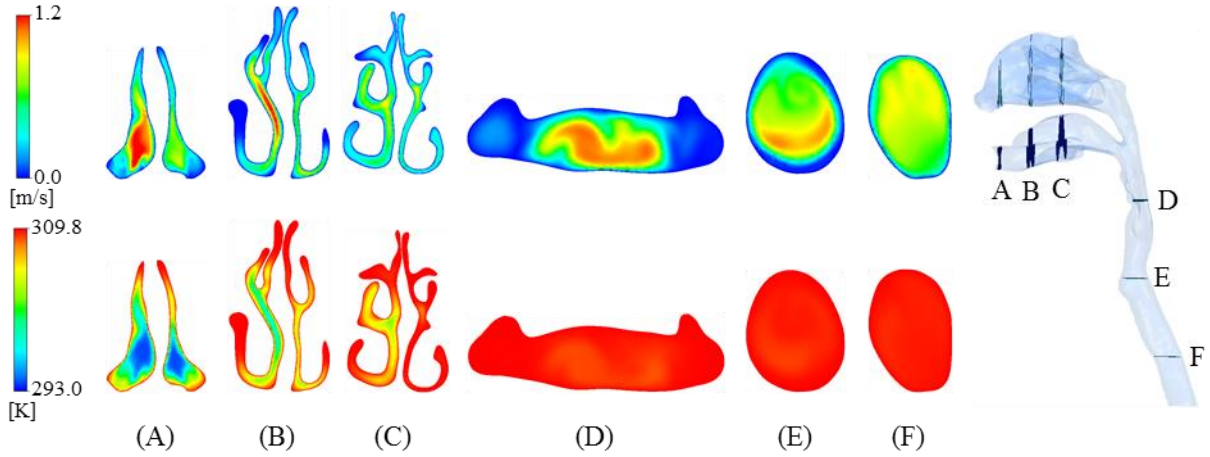

(4) Human-Model A, Asian Male

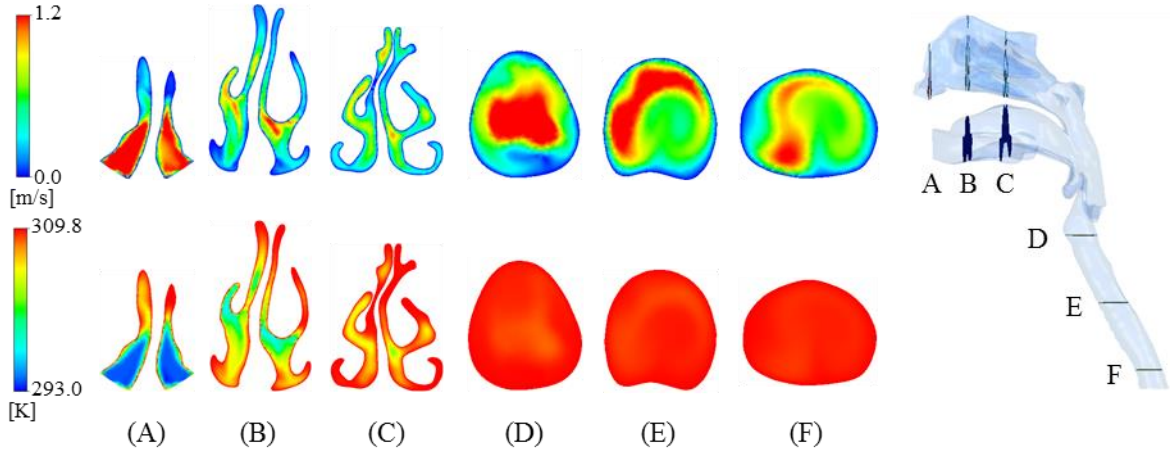

(5) Human-Model B, European Male

Figure 4.5 Scalar velocity (upper stand) and temperature distributions (lower stand) in nasal cavities for each virtual airway model (airflow rate in Case 2 conditions as basic metabilic rate)

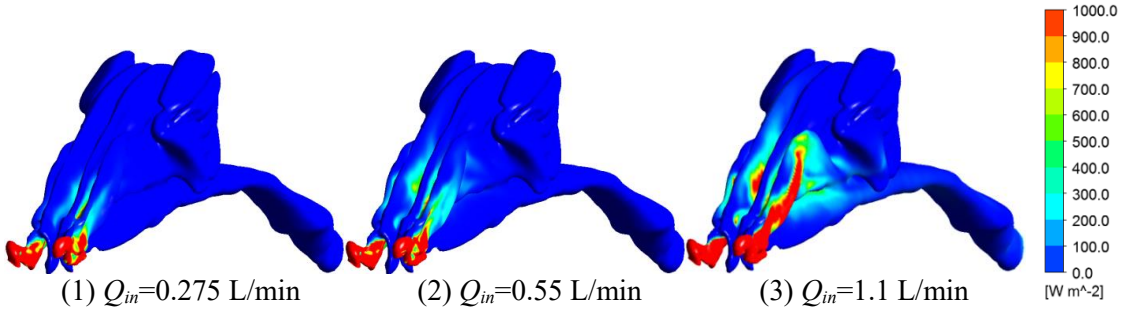

(1) Q_{in}=0.275 L/min (2) Q_{in}=0.55 L/min (3) Q_{in}=1.1 L/min

Figure 4.6 Convective heat transfer flux distributions on the upper airway surfaces of the rat virtual airway [W/m^2]

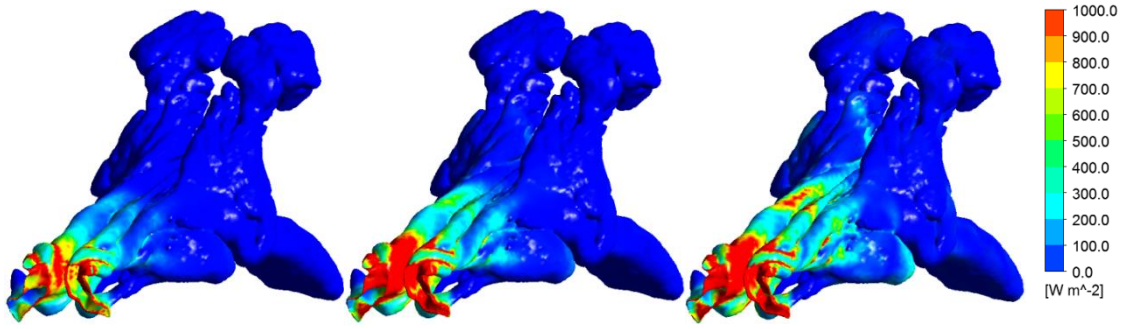

(1) Q_{in}=3.5 L/min (2) Q_{in}=7.0L/min (3) Q_{in}=10.5 L/min

Figure 4.7. Convective heat transfer flux distributions on the upper airway surfaces of the dog virtual airway [W/m^2]

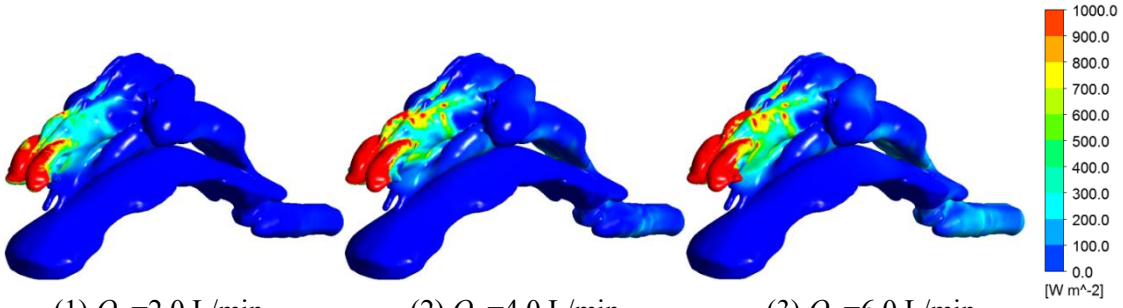

(1) Q_{in}=2.0 L/min (2) Q_{in}=4.0 L/min (3) Q_{in}=6.0 L/min

Figure 4.8. Convective heat transfer flux distributions on the upper airway surfaces of the monkey virtual airway [W/m^2]

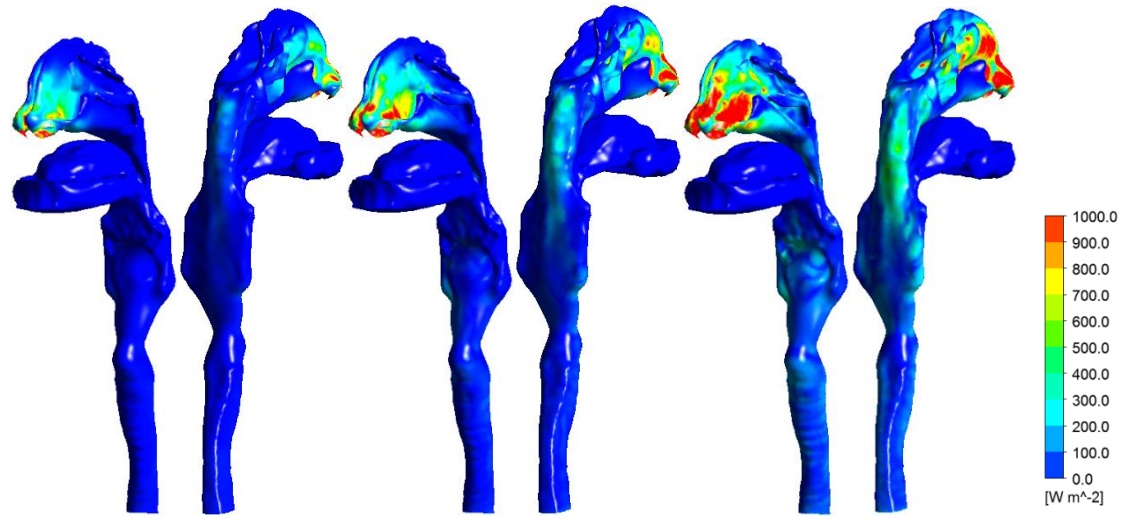

(1) Q_{in}=7.5 L/min (2) Q_{in}=15 L/min (3) Q_{in}=30 L/min

Figure 4.9. Convective heat transfer flux distributions on the upper airway surfaces of the human (Model A) virtual airway [W/m^2]

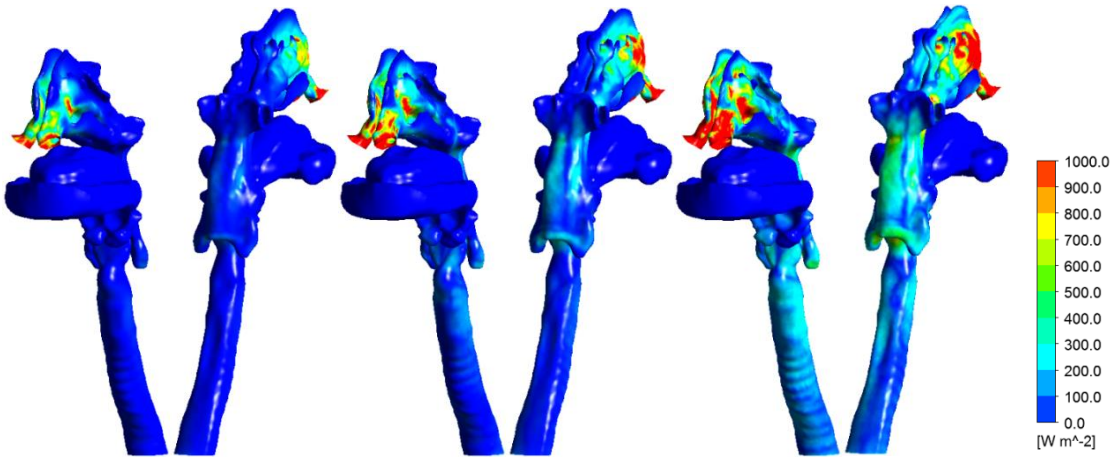

(1) Q_{in}=7.5 L/min (2) Q_{in}=15 L/min (3) Q_{in}=30 L/min

Figure 4.10. Convective heat transfer flux distributions on the upper airway surfaces of the human (Model B) virtual airway [W/m^2]

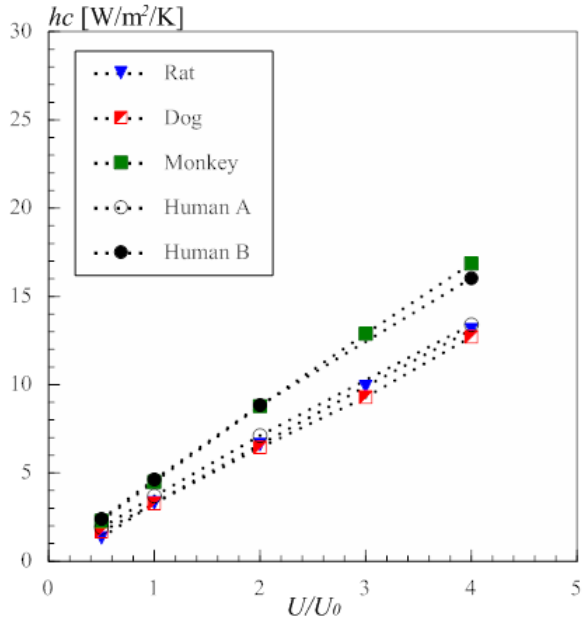

Figure 4.11. Convective heat transfer coefficients (h_c) versus non-dimensional representative velocity in upper airway

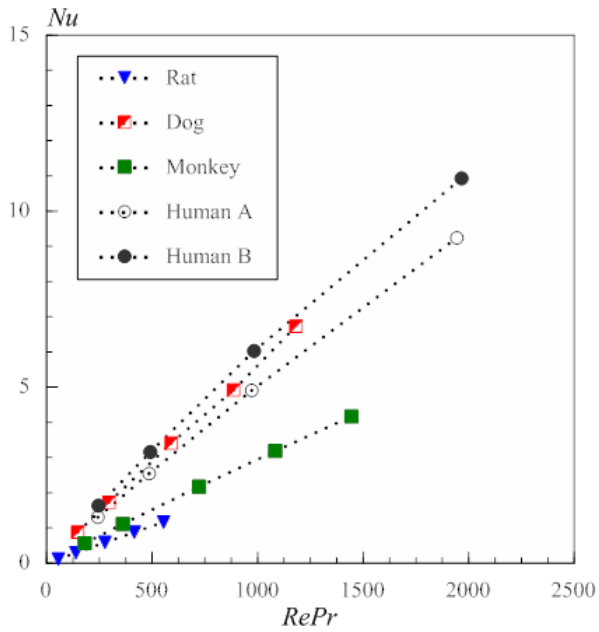

Figure 4.12. *Nu* versus product of *Re* and *Pr* for upper airways

Table 4.6 Correlation of *Nu* versus product of *Re* and *Pr*

Target airway model	Correlation function	Range of *Re*	Correlation coefficient
Rat	$Nu = 0.0021(\mathrm{Re}\cdot \mathrm{Pr})^{0.9973}$	$75 < \mathrm{Re} < 750$	$r^2 = 1$
Dog	$Nu = 0.0069(\mathrm{Re}\cdot \mathrm{Pr})^{0.9707}$	$200 < \mathrm{Re} < 1600$	$r^2 = 0.9997$
Monkey	$Nu = 0.0039(\mathrm{Re}\cdot \mathrm{Pr})^{0.9612}$	$250 < \mathrm{Re} < 2000$	$r^2 = 0.9999$
Human model A	$Nu = 0.0075(\mathrm{Re}\cdot \mathrm{Pr})^{0.9414}$	$330 < \mathrm{Re} < 2600$	$r^2 = 0.9999$
Human model B	$Nu = 0.0107(\mathrm{Re}\cdot \mathrm{Pr})^{0.9965}$	$330 < \mathrm{Re} < 2600$	$r^2 = 0.9994$

4.4 Conclusions

Three-dimensional computer models which describe the flow and heat transfer properties in upper airways have been developed and local convective heat flux distributions in upper airways and average convective heat transfer coefficients as functions of respiratory air flow rate have been discussed. Particular attention was paid to the influences of geometric variations in virtual airway models (i.e., rat, dog, monkey and two human models) upon the efficiency of the convective heat transfer. The effect of respiratory airflow rate on convective heat transfer inside airway models was investigated.

The averaged convective heat transfer coefficient and the distributions of local convective heat transfer coefficient of virtual upper airway models will be crucial parameter for discussing the turbulent heat flux in respiratory tracts. Convective heat transfer coefficient will contribute to the understanding of turbulent flow characteristics in view point of heat transport between air and inner surface of respiratory tract. The basic mechanisms and mathematics of heat and mass transport are essentially the

same and the analogy between heat and mass transfer coefficient via Lewis number is generally recognized. This means that the detail discussion about convective heat transfer coefficients in airway models could be explicated the analyses for convective mass transfer coefficients and further the approximate discussion about the scalar flux, e.g. gas-phase contaminant on epithelium tissue surfaces.

As already described before, the potential of *in silico* models to substitute for biological bodies for *in vivo* study/experimental studies, and tissue and cells for *in vitro* studies is increasing. Though animal and biological tests will always be needed in inhalation toxicology studies and the development of respiratory drug delivery systems, virtual airway models, i.e. *in silico* models, reproducing detailed geometries and physiologies of human and mammal surrogate animals, will be in great demand to substitute for using real animals.

The present study identified fundamental qualities of convective heat transfer phenomena in airways for rats, dogs, monkeys, and humans and has enabled discussions about quantitative differences of heat and mass transfer efficiency between different animals/species. The computer simulation results outlined, and physical insight provided in this study can be applied to the discussions of factor of safety between animal testing, human response, and other inhalation toxicology problems.

In order to estimate comprehensive risk of inhalation exposure in indoor environments, physiologically based pharmacokinetic (PBPK) models which harmonized CFD simulation in virtual airway models should be developed. For decades, pharmacokinetic models have been successfully applied to address issues of extrapolation between contaminants, dose, dose-rate/dose-response, or types of exposure to drugs or chemicals. The understanding of heat and mass transfer characteristics between air-phase of lumen and the surface of epithelium tissue will be the first step of the development of integrated numerical simulation scheme of CFD-Virtual airway models-PBPK model.

References

1. Gerde PYSMA, Cheng YS, Medinsky MA. 1991. In vivo deposition of ultrafine aerosols in the nasal airway of the rat. Toxicological Sciences, 16(2), 330-336.
2. Hesseltine GR, Wolff RK, Mauderly JL, Cheng YS. 1986. Deposition of ultrafine aggregate particles in exercising rats. *Journal of Applied Toxicology*, 6(1), 21-24.
3. Benson JM, Barr EB, Bechtold WE, Cheng YS, Dunnick JK, Eastin WE, Hobbs CH, Kennedy CH, Maples, K. R. 1994. Fate of inhaled nickel oxide and nickel subsulfide in F344/N rats. *Inhalation toxicology*, *6*(2), 167-183.
4. Dorman, D. C., Mokashi, V., Wagner, D. J., Olabisi, A. O., Wong, B. A., Moss, O. R., ... & Lewis, J. A. (2012). Biological responses in rats exposed to cigarette smoke and Middle East sand (dust). *Inhalation toxicology*, 24(2), 109-124.
5. Xi J, Longest PW. 2008. Numerical predictions of submicrometer aerosol deposition in the nasal cavity using a novel drift flux approach. *International Journal of Heat and Mass Transfer*, 51(23-24), 5562-5577.

6. Tian ZF, Inthavong K, Tu JY. 2007. Deposition of inhaled wood dust in the nasal cavity. *Inhalation toxicology*, 19(14), 1155-1165.
7. Inthavong K, Tian ZF, Li HF, Tu JY, Yang W, Xue CL, Li CG. 2006. A numerical study of spray particle deposition in a human nasal cavity. Aerosol Science and Technology, 40(11), 1034-1045.
8. Doorly DJ, Taylor DJ, Gambaruto AM, Schroter RC, Tolley N. 2008. Nasal architecture: form and flow. Philosophical Transactions of the Royal Society of London A: Mathematical, *Physical and Engineering Sciences*, 366(1879), 3225-3246.
9. Zachow S, Steinmann A, Hildebrandt T, Weber R, Heppt W. 2006. CFD simulation of nasal airflow: towards treatment planning for functional rhinosurgery. Int. J. Comp. Assist. Radiol. Surg, 165-167.
10. Xi J, Longest PW. 2007. Transport and deposition of micro-aerosols in realistic and simplified models of the oral airway. Annals of biomedical engineering, 35(4), 560-581.
11. Cheng KH, Cheng YS, Yeh HC, Swift DL. 1997. Measurements of airway dimensions and calculation of mass transfer characteristics of the human oral passage. Journal of biomechanical engineering, 119(4), 476-482.
12. Jayaraju ST, Brouns M, Verbanck S, Lacor C. 2007. Fluid flow and particle deposition analysis in a realistic extrathoracic airway model using unstructured grids. Journal of Aerosol Science, 38(5), 494-508.
13. Corley RA, Kabilan S, Kuprat AP, Carson JP, Minard KR, Jacob RE., ... & Wallis, C. D. (2012). Comparative computational modeling of airflows and vapor dosimetry in the respiratory tracts of rat, monkey, and human. Toxicological Sciences, 128(2), 500-516.
14. Corley, R. A., Kabilan, S., Kuprat, A. P., Carson, J. P., Jacob, R. E., Minard, K. R., ... & Einstein, D. R. (2015). Comparative risks of aldehyde constituents in cigarette smoke using transient computational fluid dynamics/physiologically based pharmacokinetic models of the rat and human respiratory tracts. Toxicological Sciences, 146(1), 65-88.
15. Tian L, Shang Y, Chen R, Bai R, Chen C, Inthavong K, Tu J. 2017. A combined experimental and numerical study on upper airway dosimetry of inhaled nanoparticles from an electrical discharge machine shop. Particle and fibre toxicology, 14(1), 24.
16. Gatlin B, Cuicchi C, Hammersley J, Olson D, Reddy R, Burnside G. 1997. Computation of converging and diverging flow through an asymmetric tubular bifurcation. In The 1997 ASME Fluids Engineering Division Summer Meeting, ASME FEDSM97, Vol. 3429, 1-7.
17. Warrell DA, Benz EJ, Cox TM, Firth JD. 2003. Oxford textbook of medicine (Vol. 1). Oxford University Press, USA.
18. Weibel ER, Cournand AF, Richards DW. 1963. Morphometry of the human lung (Vol. 1). Berlin, Springer.
19. Horsfield K, Cumming G. 1968. Morphology of the bronchial tree in man. Journal of applied physiology, 24(3), 373-383.
20. Horsfield K, Dart G, Olson DE, Filley GF, Cumming G. 1971. Models of the human bronchial tree. Journal of applied physiology, 31(2), 207-217.

21. Hammersley JR, Olson DE. 1992. Physical models of the smaller pulmonary airways. Journal of Applied Physiology, 72(6), 2402-2414.
22. Koblinger L. 1985. Analysis of human lung morphometric data for stochastic aerosol deposition calculations. Physics in Medicine & Biology, 30(6), 541.
23. Kitaoka H, Takaki R, Suki B. 1999. A three-dimensional model of the human airway tree. Journal of Applied Physiology, 87(6), 2207-2217.
24. Calay RK, Kurujareon J, Holdø AE. 2002. Numerical simulation of respiratory flow patterns within human lung. Respiratory physiology & neurobiology, 130(2), 201-221.
25. Lee DY, Lee JW. 2002. Dispersion of aerosol bolus during one respiration cycle in a model of lung airways. Journal of Aerosol Science, 33(9), 1219-1234.
26. Tawhai MH, Pullan AJ, Hunter PJ. 2000. Generation of an anatomically based three-dimensional model of the conducting airways. Annals of biomedical engineering, 28(7), 793-802.
27. Tawhai MH, Hunter P, Tschirren J, Reinhardt J, McLennan G, Hoffman EA. 2004. CT-based geometry analysis and finite element models of the human and ovine bronchial tree. Journal of applied physiology, 97(6), 2310-2321.
28. Schmidt A, Zidowitz S, Kriete A, Denhard T, Krass S, Peitgen HO. 2004. A digital reference model of the human bronchial tree. Computerized Medical Imaging and Graphics, 28(4), 203-211.
29. Gemci T, Ponyavin V, Chen Y, Chen H, Collins R. 2008. Computational model of airflow in upper 17 generations of human respiratory tract. Journal of Biomechanics, 41(9), 2047-2054.
30. Islam MS, Saha SC, Sauret E, Gemci T, Gu Y. 2017. Pulmonary aerosol transport and deposition analysis in upper 17 generations of the human respiratory tract. Journal of Aerosol Science, 108, 29-43.
31. Islam MS, Saha SC, Sauret E, Gemci T, Yang IA, Gu YT. 2017. Ultrafine particle transport and deposition in a large scale 17-generation lung model. Journal of biomechanics, 64, 16-25.
32. Kitaoka H, Nieman GF, Fujino Y, Carney D, DiRocco J, Kawase I. 2007. A 4-dimensional model of the alveolar structure. The Journal of Physiological Sciences, 57(3), 175-185.
33. Kumar H, Tawhai MH, Hoffman EA, Lin CL. 2009. The Effects of Geometry on Airflow in the Acinar Region of the Human Lung. Journal of Biomechanics, 42, 1635-1642.
34. Kitaoka H. 2011. A 4D model generator of the human lung. Forma, 26, 19-24.
35. Khajeh-Hosseini-Dalasm N, Longest PW. 2015. Deposition of particles in the alveolar airways: inhalation and breath-hold with pharmaceutical aerosols. Journal of aerosol science, 79, 15-30.
36. Sznitman J, Heimsch T, Wildhaber JH, Tsuda A, Rösgen T. 2009. Respiratory flow phenomena and gravitational deposition in a three-dimensional space-filling model of the pulmonary acinar tree. Journal of biomechanical engineering, 131(3).
37. Pidaparti RM, Burnette M, Heise RL, Reynolds A. 2013. Analysis for stress environment in the alveolar sac model. Journal of biomedical science and engineering, 6(9), 901.
38. Aghasafari P, Ibrahim IB, Pidaparti RM. 2016. Investigation of the effects of emphysema and influenza on alveolar sacs closure through CFD Simulation. Journal of Biomedical Science and

Engineering, 9(06), 287.
39. Ma B, Darquenne C. 2011. Aerosol deposition characteristics in distal acinar airways under cyclic breathing conditions. Journal of Applied physiology, 110(5), 1271-1282.
40. Sera T, Uesugi K, Yagi N, Yokota H. 2015. Numerical simulation of airflow and microparticle deposition in a synchrotron micro-CT-based pulmonary acinus model. Computer methods in biomechanics and biomedical engineering, 18(13), 1427-1435.
41. Sera T, Higashi R, Naito H, Matsumoto T, Tanaka M. 2017. Distribution of nanoparticle depositions after a single breathing in a murine pulmonary acinus model. International Journal of Heat and Mass Transfer, 108, 730-739.
42. Henry FS, Haber S, Haberthür D, Filipovic N, Milasinovic D, Schittny JC, Tsuda A. 2012. The simultaneous role of an alveolus as flow mixer and flow feeder for the deposition of inhaled submicron particles. Journal of biomechanical engineering, 134(12), 121001.
43. Sznitman J, Sutter R, Altorfer D, Stampanoni M, Rösgen T, Schittny JC. 2010. Visualization of respiratory flows from 3D reconstructed alveolar airspaces using X-ray tomographic microscopy. Journal of visualization, 13(4), 337-345.
44. Kimbell JS, Godo MN, Gross EA, Joyner DR, Richardson RB, Morgan KT. 1997. Computer simulation of inspiratory airflow in all regions of the F344 rat nasal passages. *Toxicology and applied pharmacology*, *145*(2), 388-398.
45. Wei Z, Xu Z, Li B, Xu F. 2013. Numerical simulation of airway dimension effects on airflow patterns and odorant deposition patterns in the rat nasal cavity. PloS one, 8(10).
46. Dong J, Shang Y, Tian L, Inthavong K, Tu J. 2018. Detailed deposition analysis of inertial and diffusive particles in a rat nasal passage. Inhalation toxicology, 30(1), 29-39.
47. Craven, B. A., Neuberger, T., Paterson, E. G., Webb, A. G., Josephson, E. M., Morrison, E. E., & Settles, G. S. (2007). Reconstruction and morphometric analysis of the nasal airway of the dog (Canis familiaris) and implications regarding olfactory airflow. The Anatomical Record: Advances in Integrative Anatomy and Evolutionary Biology: Advances in Integrative Anatomy and Evolutionary Biology, 290(11), 1325-1340.
48. Craven, B. A., Paterson, E. G., & Settles, G. S. (2010). The fluid dynamics of canine olfaction: unique nasal airflow patterns as an explanation of macrosmia. Journal of the Royal Society Interface, 7(47), 933-943.
49. Coppola, D. M., Craven, B. A., Seeger, J., & Weiler, E. (2014). The effects of naris occlusion on mouse nasal turbinate development. Journal of Experimental Biology, 217(12), 2044-2052.
50. Pang, B., Yee, K. K., Lischka, F. W., Rawson, N. E., Haskins, M. E., Wysocki, C. J., ... & Van Valkenburgh, B. (2016). The influence of nasal airflow on respiratory and olfactory epithelial distribution in felids. Journal of Experimental Biology, 219(12), 1866-1874.
51. Mori F, Hanida S, Kumahata K, Miyabe-Nishiwaki T, Suzuki J, Matsuzawa T, Nishimura TD. 2015. Minor contributions of the maxillary sinus to the air-conditioning performance in macaque monkeys. Journal of Experimental Biology, 218(15), 2394-2401.

52. Raabe OG, Al-Bayati MA, Teague SV, Rasolt A. 1988. Regional deposition of inhaled monodisperse coarse and fine aerosol particles in small laboratory animals. In *Inhaled particles VI* (pp. 53-63). Pergamon.
53. Asgharian B, Price O, Kabilan S, Jacob RE, Einstein DR, Kuprat AP, Corley RA. 2016. Development of a Zealand white rabbit deposition model to study inhalation anthrax. *Inhalation toxicology*, *28*(2), 80-88.
54. Kabilan S, Suffield SR, Recknagle KP, Jacob RE, Einstein DR, Kuprat AP, ... & Teeguarden JG. 2016. Computational fluid dynamics modeling of Bacillus anthracis spore deposition in rabbit and human respiratory airways. *Journal of Aerosol Science*, *99*, 64-77.
55. Ruf I. 2014. Comparative anatomy and systematic implications of the turbinal skeleton in Lagomorpha (Mammalia). *The Anatomical Record*, *297*(11), 2031-2046.
56. Doorly DJ, Taylor DJ, Schroter RC. 2008. Mechanics of airflow in the human nasal airways. Respiratory physiology & neurobiology, 163(1-3), 100-110.
57. Ge Q, Li X, Inthavong K, Tu J. 2013. Numerical study of the effects of human body heat on particle transport and inhalation in indoor environment. Building and Environment, 59, 1-9.
58. Inthavong K, Ge QJ, Li XD, Tu JY. 2012. Detailed predictions of particle aspiration affected by respiratory inhalation and airflow. Atmospheric environment, 62, 107-117.
59. Inthavong K, Ge QJ, Li X, Tu JY. 2013. Source and trajectories of inhaled particles from a surrounding environment and its deposition in the respiratory airway. Inhalation toxicology, 25(5), 280-291.
60. King Se CM, Inthavong K, Tu, J. 2010. Inhalability of micron particles through the nose and mouth. Inhalation toxicology, 22(4), 287-300.
61. Shang Y, Dong J, Inthavong K, Tu J. 2015. Comparative numerical modeling of inhaled micron-sized particle deposition in human and rat nasal cavities. Inhalation Toxicology, 27(13), 694-705.
62. Oda Y, Tani K, Kanei T, Haraguchi T, Itamoto K, Nakazawa H, Taura Y. 2013. Characterization of neuron-like cells derived from canine bone marrow stromal cells. Veterinary research communications, 37(2), 133-138.
63. Phuong NL, Ito K. 2015. Investigation of flow pattern in a realistic replica model of human respiratory tract using PIV. Building Environment, 94, 504-515.
64. Phuong NL, Yamashita M, Yoo SJ, Ito K. 2016. Prediction of convective heat transfer coefficient of human upper and lower airway surfaces in steady and unsteady breathing conditions. *Building and Environment*, *100*, 172-185.
65. Abe K, Kondoh T, Nagano Y. 1994. A new turbulence model for predicting fluid flow and heat transfer in separating and reattaching flows—I. Flow field calculations. International journal of heat and mass transfer, 37(1), 139-151.
66. Ito K, Inthavong K, Kurabuchi T, Ueda T, Endo T, Omori T, Ono H, Kato S, Sakai K, Suwa Y, Matsumoto H, Yoshino H, Zhang W and Tu JY. 2015. CFD benchmark tests for indoor environmental problems: Part 1 isothermal/non-isothermal flow in 2D and 3D room model.

International Journal of Architectural Engineering Technology, 2(1), 1-22.
67. Ito K, Inthavong K, Kurabuchi T, Ueda T, Endo T, Omori T, Ono H, Kato S, Sakai K, Suwa Y, Matsumoto H, Yoshino H, Zhang W and Tu JY. 2015. CFD benchmark tests for indoor environmental problems: Part 2 cross-ventilation airflows and floor heating systems. International Journal of Architectural Engineering Technology, 2(1), 23-49.
68. Ito K, Inthavong K, Kurabuchi T, Ueda T, Endo T, Omori T, Ono H, Kato S, Sakai K, Suwa Y, Matsumoto H, Yoshino H, Zhang W and Tu JY. 2015. CFD benchmark tests for indoor environmental problems: Part 3 numerical thermal manikins. International Journal of Architectural Engineering Technology, 2(1), 50-75.
69. Ito K, Inthavong K, Kurabuchi T, Ueda T, Endo T, Omori T, Ono H, Kato S, Sakai K, Suwa Y, Matsumoto H, Yoshino H, Zhang W and Tu JY. 2015. CFD benchmark tests for indoor environmental problems: Part 4 air-conditioning airflows, residential kitchen airflows and fire-induced flow. International Journal of Architectural Engineering Technology, 2(1), 76-102.
70. Johnson CE, Linderoth Jr LS, Nuckols ML. 1977. An analysis of sensible respiratory heat exchange during inspiration under environmental conditions of deep diving.
71. Nuckols ML. 1981. Heat and Water Vapor Transfer in the Human Respiratory System at Hyperbaric Conditions (No. NCSC-TR-364-81). NAVAL COASTAL SYSTEMS CENTER PANAMA CITY FL.
72. Zhang Z, Kleinstreuer C. 2003. Species heat and mass transfer in a human upper airway model. International Journal of Heat and Mass Transfer, 46(25), 4755-4768.

[Previously published documents related to this chapter]

Ito K, Mitsumune K, Kuga K, Phuong NL, Tani K, Inthavong K. 2017. Prediction of convective heat transfer coefficients for the upper respiratory tracts of rat, dog, monkey, and humans. Indoor and Built Environment, 26(6), 828-840.

Chapter 5: Numerical risk assessment of inhalation and dermal exposure to E-cigarette

5.1 Introduction

Tobacco smoking is addictive and has potentially harmful effects on human health such as premature death and disability [1, 2]. The harmful effects are associated with the inhalation of more than 60 hazardous chemical compounds, contained in mainstream and sidestream cigarette smoke [3-6]. Recently, a complete smoke-free law regulating indoor smoking has been adopted in 55 countries (20% global population coverage in 2016), to protect people from second-hand tobacco smoke [7]. However, e-cigarettes are at times perceived as a less harmful alternative to tobacco smoking. As such, the use of e-cigarettes has been increasing worldwide [8]. Instead of burning tobacco leaves, e-cigarettes typically produce vapors by the evaporation of an e-liquid, which mostly contains glycerol, propylene glycol, nicotine, and some flavorings. Although e-cigarettes are usually considered safer due to the lack of a combustion process [9], this may be an illusion because recent studies have detected the presence of harmful chemical compounds such as formaldehyde, acetaldehyde, acrolein, benzene, and toluene in e-cigarette vapors [10-15]. In terms of the health effects of e-cigarettes, there have been reports on the immediate adverse physiological impacts on the respiratory tract after short-term use of e-cigarettes [16-21]. For example, Vardavas *et al*. [16] observed some pulmonary effects similar to those seen with tobacco smoking after 5 min of e-cigarette use. Flouris et al. [17] found that e-cigarettes caused smaller but significant changes in lung function compared to combusted tobacco, even though short-term e-cigarette use produced a similar nicotinergic impact.

In addition to potential adverse health effects of e-cigarette vapor from first-hand smoking, second-hand e-cigarette smoking caused by exhaled air from e-cigarette users have been recognized [22-25]. Those exhaled vapors in indoor air are transported to the breathing zone and surrounding human body by airflow in the room mainly caused by air-conditioning and/or ventilation. The residents, as passive smokers, will be exposed to the harmful chemicals in exhaled vapors by respiration and dermal absorption. Hence, the ventilation system, location of e-cigarette users, and exhalation profile of e-cigarette vapor strongly affect the residents' health risk. Furthermore, dermal absorption of gas phase contaminants tends to be a somewhat overlooked exposure pathway. However, experimental data demonstrates that this pathway can make a significant contribution to the total intake of a gas phase contaminant [26-28]. In recent study, Bekö et al. [29, 30] indicated that nicotine related to a major environmental tobacco smoke can be dermally absorbed directly from indoor air at rates comparable to or higher than via inhalation. In addition to the exhalation of e-cigarette vapors from the respiratory tract to the indoor environment, adsorption and desorption phenomena of volatile organic compounds

(VOCs) caused from e-cigarette smoking might be important when estimating exact exposures in indoor environments. This has been termed 'third-hand smoke' [31].

To estimate and predict inhalation and dermal exposure risks in terms of first-hand and second-hand e-cigarette smoking, experimental studies (i.e., in vivo and in vitro studies), involving human volunteers and other surrogate animals, have been conducted. These experimental approaches are, however, limited by ethical issues and animal protection. From this perspective, a computer simulation model (i.e., in silico model) presents itself as an alternative and complementary approach that may strongly aid in understanding of the contaminant transport mechanisms in the respiratory system and the absorption of contaminants onto skin [32-34]. In the assessment of inhalation exposure risk, computational fluid dynamics (CFD) and physiologically based pharmacokinetic (PBPK) models have been applied to realistic respiratory tract models to predict inhalation dosimetry [35-45]. A majority of previous studies on the inhalation exposure to gas-phase contaminants have used integrated simulation of a realistic airway model, and the PBPK model was focused only on an inhalation period under steady-state condition. As such, these studies could not quantify the amount of inhaled contaminants that are exhaled into indoor air spaces through transient and unsteady puffing conditions.

To simulate non-uniform airflow patterns and temperature distribution surrounding the human body and indoor environments, computational simulated persons (CSPs) coupled with CFD have been developed [46-51]. Gao and Niu [48] simulated the dispersion of exhaled contaminants as a result of sneezing in a room with displacement ventilation and evaluated the amount of exposed contaminant using two CSPs. However, without connecting the exposure analysis of a passive smoker as second-hand exposure, these previous studies could not reproduce realistic contaminant distributions in an indoor environment. Thus, these studies were unable to directly discuss the health risks to residents exposed to deteriorating indoor air quality (IAQ) from e-cigarette usage.

To assess the human dermal exposure of gas phase contaminants, mathematical models are generally helpful and more cost-effective compared to experimental measurements. Weschler and Nazaroff [52, 53] developed a steady-state model of transdermal uptake of semi-volatile organic compounds (SVOCs), predicting that dermal uptake would be important for many indoor relevant SVOCs. Gong *et al*. [54] developed a transient model of transdermal uptake, accounting for transfer from air to skin and assuming Fickian diffusion through skin layers. Their model has been modified by various studies to improve prediction accuracy [55-57]. Most previous studies on dermal exposure using numerical simulation assumed homogeneous boundary conditions and could not reproduce heterogeneous distribution of contaminants absorption flux on skin surfaces. In particular, previous research has targeted relatively long-term dermal exposure. Very few studies have treated the unsteady prediction of absorption flux distributions onto skin surfaces as short-term dermal exposure.

Based on the literature, this study focuses on a qualitative and quantitative assessment of inhalation dosimetry in a human respiratory tract by first-hand e-cigarette smoking. It also assesses the

impact of second-hand exposure including inhalation and dermal absorption by the passive smoker due to the diffusion and dispersion of exhaled contaminants in an indoor environment. We developed a comprehensive numerical model and CSP to investigate the potential effects of e-cigarette smoking on local tissue dosimetry and IAQ. We also undertook demonstrative numerical analyses for first-hand and second-hand e-cigarette smoking in an indoor environment.

5.2 Methods

This study is divided into two parts, namely, (a) inhalation exposure analysis of first-hand e-cigarette smoke using a numerical respiratory tract model and (b) exhalation and passive smoking analysis of e-cigarette vapor released into indoor environments (second-hand e-cigarette smoke) by a quasi-coupling simulation method of CFD, CSPs and a numerical respiratory tract model.

5.2.1 Inhalation exposure analysis

5.2.1.1 Numerical respiratory tract models

Human respiratory tract models for CFD analysis have been developed and improved [58, 59]. Firstly, two types of numerical respiratory tract models (Models A and B) had been developed by using CT data obtained from two healthy human males. The development procedure is same to what was mentioned in section 4.2.1. These models include the oral cavity, pharynx, larynx, trachea, and bronchial tubes reproduced around the fourth bifurcation, and have 38 outlet openings. The external geometries of the two types of numerical respiratory tract models are shown in Figure 5.1, and detailed geometrical information for the two respiratory tract models is summarized in Table 5.1. Secondly, focusing on Model A, the respiratory tract model reproduced the complicated three-dimensional geometry and the respiratory tissue (mucus, epithelium, and subepithelium) by generating prism layers from the respiratory surface in order to apply the PBPK model. The combined thickness of the mucus and epithelium layers is 65 μm and that of subepithelium is 15 μm. Finally, the numerical respiratory model was excluded the nasal cavity region to reduce computational cost. We had confirmed that flow patterns in the respiratory tract did not depend on the existence of the nasal cavity region prior to inhalation exposure analysis using the respiratory tract excluding nasal cavity region [60]. This model included approximately 2×10^6 polyhedral elements and very fine prism layers (<0.1 mm prism mesh), in the near-wall region to satisfy $y+ < 1$ in all respiratory surfaces under peak air velocity. Instead of generating the prism layers for the respiratory tissues, a mathematical model to reproduce the diffusive transport into the respiratory tissue was developed (in section 5.2.1.4). To simulate the inhalation of the e-cigarette vapor in the respiratory tract model, a circular inlet opening with a diameter of 8.0 mm was set to simulate a stream of vapor coming from the mouth directly into the pharynx region. An elliptical outflow opening with an area of 1.2 cm2 [61] was established to reproduce the shape of mouth opening during the exhalation period (Figure 5.1).

Table 5.1. Detailed geometrical information for the two respiratory tract models

	Model A	Model B
Height (m)	0.34568	0.27381
Surface area (m^2)	0.057967	0.044637
Volume (m^3)	0.00017336	0.00012862
Loading factor (m^{-1}) (=Areas of respiratory surface per unit volume)	334.37	347.05

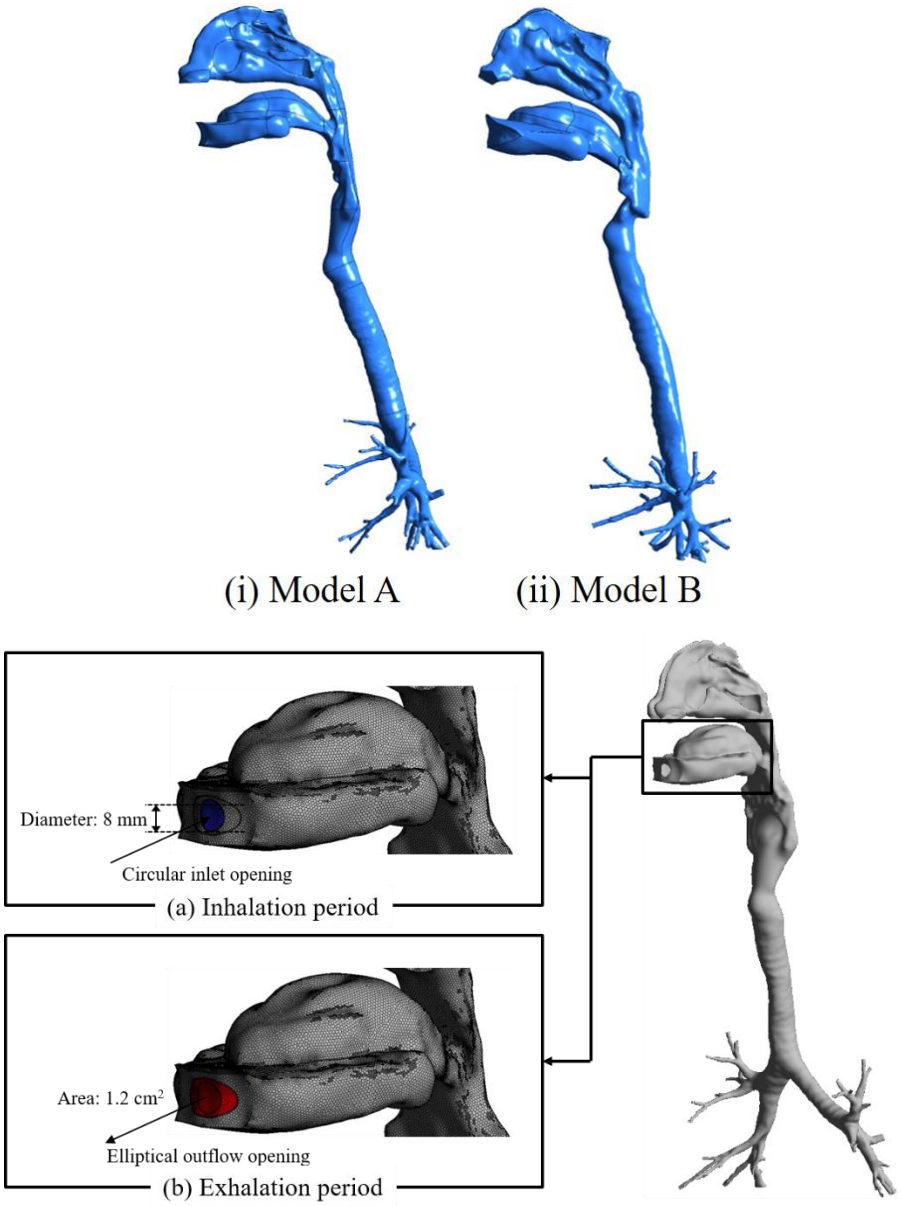

Figure 5.1 Numerical respiratory tract model for inhalation exposure analysis during e-cigarette smoking

5.2.1.2 Transient puffing profiles

Vansickel *et al*. [62] carried out a detailed measurement of the puff profile during usage of a prototype e-cigarette in exclusive cigarette smokers and e-cigarette users. They reported that e-cigarette users generally inhaled longer puffs with a longer flow rate relative to conventional cigarette smokers.

This difference in puffing behavior may have a potential impact on human health in terms of inhalation exposure. To investigate the effect of puffing behavior in terms of total respiratory uptake, two types of puffing profiles based on the measurements from Vansickel *et al*. [62] were prepared in this study. The exhalation duration for the two profiles was set as 1.8 s because no difference was observed in exhalation duration between traditional cigarette smokers and e-cigarette users [63]. The exhalation profile was described using a sinusoidal profile based on exhalation duration and inhaled volume. A measured human post-puff profile was also used [64]. In this study, three types of transient puffing profiles, shown in Figure 5.2, were set in the mouth opening (see Figure 5.1) as the inflow/outflow boundary condition.

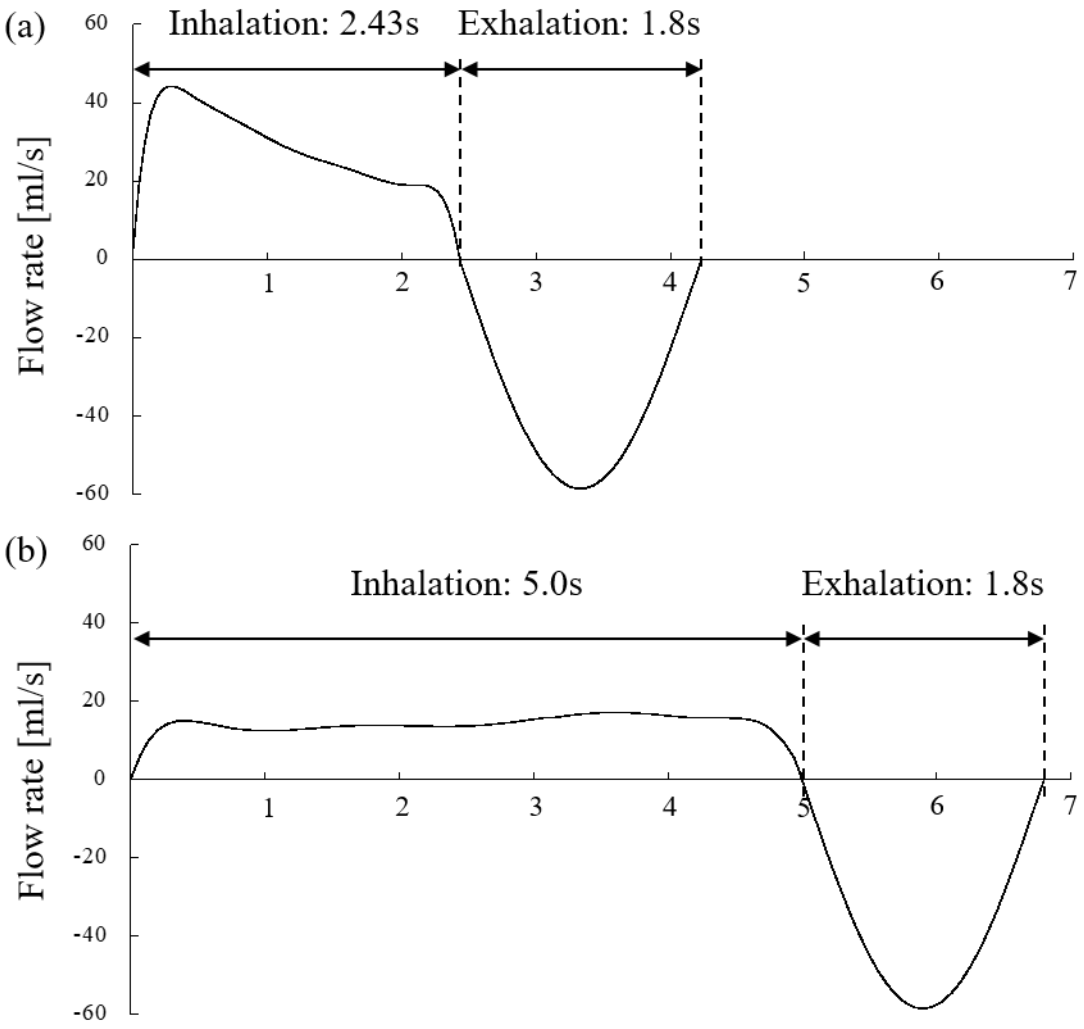

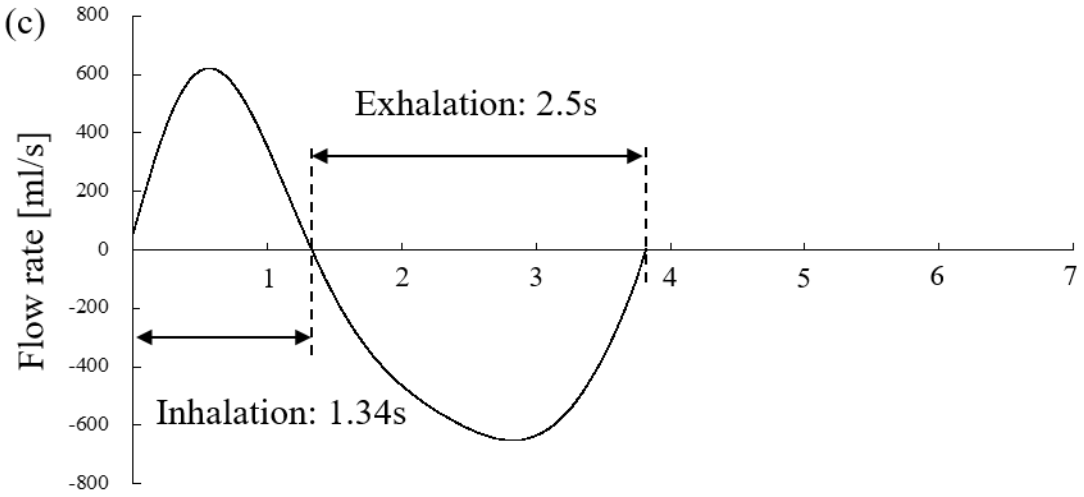

Figure 5.2. Three types of transient puffing profiles. (a) short puff, (b) long puff and (c) post puff

5.2.1.3 Establishing momentum, energy, and contaminant transport in the respiratory tract

Flow patterns, temperature, and contaminant concentration distributions under e-cigarette puffing conditions were calculated using CFD analysis. The low Reynolds (Re) number type k-ε model (Abe-Kondoh-Nagano model) [65, 66] was selected to simulate flow patterns in the respiratory tract model because it provides an accurate and numerically efficient solution for transitional and turbulent flows. Specifically, reasonable prediction accuracy of low Re number type k-ε model for airflow distribution analysis in the respiratory tract was validated using particle image velocimetry (PIV) [58]. A no-slip boundary condition was applied for the mucus wall surfaces inside the airway model. A second-order upwind scheme was used for the convection term, and a semi-implicit method for pressure linked equations (SIMPLE) algorithm was used.

Overall, the breathing simulation using the pressure boundary condition corresponding to the expansion and contraction of the lungs in the mouth opening and bronchial outlet openings was consistent with actual breathing. However, pressure boundary conditions are limited in terms of numerical stability and evaluation of total pressure loss in the respiratory tract after prescribing the pressure in the mouth opening and bronchial outlets. To address this, velocity profiles (see Figure 5.2) were directly set in the mouth opening as inflow and outflow boundary conditions. The turbulent kinetic energy at the circular inlet was prescribed by assuming 10% turbulence intensity.

To establish the boundary conditions for energy transport in the respiratory tract, the inhaled e-cigarette vapor temperature was assumed as 45°C based on previous experimental results [13, 15]. The respiratory surfaces, covered by a mucus layer, were assumed to be at a constant temperature of 36.4°C.

The contaminants transport equation for turbulent flow can be expressed in terms of contaminant concentration as:

$$\frac{\partial \overline{C_a}}{\partial t} + \frac{\partial \overline{U_i}\,\overline{C_a}}{\partial x_i} = \frac{\partial}{\partial x_i}\left\{\left(D_a + \frac{\nu_t}{\sigma}\right)\frac{\partial \overline{C_a}}{\partial x_i}\right\}, \tag{5-1}$$

where $\overline{C_a}$ is the ensemble mean contaminant concentration in a grid point, D_a is the diffusion coefficient of contaminant in air, and ν_t is the turbulent viscosity. vectors U_i and x_i are the fluid velocity and position, respectively and σ is the turbulent Schmidt number.

The total contaminant generation rate from one puff of e-cigarette smoke was determined by various fundamental experimental studies [13, 14]. The average contaminant concentrations in the inhaled air during the inhalation period were set at 0.70 μg/ml, 0.22 μg/ml, 0.02 μg/ml, 1.6×10^{-6} μg/ml, 3.1×10^{-6} μg/ml, 33.2 μg/ml, and 0.27 μg/ml for formaldehyde, acetaldehyde, acrolein, benzene, toluene, glycerol, and nicotine, respectively. Total inhaled dose of each contaminant depends on the puff volume of three different puffing profiles. During the exhalation period, the air that returned from the lungs to the bronchial tubes was hypothetically assumed to contain zero contaminant concentration. Numerical and boundary conditions for inhalation exposure analysis are summarized in Table 5.2.

Table 5.2. Numerical and boundary condition for inhalation exposure analysis (inside numerical respiratory tract model)

Turbulence Model	Low Re number type k-ε model (Abe–Kondoh–Nagano Model, 3D Cal.)
Mesh	2.0 million mesh (unstructured + prism)
Algorithm	SIMPLE (Unsteady)
Scheme	Convection Term: Second upwind scheme
Inflow boundary	Q_{in} = transient cigarette smoking profiles (see Fig. 2) $k_{in} = 3/2\,(U_{in} \times 0.1)^2$, $\varepsilon_{in} = C_\mu^{3/4} k_{in}^{3/2} l_{in}$ T_{in} = 45 ºC (=318 K)
Outflow boundary	Boundary type: Gradient zero condition
Wall treatment	Velocity: no slip Temperature; $T_{wall\ surface}$ = 36.4 ºC (= 309.4 K) Contaminant: equilibrium concentration updated by transient PBPK analysis (partitioning coefficient concept)

5.2.1.4 Modeling of contaminant adsorption onto the respiratory tissue surface

To reproduce gas-phase contaminant absorption onto the respiratory surface, diffusive transport, metabolic clearance, and blood perfusion in respiratory tissues, we assumed the respiratory tissue was comprised of three pseudo-homogenous layers. These were the mucus, epithelium, and sub-epithelium with a thickness of H_m = 15 μm, H_t = 50 μm, and H_b = 15 μm, respectively. This assumption was based on the PBPK model proposed by Tian and Longest [36-38]. The transport processes inside the tissues were assumed to be one-dimensional (1D).

The following governing equations describe the transient contaminant diffusive transport through the respiratory tissue:

$$\frac{\partial C_m(y,t)}{\partial t} = D_m \frac{\partial^2 C_m(y,t)}{\partial y^2} \quad \text{for} \quad 0 < y < H_m \tag{5-2}$$

$$\frac{\partial C_t(y,t)}{\partial t} = D_t \frac{\partial^2 C_t(y,t)}{\partial y^2} \quad \text{for} \quad H_m < y < H_m + H_t \tag{5-3}$$

$$\frac{\partial C_b(y,t)}{\partial t} = -\frac{Q_b}{V_b} C_b(y,t) + D_b \frac{\partial^2 C_b(y,t)}{\partial y^2} \quad \text{for} \quad H_m + H_t < y < H_m + H_t + H_b, \tag{5-4}$$

where C_m, C_t, and C_b are the contaminant concentrations in the mucus, epithelium and sub-epithelium (μg/m^3), respectively, D_m, D_t, and D_b are the diffusion coefficients in the mucus, epithelium and sub-epithelium (m^2/s), respectively, Q_b is the blood flow rate in the sub-epithelium (ml/s), V_b is the volume of sub-epithelium (ml), and y is the distance in the respiratory tissue from the interface between air and mucus (m). The initial concentrations of the target contaminants in the respiratory tissues are assumed to be zero. In addition, local equilibrium is assumed at the air-mucus interface, the mucus-epithelium interface and the epithelium- sub-epithelium interface. Additionally, the partition coefficient (i.e. Henry constant of linear type adsorption isotherm) is applied and the flux is conserved at each interface. Mathematically, the initial and boundary conditions are expressed as follows:

$$C_m(y,0) = C_t(y,0) = C_b(y,0) = 0 \tag{5-5}$$

$$C_m(y,t)\big|_{y=0} = P_{ma}\, C_a(y,t)\big|_{y=0} \tag{5-6}$$

$$-D_a \frac{\partial C_a(y,t)}{\partial y}\bigg|_{y=0} = -D_m \frac{\partial C_m(y,t)}{\partial y}\bigg|_{y=0} \tag{5-7}$$

$$C_t(y,t)\big|_{y=H_m} = P_{tm}\, C_m(y,t)\big|_{y=H_m} \tag{5-8}$$

$$-D_m \frac{\partial C_m(y,t)}{\partial y}\bigg|_{y=H_m} = -D_t \frac{\partial C_t(y,t)}{\partial y}\bigg|_{y=H_m} \tag{5-9}$$

$$C_b(y,t)\big|_{y=H_m+H_t} = P_{bt}\, C_t(y,t)\big|_{y=H_m+H_t} \tag{5-10}$$

$$-D_t \frac{\partial C_t(y,t)}{\partial y}\bigg|_{y=H_m+H_t} = -D_b \frac{\partial C_b(y,t)}{\partial y}\bigg|_{y=H_m+H_t} \tag{5-11}$$

$$-D_b \frac{\partial C_b(y,t)}{\partial y}\bigg|_{y=H_m+H_t+H_b} = 0, \tag{5-12}$$

where P_{ma}, P_{tm} and P_{bt} are the mucus-air partition coefficient, the tissue-mucus partition coefficient and the blood-tissue partition coefficient, respectively.

Regarding aldehydes, to reproduce the metabolic clearance of contaminants in the epithelium layer, the non-specific first-order metabolic clearance k_f, C_t and the Michaelis-Menten equation

$V_{\max C} C_t / (K_m + C_t)$ are added as sink terms in the epithelium layer. Here, k_f is the non-specific first-order metabolism rate constant, V_{maxC} is a coefficient that represents saturable metabolism per unit volume of tissue, and K_m is the Michaelis constant.

5.2.1.5 Estimation of physical properties of target chemicals for inhalation exposure analysis

For the inhalation exposure analysis of e-cigarette smoking, we selected formaldehyde, acetaldehyde, acrolein, benzene, toluene, glycerol and nicotine as representative contaminants of the e-cigarette vapors. Relevant parameters need to be determined or estimated for the coupled PBPK-CFD inhalation exposure analysis.

The physical properties of the mucus including the diffusivity and partition coefficient can be assumed equal to those found in water because mucus is ~95% water [67]. The diffusivities of target chemicals in water are determined based on multiple sources or estimated by the Stokes-Einstein equation:

$$D = \frac{KT}{6\pi\eta r_s}, \tag{3-13}$$

where K is the Boltzmann constant, T is the temperature, η is the viscosity of water and r_s is the solute radius (Å). We hypothetically set the viscosity of water as 7.0×10^{-4} [Pa s] and approximate the solute radius by the empirical equation using molecular weight (MW) of chemicals [68]:

$$4/3 r_s^3 = 0.2894 MW, \tag{3-14}$$

The diffusivities in the sub-epithelial tissue layer (blood phase) are also calculated by the Stokes–Einstein equation, by assuming the viscosity of blood as 4.0×10^{-3} [Pa s]. The diffusivities in the epithelial tissue layer are empirically calculated as one-third the value of that of mucus [69].

With respect to the partition coefficient in each interface of the respiratory tissue layers, we have estimated the values based on various sources and assumptions. The mucus-air partition coefficients (P_{ma}) are adjusted from the values of 25 ℃ to 36.4 ℃ using the temperature dependence equation described in some papers [70]. The tissue-mucus partition coefficient (P_{tm}) can be calculated by the following equation [71].

$$P_{tm} = \frac{1}{P_{bt}} \frac{P_{ba}}{P_{ma}}, \tag{3-15}$$

where P_{bt} is the blood-tissue partition coefficient which is assumed to equal one [72], and P_{ba} is the blood-air partition coefficient which is predicted by the following equation given by Pulltin et al. [73].

$$P_{ba} = P_{ow} P_{ma} (a + 0.3b) + P_{ma} (c + 0.7b), \tag{3-16}$$

where a = 0.0033 is the fraction of neutral lipids in blood, b = 0.0024 is the fraction of phospholipids in blood, c = 0.82 is the fraction of water in blood, and P_{ow} is the octanol-water partition coefficient.

For the metabolic clearance rate and the first-order reaction rate of chemicals in the epithelial tissue layer, we set the values only for formaldehyde, acetaldehyde and acrolein from various sources.

For the other target chemicals, we neglect the metabolic clearance and first-order reaction because no information about these chemicals is available in the open literature.

All physical properties of target chemicals for inhalation exposure analysis are summarized in Table 5.2.

Table 5.2. Physical properties of target chemicals for inhalation exposure analysis (parameters of PBPK model for respiratory tissue dosimetry)

	Formaldehyde	Acetaldehyde	Acrolein
Diffusivity [cm^2/s]			
Air (D_a)	0.18 [a]	0.124 [a]	0.105 [a]
Mucus (D_m)	2.00×10^{-5} [a]	1.23×10^{-5} [a]	1.12×10^{-5} [a]
Tissue (D_t)	6.67×10^{-6} [f]	4.10×10^{-6} [f]	3.73×10^{-6} [f]
Blood (D_b)	3.03×10^{-6} [e]	2.67×10^{-6} [e]	2.46×10^{-6} [e]
Partition coefficient (P)			
Mucus: Air (P_{ma})	3.65×10^{4} [g]	165 [g]	101 [g]
Tissue: Mucus (P_{tm})	0.831	0.824	0.826
Blood: Tissue (P_{bt})	1.0	1.0	1.0
Octanol: Water (P_{ow})	2.24	0.457	0.977
Blood: Air (P_{ba})	3.03×10^{4}	136	83.1
Metabolism			
K_m [$\mu g/m^3$]	2.01×10^{5} [h]	1.1×10^{9} [k]	5.0×10^{2} [j]
V_{max} [$\mu g/m^3/s$]	1.96×10^{7} [h]	3.93×10^{7}	1.12×10^{5} [j]
K_f [1/s]	1.8×10^{-2} [h]	3.573×10^{-2} [i]	2.0×10^{-2} [j]

	Benzene	Toluene	Glycerol	Nicotine
Diffusivity [cm^2/s]				
Air (D_a)	0.088 [a]	0.087 [a]	0.0877 [b]	0.065 [d]
Mucus (D_m)	9.8×10^{-6} [a]	8.6×10^{-6} [a]	9.3×10^{-6} [c]	9.38×10^{-6} [e]
Tissue (D_t)	3.23×10^{-6} [f]	2.87×10^{-6} [f]	3.1×10^{-6} [f]	3.13×10^{-6} [f]
Blood (D_b)	2.20×10^{-6} [e]	2.08×10^{-6} [e]	2.08×10^{-6} [e]	1.73×10^{-6} [e]
Partition coefficient (P)				
Mucus: Air (P_{ma})	2.65 [g]	2.31 [g]	3.25×10^{9} [g]	8.18×10^{6} [g]
Tissue: Mucus (P_{tm})	1.36	2.98	0.826	0.881
Blood: Tissue (P_{bt})	1	1	1	1
Octanol: Water (P_{ow})	135	537	0.977	14.8
Blood: Air (P_{ba})	3.61	6.88	2.68×10^{9}	7.21×10^{6}

[a] GSI chemical database https://www.gsi-net.com/en/publications/gsi-chemical-database.html.
[b] Feng *et al.* [42]
[c] Hayduk and Laudie [74]
[d] Eatough *et al.* [75]
[e] Estimated using the Stokes-Einstein equation.
[f] Calculated as one-third the value of mucus.
[g] Sander [70]
[h] Conolly *et al.* [76]
[i] Teeguarden *et al.* [77]
[j] Schroeter *et al.* [78]
[k] Bogdanffy *et al.* [79]

5.2.2 Dispersion of exhaled vapor and passive smoking analysis

5.2.2.1 Computer simulated person and room model analysis

We developed a CSP that reproduces the detailed geometry of the shape of a human body surface for CFD analysis [32, 43, 44, 80, 81]. Transient analysis for exhaled vapor dispersion and passive smoking of the resident were conducted using two types of CSPs and a displacement ventilated room model (27 m^3) with a small supply inlet and exhaust outlet openings of 0.09 m^2. One of the CSPs is the e-cigarette user (i.e., an active smoker), and the other is a resident (i.e., a passive smoker). They stand face to face maintaining a distance of 1 m. The fresh outdoor air was assumed to be entering from the front wall at the floor level with an inlet velocity of 0.05 m/s. The supply air temperature was 22 °C and the turbulent intensity I, was assumed at 10 %. The ventilation rate was 0.0045 m^3/s, providing the ventilated room with a general air change rate of 0.6 h^{-1}. The exhaust outlet opening was located at the ceiling level.

The e-cigarette user releases the e-cigarette vapor into the indoor environment via exhalation. The flow boundary condition of the mouth opening was quasi-coupled with time-dependent results (velocity, turbulence, temperature, and contaminant concentrations) of inhalation exposure analysis in the respiratory tract model. In this study, the post-puff condition focused on second-hand exposure analysis. This was because the exhaled contaminants in the post-puff can be easily transported to the passive smoker due to the higher flow rate compared with short and long-puff conditions. Therefore, the post-puff condition leads to a high exposure risk and the worst case scenario for the passive smoker.
The passive smoker inhales the contaminants exhaled from the e-cigarette user via nasal breathing and also absorbs the contaminants through the dermal pathway. Fig. 5.3 illustrates the room model with a displacement ventilation system.

Gupta *et al*. [61] proposed a nasal breathing cycle as a function of body height, body weight and body surface area. We applied the nasal breathing cycle model as the inflow boundary condition of the CSP for the passive smoker. The nasal breathing cycle model is shown in Fig. 5.4. In this study, the breathing cycle and transient inhaled/exhaled air-flow rate was determined based on the breathing model of standard adult males.

To reproduce the thermo-physiological sensible heat generation from human bodies, a simple calculation routine for skin surface temperature was applied to a CSP and a coupled analysis of the skin surface temperature was enforced. The calculation procedure was expressed as a heat balance equation, Equation (5-17), in which the skin surface temperature was determined to be the convergence value for heat exchange between the indoor environment and the CSP. Equation (5-17) is the heat balance equation in thermal neutralization and Equation (5-18) was derived by transforming Equation (5-17). This method was equivalent to the control method used in the experimental thermal manikin for surface sensible heat generation [82, 83]:

$$T_{sk} = 309.4 - (0.054 + R_{cl})Q_t \tag{5-17}$$

$$Q_t = \frac{1}{(0.054 + R_{cl})}(309.4 - T_{sk}) \tag{5-18}$$

Here, T_{sk} is the skin surface temperature [K]; Q_t is the amount of sensible heat flux from the skin surface [W/m^2]; and R_{cl} is the thermal resistance of the clothes [(m^2 K)/W] (reciprocal of the heat conductance value). To execute the benchmark test under simplified boundary conditions, the numerical analysis was carried out under nude conditions (R_{cl} = 0).

To analyze the flow field in the boundary layer for this CFD simulation, the center of the computational cells closest to the wall surfaces (wall surfaces of the room model and skin surfaces of the CSP), should be a non-dimensional distance (wall unit) of y^+<1, where $y^+ = u^* y_1/\nu$; y_1 is the distance normal to the wall surface, ν is the kinematic viscosity and $u^* = \sqrt{\tau_w/\rho}$ is the friction velocity (ρ is the air density and τ_w is the wall shear stress). A grid independence check was executed carefully and elaborately and the minimum mesh size near the wall surface, skewness and size ratio of adjoining meshes were elaborately designed [84-88].

Numerical and boundary conditions for exhalation and passive smoking analysis are summarized in Table 5.3.

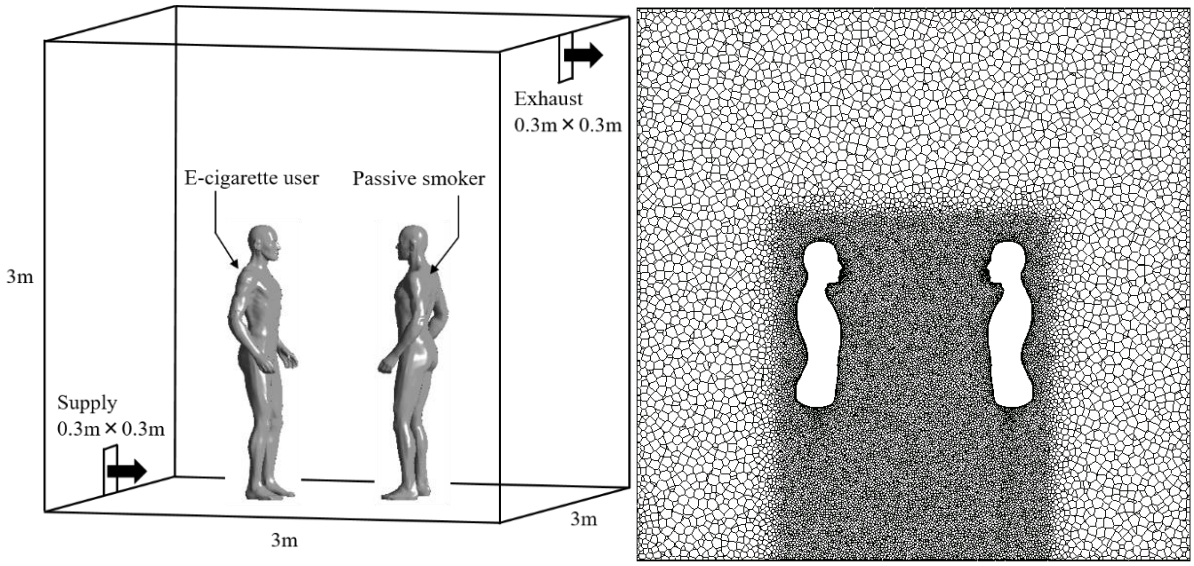

Figure 5.3. Room model with displacement ventilation system

Table 5.3. Numerical and boundary conditions for exhalation and passive smoking analysis.

Turbulence Model	Low Re number type k-ε model (Abe–Kondoh–Nagano Model, 3D Cal.)
Mesh	1.2 million mesh (unstructured + prism)
Algorithm	SIMPLE (Unsteady)
Scheme	Convection Term: Second upwind scheme
Inflow boundary of the room model	U_{in} = 0.05 m/s $k_{in} = 3/2\,(U_{in} \times 0.1)^2$, $\varepsilon_{in} = C_\mu^{3/4} k_{in}^{3/2} l_{in}$ T_{in} = 22 ºC (=295 K) C_{in} = 0
Outflow boundary of the room model	U_{out}, k_{out}, ε_{out} = Gradient zero
Wall treatment of the room model	Velocity: no slip Temperature; adiabatic Contaminant: gradient zero
Inflow boundary of CSP	U_{in} = Transient cigarette smoking profile in exhalation period (see Fig. 3.2) (for e-cigarette user) U_{in} = Transient inhalation/exhalation nasal breathing profile (see Fig. 3.4) (for passive smoker)
Wall treatment of CSP	Velocity: no slip Temperature: calculated by Fanger model (T_{sk}) Contaminant: dermal absorption model (see section 2.2.2)
Others	Radiation model: S2S model, ray tracing method Body height H = 1.736 [m], Body weight W = 65 [kg], Body surface area BSA = 1.745 [m^2]

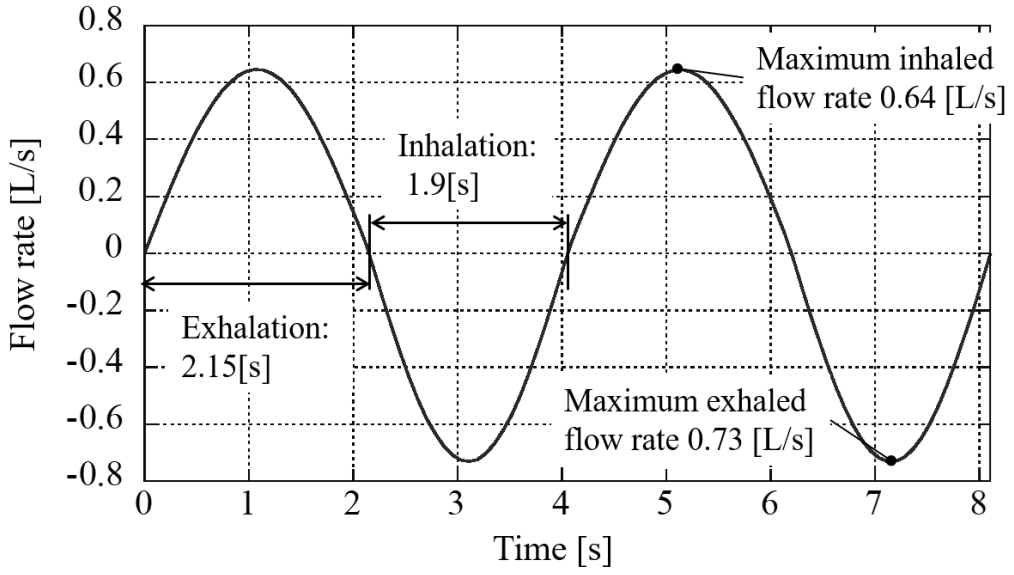

Figure 5.4. Transient nasal breathing flow rate profile determined by the nasal breathing cycle model

5.2.2.2 Dermal absorption model for short-term exposure

To simulate short-term dermal exposure of gas-phase contaminants released from exhalation

by the e-cigarette user, a specific dermal absorption model based on the transdermal model described by Morrison *et al.*[55] was developed for our CSP. In this transdermal model, the skin consists of the three layers; skin surface lipid (SSL), stratum corneum (SC) and viable epidermis (VE). In terms of short-term exposure such as smoking, contaminant concentrations in the VE is negligible. Thus, only two layers, the SSL and SC layers, were reproduced in our dermal model. Although the SC is constructed of corneocyte and lipids which have different specific properties, we assumed the SC as a pseudo-homogenous layer for simplicity. Based on these assumptions, the governing equations that describe transient mass diffusion through the skin are:

$$\frac{\partial C_{SSL}(y,t)}{\partial t} = D_{SSL}\frac{\partial^2 C_{SSL}(y,t)}{\partial y^2} \quad \text{for} \quad 0 < y < H_{SSL} \tag{5-19}$$

$$\frac{\partial C_{SC}(y,t)}{\partial t} = D_{SC}\frac{\partial^2 C_{SC}(y,t)}{\partial y^2} \quad \text{for} \quad H_{SSL} < y < H_{SSL} + H_{SC} \tag{5-20}$$

where C_{SSL} and C_{SC} are the contaminant concentrations in the SSL and SC (μg/m^3), respectively; D_{SSL} and D_{SC} are diffusion coefficients in the SSL and SC (m^2/s), respectively; H_{SSL} and H_{SC} are the thickness of SSL and SC (m), respectively; and y is the distance in the respiratory tissue from the interface between air and SSL (m). The skin tissue initial concentrations were assumed as zero. The local equilibrium was assumed at the air-SSL and SSL-SC interfaces, using the partition coefficient. The flux was conserved at each interface. The initial and boundary conditions are expressed as follows:

$$C_{SSL}(y,0) = C_{SC}(y,0) = 0 \tag{5-21}$$

$$C_{SSL}(y,t)\big|_{y=0} = P_{SSL:a}\, C_a(y,t)\big|_{y=0} \tag{5-22}$$

$$-D_a \frac{\partial C_a(y,t)}{\partial y}\bigg|_{y=0} = -D_{SSL}\frac{\partial C_{SSL}(y,t)}{\partial y}\bigg|_{y=0} \tag{5-23}$$

$$C_{SC}(y,t)\big|_{y=H_{SSL}} = P_{SC:SSL}\, C_{SSL}(y,t)\big|_{y=H_{SSL}} \tag{5-24}$$

$$-D_{SSL}\frac{\partial C_{SSL}(y,t)}{\partial y}\bigg|_{y=H_{SSL}} = -D_{SC}\frac{\partial C_{SC}(y,t)}{\partial y}\bigg|_{y=H_{SSL}} \tag{5-25}$$

$$C_{SC}(y,t)\big|_{y=H_{SSL}+H_{SC}} = 0\,, \tag{5-26}$$

where $P_{SSL:a}$ and $P_{SC:SSL}$ are the lipid-air partition and SC-lipid partition coefficients, respectively.

5.2.2.3 Estimation of physical properties of target chemicals for dermal exposure analysis

To calculate dermal absorption of the gas-phase contaminants using the dermal absorption model, the relevant physical properties of target chemicals were determined. In this study, we estimated the diffusion coefficient in the SSL and SC (D_{lipid}, D_{SC}) and the partition coefficient in air-SSL interface and SSL-SC interface ($P_{SSL:a}$, $P_{SC:SSL}$) based on several assumptions.

In the SSL, the diffusion coefficient was related to the solute radius as described in the

literature [89, 90]:

$$D_{lipid} = \begin{cases} 2\times10^{-9}\exp(-0.46r_s^{\,2}), & MW \le 380Da \\ 3\times10^{-13}, & MW > 380Da \end{cases} \quad (5\text{-}27)$$

The effective diffusion coefficient in the SC was determined assuming that the corneocytes were impermeable and using the theoretical equation described by Kushner *et al.*[91]:

$$D_{sc} = \frac{D_{lipid}}{\tau_{flux}\tau_{volume}} \quad (5\text{-}28)$$

where τ_{flux} and τ_{volume} are tortuosity factors to account for parallel and branched transport or active in lipid region. τ_{flux} and τ_{volume} were calculated from the geometric parameters of SC:

$$\tau_{volume} = \frac{Nh + (N-1)g + (N-1)d}{Nh + (N-1)g}, \quad (5\text{-}29)$$

$$\tau_{flux} = \frac{Nh + (N-1)g + (N-1)\dfrac{\omega}{(1-\omega)^2}d}{Nh + (N-1)g}, \quad (5\text{-}30)$$

where N=12 is the number of corneocyte layers; h=0.88 (μm) is the thickness of the corneocyte; g=0.075 (μm) is the width of the lipid channel; ω=8 is the offset ratio; and d=40 (μm) is corneocyte width.

It is typically difficult to directly measure the $P_{SSL:a}$, as such, the $P_{SSL:a}$ was obtained by multiplying the water-air partition coefficient ($P_{w:a}$) and the lipid-water partition coefficient ($P_{lipid:w}$):

$$P_{SSL:a} = P_{lipid:w} \times P_{w:a} \quad (5\text{-}31)$$

The $P_{SC:SSL}$ was obtained by dividing the SC-water partition coefficient ($P_{SC:w}$) in the $P_{lipid:w}$:

$$P_{SC:SSL} = \frac{P_{SC:w}}{P_{lipid:w}} \quad (5\text{-}32)$$

The coefficients $P_{lipid:w}$ and $P_{SC:w}$, were estimated assuming that the SC was partially hydrated (0.43 g water/1 g dry SC). Using the empirically derived equation described by Nitsche *et al.*[92], we get:

$$P_{lipid:w} = 0.43P_{ow}^{\,0.81} \quad (5\text{-}33)$$

$$P_{SC:w} = 0.040P_{ow}^{\,0.81} + 4.06P_{ow}^{\,0.27} + 0.359 \quad (5\text{-}34)$$

All physical properties of the target chemicals for dermal exposure analysis are summarized in Table 5.4.

Table 5.4. Physical properties of target chemicals for dermal exposure analysis.

	Formaldehyde	Acetaldehyde	Acrolein
Diffusivity [cm^2/s]			
Lipid (D_{lipid})	4.02×10^{-6}	2.52×10^{-6}	1.75×10^{-6}
SC (D_{SC})	1.39×10^{-8}	8.69×10^{-9}	6.05×10^{-9}
Partition coefficient (P)			
SSL: Air ($P_{SSL:a}$)	3.02×10^{4}	40.0	44.7
SC:SSL ($P_{SC:SSL}$)	6.64	16.1	10.5

	Benzene	Toluene	Glycerol	Nicotine
Diffusivity [cm^2/s]				
Lipid (D_{lipid})	9.61×10^{-7}	6.75×10^{-7}	6.75×10^{-7}	1.43×10^{-7}
SC (D_{SC})	3.32×10^{-9}	2.33×10^{-9}	2.33×10^{-9}	4.93×10^{-10}
Partition coefficient (P)				
SSL: Air ($P_{SSL:a}$)	68.2	233	1.53×10^{9}	1.15×10^{7}
SC:SSL ($P_{SC:SSL}$)	0.777	0.415	10.5	2.39

5.3 Results and discussion

5.3.1 Primary inhalation exposure of e-cigarette users

Fig. 5.5 shows a time series of velocity magnitude distributions in the respiratory tract under the short-puff condition. An instantaneous jet-stream was generated from the circular inlet opening to the respiratory airway and impacts onto the tongue region. A recirculating flow was formed near the upper palate because of the turbulent shear layer induced by the velocity difference inside and outside the jet-stream. The jet-stream and recirculating flow characteristics were similar to flow patterns reported by Feng and Kleinstreuer [93] within the upper airway of a human body. Accelerated flow was confirmed in the oropharyngeal and laryngeal regions because of the reduction in cross-sectional area. An accelerated flow from the oropharyngeal region toward the upper palate and elliptical mouth opening was formed during the exhalation periods. The flow patterns during these periods are clearly different from those during the inhalation period. The prediction quality of flow patterns was carefully controlled. For example, the grid independence check was carefully conducted and a significant number of elements were generated. For the CFD study, the time step required to analyze transient flow was also carefully determined to meet the Courant–Friedrichs–Lewy (CFL) condition [94]. The CFD result was found to be reasonably consistent with those previously reported and good agreement is observed [58].

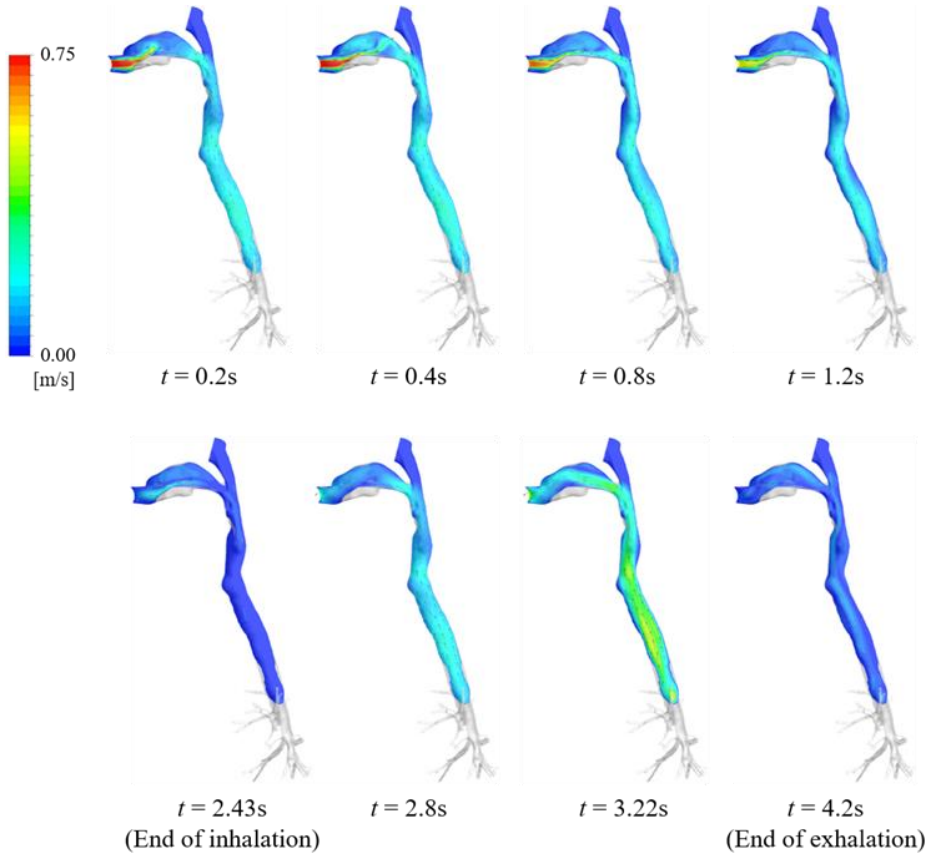

Figure 5.5. Time series of velocity magnitude distributions in the respiratory tract model under the short-puff profile

Fig. 5.6 shows a time series of contaminant concentration distributions in the respiratory tract under the short-puff profile. Formaldehyde and benzene were selected as the high and low absorptive contaminants. Fig. 5.7 illustrates a time series of contaminant (formaldehyde and benzene) absorption flux distributions in the respiratory mucus layer under the short-puff profile. The mass rate of formaldehyde transported to the lungs and exhaled to the indoor environment is significantly low compared to other contaminants as most of the inhaled formaldehyde was absorbed onto the mucus surface of tongue region and upper palate.

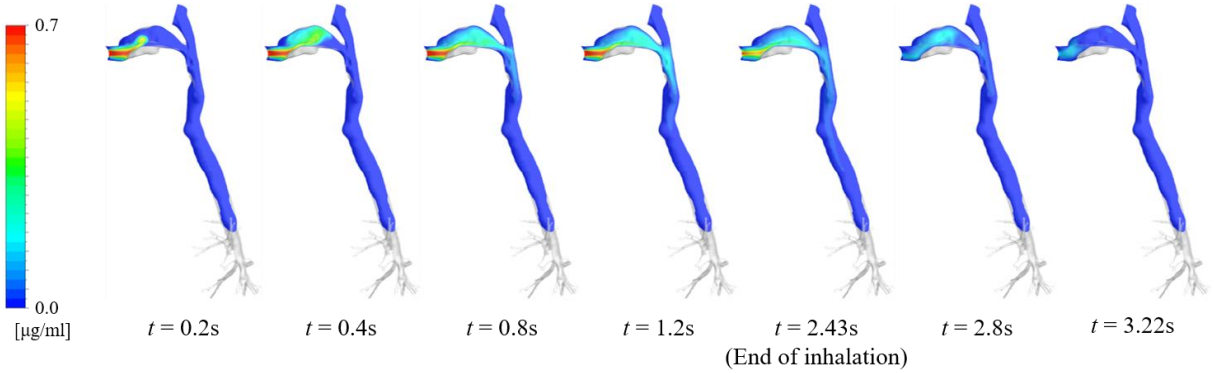

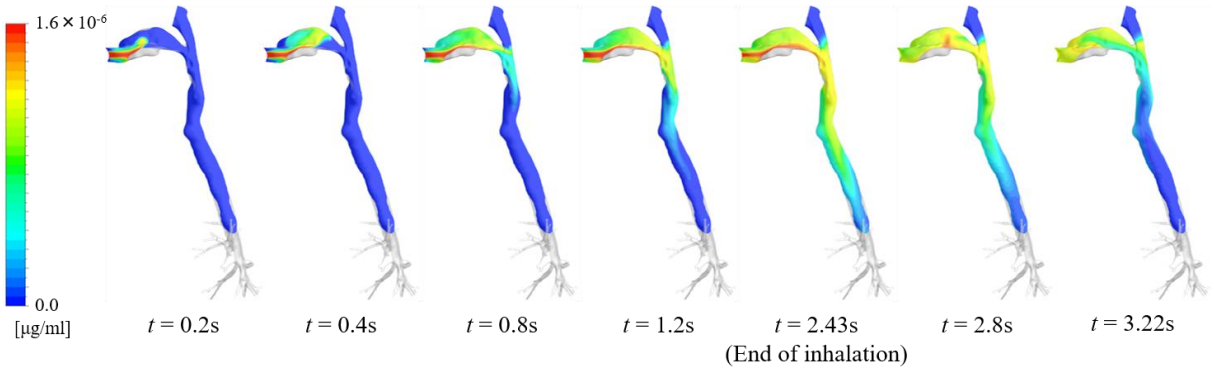

Figure 5.6. Time series of contaminant concentration distributions in the respiratory tract model under the short-puff profile: (a) formaldehyde and (b) benzene

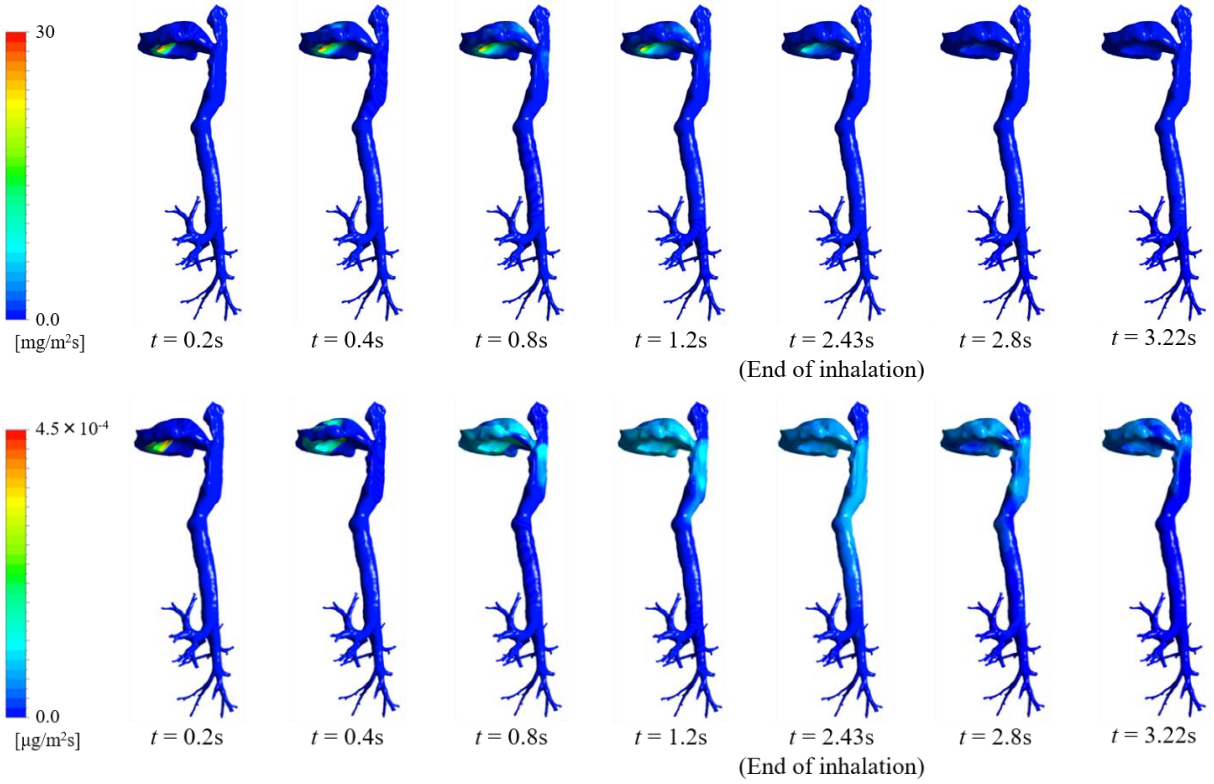

Figure 5.7. Time series of contaminants absorption flux distributions onto the respiratory surface under the short-puff profile: (a) formaldehyde and (b) benzene

Fig. 5.8 summarizes the contribution and distribution of contaminants generated from e-cigarette smoking under three different puffing profiles separating into (a) absorption rate, (b) exhalation rate and (c) rate of the remaining respiratory tract or transport lungs. The higher absorption rate of formaldehyde (88~95 %), glycerol (76~90 %), and nicotine (70~86 %) may be attributed to their higher solubility in the mucus layer compared with acetaldehyde (32~81 %), acrolein (23~72 %), benzene (0.2~2.2 %), and toluene (0.3~3.1 %). These relationships significantly affect the exhalation rate and the rate of the remaining respiratory tract of transport lungs. The absorption rate of the long-puff leads to elevated contaminant uptakes compared to the short-puff. Therefore, if the total puff volume is almost

the same, the long-puff with a lower puff intensity induces higher total absorption than the short-puff with a higher puff intensity. The post-puff with a high flow rate leads to lower absorption rates with larger contaminant quantities transported to the lungs compared to the two other puffing profiles. This means that this puffing profile has the lowest exhalation rate of all contaminants among the three post-puffing behaviors.

Zhang *et al*. [39] conducted CFD simulations focusing on the deposition fraction of acetaldehyde and acrolein on the respiratory surface under three puffing profiles; (i) potential reduced exposure product (PREP) puff, (ii) conventional cigarette (CC) puff and (iii) post-puff. They used the quasi-steady mucus absorption boundary condition proposed by Keyhani *et al*. [35] to estimate the absorption flux on the respiratory surface. They focused only on the deposition fraction during the inhalation period. The deposition fraction was 83, 74 and 64 % for acetaldehyde, and 79, 68 and 53 % for acrolein under PREP puff, CC puff and post-puff, respectively. Their acetaldehyde and acrolein deposition fractions under PREP puff and post-puff were higher than the short and post-puffs in the present study, despite neglecting the exhalation period. Conversely, Tian and Longest [37] analyzed the deposition fraction of acetaldehyde and benzene under ordinary breathing (inhalation and exhalation) conditions, similar to the post-puff profile in the present study. They developed an air-mucus-tissue-blood (AMTB) boundary condition to predict different absorption concentrations in each layer for realistic transient flux conditions. The deposition fraction was 21.49 % for acetaldehyde and 0.82 % for benzene. Our results were in good agreement with these results.

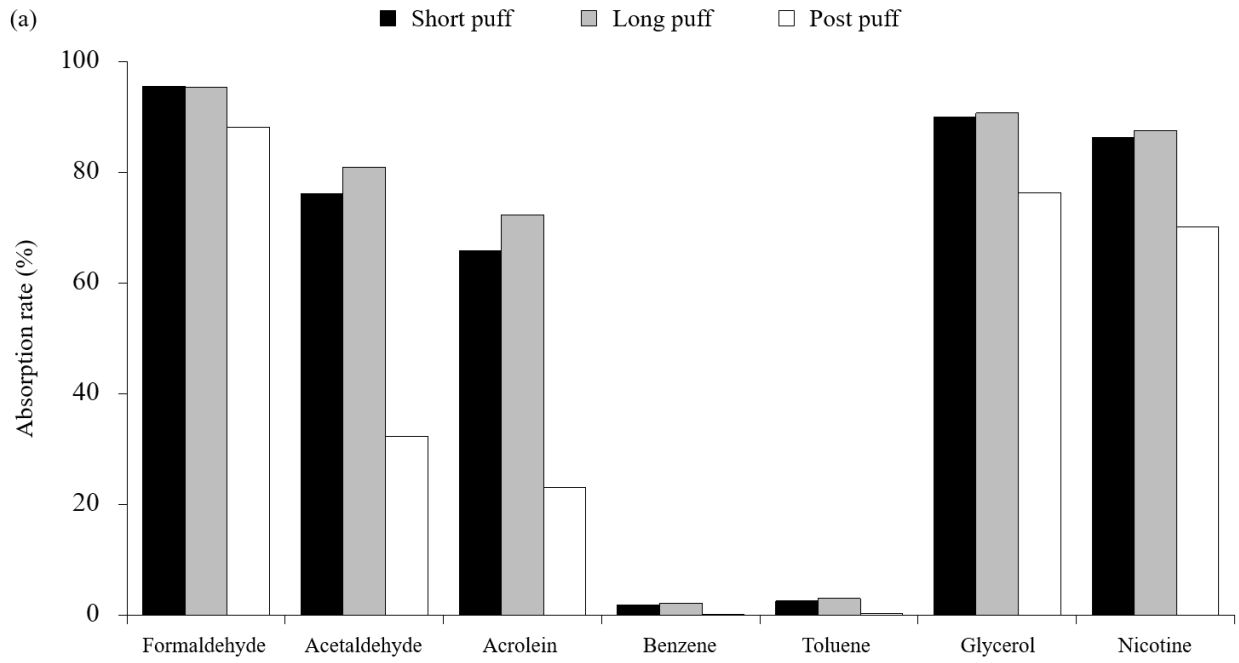

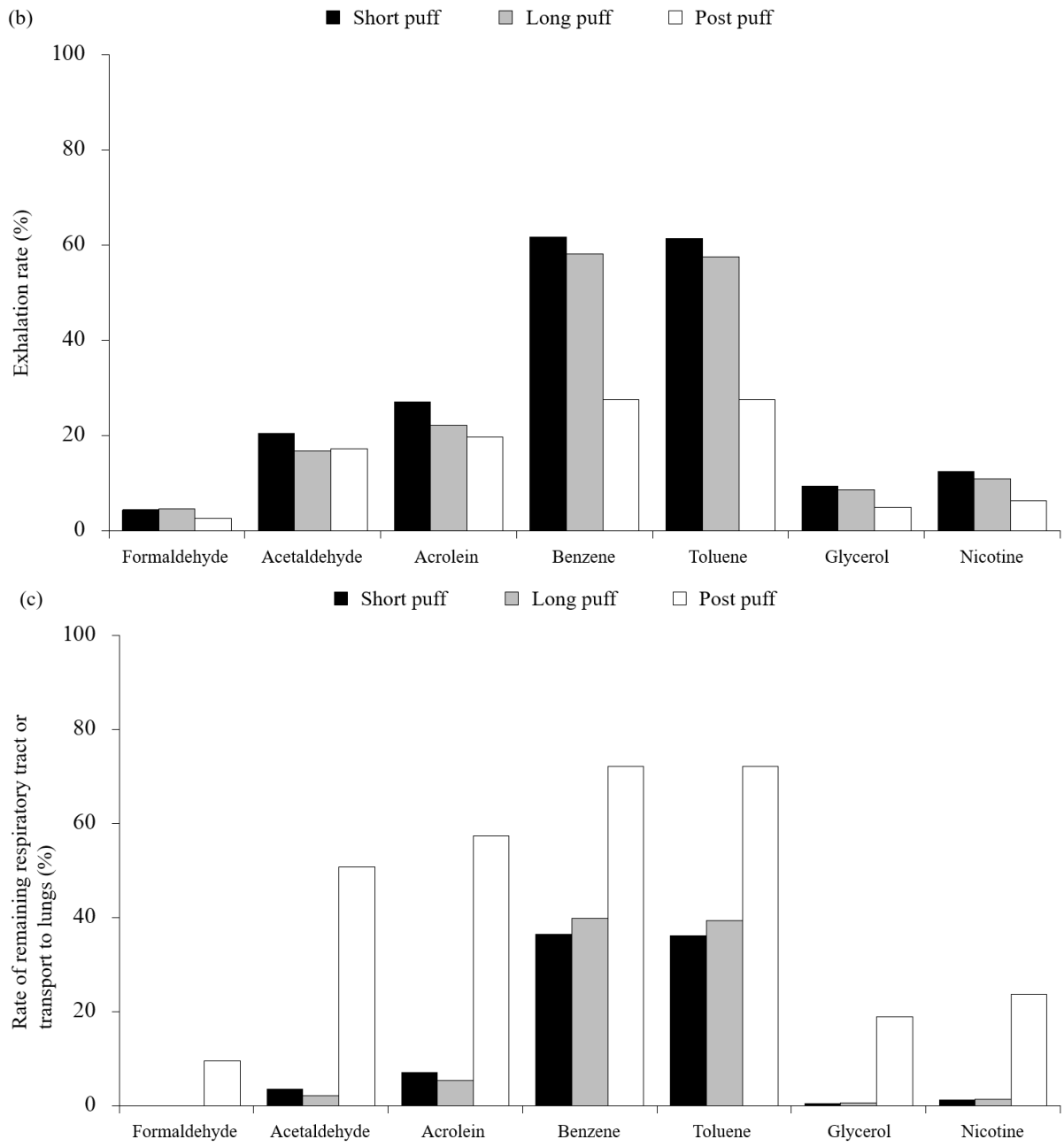

Figure 5.8. Distributions/contributions of contaminants generated from e-cigarette smoking under three different puffing profiles: (a) absorption rate onto respiratory surface, (b) exhalation rate in indoor environment, and (c) rate of remaining respiratory tract or transport lungs

Fig. 5.9 shows a time series of contaminant concentration distributions plotted against the penetration depth in the respiratory tissue. The concentrations of formaldehyde, benzene, and nicotine were depicted at the hotspot where high absorption flux was confirmed in the oral cavity. The concentration profiles in the respiratory tissues gradually changed due to diffusive transport and time-dependent change of absorbed contaminants in the interface between the air-side and mucus. These profiles were strongly affected by the diffusion and partition coefficients along with the metabolic clearance rate of each chemical compound. Formaldehyde transported into the epithelium layer reacted

and decomposed due to metabolism. However, without considering the metabolic clearance of benzene and nicotine, these were not decomposed and transported into the sub-epithelium layer. This highlights that the metabolic clearance rate is an important factor for assessing chemical dosimetry. The concentration gap at the interface between the mucus and epithelial layers for benzene and nicotine were due to the effect of the mucus-epithelium partition coefficient. For example, formaldehyde is less soluble in tissue than in mucus at the mucus-tissue interface (P_{tm} = 0.831) whilst benzene is more soluble (P_{tm} = 1.36). As such, concentrations of formaldehyde are lower in the epithelium compared with the mucus, and those of benzene are higher.

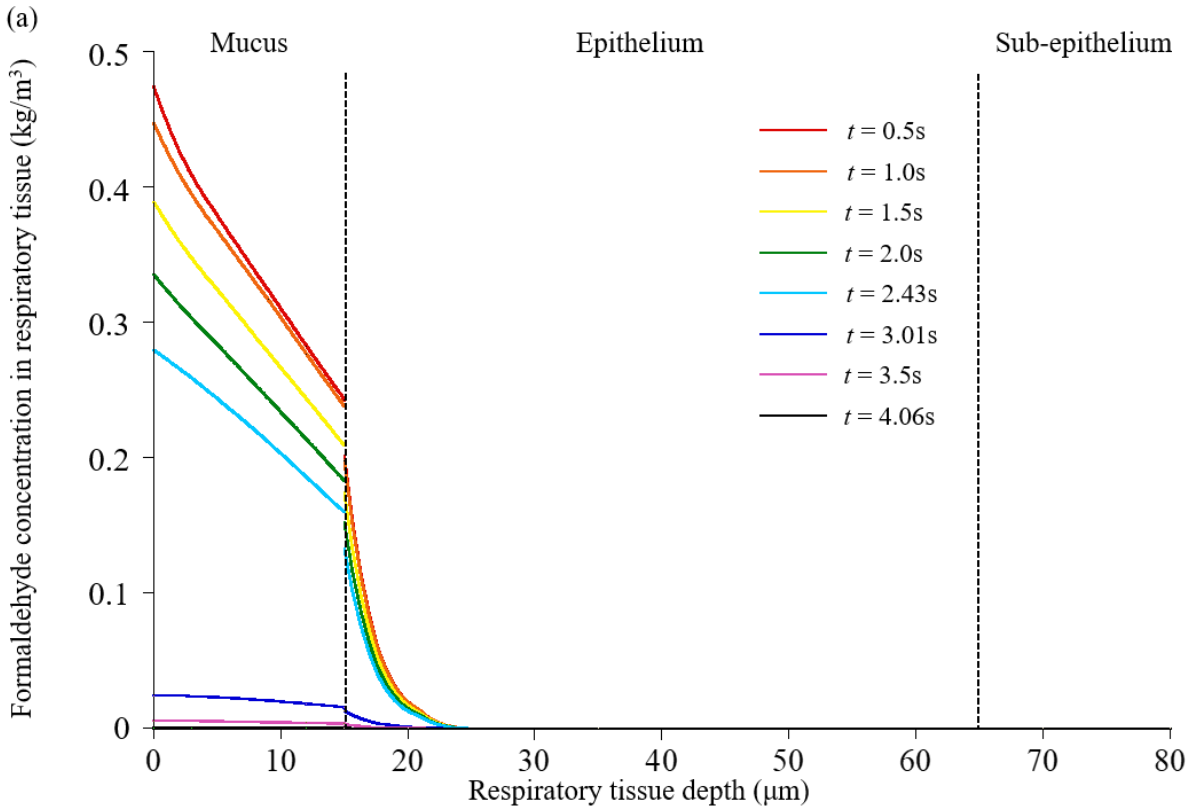

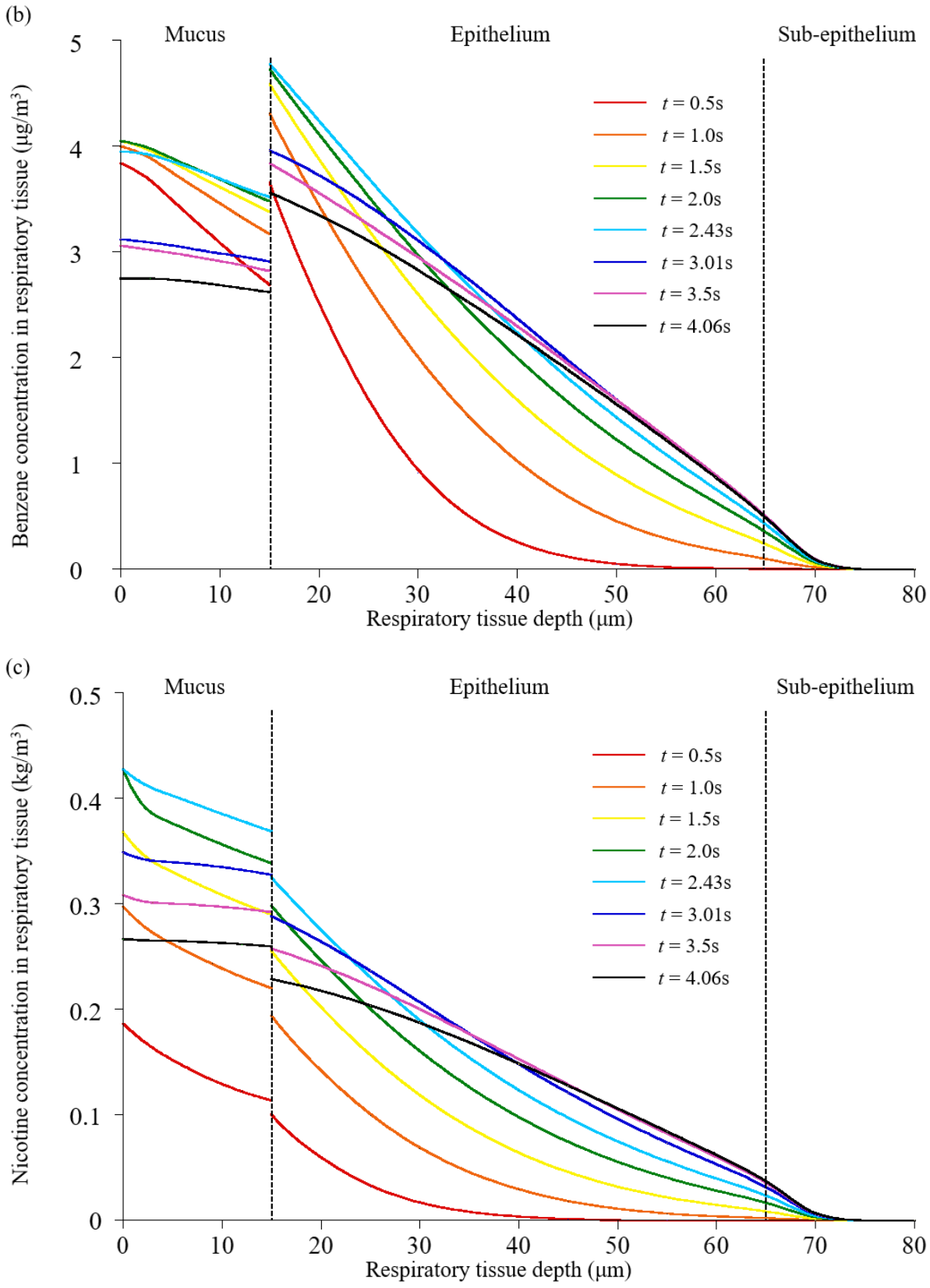

Figure 5.9. Time series of contaminant concentration profiles inside the respiratory tissue at the hotspot in the oral cavity: (a) formaldehyde, (b) benzene, and (c) nicotine

5.3.2 Validation of inhalation exposure analysis

Our simulations of inhalation exposure analyses are typical of in silico models which generally should be validated through comparisons with experimental results including in vivo and in vitro studies. However, for in silico models targeting human health, experiments using human subjects are limited because of ethical considerations. This means the prediction accuracy of our simulations in terms of contaminant concentration distribution and absorption flux distribution cannot be directly validated. Instead, prediction accuracy was validated via respiratory retention by comparison with other experimental research. A respiratory retention rate (%) was calculated for each contaminant using Equation (34):

$$\text{Retention (\%)} = \left(1 - \frac{\text{the amount of exhaled comtaminant}}{\text{the amount of inhaled contaminant}}\right) \times 100 \tag{5-34}$$

St. Helen *et al*. [95] performed subjective tests by recruiting 13 healthy adult e-cigarette users to measure the respiratory retention of nicotine, propylene glycol (PG) and vegetable glycerin (VG) in e-cigarette users. Their research results indicated that 93.8, 84.4, 91.7 % of inhaled nicotine, PG and VG, respectively, was systemically retained. Sleiman *et al*. [96] reported on the respiratory retention of nine inhaled chemicals (formaldehyde, acetaldehyde, acrolein, diacetyl, acetol, glycidol, nicotine, nicotyrine, and benzene) in four volunteer e-cigarette users. The average respiratory retention of formaldehyde, acetaldehyde, acrolein, nicotine, and benzene was 94, 70, 93, 99, and 57 %, respectively. Samburova *et al*. [97] estimated the respiratory retention of formaldehyde and acetaldehyde by measuring concentrations in e-cigarette vapors produced directly by using e-cigarettes and in the exhaled breath of 12 volunteers. Their results showed that the mean retention of formaldehyde was 99.6 ± 0.9 % for all subjects while that of acetaldehyde was 91.6 ± 9.9 %. Moldoveanu and St. Charles [98] investigated the respiratory retention of 160 chemical compounds in the smoke of traditional cigarettes using eight subjects. Their results showed that the average retention rate was 77.2 % for benzene, 52.2 % for glycerol and 85.1 % for nicotine. A comparison of respiratory retention between our simulation and these experimental results are summarized in Fig. 5.10. The experimental results of this study show large variability in respiratory retention due to individual differences attributed to puffing behaviors, geometrical differences in the respiratory tract and the variety of cigarettes. However, the trends of respiratory retention for each contaminant in our simulations agree well with that in the literature.

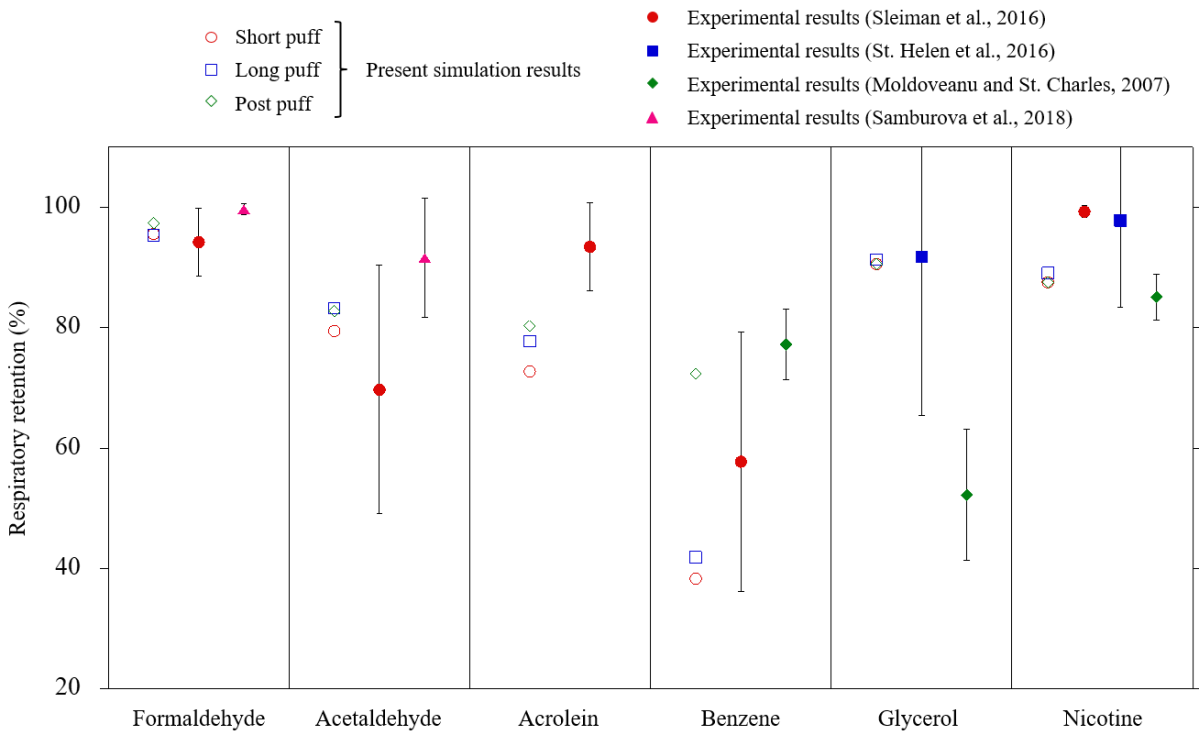

Figure 5.10. Comparison of respiratory retention between the present simulation results and published experimental results

5.3.3 Inhalation and dermal exposure of the passive smoker

Fig. 5.11 presents the velocity magnitude and temperature distributions in the periphery of the e-cigarette user and passive smoker under steady-state conditions (with metabolic heat generation and without respiration). A clear thermal plume and thermal stratification caused by heat generation from the bodies was confirmed. These flow patterns and temperature distributions were used to setup the initial conditions needed for the analysis of contaminant distributions exhaled from e-cigarette users and contaminant exposure to the passive smoker.

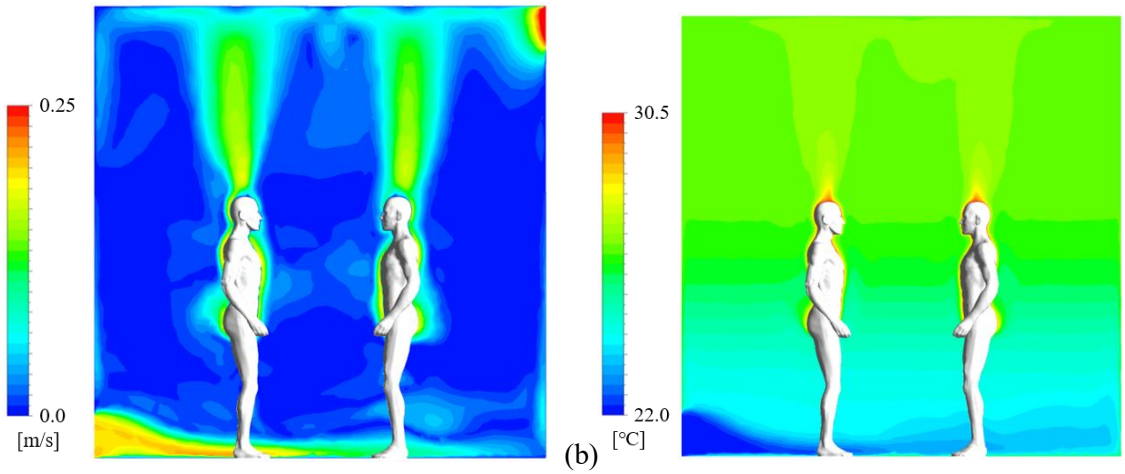

Figure 5.11. The velocity magnitude and temperature distributions in the periphery of the e-cigarette user and passive smoker under steady-state conditions

Fig. 5.12 illustrates a time series of formaldehyde distribution exhaled from the e-cigarette user under a post-puff profile and exposure to the passive smoker. Fig. 5.13 shows a time series of dermal absorption flux distribution of the passive smoker. This transient simulation was initialized using the steady-state analysis results in Fig. 5.11, as the initial conditions.

The contaminants that remained in the respiratory tract of the e-cigarette user were exhaled indoors and transported to the front of the passive smoker's face in approximately 2.0 s. The high flow rate of the post-puff profile led to a long transport distance via exhalation. In this ventilation and room volume conditions, we can assume the exhaled contaminants to be similar to pulse generation phenomenon when compared to a nominal time scale. As such, the exhaled contaminant concentrations were diluted instantaneously in the indoor environment. This dilution meant that the contaminant concentrations in the inhalation area of the passive smoker were approximately 10 % that of the initial exhaled contaminant concentrations. The dermal absorption was concentrated on the surface of the face of the passive smoker because contaminants were transported straight to the front of the face. The dermal absorption flux reduced as contaminant concentration diluted with time.

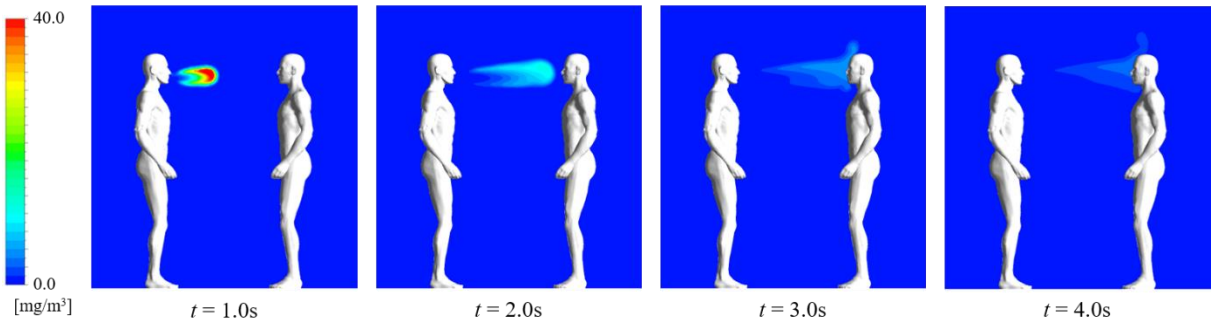

Figure 5.12. Distributions of formaldehyde exhaled from the e-cigarette user under a post-puff profile and exposure to the passive smoker

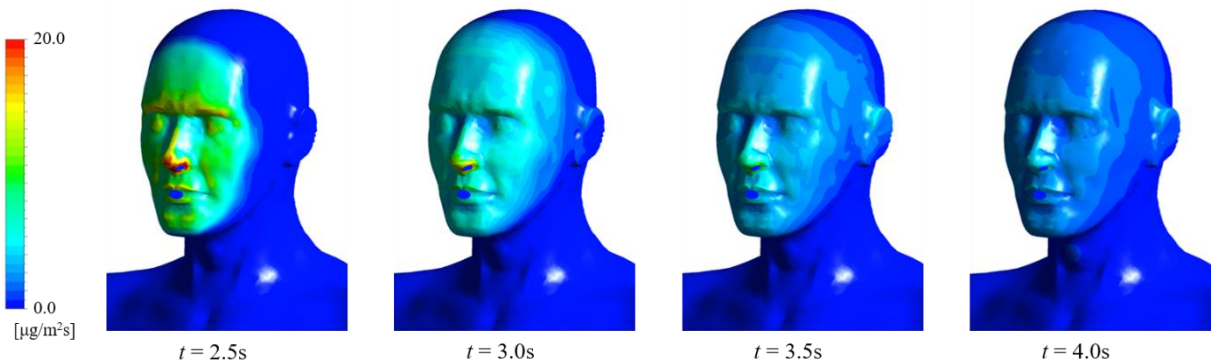

Figure 5.13. Time series of dermal absorption flux distribution of formaldehyde onto face surface of passive smoker

Fig. 5.14 presents a time series of inhaled and dermal absorbed formaldehyde mass flow rate. The passive smoker was exposed to contaminants released indoors by exhalation from the e-cigarette user. These contaminants were inhaled by the passive smoker via transient nasal breathing. The total inhaled mass of contaminants was dependent on the nasal breathing cycle, the start time of inhalation/exhalation of the e-cigarette user and passive smoker and the ventilation system and ventilation rate. We estimated that approximately 5.7 % of the formaldehyde exhaled by the e-cigarette user was inhaled by the passive smoker in three inhalations. On the other hand, 6.4 % of exhaled formaldehyde was taken up by the passive smoker via dermal uptake. The exposure rates of the other contaminants are summarized in Fig. 5.15. The inhalation uptake of each contaminant had low dependence on the chemical species and was approximately 6 % of the exhaled contaminant from the e-cigarette user. This inhalation uptake means the absorption of the contaminant to the body is via nasal breathing. Instead of applying the PBPK model to the inhalation exposure of the passive smoker, we assumed that the whole contaminant inhaled by nasal breathing was absorbed into the respiratory tract and the exhaled contaminant concentration of the passive smoker was zero. This may somewhat reflect reality because the geometry of the nasal cavity is narrow and complicated and absorption during nasal breathing was much higher than oral breathing. This means this case may be representative of the worst-case scenario. However, the contribution of the dermal uptake is strongly dependent on the chemical compound in question. Approximately 0.4 % of the formaldehyde inhaled by the e-cigarette user was retained by the passive smoker through inhalation exposure (first-hand exposure). Weschler and Nazaroff [53] estimated that formaldehyde dermal uptake was small compared to inhalation. In contrast, our simulation results showed that formaldehyde dermal uptake was higher than inhalation because we used a high SSL-air partition coefficient of formaldehyde ($P_{SSL:a}$=3.02×10^4), compared to Weschler and Nazaroff [53] ($P_{SC:a}$<100).

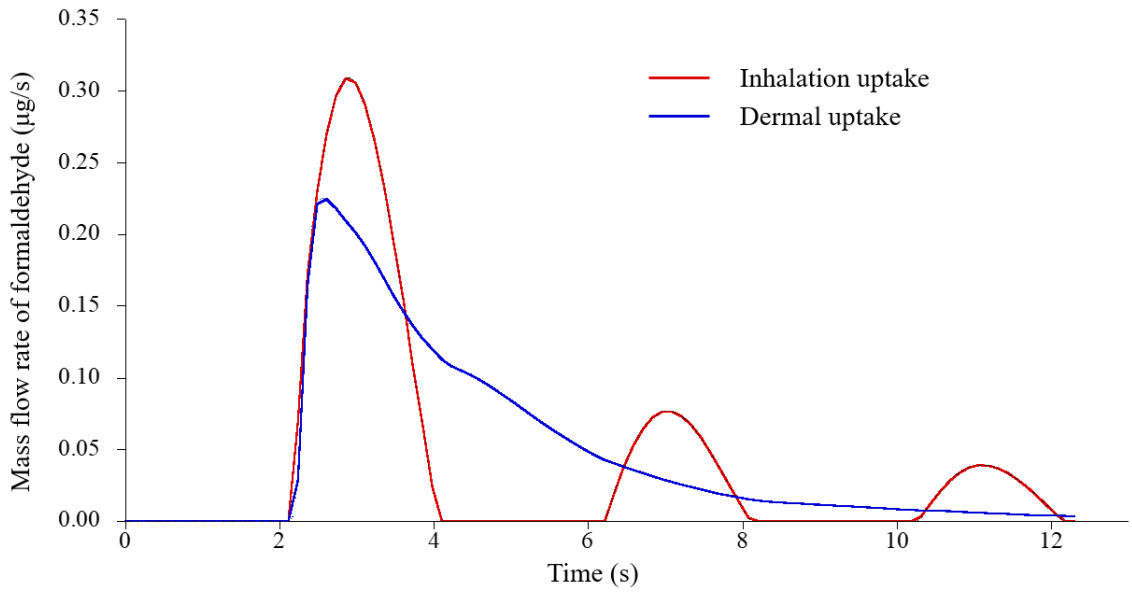

Figure 5.14. Time series of mass flow rate of inhaled formaldehyde and dermal absorption of formaldehyde for the passive smoker

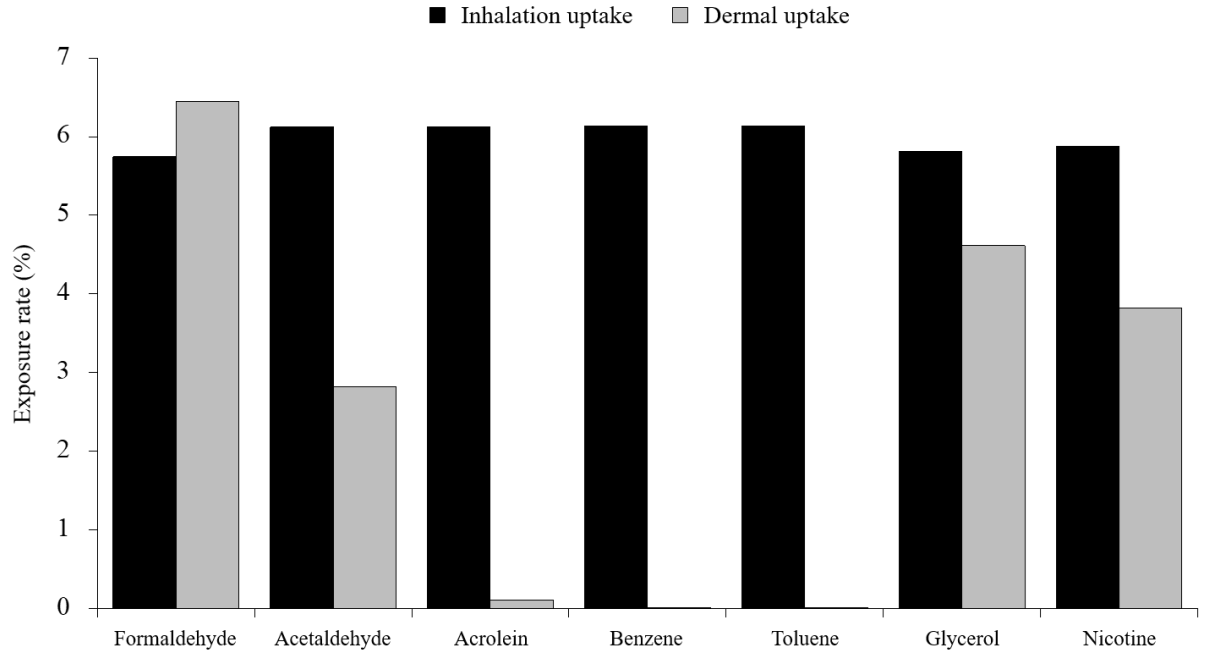

Figure 5.15. Impact of a single puff from an e-cigarette smoker on the exposure rate of passive smoking

5.4 Limitations of this study

There have been reports of inhalation exposure/toxicology analysis of inhaled gas-phase contaminants using integrated simulations of a realistic numerical airway model and the PBPK model. The prediction accuracies and consistencies of these studies with in vivo and in vitro results were discussed in Section 5.3.2. CFD analyses for airflow and contaminant concentration distributions in indoor environments have also been conducted in recent decades. Benchmark test results confirming the prediction accuracy of indoor CFD analyses have been adopted for validation and verification. In this study, we proposed an integrated and consecutive numerical analysis to investigate inhalation and dermal exposure of first-hand and second-hand smoking from indoor e-cigarette usage. The proposed method was verified theoretically or experimentally through individual elements of numerical models/analyses. However, discussion on the overall prediction accuracy is difficult and this may be an issue in the future.

In this study, we focused on gas-phase chemical compounds as contaminants generated by e-cigarette smoking and disregarded aerosols. Although temperature conditions were carefully considered, water vapor concentration was not considered in this analysis. The effects of gas-phase chemicals on inhalation exposure risk when coexisting with aerosol particles were not been fully elucidated and further research to investigate this may be required.

Fig. 5.10 demonstrates that the agreement of respiratory retention between experimental and simulated results is reasonable for each chemical compound. However, there are limitations with the accuracy of estimated parameters. Although the physical properties of the mucus including the

diffusivity and partition coefficient was assumed to be equal to that of water, the properties of mucus are not always the equivalent of to those of water. In particular, the mucus-air partition coefficient (P_{ma}) may be relatively high compared to the water-air partition coefficient (P_{wa}) [99]. Moreover, the diffusion coefficient in mucus may be less than that for water [100]. As such, absorption onto the mucus layer may be an under or overestimate. Uncertainty in the accuracy of the PBPK model is a major limitation of this study.

Whilst the exposure rate of the passive smoker was made explicit in this study, this rate is strongly dependent on the boundary conditions; in particular, the location of the e-cigarette user relative to the passive smoker. As such, the current simulation adopts a worst case scenario which demonstrates the deterioration of IAQ by e-cigarette smoking and determines the second-hand exposure. In terms of dermal exposure, we focused on short term exposure to e-cigarette smoke. In contrast, all experimental studies on dermal exposure have focused on the long term exposure, indicating that it was difficult to directly validate our simulations of dermal exposure by comparing them with those in previous experimental studies.

5.5 Conclusions

The exhaled air of an e-cigarette user may be a new source of contaminant emissions in an indoor environment exposing non-smokers via the respiratory and dermal pathways. The various gas-phase volatile and semi-volatile organic compounds from e-cigarette devices are first transported to the human respiratory system as mainstream smoke. To quantify the deterioration of IAQ due to e-cigarette smoking, it is essential to establish an accurate numerical prediction that can concurrently reproduce a series of transient puffing profiles, that is, the inhalation and exhalation processes in the respiratory tract within an indoor environment.

In this study, we developed comprehensive numerical analyses using CSPs with respiratory tract and indoor CFD techniques to investigate the contribution ratio of exposures to emitted chemical compounds from e-cigarette smoking for smokers and non-smokers. The numerical analyses were undertaken using a simple room model occupied by two residents; a smoker and non-smoker. The results showed that the amount of chemical compounds absorbed in the respiratory tract and the concentration of chemical compounds contained in the exhaled air are strongly dependent on the type of chemical. The retention rate of inhaled chemical compounds in the respiratory tract agreed well with previous experimental results. Our results also confirmed that chemicals exhaled into the indoor environment by the e-cigarette user become emerging indoor air pollutants and are taken up by the non-smoker through inhalation and dermal exposure by way of advection and diffusion that occur indoors. Formaldehyde taken up by the non-smoker through inhalation and dermal exposure under a worst case scenario was estimated to be 5.7 and 6.4 %, respectively.

References

1. Murray CJ, Lopez AD. 1997. Global mortality, disability, and the contribution of risk factors: Global Burden of Disease Study. The lancet, 349(9063), 1436-1442.
2. Peto R, Boreham J, Lopez AD. 1996. Mortality from smoking in developed countries. Oxford University Press.
3. Hecht SS. 2002. Cigarette smoking and lung cancer: chemical mechanisms and approaches to prevention. The lancet oncology, 3(8), 461-469.
4. Hecht SS. 2003. Tobacco carcinogens, their biomarkers and tobacco-induced cancer. Nature Reviews Cancer, 3(10), 733-744.
5. Hecht SS, Yuan JM, Hatsukami D. 2010. Applying tobacco carcinogen and toxicant biomarkers in product regulation and cancer prevention. Chemical research in toxicology, 23(6), 1001-1008.
6. Burns DM, Dybing E, Gray N, Hecht S, Anderson C, Sanner T, O'Connor R, Djordjevic M, Dresler C, Hainaut P, Jarvis M. 2008. Mandated lowering of toxicants in cigarette smoke: a description of the World Health Organization TobReg proposal. Tobacco control, 17(2), pp.132-141.
7. World Health Organization. 2017. WHO report on the global tobacco epidemic, 2017: monitoring tobacco use and prevention policies. World Health Organization.
8. Barrington-Trimis JL, Berhane K, Unger JB., Cruz TB, Urman R, Chou CP, ... & Huh J. 2016. The e-cigarette social environment, e-cigarette use, and susceptibility to cigarette smoking. Journal of Adolescent Health, 59(1), 75-80.
9. Pearson JL, Richardson A, Niaura RS, Vallone DM, Abrams DB. 2012. e-Cigarette awareness, use, and harm perceptions in US adults. American journal of public health, 102(9), 1758-1766.
10. Goniewicz ML, Hajek P, McRobbie H. 2014. Nicotine content of electronic cigarettes, its release in vapour and its consistency across batches: regulatory implications. Addiction, 109(3), 500-507.
11. Allen JG, Flanigan SS, LeBlanc M, Vallarino J, MacNaughton P, Stewart JH, Christiani DC. 2016. Flavoring chemicals in e-cigarettes: diacetyl, 2, 3-pentanedione, and acetoin in a sample of 51 products, including fruit-, candy-, and cocktail-flavored e-cigarettes. Environmental health perspectives, 124(6), 733-739.
12. Flora JW, Wilkinson CT, Wilkinson JW, Lipowicz PJ, Skapars JA, Anderson A, Miller JH. 2017. Method for the determination of carbonyl compounds in e-cigarette aerosols. Journal of chromatographic science, 55(2), 142-148.
13. Wang P, Chen W, Liao J, Matsuo T, Ito K, Fowles J, Shusterman D, Mendell M, Kumagai K. 2017. A device-independent evaluation of carbonyl emissions from heated electronic cigarette solvents. PloS one, 12(1).
14. Zhao J, Nelson J, Dada O, Pyrgiotakis G, Kavouras IG, Demokritou P. 2018. Assessing electronic cigarette emissions: linking physico-chemical properties to product brand, e-liquid flavoring additives, operational voltage and user puffing patterns. Inhalation toxicology, 30(2), 78-88.
15. Chen W, Wang P, Ito K, Fowles J, Shusterman D, Jaques PA, Kumagai K. 2018. Measurement of heating coil temperature for e-cigarettes with a "top-coil" clearomizer. PloS one, 13(4), e0195925.

16. Vardavas CI, Anagnostopoulos N, Kougias M, Evangelopoulou V, Connolly GN, Behrakis PK. 2012. Short-term pulmonary effects of using an electronic cigarette: impact on respiratory flow resistance, impedance, and exhaled nitric oxide. Chest, 141(6), 1400-1406.
17. Flouris AD, Chorti MS, Poulianiti KP, Jamurtas AZ, Kostikas K, Tzatzarakis MN, Wallace Hayes A, Tsatsakis AM, Koutedakis Y. 2013. Acute impact of active and passive electronic cigarette smoking on serum cotinine and lung function. Inhalation toxicology, 25(2), pp.91-101.
18. Hua M, Alfi M, Talbot P. 2013. Health-related effects reported by electronic cigarette users in online forums. Journal of medical Internet research, 15(4), e59.
19. Popa C. 2014. Infrared spectroscopy study of the influence of inhaled vapors/smoke produced by cigarettes of active smokers. Journal of biomedical optics, 20(5), 051003.
20. Löhler J, Wollenberg B. 2019. Are electronic cigarettes a healthier alternative to conventional tobacco smoking?. European Archives of Oto-Rhino-Laryngology, 276(1), 17-25.
21. Rehan HS, Maini J, Hungin AP. 2018. Vaping versus smoking: A quest for efficacy and safety of e-cigarette. Current drug safety, 13(2), 92-101.
22. Popa C. 2016. Breathing disorders using photoacoustics gas analyzer. Journal of Medical Imaging and Health Informatics, 6(8), 1893-1895.
23. Schripp T, Markewitz D, Uhde E, Salthammer T. 2013. Does e-cigarette consumption cause passive vaping?. Indoor air, 23(1), 25-31.
24. Czogala J, Goniewicz ML, Fidelus B, Zielinska-Danch W, Travers MJ, Sobczak A. 2014. Secondhand exposure to vapors from electronic cigarettes. nicotine & tobacco research, 16(6), 655-662.
25. Marcham CL, Springston JP. 2019. Electronic cigarettes in the indoor environment. Reviews on environmental health, 34(2), 105-124.
26. Rauma M, Boman A, Johanson G. 2013. Predicting the absorption of chemical vapours. Advanced drug delivery reviews, 65(2), 306-314.
27. Rehal B, Maibach H. 2011. Percutaneous absorption of vapors in human skin. Cutaneous and ocular toxicology, 30(2), 87-91.
28. Bader, M., Wrbitzky, R., Blaszkewicz, M., Schäper, M., & van Thriel, C. (2008). Human volunteer study on the inhalational and dermal absorption of N-methyl-2-pyrrolidone (NMP) from the vapour phase. Archives of toxicology, 82(1), 13-20.
29. Bekö G, Morrison G, Weschler CJ, Koch HM, Pälmke C, Salthammer T, Schripp T, Toftum J, Clausen G. 2017. Measurements of dermal uptake of nicotine directly from air and clothing. Indoor Air, 27(2), pp.427-433.
30. Bekö G, Morrison G, Weschler CJ, Koch HM, Pälmke C, Salthammer T, Schripp T, Eftekhari A, Toftum J, Clausen G. 2018. Dermal uptake of nicotine from air and clothing: Experimental verification. Indoor Air, 28(2), pp.247-257.
31. Protano C, Vitali M. 2011. The new danger of thirdhand smoke: Why passive smoking does not stop at secondhand smoke. Environmental health perspectives, 119(10), a422-a422.

32. Ito K. 2016. Toward the development of an in silico human model for indoor environmental design. Proceedings of the Japan Academy, Series B, 92(7), 185-203.
33. Murga A, Sano Y, Kawamoto Y, Ito K. 2017. Integrated analysis of numerical weather prediction and computational fluid dynamics for estimating cross-ventilation effects on inhaled air quality inside a factory. Atmospheric Environment, 167, 11-22.
34. Murga A, Kuga K, Yoo SJ, Ito K. 2019. Can the inhalation exposure of a specific worker in a cross-ventilated factory be evaluated by time-and spatial-averaged contaminant concentration?. Environmental Pollution, 252, 1388-1398.
35. Keyhani K, Scherer PW, Mozell MM. 1997. A numerical model of nasal odorant transport for the analysis of human olfaction. Journal of Theoretical Biology, 186(3), 279-301.
36. Tian G, Longest PW. 2010. Development of a CFD boundary condition to model transient vapor absorption in the respiratory airways. Journal of biomechanical engineering, 132(5).
37. Tian G, Longest PW. 2010. Application of a new dosimetry program TAOCS to assess transient vapour absorption in the upper airways. Inhalation toxicology, 22(13), 1047-1063.
38. Tian G, Longest PW. 2010. Transient absorption of inhaled vapors into a multilayer mucus–tissue–blood system. Annals of biomedical engineering, 38(2), 517-536.
39. Zhang, Z., Kleinstreuer, C., & Feng, Y. (2012). Vapor deposition during cigarette smoke inhalation in a subject-specific human airway model. Journal of Aerosol Science, 53, 40-60.
40. Corley RA, Kabilan S, Kuprat AP, Carson JP, Minard KR, Jacob RE, Timchalk C, Glenny R, Pipavath S, Cox T, Wallis CD. 2012. Comparative computational modeling of airflows and vapor dosimetry in the respiratory tracts of rat, monkey, and human. Toxicological Sciences, 128(2), 500-516.
41. Corley RA, Kabilan S, Kuprat AP, Carson JP, Jacob RE, Minard KR, Teeguarden JG, Timchalk C, Pipavath S, Glenny R, Einstein DR. 2015. Comparative risks of aldehyde constituents in cigarette smoke using transient computational fluid dynamics/physiologically based pharmacokinetic models of the rat and human respiratory tracts. Toxicological Sciences, 146(1), 65-88.
42. Feng Y, Kleinstreuer C, Castro N, Rostami A. 2016. Computational transport, phase change and deposition analysis of inhaled multicomponent droplet–vapor mixtures in an idealized human upper lung model. Journal of aerosol science, 96, 96-123.
43. Yoo SJ, Ito K. 2018. Assessment of transient inhalation exposure using in silico human model integrated with PBPK-CFD hybrid analysis. Sustainable cities and society, 40, 317-325.
44. Yoo SJ, Ito K. 2018. Numerical prediction of tissue dosimetry in respiratory tract using computer simulated person integrated with physiologically based pharmacokinetic–computational fluid dynamics hybrid analysis. Indoor and Built Environment, 27(7), 877-889.
45. Haghnegahdar A, Feng Y, Chen X, Lin J. 2018. Computational analysis of deposition and translocation of inhaled nicotine and acrolein in the human body with e-cigarette puffing topographies. Aerosol Science and Technology, 52(5), 483-493.
46. Gao N, Niu J. 2004. CFD study on micro-environment around human body and personalized

ventilation. Building and Environment, 39(7), 795-805.
47. Gao N, Niu J, Zhang H. 2006. Coupling CFD and human body thermoregulation model for the assessment of personalized ventilation. Hvac&R Research, 12(3), 497-518.
48. Gao N, Niu J. 2006. Transient CFD simulation of the respiration process and inter-person exposure assessment. Building and Environment, 41(9), 1214-1222.
49. Gao NP, Zhang H, Niu JL. 2007. Investigating indoor air quality and thermal comfort using a numerical thermal manikin. Indoor and built environment, 16(1), 7-17.
50. Zhu S, Kato S, Ooka R, Sakoi T. 2007. Development of a computational thermal manikin applicable in a nonuniform thermal environment—Part 1: Coupled simulation of convection, radiation, and Smith's human thermal physiological model for sensible heat transfer from a seated human body in radiant environment. HVAC&R Research, 13(4), 661-679.
51. Zhu S, Kato S, Ooka R, Sakoi T, Tsuzuki K. 2008. Development of a computational thermal manikin applicable in a non-uniform thermal environment—Part 2: Coupled simulation using Sakoi's human thermal physiological model. HVAC&R Research, 14(4), 545-564.
52. Weschler CJ, Nazaroff WW. 2012. SVOC exposure indoors: fresh look at dermal pathways. Indoor air, 22(5), 356-377.
53. Weschler CJ, Nazaroff WW. 2014. Dermal uptake of organic vapors commonly found in indoor air. Environmental science & technology, 48(2), 1230-1237.
54. Gong M, Zhang Y, Weschler CJ. 2014. Predicting dermal absorption of gas-phase chemicals: transient model development, evaluation, and application. Indoor Air, 24(3), 292-306.
55. Morrison GC, Weschler CJ, Bekö G. 2016. Dermal uptake directly from air under transient conditions: advances in modeling and comparisons with experimental results for human subjects. Indoor air, 26(6), 913-924.
56. Morrison GC, Weschler CJ, Bekö G. 2017. Dermal uptake of phthalates from clothing: Comparison of model to human participant results. Indoor Air, 27(3), 642-649.
57. Cao J, Zhang X, Zhang Y. 2018. Predicting dermal exposure to gas-phase semivolatile organic compounds (SVOCs): a further study of SVOC mass transfer between clothing and skin surface lipids. Environmental science & technology, 52(8), 4676-4683.
58. Phuong NL, Ito K. 2015. Investigation of flow pattern in a realistic replica model of human respiratory tract using PIV. Build Environ, 94, 504-515.
59. Phuong NL, Yamashita M, Yoo SJ, Ito K. 2016. Prediction of convective heat transfer coefficient of human upper and lower airway surfaces in steady and unsteady breathing conditions. Building and Environment, 100, 172-185.
60. Xi J, Longest P. 2008. Effects of oral airway geometry characteristics on the diffusional deposition of inhaled nanoparticles. Journal of biomechanical engineering, 130(1).
61. Gupta JK, Lin CH, Chen Q. 2010. Characterizing exhaled airflow from breathing and talking. Indoor air, 20(1), 31-39.
62. Vansickel AR, Edmiston JS, Liang Q, Duhon C, Connell C, Bennett D, Sarkar M. 2018.

Characterization of puff topography of a prototype electronic cigarette in adult exclusive cigarette smokers and adult exclusive electronic cigarette users. Regulatory Toxicology and Pharmacology, 98, 250-256.

63. Farsalinos KE, Romagna G, Tsiapras D, Kyrzopoulos S, Voudris V. 2013. Evaluation of electronic cigarette use (vaping) topography and estimation of liquid consumption: implications for research protocol standards definition and for public health authorities' regulation. International journal of environmental research and public health, 10(6), 2500-2514.
64. Charles FK, Krautter GR, Mariner DC. 2009. Post-puff respiration measures on smokers of different tar yield cigarettes. Inhalation toxicology, 21(8), 712-718.
65. Abe K, Kondoh T, Nagano Y. 1994. A new turbulence model for predicting fluid flow and heat transfer in separating and reattaching flows—I. Flow field calculations. International journal of heat and mass transfer, 37(1), 139-151.
66. Abe K, Kondoh T, Nagano Y. 1995. A new turbulence model for predicting fluid flow and heat transfer in separating and reattaching flows—II. Thermal field calculations. International Journal of Heat and Mass Transfer, 38(8), 1467-1481.
67. Lopez-Vidriero MT. 1984. Airway secretions: source, biochemical and rheological properties. Lung Biology in Health and Disease, Vol. 5, Respiratory Defence Mechanism, 239-356.
68. Mitragotri S, Johnson ME, Blankschtein D, Langer R. 1999. An analysis of the size selectivity of solute partitioning, diffusion, and permeation across lipid bilayers. Biophysical journal, 77(3), 1268-1283.
69. George SC, Babb AL, Deffebach ME, Hlastala, MP. 1996. Diffusion of nonelectrolytes in the canine trachea: effect of tight junction. Journal of Applied Physiology, 80(5), 1687-1695.
70. Sander R. 2015. Compilation of Henry's law constants (version 4.0) for water as solvent. Atmos. Chem. Phys, 15(8), 4399-4981.
71. Anderson JC, Babb AL, Hlastala MP. 2003. Modeling soluble gas exchange in the airways and alveoli. Annals of biomedical engineering, 31(11), 1402-1422.
72. Young IH, Wagner PD. 1979. Solubility of inert gases in homogenates of canine lung tissue. Journal of Applied Physiology, 46(6), 1207-1210.
73. Poulin P, Krishnan K. 1996. Molecular structure-based prediction of the partition coefficients of organic chemicals for physiological pharmacokinetic models. Toxicology Methods, 6(3), 117-137.
74. Hayduk W, Laudie H. 1974. Prediction of diffusion coefficients for nonelectrolytes in dilute aqueous solutions. AIChE Journal, 20(3), 611-615.
75. Eatough DJ, Benner CL, Bayona JM, Richards G, Lamb JD, Lee ML, Lewis EA, Hansen LD. 1989. Chemical composition of environmental tobacco smoke. 1. Gas-phase acids and bases. Environmental science & technology, 23(6), 679-687.
76. Conolly RB, Lilly PD, Kimbell JS. 2000. Simulation modeling of the tissue disposition of formaldehyde to predict nasal DNA-protein cross-links in Fischer 344 rats, rhesus monkeys, and humans. Environmental health perspectives, 919-924.

77. Teeguarden JG, Bogdanffy MS, Covington TR, Tan C, Jarabek AM. 2008. A PBPK model for evaluating the impact of aldehyde dehydrogenase polymorphisms on comparative rat and human nasal tissue acetaldehyde dosimetry. Inhalation toxicology, 20(4), 375-390.
78. Schroeter JD, Kimbell JS, Gross EA, Willson GA, Dorman DC, Tan YM, Clewell III HJ. 2008. Application of physiological computational fluid dynamics models to predict interspecies nasal dosimetry of inhaled acrolein. Inhalation toxicology, 20(3), 227-243.
79. Bogdanffy MS, Sarangapani R, Kimbell JS, Frame SR, Plowchalk DR. 1998. Analysis of Vinyl Acetate Metabolism in Rat and Human Nasal Tissues by anin VitroGas Uptake Technique. Toxicological Sciences, 46(2), 235-246.
80. Yoo S, Ito K. 2019. Multi-stage optimization of local environmental quality by comprehensive computer simulated person as a sensor for HVAC control. Advances in Building Energy Research, 1-18.
81. Wang C, Yoo SJ, Ito K. 2019. Does detailed hygrothermal transport analysis in respiratory tract affect skin surface temperature distributions by thermoregulation model?. Advances in Building Energy Research, 1-21.
82. Fanger PO. 1970. Thermal comfort. Analysis and applications in environmental engineering. Thermal comfort. Analysis and applications in environmental engineering.
83. Tanabe SI, Arens EA, Bauman F, Zhang H, Madsen T. 1994. Evaluating thermal environments by using a thermal manikin with controlled skin surface temperature.
84. Sørensen DN, Nielsen PV. 2003. Quality control of computational fluid dynamics in indoor environments. Indoor air, 13(1), 2-17.
85. Ito K, Inthavong K, Kurabuchi T, Ueda T, Endo T, Omori T, Ono H, Kato S, Sakai K, Suwa Y, Matsumoto H. 2015. CFD benchmark tests for indoor environmental problems: Part 1 isothermal/non-isothermal flow in 2D and 3D room model. International Journal of Architectural Engineering Technology, 2(1), 1-22.
86. Ito K, Inthavong K, Kurabuchi T, Ueda T, Endo T, Omori T, Ono H, Kato S, Sakai K, Suwa Y, Matsumoto H. 2015. CFD benchmark tests for indoor environmental problems: Part 2 cross-ventilation airflows and floor heating systems. International Journal of Architectural Engineering Technology, 2(1), 23-49.
87. Ito K, Inthavong K, Kurabuchi T, Ueda T, Endo T, Omori T, Ono H, Kato S, Sakai K, Suwa Y, Matsumoto H. 2015. CFD benchmark tests for indoor environmental problems: Part 3 numerical thermal manikins. International Journal of Architectural Engineering Technology, 2(1), 50-75.
88. Ito K, Inthavong K, Kurabuchi T, Ueda T, Endo T, Omori T, Ono H, Kato S, Sakai K, Suwa Y, Matsumoto H. 2015. CFD benchmark tests for indoor environmental problems: Part 4 air-conditioning airflows, residential kitchen airflows and fire-induced flow. International Journal of Architectural Engineering Technology, 2(1), 76-102.
89. Chen L, Lian G, Han L. 2008. Use of “bricks and mortar” model to predict transdermal permeation: model development and initial validation. Industrial & engineering chemistry research, 47(17),

6465-6472.
90. Mitragotri S. 2002. A theoretical analysis of permeation of small hydrophobic solutes across the stratum corneum based on scaled particle theory. Journal of pharmaceutical sciences, 91(3), 744-752.
91. Kushner IV J, Deen W, Blankschtein D, Langer R. 2007. First-principles, structure-based transdermal transport model to evaluate lipid partition and diffusion coefficients of hydrophobic permeants solely from stratum corneum permeation experiments. Journal of pharmaceutical sciences, 96(12), 3236-3251.
92. Nitsche JM, Wang TF, Kasting GB. 2006. A two-phase analysis of solute partitioning into the stratum corneum. Journal of pharmaceutical sciences, 95(3), 649-666.
93. Feng Y, Kleinstreuer C. 2011. Computational analysis of droplet evaporation and deposition in a realistic respiratory tract subject to puff-like inhalation waveforms. In Proceedings of the 2nd International Conference on Computational & Mathematical Biomedical Engineering (CMBE11).
94. Patankar S. 2018. Numerical heat transfer and fluid flow. Taylor & Francis.
95. St. Helen G, Havel C, Dempsey DA, Jacob III P, Benowitz NL. 2016. Nicotine delivery, retention and pharmacokinetics from various electronic cigarettes. Addiction, 111(3), 535-544.
96. Sleiman M, Logue J, Montesinos VN, Litter M, Russell M, Gundel L, Destaillats H. 2016. Indoor vaping: composition and health impacts of mainstream and secondhand emissions. Indoor air.
97. Samburova V, Bhattarai C, Strickland M, Darrow L, Angermann J, Son Y, Khlystov A. 2018. Aldehydes in exhaled breath during e-cigarette vaping: pilot study results. Toxics, 6(3), 46.
98. Moldoveanu SC, Charles FS. 2007. Differences in the chemical composition of the particulate phase of inhaled and exhaled cigarette mainstream smoke. Beiträge zur Tabakforschung International/Contributions to Tobacco Research, 22(4), 290-302.
99. Scott JW, Sherrill L, Jiang J, Zhao K. 2014. Tuning to odor solubility and sorption pattern in olfactory epithelial responses. Journal of Neuroscience, 34(6), 2025-2036.
100. Khanvilkar K, Donovan MD, Flanagan DR. 2001. Drug transfer through mucus. Advanced drug delivery reviews, 48(2-3), 173-193.

[Previously published documents related to this chapter]

1. Kuga K, Ito K, Yoo SJ, Chen W, Wang P, Liao J, Fowles J, Shusterman D, Kumagai K. 2018. First- and second-hand smoke dispersion analysis from e-cigarettes using a computer-simulated person with a respiratory tract model. Indoor and Built Environment, 27(7), 898-916.
2. Kuga, K., Ito, K., Chen, W., Wang, P., & Kumagai, K. (2020). A numerical investigation of the potential effects of e-cigarette smoking on local tissue dosimetry and the deterioration of indoor air quality. Indoor air.

Chapter 6: Experimental investigation of effect of environmental factors on CO_2 emission from humans and physiological response

6.1 Introduction

Indoor carbon dioxide (CO_2) concentration is used as a surrogate of indoor air quality (IAQ) and thus as an indicator of ventilation efficiency in buildings. In the absence of any other indicators of IAQ, numerous studies have correlated measured CO_2 levels in buildings with occupant complaints, subjective ratings, health, performance of office work, learning and absence rates [1,2]. Measured concentrations of CO_2 have also been used to estimate the outdoor air supply rates in buildings and the estimated ventilation rate often correlated with the outcomes mentioned above [3]. To estimate outdoor air supply rates the CO_2 emission rate from building occupants is normally assumed to take the values listed by standards and handbooks [4] for different activity (metabolic) levels. It is further assumed that no other factors have a significant impact on the occupant emission rates of CO_2.

Recently, Tsushima et al. [5] studied how human bioeffluents influence perceived levels of IAQ. They determined the impact of bioeffluents emitted through skin (dermally), exhaled (during respiration) and by the whole-body i.e. both dermally emitted and exhaled. Subjects assessed the quality of air extracted from chambers where other subjects sat and performed light office work at two temperatures, 23°C and 28°C; these subjects wore similar clothing at both temperatures. The subjects who assessed the air quality did not know the source of the odour but rated it higher when the temperature in the upstream chamber was higher after controlling for an effect of temperature on perception by providing clean air at the same temperature for sensory comparison [6]. The authors suggested that the higher odour intensity could be caused by an increased rate of emission of bioeffluents at increased temperature. They concluded that when experiencing thermal discomfort due to warmth people emit more bioeffluents, including CO_2, even though their activity level remains the same. However, activity was not measured by Tsushima et al. and they did not observe any changes in CO_2 level in the chamber. It would be logical to assume that activity level would be consciously or unconsciously reduced to avoid thermal discomfort, and that this would reduce the emission rate of CO_2, but the opposite was found. Another possible explanation was that heat was removed mainly by an increase in sweat rate and not by an increase in respiration but it requires further explanation. If occupant emission rates of bioeffluents and CO_2 increase at temperatures that cause thermal discomfort, the ventilation rates prescribed by ventilation standards should be adjusted accordingly, but they are not except in the Australian standard which recommends higher ventilation rates when the air temperature is 27°C and above, presumably to deal with an increased level of bioeffluents [7].To this end another

important question is whether remaining thermally neutral at elevated temperatures by e.g. adjusting clothing or increasing the air velocity will have no effect on CO_2 emission rate i.e. whether other physiological processes are activated at elevated temperatures that would result in energy use and thus increase on CO_2 emission rates. Further studies are needed to determine whether this is true.

In a reanalysis of the results of studies examining the effects of air quality on the performance of office work, Bako-Biro et al. [8] showed that occupant CO_2 emission rates were affected by air quality. They showed that it was significantly reduced, by about 13%, when the percentage dissatisfied with the air quality increased from 8% to 40%. It was suggested by the authors that a change in breathing pattern (shallow breathing) or a reduction in workrate in polluted air may have given rise to the observed result, they had no measures of either of these factors and cited Danuser [9] on breathing patterns. This author had reviewed several studies and showed that changes in breathing patterns (tidal volume) can be induced by exposure to chemicals at environmentally relevant levels. One finding was that these changes can be elicited even in anosmic people, i.e. in those who are deprived of any olfactory sense. Changes in breathing patterns in response to chemicals present in the inhaled air were also observed in mouse bioassay reported by Larsen et al. [10].

Recently, Zhang et al. [11] studied the physiological responses of subjects exposed for 255 minutes to an elevated concentration of CO_2 with or without other bioeffluents. They observed that when CO_2 concentration increased from 500 ppm to 3,000 ppm (either by dosing CO_2 from a cylinder, i.e. keeping levels of other bioeffluents unchanged and varying the level of CO_2, or by reducing ventilation rate so as to increase the levels of metabolically generated CO_2 and other bioeffluents), the end-tidal CO_2 concentration ($ETCO_2$) increased. $ETCO_2$ is the concentration of CO_2 in exhaled air at the end of an exhalation and reflects the blood gas concentration of CO_2 in the alveoli of the lungs. This suggests that the exposures they studied could influence gas exchange in the lungs, as postulated by Bako-Biro et al. [8] and Danuser [9]. During gas exchange, CO_2 that has been metabolically generated in cells enters the bloodstream and is transported through the venous blood into the lungs where it diffuses into the air in the alveoli of the lungs due to the CO_2 concentration difference between the blood and the air in the alveoli. It is then released into the extracorporeal environment by exhalation [12]. When the inhaled CO_2 concentration is elevated above normal ambient levels (currently >400 ppm), the CO_2 concentration in the alveoli is also higher and the transportation of CO_2 from the blood to the air in the alveoli may be decreased. This would cause the CO_2 concentration in blood to be elevated, and acute health symptoms could then occur. Consequently, these processes can affect the occupant emission rate of CO_2 and cause health problems [13]. The effect observed by Zhang et al. [11] was postulated to be caused by a reduced minute ventilation, although this was not measured. The authors measured heart rate and observed that it was lower at the higher CO_2 concentration. As the heart rate and minute ventilation are strongly correlated [14] they inferred that this was what had increased $ETCO_2$. Changes in respiration rate and tidal volume could have affected $ETCO_2$ but the former did not change and the

latter was not measured. The studies mentioned above suggest that increased air pollution caused by increasing the levels of CO_2, bioeffluents or other pollutants to the levels that are typically observed indoors may reduce the rate of elimination of CO_2 from the lungs. If so, it may be expected that it will also affect the CO_2 produced and exhaled by humans.

The present study was consequently undertaken to examine the effects on occupant emission of CO_2 of an increased background CO_2 concentration level with and without other bioeffluents, and of elevated temperature causing thermal discomfort. An additional aim was to develop physiological explanations for these effects should CO_2 emission rates prove to be affected.

6.2 Fundamental knowledge of CO_2 and ventilation

6.2.1 Estimation of ventilation rates

Methods using CO_2 as a tracer gas are based on a fully mixed mass balance model:

$$V\frac{dC_{in}(t)}{dt} = QC_{out}(t) - QC_{in}(t) + G(t), \quad (6\text{-}1)$$

where V is space volume (m^3), $C_{in}(t)$ is indoor CO_2 concentration at time t (ppm), Q is volumetric airflow rate into (and out of) the space (m^3/h), $C_{out}(t)$ is supply outdoor CO_2 concentration at time t (ppm), $G(t)$ is CO_2 generation rate in the space at time t (mL/h).

Assuming Q, C_{out}(t) and $G(t)$ are constant, Eq. (6-1) can be solved as follows:

$$C_{in}(t) = C_{out} + \frac{G}{Q} + (C_{in}(0) - C_{out} - \frac{G}{Q})e^{-\frac{Q}{V}t}, \quad (6\text{-}2)$$

where $C_{in}(0)$ is indoor CO_2 concentration at time 0, and Q/V means space air change rate (h^{-1}).

When CO_2 generation rate G is zero, Eq. (6-2) can be expressed as:

$$C_{in}(t) = C_{out} + (C_{in}(0) - C_{out})e^{-\frac{Q}{V}t}. \quad (6\text{-}3)$$

If CO_2 generation rate is constant for a sufficient time, the last term on the right side of Eq. (6-2) converges to zero, and the CO_2 concentration at steady-state $C_{in}(\infty)$ can be expressed as:

$$C_{in}(\infty) = C_{out} + \frac{G}{Q}. \quad (6\text{-}4)$$

After a space becomes occupied by CO_2, the indoor CO_2 concentration begins to build up. This building up of CO_2 level continues until a steady-state is reached. The raising concentration in a well-mixed space can be expressed as eq. (6-2). The space air change rate can be solved using eqs. (6-2) and (6-3):

$$\frac{Q}{V} = \frac{1}{t}\ln\left(\frac{C_{in}(\infty) - C_{in}(0)}{C_{in}(\infty) - C_{in}(t)}\right) \quad (6\text{-}5)$$

The above equation requires knowledge of the steady state concentration $C_{in}(\infty)$, which can be

either observed by following the build-up as long as to reaching the equilibrium, or by solving the equilibrium level form the buildup curve [15]:

$$C_{in}(\infty) = \frac{C_b{}^2 - C_a C_c}{2C_b - C_a - C_c} \tag{6-6}$$

where C_a, C_b and C_c are concentrations (ppm) at equally spaced times a, b and c during the build-up (i.e., for which it holds that $a < b < c$ and $b - a = c - b$).

6.2.2 Estimation of CO_2 emission rate

Human CO_2 emission rate is a function of metabolic rate, which in turn is a function of physical activity level and body size [16]. The empirical equation for metabolic rate was derived from indirect calorimetry [17]:

$$EE = (3.941V_{O_2} + 1.11V_{CO_2}) \times 1.44, \tag{6-7}$$

where EE is Energy expenditure (kcal/day), V_{O2} is oxygen consumption rate (mL/min), and V_{CO2} is carbon dioxide production rate (mL/min).

When V_{CO2} is known, the Weir equation can be used to calculate V_{O2}, assuming the respiratory quotient (RQ), which is the ratio between V_{CO2} and V_{O2}. Thus, the EE can be calculated without the V_{O2} value. Converting EE (kcal/day) to metabolic rate M (W/m^2) using body surface area A_d, the empirical equation of metabolic rate was expressed as [18]:

$$M = \frac{0.35(0.23RQ + 0.77)\dot{V}_{O_2}}{A_d}, \tag{6-8}$$

The CO_2 emission rate V_{CO2} is the product of the O_2 consumption and RQ. Therefore, the equation to estimate CO_2 emission rate is:

$$\dot{V}_{CO_2} = \frac{RQ \cdot M \cdot A_d}{0.35(0.23RQ + 0.77)}. \tag{6-9}$$

Typical metabolic rate M for various activities given by the ASHRAE Handbooks are listed in the Table 6.1 [19].

Table 6.1. Values of physical activity levels (M) from the ASHRAE Handbooks [19]

Activity	M (W/m^2)	Met*
Sleeping	40	0.69
Reclining	45	0.77
Seated, quiet	60	1.03
Standing, relaxed	70	1.20
Walking about	100	1.72
Lifting/ packing	120	2.06

*Calculated as 1 Met = 58.2 W/m^2

Coley and Beisteiner [20] used empirical equations of carbon dioxide production rate derived by Ruch & Patton [21], which were adjusted for sex and age to predict the ventilation rate of classrooms. The empirical equations are expressed as:

Male teacher: $\dot{V}_{CO_2} = k$, (6-10)

Female teacher: $\dot{V}_{CO_2} = 0.9k$, (6-11)

Male student: $\dot{V}_{CO_2} = \frac{-0.78(a-5)+53}{40}k$, (6-12)

Female student: $\dot{V}_{CO_2} = \frac{-1.1(a-5)+51.6}{40}k$, (6-13)

Average student: $\dot{V}_{CO_2} = \frac{-0.94(a-5)+52.3}{40}k$, (6-14)

where $k = 0.148 A_d M \left(\frac{273+T_{in}}{273}\right)$, (6-15)

and V_{CO2} is carbon dioxide generation rate (L/h), a is age of student, M is metabolic rate (W/m^2) of the standard adult, A_d is body surface area (m^2), T_{in} is indoor air temperature (°C).

On the other estimation, Persily and de Jonge [22] introduce the following equation to estimate the human CO_2 emission rate, G (L/s):

$$G = 0.000569 RQ \cdot BMR \cdot M \quad (6\text{-}16)$$

where BMR is basal metabolic rate (MJ/day) that is energy requirement for the diary life (maintenance of body temperature, brain function, and cardiac and respiratory function) and depend of age and mass of the person [23] (see Table 6.2), and M is metabolic rate (met), that depends of physical activity [24] (Table 6.3).

This equation is derived based on that 1 kcal (0.0042 MJ) of energy expenditure is equal to 0.206 L of oxygen consumption [25].

Table 6.2. Schofield BMR values. (m is body mass in units of kg)

Age (yr)	BMR: MJ/day	
	Males	Females
<3	$0.249m - 0.127$	$0.244m - 0.130$
3 to 10	$0.095m + 2.110$	$0.085m + 2.033$
10 to 18	$0.074m + 2.754$	$0.056m + 2.898$
18 to 30	$0.063m + 2.896$	$0.062m + 2.036$
30 to 60	$0.048m + 3.653$	$0.048m + 3.653$
>= 60	$0.049m + 2.459$	$0.038m + 2.755$

Table 6.3. Values of physical activity levels (M) from compendium

Activity	*M* (met)	Range
Calisthenics—light effort	2.8	
Calisthenics—moderate effort	3.8	
Calisthenics—vigorous effort	8.0	
Child care		2.0 to 3.0
Cleaning, sweeping—moderate effort	3.8	
Custodial work—light	2.3	
Dancing—aerobic, general	7.3	
Dancing—general	7.8	
Health club exercise classes—general	5.0	
Kitchen activity—moderate effort	3.3	
Lying or sitting quietly		1.0 to 1.3
Sitting reading, writing, typing	1.3	
Sitting at sporting event as spectator	1.5	
Sitting tasks, light effort (e.g, office work)	1.5	
Sitting quietly in religious service	1.3	
Sleeping	0.95	
Standing quietly	1.3	
Standing tasks, light effort (e.g, store clerk, filing)	3.0	
Walking, less than 2 mph, level surface, very slow	2.0	
Walking, 2.8 mph to 3.2 mph, level surface, moderate pace	3.5	

Furthermore, our country, Japan has two standards for CO_2 emission rate: JIS A1406[1974] [26], SHASE-S102 [27]. As shown in Table 6.4 and 6.5, these CO_2 emission rate in the standards are described simply and not considered body height and weight. Against these backgrounds, Tajima *et al*. [28] measured CO_2 emission rate, O_2 consumption rate, and metabolic rate by using Douglas bag method with approximately total 70 voluntary Japanese subjects under different activity conditions. Moreover, they developed a prediction equation for human CO_2 production rate by regression analysis of obtained data. The prediction equation of CO_2 production rate $\dot{V}_{CO_2}$ (L/h) was expressed as:

$$\dot{V}_{CO_2} = 0.1589(94.4A_d + 83.9Met + 21.0C_g - 149.7), \tag{6-17}$$

where A_d is the body surface area for Japanese adult (m^2) and is expressed as:

$$A_d = 0.229W^{0.425}H^{0.725}, \tag{6-18}$$

Met is an occupants' activity level normalized by the metabolic rate of relax seated M_S (W):

$$Met = \frac{M}{M_S}, \tag{6-19}$$

C_g is the coefficient of gender (0: female, 1: male).

Table 6.4. CO_2 emission rate according to JIS A1406 [26] (adult male)

Work load	Metabolic rate		CO_2 emission rate (L/h)
	RMR	Met	
Resting	0.0	1.00	11.0
Sedentary work	0.0 ~ 1.0	1.00 ~ 1.83	12.9 ~ 23.0
Slow walk	1.0 ~ 2.0	1.83 ~ 2.66	23.0 ~ 33.0
Light work	2.0 ~ 4.0	2.66 ~ 4.32	33.0 ~ 53.8
Moderate work	4.0 ~ 7.0	4.32 ~ 6.81	53.8 ~ 84.0
Hard work	7.0 ~	6.81	84.0 ~

*Female and child CO_2 emission rate is 90% and 50% of male CO_2 emission rate, respectively

Table 6.5. CO_2 emission rate according to SHASE-S 102-2011 [27] (adult male)

Work load	Metabolic rate		CO_2 emission rate (L/h)
	RMR	Met	
Resting	0	1.0	13.2
Very light work	0～1	1.00 ~ 1.83	13.2 ~ 24.2
Light work	1～2	1.83 ~ 2.66	24.2 ~ 35.2
Moderate work	2～4	2.66 ~ 4.32	35.2 ~ 57.2
Hard work	4～7	4.32 ~ 6.81	57.2 ~ 90.2

*Female and child CO_2 emission rate is 90% and 50% of male CO_2 emission rate, respectively

6.3 Methods

6.3.1 Experimental facilities

The experiments were carried out in a small climate chamber whose volume was 1.7 m^3 (1.4 × 0.75 × 1.62 m) (Fig. 6.1). The experimental chamber was placed in a large thermal climatic chamber designed for studying thermal comfort [29,30]. The small chamber frames were made of wooden beams, and the walls were made of plastic foil. The small chamber was ventilated with outdoor air supplied to a ceiling plenum. The air entered the chamber uniformly through a perforated panel that formed the ceiling of the chamber, establishing a laminar downward piston flow from the whole ceiling. Due to the large size of the air supply area (1.4 m × 0.75 m) the velocity of the supplied air was very low (<< 0.2 m/s). The air was exhausted through an opening located 10 cm above the floor. An exhaust duct connected to an exhaust fan was used to exhaust the air from the chamber. The flow rate established by the exhaust fan was the same as the flow rate established by the supply fan. The rate of outdoor air supplied to and exhausted from the chamber was measured by an orifice equipped with an electronic manometer. The supply air was conditioned to the required temperature. Inside the small chamber, small

desktop fans ensured good mixing of the air.

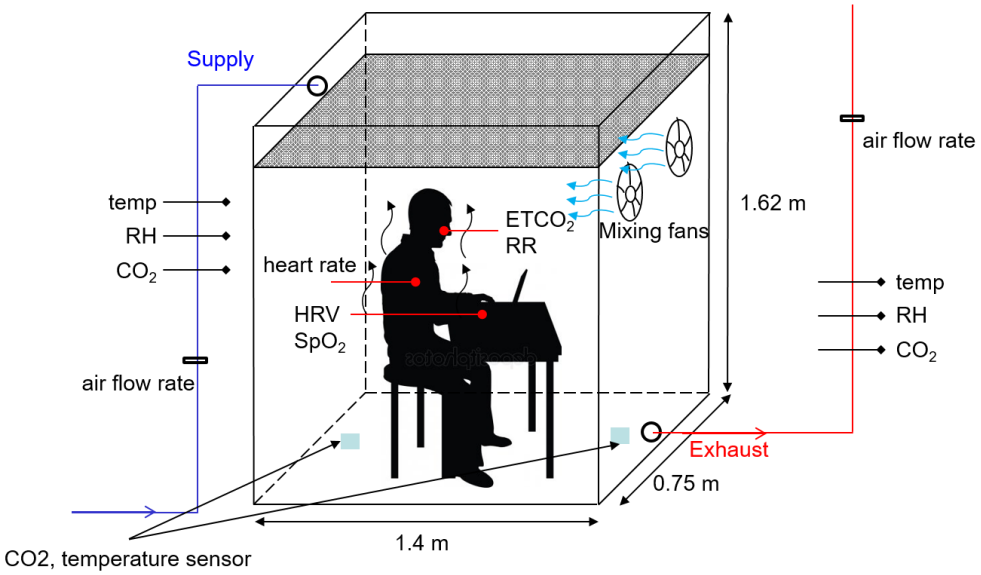

Figure 6.1. Schematic of the climate chamber and experimental setup.

6.3.2 Volunteers

Six male volunteers were recruited: four Asians and two Europeans. Their demographic data are shown in Table 6.6. The body surface area (BSA) was estimated using the empirical equation derived by DuBois [31].

Table 6.6. Demographic data of participants

Volunteer	Origin	Age (yr)	Height (m)	Weight (kg)	BSA* (m^2)	BMI** (kg/m^2)
1	Asian	26	1.67	61	1.68	21.9
2	Asian	25	1.66	56	1.61	20.3
3	Asian	35	1.77	59	1.73	18.8
4	Asian	23	1.75	68	1.82	22.2
5	European	56	1.87	94	2.19	26.9
6	European	30	1.78	78	1.95	24.6

*BSA = body surface area (m^2)
**BMI = body mass index (kg/m^2)

6.3.3 Experimental conditions

Five exposure conditions were established in the small chamber (Table 6.7). Each volunteer was exposed individually to each condition in random order for 2.5 hours. In one condition, termed M800, the ventilation rate to the small chamber was set so that the concentration of metabolically generated CO_2 was 800 ppm. In two other conditions, termed respectively MP1400 and MP3000, the

ventilation rate was maintained as at M800 and pure CO_2 was supplied to the chamber from a cylinder to maintain CO_2 concentrations of 1400 ppm and 3000 ppm, respectively; the concentration of other bioeffluents emitted by the subject did not change at these conditions so it was the same as in M800. In a further condition, termed M1400, the ventilation rate was reduced so that the metabolically generated CO_2 increased to 1400 ppm and in this condition the concetration of other bioeffluents also increased. This condition was established at both 23°C and 28°C and the latter was termed M1400W. In all other conditions the temperature was 23°C (see Table 6.7).

Conditions MP1400, MP3000, M1400, and M800 examined the effect of background CO_2 on the rate of CO_2 emitted by volunteers; they examined the impact of elevated pure CO_2 with other bioeffluent concentrations unchanged or elevated CO_2 with elevated levels of other bioeffluents. Conditions M1400 and M1400W examined the impact of elevated temperature causing thermal discomfort on the rate at which CO_2 was emitted by the subjects. In all conditions subjects wore similar clothing with thermal insulation estimated to be 1.0 clo. Figure 6.2 shows the five conditions whose effects were compared.

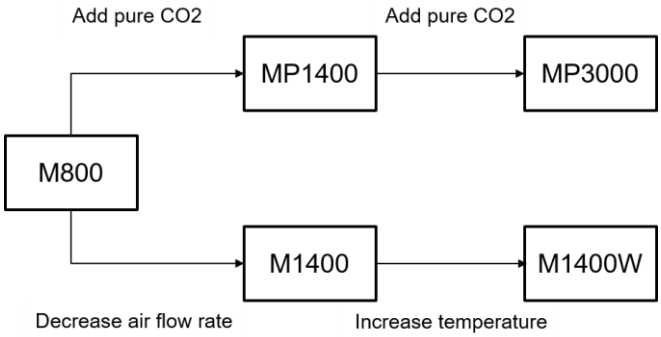

Figure 6.2. The five exposure conditions

Table 6.7. Planned conditions for different exposures

Condition	Outdoor air supply rate to the chamber (m^3/h)	Air change rate (h^{-1})	Pure CO_2 dosed from cylinders (l/min)	CO_2 level in the chamber (outdoor level at 400 ppm)	Temperature in the chamber (°C)
M800	47.5	27.9	-	800	23
M1400	19	11.1	-	1400	23
M1400W	19	11.1	-	1400	28
MP1400	47.5	27.9	0.475	1400	23
MP3000	47.5	27.9	1.74	3000	23

6.3.4 Measurements

During each experiment, CO_2, temperature, and relative humidity (RH) were measured in the small chamber. CO_2 was measured with an INNOVA 1302 monitor, with an accuracy of ± 2%, and by a Vaisala sensor connected to a Hobo logger, which registered temperature and relative humidity (RH) in the chamber with an accuracy of ±0.21°C for temperature and ±5% for RH. All the instruments had been calibrated. The exposures were performed in the morning, from 9:00 to 12:00, or in the afternoon, from 13:00 to 16:00.

The physiological responses that were measured included heart rate, End-Tidal partial CO_2 ($ETCO_2$), respiration rate, skin temperature at the temple, blood oxygen saturation (SpO_2), and heart rate variability (HRV). Heart rate was measured continuously with a Suunto smart belt (model: SS020566000) worn by the subjects. Skin temperature was measured continuously using iButtons™. $ETCO_2$, SpO_2, and respiration rate were measured simultaneously using a Lifesense Monitor by MedAir AB. The measurable range of $ETCO_2$ was 0–9.9 kPa, and the accuracy was ±0.2 kPa+6% of the reading, according to the manufacturer's specifications. The measurable range of SPO_2 was 0%–100%, and the accuracy was ±2%. The instrument estimated respiration rate and $ETCO_2$ by continuously monitoring the concentration of CO_2 in air sampled at the nostril of each subject, i.e. the concentration in the air that was inhaled and exhaled. HRV was measured by attaching an infra-red sensor to the subject's finger to monitor changes in peripheral blood circulation (CorSense® Heart Rate Variability Monitor). The time-domain measure of HRV was determined by the percentage of inter-beat intervals differing by more than 50 ms (pNN50). The value of pNN50 reflects the parasympathetic modulation of the heart and can be affected by stress [32]; the lower the PNN50 value, the higher the stress level. pNN50 denotes the percentage difference between adjacent normal and R-wave peak intervals (RR intervals) greater than 50 ms and is an indicator of heart rate variability.

Measurements of CO_2 concentration in the supply and exhaust air were used to estimate the rate of CO_2 emission from the subject.

For conditions where CO_2 was not added to the chamber from a gas cylinder (i.e., M800, M1400, and M1400W), the mean CO_2 concentration and the emission rate was estimated after the CO_2 level reached steady state using the following equation:

$$G = Q\left(C_{in} - C_{out}\right), \tag{6-20}$$

where C_{in} is the indoor CO_2 concentration at steady state (ppm), Q is volumetric airflow rate (m^3/h), C_{out} is the outdoor CO_2 concentration (ppm), and G is the CO_2 emission rate (mL/h). The air change rate was 28 h^{-1} so steady state concentration was obtained in less than 15 minutes.

For MP1400 and MP3000, when CO_2 was added to the chamber from a gas cylinder, the following equation was used:

$$G = Q\left(C_{pure+met} - C_{pure}\right), \tag{6-21}$$

where $C_{pure+met}$ is the CO_2 concentration comprising the pure CO_2 delivered from the cylinder and the metabolically generated CO_2 that was emitted by the subject, C_{pure} is the CO_2 concentration contributed only by pure CO_2, which was measured from the indoor CO_2 level that was reached within a few minutes after the subject had left the chamber.

Measurements of CO_2 were also used to estimate the air change rate in the chamber. For this purpose, the decay of CO_2 concentration was measured after the subject had left the chamber. The estimated air change rates from decay were compared with the rates measured using an orifice and an electronic manometer.

6.3.5 Statistical Analysis

Analysis of variance (ANOVA) was used to evaluate the effects of background CO_2 concentration and temperature on the parameters measured. The statistical analysis was performed with Microsoft Office Excel software (2016 version) with Visual Basic for Application code that was developed for the purpose. The significance level was set to P = 0.05.

6.4 Results

All measured physical parameters (temperature, and CO_2 concentration), and physiological parameters (skin temperature at the temple, $ETCO_2$, heart rate, HRV, and SpO_2) are listed in the supplementary material. CO_2 concentrations and temperatures in the chamber for each experimental condition were maintained as close to the intended level as possible.

Figure 6.3 shows an example of the time series of CO_2 concentration in the climate chamber for six volunteers under the M1400 condition. During this condition, the CO_2 concentration in the chamber reached steady state at approximately 10 min from the start of the experiment, i.e. from the moment each subject entered the chamber. Each experiment started immediately after the subject entered the chamber. Figure 3 shows differences in the steady-state CO_2 concentration levels due to individual

differences in the CO_2 emission rate. To determine the individual CO_2 emission rate, the steady-state CO_2 concentration was calculated as the time-averaged value for 60 min (t = 90–150 min from the test start). After 150 min, the subject left the chamber, and air change per hour (ACH) was then calculated from the CO_2 concentration decay curve.

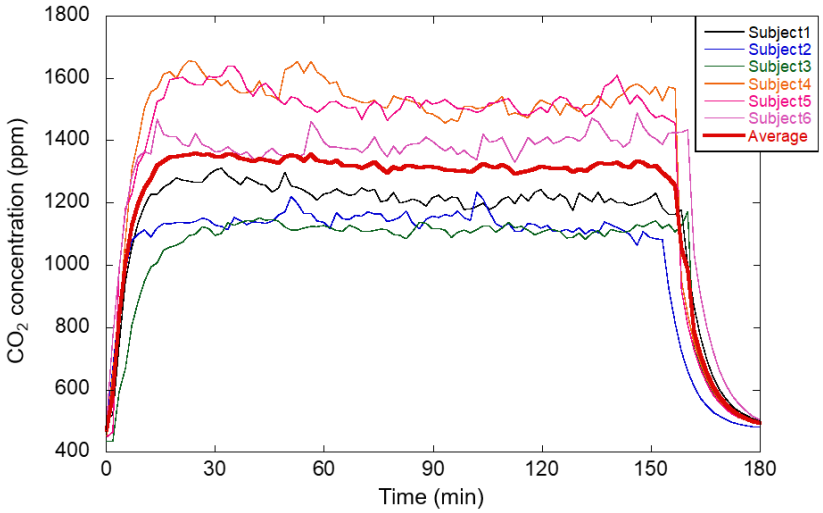

Figure 6.3. An example of the evolution of CO_2 concentration in the chamber at condition M1400

Figure 6.4 shows the estimated CO_2 emission rates in each experimental condition. Compared with the M800 condition, which can be considered as a baseline, CO_2 emission rates at higher background CO_2 concentrations decreased slightly but significantly. Significant differences ($P<0.05$) in CO_2 emission rate between M800 and M1400, and between M800 and MP3000 were observed. The difference between M800 and MP1400 approached significance ($P=0.068$). When room temperature was increased from 23°C to 28°C, the CO_2 emission rate increased significantly ($P<0.05$).

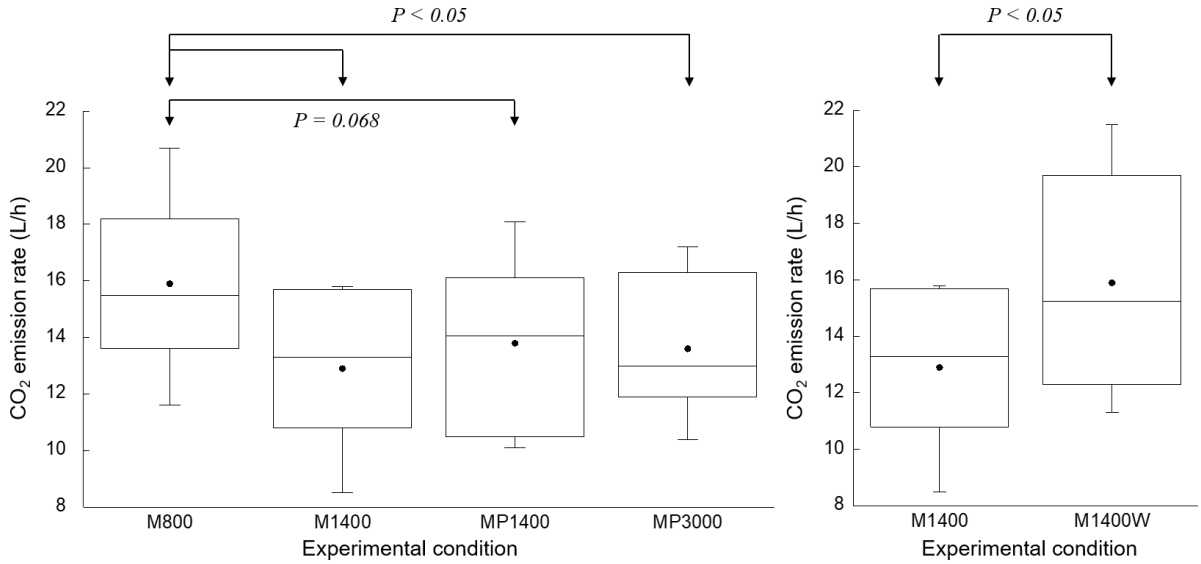

Figure 6.4. Calculated CO_2 emission rates under different experimental conditions.

Figure 6.5 shows the mean $ETCO_2$ under each experimental condition. The $ETCO_2$ increased as the CO_2 concentration in the chamber increased, indicating that raised blood gas levels were the reason for the reduced emission rate. The differences were significant between M1400 and MP1400 and between M1400 and MP3000 ($P<0.05$). The difference between M800 and MP3000 approached significance ($P=0.054$). There was no significant difference in $ETCO_2$ between M1400 and M1400W, i.e. there was no effect of air temperature on $ETCO_2$. Also, there were no differences when CO_2 levels was increased by restricting ventilation (M800 vs M1400) i.e. when the level of bioeffluents increased in the chamber; only by increasing CO_2 level artificially by dosing it from the cylinder increased $ETCO_2$.

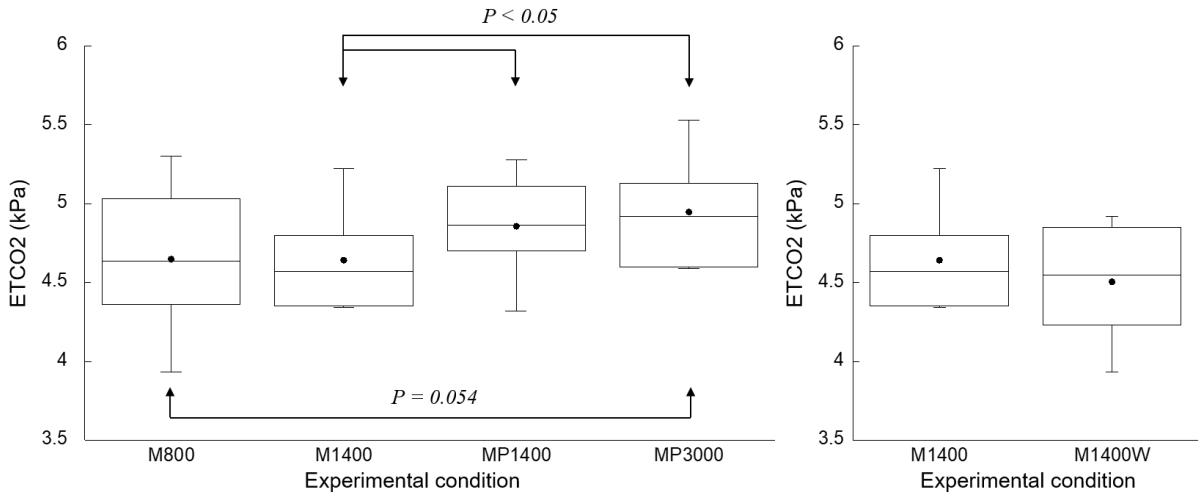

Figure 6.5. $ETCO_2$ under different experimental conditions

Figure 6.6 shows the results for heart rate under each experimental condition. Significant differences ($P<0.05$) were seen between M800 and M1400W and between M1400W and MP1400, indicating an effect of temperature (as would be expected) and of other bioeffluents, but no effect of pure CO_2 on HR.

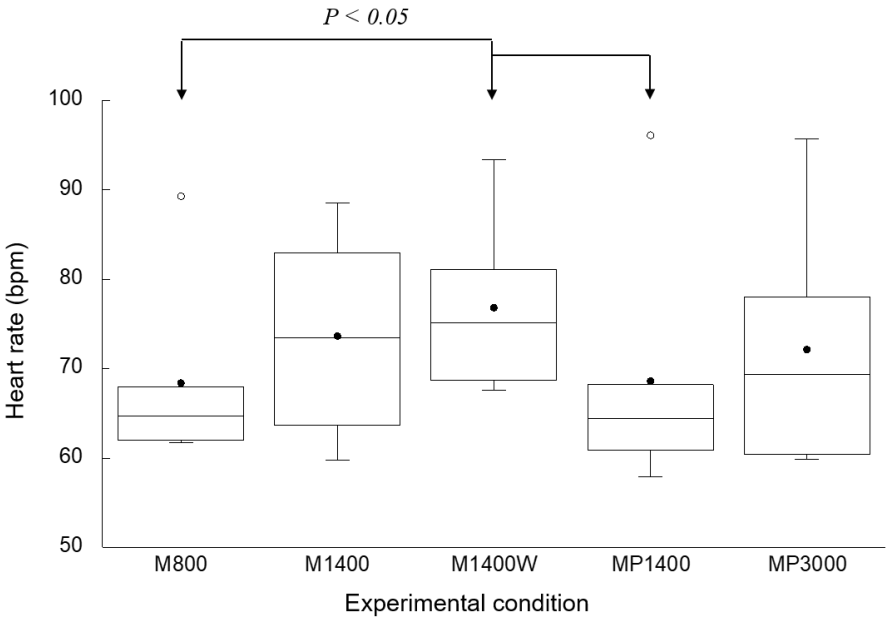

Figure 6.6. Heart rate under experimental conditions

Figure 6.7 shows the respiration rate under each experimental condition. Respiration rate did not differ significantly between the conditions.

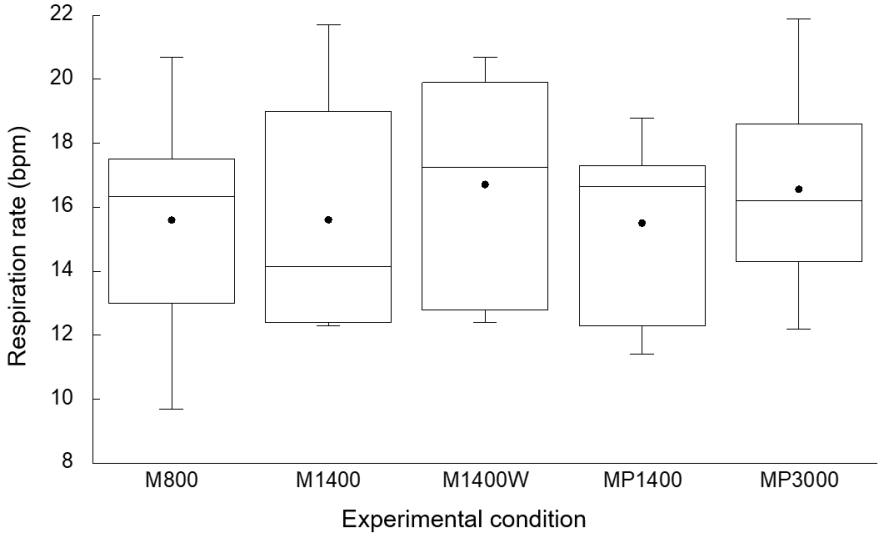

Figure 6.7. Respiration rate under different experimental conditions

Figure 6.8 shows no difference between conditions in terms of HRV (Heart Rate Variability). The pNN50 value in the M1400W condition was low, as would be expected if thermal discomfort had given rise to some stress, but was not significantly different from other experimental conditions.

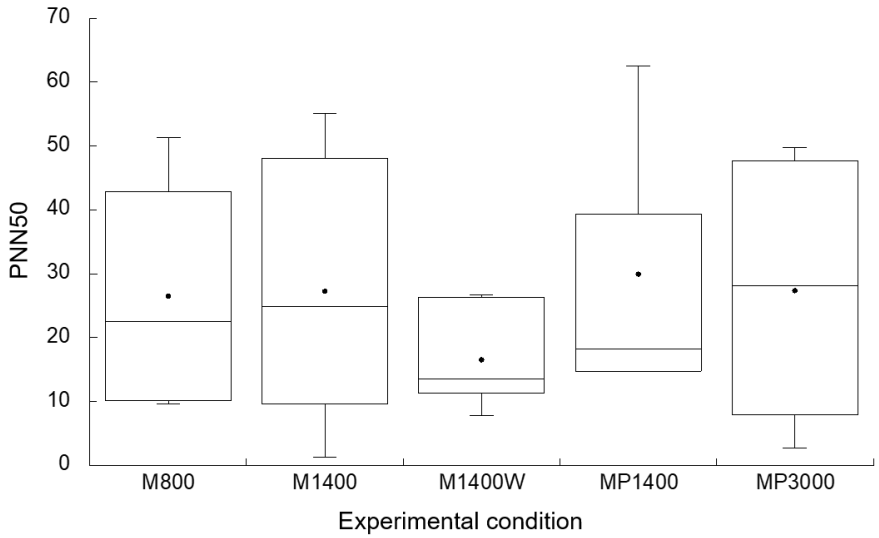

Figure 6.8. Heart rate variability (pNN50) under different experimental conditions

Figure 6.9 shows skin temperature measured at the temple under each experimental condition. Temple temperature increased with elevated room temperature, as would be expected: in M1400W it was significantly higher than in any of the other conditions ($P<0.05$), but there were no other significant differences.

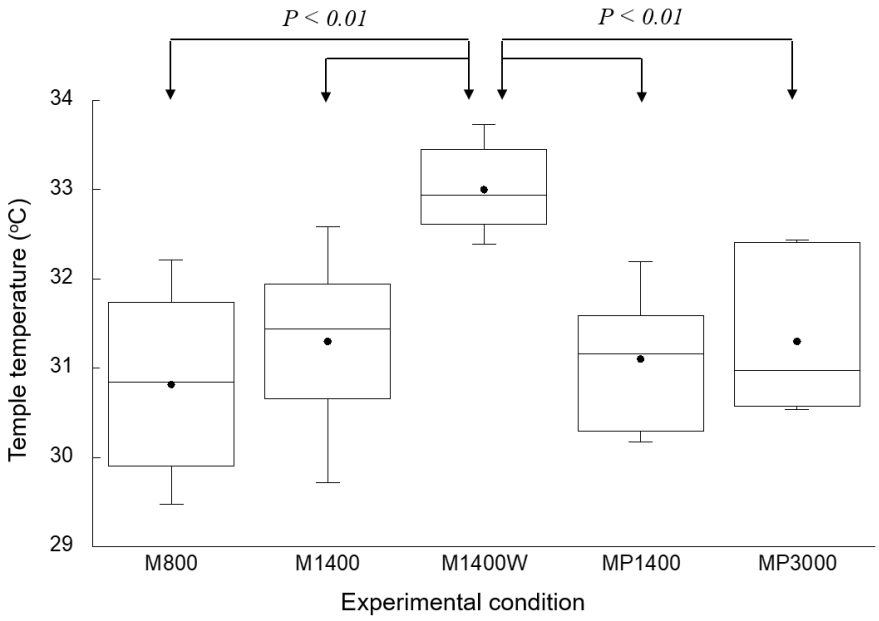

Figure 6.9. Skin temperature at the temple under different experimental conditions

6.5 Discussions

The present study indicates that the emission rate of CO_2 by occupants is affected not only by their activity but also by such environmental factors as temperature and airborne pollution, specifically the concentration of CO_2 and other bioeffluents. They cause physiological reactions that either reduce

or increase the elimination of CO_2 by respiration. Increased temperature causing discomfort and thermal discomfort will increase the emission rate while increased CO_2 will reduce it. Since only six subjects participated in the present work, the magnitude of these changes in CO_2 emission rate cannot be determined with any certainty, but it must be emphasized that despite the considerable variations between subjects (see supplementary material) these effects reached statistical significance at $P<0.05$ or approached this level of formal significance very closely ($P <0.06$), so they should be considered non-random. Similar studies with larger groups are required to determine and generalize the size of the observed effects so as to be able to draw conclusions regarding the implications of the present findings for determination of ventilation rate based on CO_2 concentration and control of ventilation using CO_2 as an input variable in practice. It might still be the case that changes due to activity, age, food intake etc., which are all likely to affect the generation rate of CO_2 are more meaningful that changes in production rate due to background CO_2 and temperature. And these additional studies need to determine whether this is the case or not.

Increased temperature increased the emission rate of CO_2. At the same time, heart rate increased (Fig. 6) suggesting increased metabolic activity. The metabolic rate at these two temperatures was calculated using conventional assumptions (supplementary material) and it was found that metabolic rate at 28°C was 92 W/m^2 (1.57 met) and at 23°C it was 66 W/m^2 (1.13 met). Raised air temperature therefore increased the metabolic rate by as much as increasing activity from light sedentary to moderate work. The present results are therefore in accordance with the study by Luo et al. [33], which showed that when building occupants feel either warm or cool, these sensations affect their metabolism and increase CO_2 emissions compared with what is observed at thermal neutrality. In the present work, skin temperature at the temple (Fig. 6.9) provides evidence that subjects felt warm. Furthermore, HRV was lowest at M1400W (Fig. 6.8), and although this was not a significant effect it is consistent with higher stress as a result of increased temperature.

Current ventilation standards do not prescribe higher ventilation rates at higher temperatures except in the Australian standard in which ventilation rates must be increased at temperatures higher than 27°C [7]. If thermal neutrality is achieved at elevated temperatures, there is no need to increase ventilation rate because the emission rate of CO_2 would not change. This must be determined experimentally. However, at temperatures higher than 26°C-27°C it may be difficult to maintain thermal neutrality. This would initiate physiological activity to reduce the impact of increased temperature. According to the Adaptive Thermal Comfort model, thermal comfort can be achieved by psychological and behavioural adaptation even at higher temperatures. The latter involve reducing clothing insulation and activity and additional cooling, e.g. by increasing the air movement. Reducing activity will reduce metabolic rate and the production rate of CO_2 but it will also influence work output [34]. The impact of psychological adaptation should be studied in future experiments, so that the implications for ventilation rates based on CO_2 can be determined.

If the occupant rates of emission of CO_2 are lower when pollution is higher, then the control of ventilation using CO_2 may be affected. In other words, the simple linear relationship between the level of CO_2 and level of other pollutants may not be preserved and ventilation rates may have to be increased to adjust for reduced CO_2 emission as pollution increases. Increased retention of CO_2 may also have implications for the estimation of actual outdoor air supply rates from observed CO_2 levels. In many research studies in the field, it is impossible to measure ventilation rates. They are consequently estimated based on the measured CO_2 concentration, assuming that CO_2 emission rate will not change. However, the present results suggest that this assumption may not be valid and that ventilation rates may therefore be estimated erroneously, especially when the CO_2 levels measured are high. The present results suggest that at high CO_2 levels (or when air pollution is high as CO2 is a marker of such an instance) ventilation rates may in fact be lower than these that are estimated by assuming that CO_2 emission rates from humans is unchanged.

As described in the introduction section, a reduced CO_2 emission rate may be caused by reduced elimination of CO_2 from the blood by respiration, as indicated by the present $ETCO_2$ results, and the resulting increased acidosis as stipulated by Bako-Biro *et al*. [8] and Wargocki and Wyon [35] would explain the headache and difficulty in thinking clearly that have been reported when the outdoor air supply rate is reduced. The retained CO_2 would eventually be eliminated through the kidneys or stored in bone marrow but in the short term it would be a plausible mechanism for the observed negative effects of raised CO_2 on mental performance [11]. $ETCO_2$ increased in the present study with increased CO_2 but there were no effects on respiration rate (Figs. 6.5 and 6.7); that respiration did not change is also indicated by the absence of any effects on HRV (pNN50), as heart rate variability is closely related to respiration rate [14]. $ETCO_2$ was not changed at elevated temperature, despite the expectation that increased metabolic rate (indicated by raised HR) must have increased the rate at which of CO_2 was generated in the body, indicating increased elimination of CO_2. As heart rate increased and respiration rate did not, the increased elimination of CO_2 seems likely to have occurred because of a higher minute volume or tidal volume, i.e. deeper breathing. We did not perform other measurements such as Respiratory Inductive Plethysmography to further characterize breathing, so this should be a priority in future studies.

When the CO_2 concentration was 1400 ppm, $ETCO_2$ was significantly higher when the CO_2 concentration was increased by dosing CO_2 from a cylinder (MP1400) than it was when the air supply was reduced to allow the concentration of metabolically generated CO_2 to increase (M1400) (Fig. 6.5). This suggests that the presence of other bioeffluents could have counteracting somewhat the physiological response to pure CO_2 and this possibility should be examined in future experiments. If this is the case, it would explain why experiments showing that mental performance is reduced when CO_2 levels are increased by adding pure CO_2 summarized by Fisk et al. [36] could potentially overestimate the effects that occur when the outdoor air supply rate is reduced to achieve the same CO_2

concentrations.

Heart Rate Variability (HRV) as indicated by pNN50 did not change when CO_2 was increased. This is in accordance with the study reported by Cao et al. [37] who showed that elevated CO_2 in a cockpit simulation did not affect the stress level of pilots taking the test. But this result differs slightly from the study reported by Zhang et al. [11] whose results suggest increased stress by increased level of alpha-amylase at higher CO_2 concentration. In addition, $ETCO_2$ increased when the CO_2 emission rate was reduced but this had no significant effects on respiration rate, heart rate or heart rate variability (Figure 6.10).

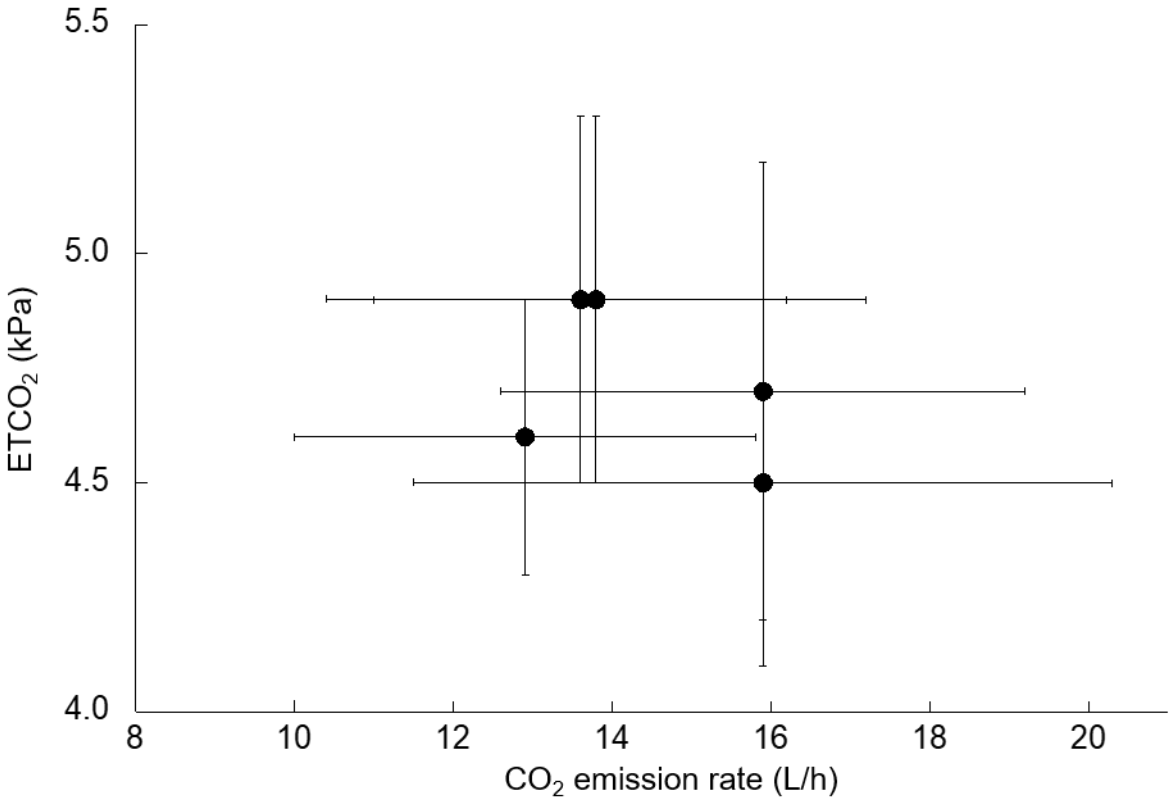

Figure 6.10. Relationship between $ETCO_2$ and CO_2 emission rate

The measured CO_2 emission rate for each subject under the reference exposure condition (M800) was compared with the CO_2 emission rate estimated by the empirical equations recommended in the ASHRAE Handbook [19] and by Persily and de Jonge [22] (see section 6.2.2). We assumed metabolic rate of 60 to 70 W/m2 and 1.3 to 1.5 met associated with light work when seated, and a respiratory quotient of 0.83 for estimating the CO_2 generation rate. Figure 6.11 shows the comparison of CO_2 emission rate with estimated value from empirical equations and the other researches. The CO_2 emission rate predicted in this way was slightly higher than the CO_2 emission rate measured in the present study. Instead of the empirical equation proposed by ASHRAE Handbook, the empirical

equation proposed by Persily and Jonge may predict the CO_2 emission rate more accurately because the equation takes into account the age of the subject. It can be concluded that current method proposed in the standard may overestimate the emission rate of CO_2 and this needs to be verified in the future studies. Actually another experiment of Qi et al. [38], Fan et al. [39], Zhai et al. [40] seem to support this observation.

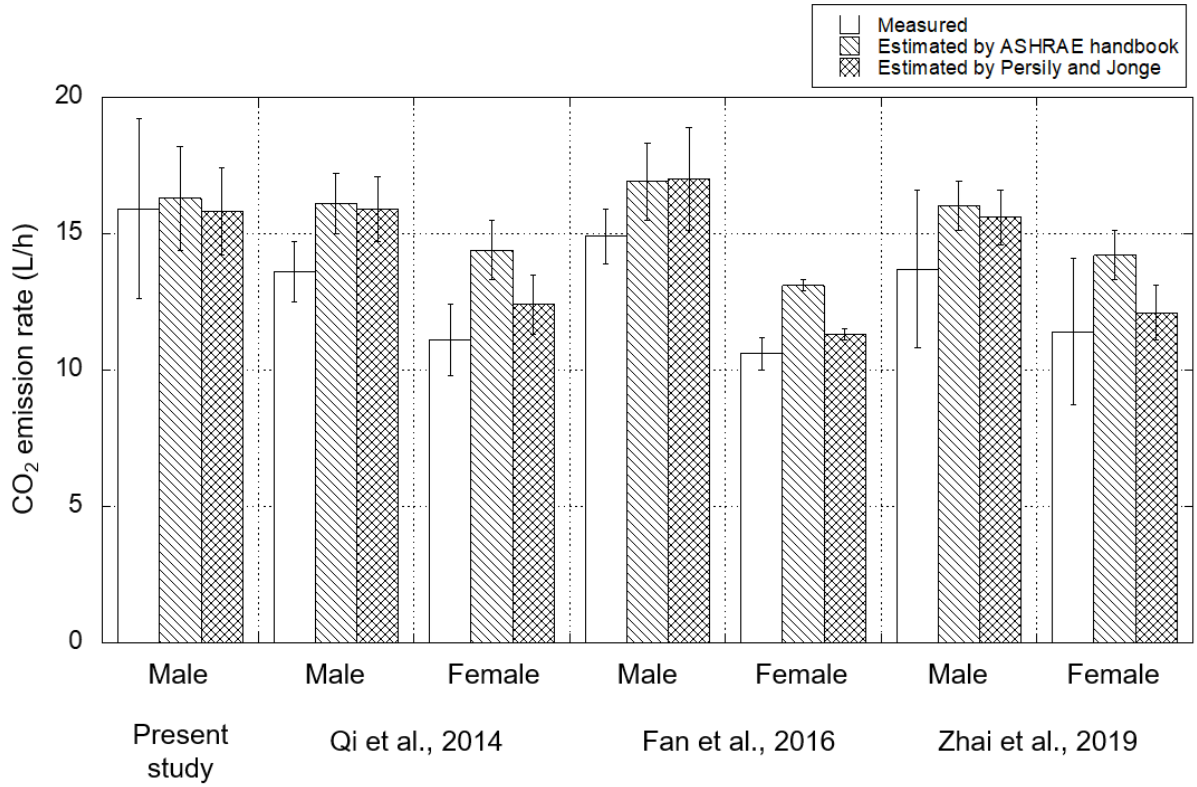

Figure 6.11. Comparison of CO_2 emission rate with estimated value from empirical equations and the other researches.

Although only six subjects participated, systematic and significant differences were found. The results will have to be validated with larger groups and the changes compared directly with changes in CO_2 emission rates caused by changes in activity level. Subjects were blind to exposure conditions except for the raised temperature condition in which they could perceive that the temperature was higher. The subjects were exposed for only 2,5 hours to each condition. It is not known whether the observed changes would be maintained or would become even larger if exposures were longer. This should also be investigated in future experiments. The emission rates of CO_2 were quite low, suggesting low activity levels.

6.6 Conclusions

The experiments reported here investigated the effect of raised temperature and background CO_2 on the rate at which CO_2 is emitted by occupants. Increasing the temperature from 23 °C to 28 °C

significantly increased the measured CO_2 emission rate. Increasing the background CO_2 concentration from 800 ppm to 1400 ppm and 3000 ppm significantly reduced the CO_2 emission rate. Measured $ETCO_2$ increased, indicating increased acidosis (an increase in the blood gas concentration of CO_2) but no changes in respiration rate were found. Stress as indicated by heart rate variability did not change at higher background CO_2 or at raised temperature although skin temperature at the temple increased at 28°C. Although only 6 subjects participated, these effects were statistically significant.

References

1. Wargocki P, Wyon DP, Baik YK, Clausen G, Fanger PO. 1999. Perceived air quality, sick building syndrome (SBS) symptoms and productivity in an office with two different pollution loads. Indoor air, 9(3), 165-179.
2. Sundell J, Levin H, Nazaroff WW, Cain WS, Fisk WJ, Grimsrud DT, Gyntelberg F, Li Y, Persily AK, Pickering AC, Samet JM, Spengler JD, Taylar ST, Weschler CJ. 2011. Ventilation rates and health: multidisciplinary review of the scientific literature. Indoor air, 21(3), 191-204.
3. Wargocki P, Wyon DP. 2013. Providing better thermal and air quality conditions in school classrooms would be cost-effective. Building and Environment, 59, 581-589.
4. Persily A. 2015. Challenges in developing ventilation and indoor air quality standards: The story of ASHRAE Standard 62. Building and Environment, 91, 61-69.
5. Tsushima S, Wargocki P, Tanabe S. 2018. Sensory evaluation and chemical analysis of exhaled and dermally emitted bioeffluents. Indoor air, 28(1), 146-163.
6. Fang L, Clausen G, Fanger PO. 1998. Impact of temperature and humidity on the perception of indoor air quality. Indoor air, 8(2), 80-90.
7. Australia, Green Building Council. Green Star-Design & As Built. 2014.
8. Bakó-Biró Z, Wargocki P, Weschler CJ, Fanger PO. 2005. Poor indoor air quality slows down metabolic rate of office workers. In Proceedings of Indoor Air 2005, Beijing, Vol. I (1):76 –80.
9. Danuser B. 2001. Candidate physiological measures of annoyance from airborne chemicals. Chemical senses, 26(3), 333-337.
10. Larsen ST, Nielsen GD. 2000. Effects of methacrolein on the respiratory tract in mice. Toxicology letters, 114(1-3), 197-202.
11. Zhang X, Wargocki P, Lian Z. 2017. Physiological responses during exposure to carbon dioxide and bioeffluents at levels typically occurring indoors. Indoor Air, 27(1), 65-77.
12. Lifson N, Gordon GB, Visscher MB, Nier AO. 1949. The fate of utilized molecular oxygen and the source of the oxygen of respiratory carbon dioxide, studied with the aid of heavy oxygen. J Biol Chem, 180(2), 803-11.
13. Guais A, Brand G, Jacquot L, Karrer M, Dukan S, Grévillot G, ... Schwartz L. 2011. Toxicity of carbon dioxide: a review. Chemical research in toxicology, 24(12), 2061-2070.

14. Vai F, Bonnet JL, Ritter PH, Pioger G. 1988. Relationship between heart rate and minute ventilation, tidal volume and respiratory rate during brief and low level exercise. Pacing and Clinical Electrophysiology, 11(11), 1860-1865.
15. Hänninen O. 2013. Novel second-degree solution to single zone mass-balance equation improves the use of build-up data in estimating ventilation rates in classrooms. Journal of Chemical Health & Safety, 20(2), 14-19.
16. Persily AK. 1997. Evaluating building IAQ and ventilation with indoor carbon dioxide (No. CONF-970668-). American Society of Heating, Refrigerating and Air-Conditioning Engineers, Inc., Atlanta, GA (United States).
17. Weir JDV. 1949. New methods for calculating metabolic rate with special reference to protein metabolism. The Journal of physiology, 109(1-2), 1-9.
18. Nishi Y. 1981. Measurement of thermal balance of man. In Studies in environmental science (Vol. 10, pp. 29-39). Elsevier.
19. ASHRAE. 2013. ASHRAE Handbook – Fundamentals, Atlanta, GA, American Society of Heating, Refrigerating and Air-Conditioning Engineers.
20. Coley DA, Beisteiner A. 2002. Carbon dioxide levels and ventilation rates in schools. International journal of ventilation, 1(1), 45-52.
21. Ruch TC, Patton HD. 1965. Physiology and biophysics. W.B. Saunders, Philadelphia.
22. Persily A, de Jonge L. 2017. Carbon dioxide generation rates for building occupants. Indoor air, 27(5), 868-879.
23. Schofield WN. 1985. Predicting basal metabolic rate, new standards and review of previous work. Human nutrition. Clinical nutrition, 39, 5-41.
24. Ainsworth BE, Haskell WL, Herrmann SD, Meckes N, Bassett Jr. DR, Tudor-Locke C, ... & Leon AS. 2011 Compendium of Physical Activities: a second update of codes and MET values. Medicine & science in sports & exercise. 2011; 43: 1575-1581.
25. Lusk G. 1924. Analysis of the oxidation of mixtures of carbohydrate and fat: a correction. J. Biol. Chem, 59, 41-42.
26. JIS. 2010. JIS A 1406[1974] Method for Measuring Amount of Room Ventilation (Carbon Dioxide Method), Japanese Industrial Standards Committee
27. SHASE. 2011. SHASE-S102-2011 Ventilation Requirements for Acceptable Indoor Air Quality. The Society of Heating, Air-Conditioning and Sanitary Engineers of Japan.
28. Tajima M, Inoue T, Ohnishi Y. 2014. Derivation of equation for personal carbon dioxide in exhaled breath intended to estimation of building ventilation. In Proceedings of the 35th AIVC Conference 'Ventilation and Airtightness in Transforming the Building Stock to High Performance (pp. 24-25).

29. Kjerulf-Jensen P, Fanger PO, Nishi Y, Gagge AP. A new type test chamber in Copenhagen and New Haven for common investigation of man's thermal comfort and physiological reactions, ASHRAE Journal, January, 1975, pp. 65–68.
30. Toftum J, Langkilde G, Fanger PO. 2004. New indoor environment chambers and field experiment offices for research on human comfort, health and productivity at moderate energy expenditure. Energy and Buildings, 36(9), 899-903.
31. DuBois DF. A formula to estimate the approximate surface area if height and body mass be known. Arch Intern Med, 17, 863-871, 1916.
32. Stein PK, Kleiger RE. 1999. Insights from the study of heart rate variability. Annual review of medicine, 50, 249.
33. Luo M, Zhou X, Zhu Y, Sundell J. 2016. Revisiting an overlooked parameter in thermal comfort studies, the metabolic rate. Energy and Buildings, 118, 152-159.
34. Lan L, Wargocki P, Wyon DP, Lian Z. 2011. Effects of thermal discomfort in an office on perceived air quality, SBS symptoms, physiological responses, and human performance. Indoor air, 21(5), 376-390.
35. Wargocki P, Wyon DP. 2017. Ten questions concerning thermal and indoor air quality effects on the performance of office work and schoolwork. Building and Environment, 112, 359-366.
36. Fisk W, Wargocki P, Zhang X. 2019. Do Indoor CO 2 Levels Directly Affect Perceived Air Quality, Health, or Work Performance?. ASHRAE Journal, 61(9).
37. Cao X, MacNaughton P, Cadet LR, Cedeno-Laurent JG, Flanigan S, Vallarino J, ... & Allen JG. 2019. Heart rate variability and performance of commercial airline pilots during flight simulations. International journal of environmental research and public health, 16(2), 237.
38. Qi, M. W., Li, X. F., Weschler, L. B., & Sundell, J. CO 2 generation rate in Chinese people. Indoor Air, 24(6), 559-566, 2014.
39. Fan G, Xie J, Liu J. 2016. Human CO2 generation rate calculation based on field measurement of CO2 concentration in a naturally ventilated room. Proceedings of Indoor Air, 2016, 223.
40. Zhai Y, Li M, Gao S, Yang L, Zhang H, Arens E, Gao Y. 2018. Indirect calorimetry on the metabolic rate of sitting, standing and walking office activities. Building and Environment, 145, 77-84.

Chapter 7: Summary and Future works

7.1 Summary

The life of modern people, who spend most of their lives indoors and have connections to various communities, poses health risks on various scales. In order to assess the health risks, it is essential to predict the risks in social scale and indoor scale separately. In Chapter 2 and 3, focusing on epidemic spread of infectious diseases on the social scale, we developed a deterministic mathematical epidemic model to replace the stochastic multi agent simulation and examined the effect of vaccination behavior on epidemic dynamics. In Chapter 4 and 5, focusing on exposure phenomenon on the indoor scale, we developed of numerical human body model for indoor environment analysis which enables risk assessment of inhalation and dermal exposure. Although Chapter 6 also focused on health risk on the indoor scale, we investigated the effects of indoor environmental factors on the CO_2 emission and physiological responses by using experimental approach.

In Chapter 2, we proposed three theoretical frameworks of the vaccination game that considers imperfect vaccination and intermediate protective measures corresponding to (i) an infinite and well-mixed population using mean field approximation, (ii) Complex networks using mean field approximation with different degree distributions (Poisson's degree distribution and power law distribution), and (iii) regular random graph using pair approximation. For expressing the stochastic effect of imperfect vaccination and intermediate protective measure on epidemic dynamics, we developed two scenarios: effectiveness model and efficiency model. The exact mathematical formulas for both dynamic processes, namely, epidemic spreading and strategy updating, are explicitly discussed. When solving the ODEs for three epidemic models, the critical vaccination coverage and the final fractions for each individual were derived. We validated our frameworks by comparing its predictions with simulation results. As long as the same coefficient values, namely effectiveness and efficiency, are assumed, an intermediate protective measure is marginally inferior to an imperfect vaccination

In Chapter 3, to examine the optimal vaccination-subsidizing policies for combating seasonal epidemics, we used a comprehensive 'vaccination game' with intertwined decision-making dynamics and epidemic dynamics described in Chapter 2. In this study, we considered four subsidy variants; three free-ticket subsidies targeting different individuals (voluntary vaccinators, non-vaccinators, or both) and a discount subsidy aimed exclusively at voluntary vaccinators to partly offset their vaccination cost. We implemented these games as multi-agent simulations (MAS)and a mean-field approximation. The MAS approach allowed us to investigate how the underlying topologies of the social network affect the

performance of subsidized vaccination. The mean-field approach helped us to independently confirm some of the key the results obtained using the MAS approach, and to better understand the effects of an imperfect vaccine. We evaluated the performance of different subsidies by tracking three quantities: vaccination coverage, the final epidemic size, and the total social payoff. The total social payoff in particular was an aggregate measure taking into account the vaccination cost, the cost of an epidemic, and the tax burden to subsidize vaccination.

In Chapter 4, we developed three-dimensional computer models based on CT data, which describe the flow and heat transfer properties in upper airways as a first step of inhalation exposure analysis. Through the analysis of flow patterns and temperature, the local convective heat flux distributions in upper airways and the average convective heat transfer coefficients as functions of respiratory air flow rate were discussed. In addition, the influences of geometric variations in numerical airway models (i.e., rat, dog, monkey and two human models) on the efficiency of the convective heat transfer were discussed. Moreover, the effect of respiratory airflow rate on convective heat transfer inside airway models was investigated.

In Chapter 5, we developed a comprehensive numerical analysis using CSP with respiratory tract and indoor CFD technique to explore the contribution ratio of first- and secondhand exposure of smokers and nonsmokers to the chemicals emitted from e-cigarettes. The numerical analyses were performed using a simple room model occupied by two occupants: smoker and non-smoker. As a result, the amount of chemical compounds absorbed into the respiratory tract and the concentration of chemical compounds contained in exhaled air strongly depend on the type of chemical compounds. The respiratory retention of chemicals in the respiratory tract was in good agreement with previous experimental results. Our results also confirmed that chemicals exhaled by e-cigarette users into the indoor environment become new indoor air pollutants that are exposed to nonsmokers by inhalation and dermal exposure due to advection and diffusion in indoor environment. Formaldehyde ingested by nonsmokers via inhalation and dermal exposure in the worst-case scenario was estimated at 5.7% and 6.4%, respectively.

In Chapter 6, to investigate the effect of raised temperature and background CO_2 on the CO_2 emission rate from occupants, we conducted the subjective experiments using a small chamber. Increasing the temperature from 23 °C to 28 °C significantly increased the measured CO_2 emission rate. Increasing the background CO_2 concentration from 800 ppm to 1400 ppm and 3000 ppm significantly reduced the CO_2 emission rate. Measured $ETCO_2$ increased, indicating increased acidosis (an increase in the blood gas concentration of CO_2) but no changes in respiration rate were found. Stress as indicated by heart rate variability did not change at higher background CO_2 or at raised temperature although skin temperature at the temple increased at 28°C. Although only 6 subjects participated, these effects were statistically significant.

7.2 Planed future works

7.2.1 Research related to epidemic dynamics on complex networks (Chapter 2 and 3)

To develop a mathematical epidemic model as an alternative to MAS, we have selected the epidemic models corresponding to the simplest infinite and well-mixed population, as well as the representative complex networks such as BA scale free network, ER random network, and random regular graph. However, they are not enough to be alternative to MAS. As future works, there are the adaptation of theoretical epidemic model to lattice networks with stronger locality and temporal networks which captures changes in network topologies due to movement of people in the real world.

7.2.2 Research related to inhalation and dermal exposure to e-cigarette (Chapter 5)

Recently, it has become popular in the US to use a solution containing a cannabis component in electronic cigarettes, and it has become a social problem that people suffer from health damage. Against this background, it is a future work to understand the exposure risk of cannabis components due to the use of electronic cigarettes. Furthermore, since our numerical analysis model solves by coupling the gas phase region with the concentration distribution in the airway tissue and skin tissue, it takes much time to stabilize the numerical analysis. Therefore, it is an urgent work to speed up the analysis without lowering the prediction accuracy of the analysis.

7.2.3 Research related to CO_2 emission and physiological responses to indoor environment (Chapter 6)

In Chapter 6, we recruited six subject to conduct the experiment for CO_2 emission rate. However, the number of volunteers were not enough to develop the empirical equation for CO_2 emission rate with consideration of internal and external factors. Thus, we must have additional experiments. To examine the influence of internal factors such as race, age, and gender, we will recruit a sufficient number of subjects so that the experimental results can be analyzed at multiple levels. Furthermore, to investigate the influence of external factors such as indoor temperature and humidity, CO_2 concentration, and clothing, subjective experiments are conducted in the climate chamber under different indoor environmental conditions. Specifically, to study the temperature effect, the indoor temperature is set in three conditions: the thermally neutral condition (23°C), low temperature condition (18°C), and high temperature condition (28°C). Moreover, to study the effect of indoor CO_2 concentration, the ventilation rate is controlled so that the CO_2 concentration is about 800, 1400, and 3000 ppm. By measuring the CO_2 concentration under the above different environmental conditions, we will develop the empirical equation for the CO_2 emission rate with consideration of the internal and external factors. Furthermore, we will investigate the effect on other physiological responses to the environmental factors.

For calculation of CO_2 emission rate by monitoring CO_2 concentration in the climate chamber, the room is assumed a completely mixed field. Although the mixing fan is installed so that the air is

sufficiently agitated in many studies, it is difficult to form a complete mixing field without any distribution. Therefore, there is a difference between the CO_2 emission rate calculated from the CO_2 concentration observed indoors and the CO_2 actually emitted from the nose or mouth. To evaluate this difference accurately, it is necessary to predict the non-uniform concentration distribution formed around the human body, especially in the respiratory region. Therefore, based on the numerical human model which has been developed in Chapter 3, we will develop a model that reproduces the subject experiment by precisely integrating the O_2-CO_2 gas exchange model using CFD technique. The developed model is verified by comparison with the results of subjective experiment, and the indoor volume average concentration and the concentration in the respiration region which cannot be observed in the subjective experiment are clarified.